

From quantum spin chains to square lattice Heisenberg anti-ferromagnets

Thèse N° 9724

Présentée le 6 septembre 2019
à la Faculté des sciences de base
Laboratoire de magnétisme quantique
Programme doctoral en physique

pour l'obtention du grade de Docteur ès Sciences

par

Noore Elahi SHAIK

Acceptée sur proposition du jury
Prof. P. Ricci, président du jury
Prof. H. M. Rønnow, directeur de thèse
Prof. F. Becca, rapporteur
Prof. K. Lefmann, rapporteur
Prof. F. Mila, rapporteur

2019

Acknowledgements

First and foremost, I would like to thank my advisor Prof. Henrik M. Rønnow for inviting me into his research group. Working under his guidance at Laboratory for Quantum Magnetism, both during my masters and my doctoral research, has been a very fulfilling experience. Henrik has always surprised me with his keen observation for important details in a complex mess of results that I used to bring him. While I constantly dabbled in various irrelevant details of my work, Henrik with his intuitive understanding of the underlying picture, has always helped me to focus my attention on the relevant aspects. His deep insight and understanding of the underlying physics, his experience and wisdom, have been pivotal in making this research work possible and I shall forever be thankful for his guidance.

I would also like to express my deep gratitude towards Dr. Dimitri Ivanov who, despite not being directly affiliated to our research group, took some personal time off from his busy schedule to help me in times of need. He has always been available to answer my theoretically motivated questions and his guidance has been an immense help in carrying this project forward. I shall be greatly indebted to Dr. Bastien Dalla Piazza a former doctoral student at LQM, whose research work underlies the motivation for mine. My project is an extension of his work and all the mathematical and computational framework built by him were pivotal for this project. The ‘Quantum wolf’ cluster built by him has been the only source of computational power without which this research work would not have been possible and I believe that he is more than an equal participant in this research work.

I would like to thank all the members I had a pleasure of meeting at LQM, who have been part of this journey (chronologically of course). I would like to thank Dr. Julian Piatek who guided me in my initial days of dabbling in experimental work. I am glad that I did not break anything more than a glass tube on the SQUID device. I would like to thank Prof. Johan Chang and his former doctoral student Dr. Claudia G. Fatuzzo for their collaborative work and providing me with an opportunity to visit PSI synchrotron facility to see the the ARPES experiment. Through them I was able to understand the real complexities and difficulties involved in experimental research. I am extremely happy and thankful to have met two of my closest colleagues and friends Dr. Ivan Kovacevich and Dr. Peter Babkevich who have made LQM more than a work place for me. I would always cherish their friendship. I would like to thank Prof. Marco Grioni, Dr. Simon K. Moser for their collaborative work. Special thanks to Prof. Frédéric Mila who has not only been a collaborator on various projects but also my mentor. It has been a

Acknowledgements

great pleasure working alongside colleagues from the 'old LQM gang' including Dr. Mingee Chung, Dr. Alex J. Kruchkov, Dr. Ping Huang, Dr. Ursula Bengaard Hansen. Special thanks to Dr. Ivica Zikovic, the captain of our US roadtrip. It has also been a great pleasure to work alongside the 'new LQM gang' Thomas Schonenberger, Luc Testa, Virgile Favre, Tarek vennemann, Nagabhushan Hegde and Yikai Yang. I wish them all the best for their future endeavors. All the collaborations, scientific discussions, lunch groups and activities with the current and former members of the LQM group has been an unforgettable experience and I apologize if I have forgotten to mention anyone.

I would like to thank all my friends and especially my girlfriend Laure Pernin, who have been a constant support to me during tough times. I would like to thank my family and friends back home for their constant support.

Lastly, I would like to thank all the teachers, project advisors, professors during my early years in physics, who have nurtured my interest in physics and encouraged me at every step. Their hard work and passion towards science has been an inspiration, and this thesis is dedicated to them.

Lausanne, 10 June 2019

N. E. S

Abstract

This thesis presents a theoretical study of the Heisenberg model on a two dimensional lattice with asymmetric couplings along x and y directions. By gradually varying the coupling along y-direction we traverse the 1D, quasi 1D and 2D domains of this model. Primary focus of the research revolves around exploring the merits and de-merits of the staggered-flux state, a prototypical disordered resonating valance bond state, as a candidate wavefunction within this domain. Novel features like the fractionalization of spin-1 'magnon' excitations into spin-1/2 'spinon' excitations, which qualitatively explain the experimentally observed $(\pi, 0)$ quantum anomaly, demand further investigation into this novel wave function.

Theoretical framework involving construction of a Gutzwiller projected staggered flux state, a wavefunction depending on variational parameters, is developed. A numerical method based on MonteCarlo simulation is used to optimize the variational wave function and calculate the relevant physical observables. Exploring the gradual evolution of these observables with the coupling ratio $\gamma = J_y/J_x$ provides us with a clear picture of the evolution of spin excitations on this RVB state, as the dimensionality of the model is changed from 1D to 2D.

Keywords: Rectangular Heisenberg anti-ferromagnet, staggered flux, magnons, spinons, resonating valance bond, confinement/de-confinement.

Résumé

Cette thèse présente l'étude théorique du modèle d'Heisenberg appliqué à un réseau deux dimensionnel avec couplage asymétrique entre l'axe x et y . En faisant varier graduellement le couplage selon l'axe y , nous traversons les domaines 1D, quasi 1D et 2D de ce modèle. L'objectif premier de cette étude porte sur les avantages et désavantages de l'état dit de flux échelonné, un état prototype décrivant les liaisons de valence résonnantes désordonnées, en tant que fonction d'onde candidate pour ce domaine. De nouvelles propriétés comme la fractionalisation des excitations 'magnon' spin-1 en 'spinon' spin-1/2, expliquant qualitativement l'anomalie quantique $(\pi,0)$ observée expérimentalement, exigent une étude plus profonde de cette fonction d'onde novatrice.

Le cadre théorique y est développé, impliquant la construction d'un état projeté de Gutzwiller dit de flux échelonné, une fonction d'onde dépendant de paramètres variationnels. Une méthode numérique basée sur de la simulation MonteCarlo est utilisée pour optimiser la fonction d'onde variationnelle et calculer les observables physique pertinentes. L'évolution de ces observables avec le ratio $\gamma = J_y/J_x$ nous apporte des renseignements clairs sur l'évolution des excitations de spin pour cet état de liaison de valence résonnante, à mesure que la dimensionnalité du modèle passe de 1D à 2D.

Mots-clefs : anti-ferromagnétisme rectangulaire d'Heisenberg, flux échelonné, magnons, spinons, liaison de valence résonnante, confinement, déconfinement

Abbreviations

ABC	Anti periodic boundary condition along x-direction
CDF	Cumulative Distribution Function
CFTD	Copper Formate Tetra Deuterate ($\text{Cu}(\text{DCOO})_2 \cdot 4\text{D}_2\text{O}$)
INS	Inelastic Neutron Scattering
MBZ	Magnetic Brillouin Zone
PBC	Periodic boundary condition along x-direction
QSHAF	Quantum Square Heisenberg Anti Ferromagnet
QSL	Quantum Spin Liquid
RMS	Root Mean Square
RVB	Resonating Valance Bond
SBGP	Gutzwiller Projected Schwinger Boson
SF	Gutzwiller Projecte Staggered Flux
SWT	Spin Wave Theory
VMC	Variational Monte Carlo

Contents

Acknowledgements	i
Abstract (English/Français/Deutsch)	iii
1 Introduction	1
2 Theoretical Overview	11
2.1 Heisenberg Model	11
2.2 Fermions on Spin Chain	14
2.3 Bethe Ansatz	17
2.3.1 Mathematical Structure	18
2.3.2 Bethe quantum numbers	23
2.3.3 Ground State	23
2.3.4 Transverse Excitations	24
2.4 Other Methods	26
2.4.1 Abelian Bosonization	26
2.4.2 Continuous similarity transformations	29
2.5 Quantum spin liquids	31
3 Spin Wave Theory	37
3.1 Mathematical Framework	37
3.1.1 First Quantum Correction	41
3.1.2 Instability at low Coupling	43
3.1.3 Correlation functions	44
3.2 Results	45
3.3 Summary	52
4 Staggered flux:Ground state	53
4.1 Mathematical Framework	53
4.1.1 Fermionized Heisenberg Hamiltonian	54
4.1.2 Mean Field decoupling	55
4.1.3 Staggered Flux Hamiltonian	56
4.1.4 Staggered flux as the superposition of singlets	58
4.1.5 Boundary Conditions	61

Contents

4.1.6	Calculation of observables	62
4.1.7	Montecarlo Algoritm	64
4.2	Results	65
4.2.1	Optimization of parameters	65
4.2.2	Instantaneous spin correlation	72
4.3	Summary	77
5	Staggered flux:Excited State	79
5.1	Mathematical Framework	80
5.1.1	Transverse Excitation Subspace	81
5.1.2	Monte Carlo Method	83
5.1.3	Dynamical structure factor	85
5.1.4	Spinon pair separation distribution	86
5.1.5	Real space picture	89
5.2	Results	91
5.2.1	Quasi-1D	94
5.2.2	Rectangular lattice	101
5.2.3	Finite size analysis	103
5.2.4	Spinon pair separation	108
5.3	Summary	118
6	Conclusion	121
A	Simulation details	125
A.1	Metropolis MonteCarlo	125
A.2	Overlap Amplitudes	126
A.3	Computational detalis	129
B	Error Analysis	131
B.1	Statistical Errors	131
B.2	Fitting Errors	134
C	Additional figures	137
	Bibliography	163
	Curriculum Vitae	165

1 Introduction

Ever since the inception of human inquiry and scientific thought, one of the most fundamental questions scientist and philosophers kept asking themselves was "What is matter made of?". More clearly, as reductionists would like to ask "What are the fundamental constituents of matter and how do they interact?". Hundreds of years of scientific inquiry has led us through a multitude of explanations and pictures describing the nature. As mathematical formulations and physical experiments became sophisticated, so did our understanding of the constituents of nature. With each discovery the true picture of the universe became more clear.

Today we understand that a significant part of physical matter(apart from dark matter and dark energy) around us is made up of fields of leptons and quarks with the interactions being mediated by gauge fields. Three out of the four forces have been unified under the umbrella of the standard model with gravity still eluding a unified theory. This description involves the particles being described as quantized fields permeating the physical vacuum and this duality of particle-wave like behavior is at the heart of modern physics. Although the notion of fundamental particles of matter is ascribed to quarks and leptons today, quarks do not exist individually. At low energies they are always found in combinations, preserving certain symmetries, a phenomenon known as 'confinement'. A proper theoretical framework to describe confinement still eludes physicists and mathematicians and hence still remains one of the millennium problems of this century [Devlin (2002)].

The notion of confinement is not limited to fundamental particles that are investigated in high energy physics. Condensed matter physics is a branch of physics that deals with condensed phases of large number of constituent particles, with strong interactions, that could be typically described in a non-relativistic framework. Within condensed matter physics, there are various examples of excitations, at model level [Fonseca and Zamolodchikov (2003); Delfino et al. (1996); Delfino and Mussardo (1998)], that tend to confine/de-confine into other types of excitations which carry fractional quantum numbers. An important distinction to be made here, as compared to high energy physics, is the concept of 'emergence'. The emergent degrees of freedom are those that are exhibited on a macroscopic scale but are completely invisible on microscopic level. This is quite contrary to a reductionist notion that a macroscopic system is

fully understood in terms of its microscopic constituents. Excitations that have their origin in emergent degrees of freedom are particularly important in condensed matter physics, where at low energy scales, the intra-nuclear degrees of freedom do not explicitly play a major role in overall physics.

A key example showing the emergent degrees of freedom is the spin-charge separation in 1D electronic systems [Lieb and Wu (1968)]. Due to the special nature of 1D physics, where particles have to push its neighbors to move, free movement is not possible. This leads to all excitations behaving as collective excitations. This dimensional restriction lead to deconfinement of electronic charge and spin degrees of freedom into ‘holons’ and ‘spinons’ respectively. These excitations along with theoretically predicted ‘orbitons’ [Pen et al. (1997); van den Brink et al. (1998)] have experimentally been observed [Kim et al. (1996); Schlappa et al. (2012)]. The main focus of our research work is dedicated to spinons which are fractional excitations carrying a spin quantum number $1/2$. Spinons are the fundamental excitations in 1D nearest neighbor $S=1/2$ Heisenberg model, which can be exactly solved analytically using Bethe ansatz [Bethe (1931)]. Normally, in the case of a spin chain of non interacting spins a $\Delta S = 1$ excitation at a particular site corresponds to a flip of $s = -1/2$ spin to a $s = 1/2$ state. But in the case of an interacting chain with Heisenberg coupling between nearest neighbors, the $\Delta S = 1$ excitation deconfines into freely moving $s = 1/2$ excitations. The deconfinement of these fractional spin $1/2$ excitations has been theoretically predicted [Müller et al. (1981); Faddeev and Takhtajan (1981)] and experimentally validated [Tennant et al. (1995); Lake et al. (2005); Mourigal et al. (2013)]. The existence of these fermionic fractional excitations is strikingly different from the higher dimensional(unfrustrated) versions of the model where a transverse excitation induced through a spin flip, manifests itself as a bosonic(hard-core for quantum $S = 1/2$ spin) spin $s = 1$ excitation. The qualitative difference between these scenarios can be seen by looking at their spin excitation spectrum from Fig(1.1), where the 1D quantum spin AFM chains exhibits a continuum, the 2D spectrum shows a sharp mode.

The phenomenon of de-confined spin flip is not limited to 1D physics. Frustrated magnetic 2D lattices are one of the most extensively studied systems in the area of quantum magnetism. Frustration could be of geometric origin(see Fig(1.2a)), for example as in triangular lattices [Coldea et al. (2001(a))] and kagome lattices [de Vries et al. (2009); Jeong et al. (2011)], or due to competition from extended couplings, as in compounds with significant next nearest neighbor hopping amplitude. The interest in these structures is primarily driven by the search for quantum spin liquid state(QSL) in materials [Balents (2010)]. QSL contain disordered magnetic configurations till very low temperatures($T = 0$ in principle), due competing magnetic interactions that lead to massive degeneracy. QSL are expected to play a fundamental role in understanding high temperature superconductivity through Anderson’s theory of Resonating Valance Bond state(RVB) [Anderson et al. (1987)]. This state could be imagined as a superposition of local and non-local singlet pairs on a lattice. A transverse spin excitation induced on this state, breaks the singlet into two un-paired up spins. Each of this un paired spins, can move in the background of the RVB at a minimal energy cost(see Fig(1.2)(b)), and can be referred to as a ‘spinon’ in this context. QSL are also expected to play a key role in

topological quantum computation [Freedman et al. (2003)]. Two dimensional honeycomb lattices with Kitaev interaction are predicted to host two-dimensional quasi-particles called anyons [Kitaev (2006)]. Unlike bosons or fermions, anyons attain a complex phase shift upon exchange. Due to the topological nature of braiding of these quasi-particles, logical gates (quantum) constructed out of these braids are weakly affected by small perturbations that tend to decohere qubits. This makes them robust candidates for quantum operations.

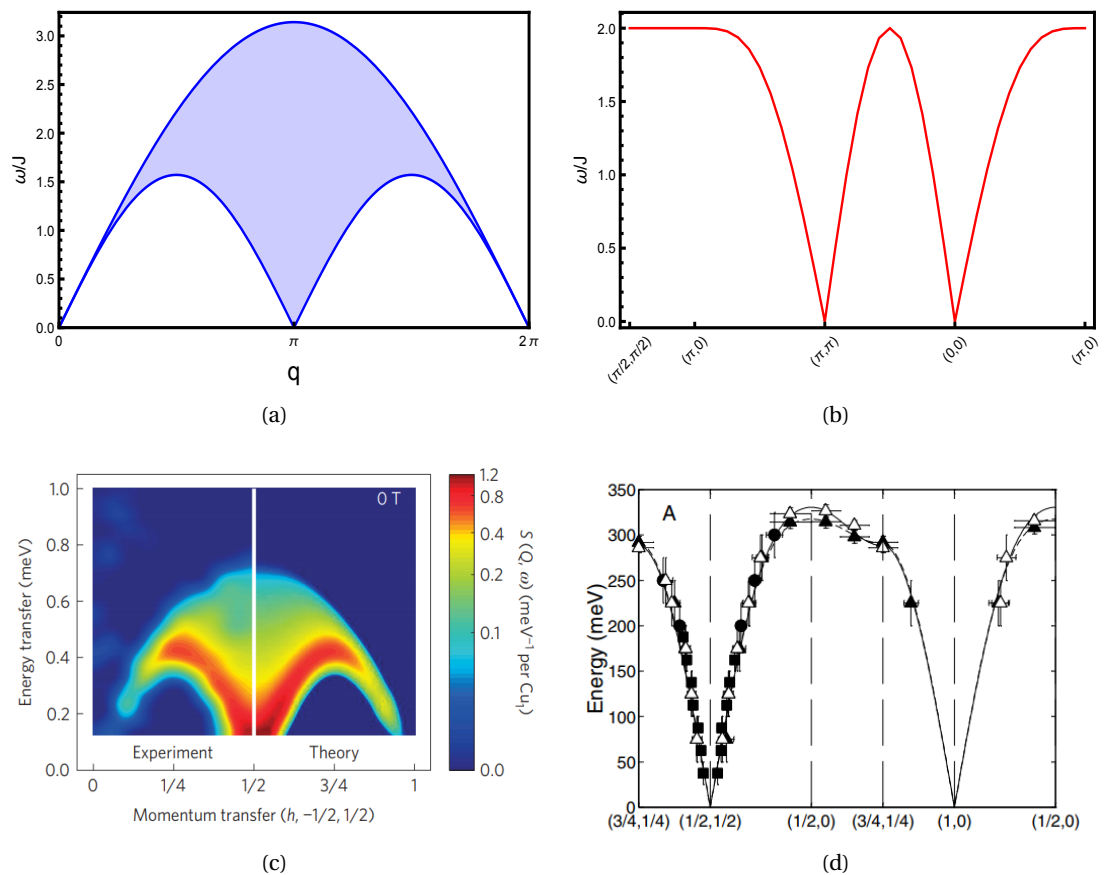


Figure 1.1 – (a) An illustration of possible eigen energy values on a 1D quantum AFM spin chain (b) Magnon dispersion from linear SWT on a 2D QSHAE, along a selected k -path. (c) Spin excitation spectrum of CFTD a spin 1/2 Heisenberg AFM chain from Mourigal et. al(2013) (d) Spin wave dispersion on La_2CuO_4 the parent compound of a high temperature superconductor from Coldea et al. (2001b).

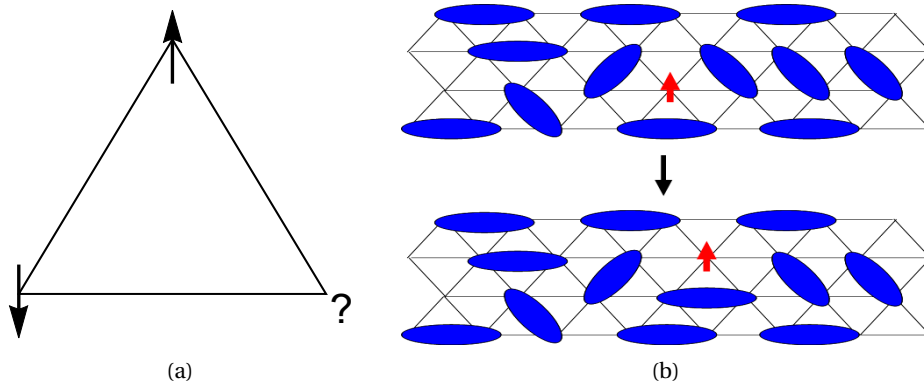


Figure 1.2 – (a) Geometric frustration because of competing Heisenberg interactions on a trigangular lattice (b) Spinon movement on a QSL background.

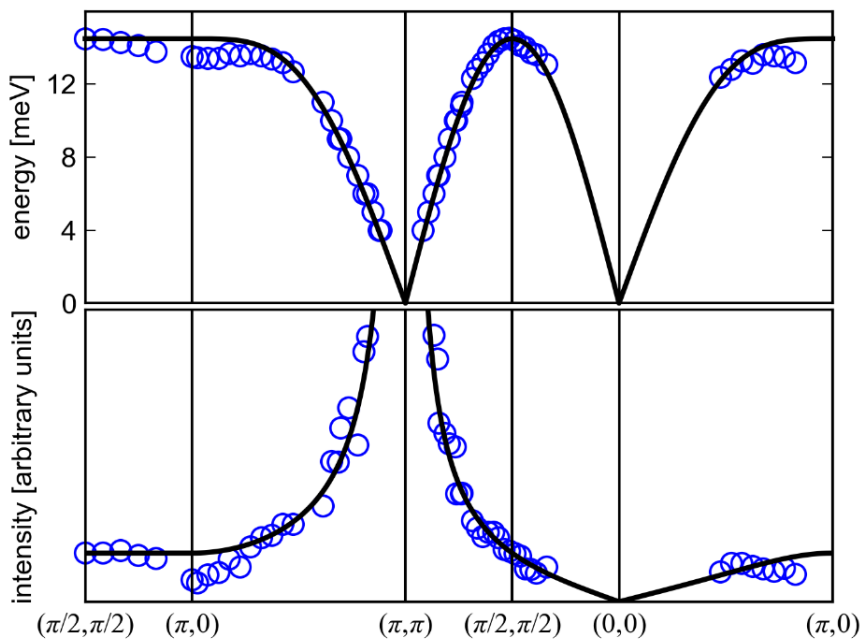


Figure 1.3 – Dispersion(top) and Intensity(bottom) corresponding to the INS measurements on CFTD from Christensen et al. The blue circles correspond to the data and the solid lines corresponds to the linear spin wave result with J adjusted such that $\omega(\pi/2, \pi/2)$ matches the experiment.

Search for spinons in unfrustrated lattices and their characterization is an ongoing challenge. Weakly coupled spin ladders are shown to host the experimental realization of spinon confinement [Lake et al. (2009)], where at low energies the spinons are confined, and at high energies the spin chains are effectively decoupled. A particular interesting case that reinvigorated our interest towards spinons in 2D is the $(\pi, 0)$ quantum anomaly observed in the inelastic neutron scattering(INS) measurements on $\text{Cu}(\text{DCOO})_2 \cdot 4\text{D}_2\text{O}$ (CFTD) [Rønnow et al. (2001)].

The CFTD material being a physical realization of a quantum square lattice anti-ferromagnet (QSHAF) is expected to host a spin excitation spectrum well accounted by spin wave theory (SWT)[Bloch (1930); Kubo (1952); Anderson (1952)]. The $(\pi,0)$ quantum anomaly evidenced some important deviations from SWT at the high energy/small wavelength part of the excitation spectrum [Rønnow et al. (2001); Christensen et al. (2007)]. It constitutes a 7% downward dispersion in the magnetic zone boundary compared to SWT as can be seen in Fig(1.3). Also observed is a subsequent loss of spectral weight at $(\pi,0)$ symmetry point in the INS data on CFTD. The spectral weight seems to have been pushed to a continuum at high energies. Polarized INS measurements on the same compound by Mourigal et al., [Mourigal (2011)] have indicated that the excitations corresponding to the high-energy continuum could be spin isotropic in nature. The anomaly has also been found to exist in La_2CuO_4 [Headings et al. (2010)]. These observations motivated Dalla Piazza et al., [Dalla Piazza et al. (2014a); Dalla Piazza (2014b)] to consider a disordered QSL state as a ground state which ended up qualitatively reproducing most of the observations. By considering a Gutzwiller projected RVB state, referred to as Staggered Flux state(SF), as a groundstate ansatz they were able to show that the particle hole excitations induced in this state, exhibit spinon like excitations at specific q-vectors i.e $(\pi,0)$. Moreover, the spectrum at these q-vector exhibited a strong continuum of energies and loss of spectral weight from magnon like mode as observed in case of CFTD.

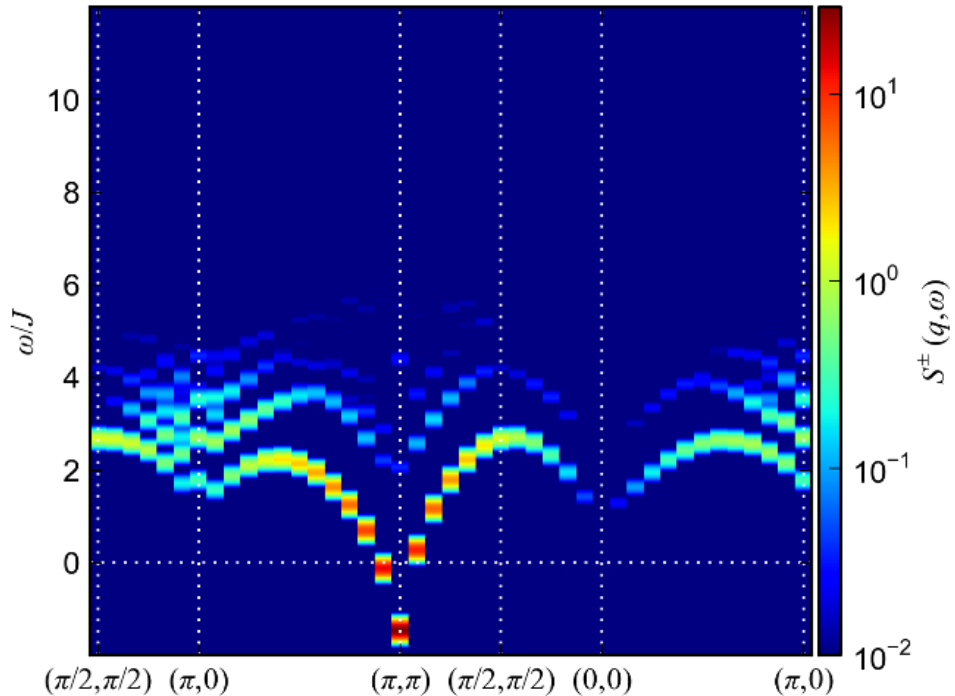


Figure 1.4 – Transverse Dynamic structure factor of SF state on a $L = 24 \times 24$ lattice from DallaPiazza et al(2014b).

Although the SF wavefunction has the merit of qualitatively explaining the experimental observations, which are unexplained by SWT, there are a few caveats to this procedure. Firstly, the SF state has no long range order and hence it cannot be the true ground state of a QSHAF. This is reflected in the fact that the groundstate energy of this state $E_{SF} = -0.638J$ is higher than other numerical methods. Green function Monte Carlo for example has a groundstate energy of $-0.664J$ [Trivedi and Ceperley (1989); Runge (1992); Calandra Buonaura and Sorella (1998)]. This also can be seen through the unphysical negative energies observed at (π, π) point in the Transverse dynamic spin structure factor (see Fig(1.4)). To address this issue Dalla Piazza et al, also worked with a state having long range order obtained through inducing a neel mean field (SF+N). This state proved to be a better wave function in terms of the ground state energy being $E_{SF+N} = -0.664$ a value much closer to the Green function Monte Carlo and also managed to reproduce the 7% reduction in dispersion along MZB (Fig(1.6)(a)). However, this state did not exhibit the experimentally observed continuum and the high energy excitations were gapped from the magnon mode (Fig(1.5)). Also, the intensity loss of magnon peak was minimal (Fig(1.6(c))). This state also exhibited an exponentially decaying instantaneous spin correlation function, where one would expect a power-law decay (Fig(1.6(b))). In conclusion both these states were able to capture complimentary aspects of the excitation spectrum. The SF state captures the long wavelength/high energy spin rotationally invariant features and the SF+N state capturing the spin symmetry broken features.

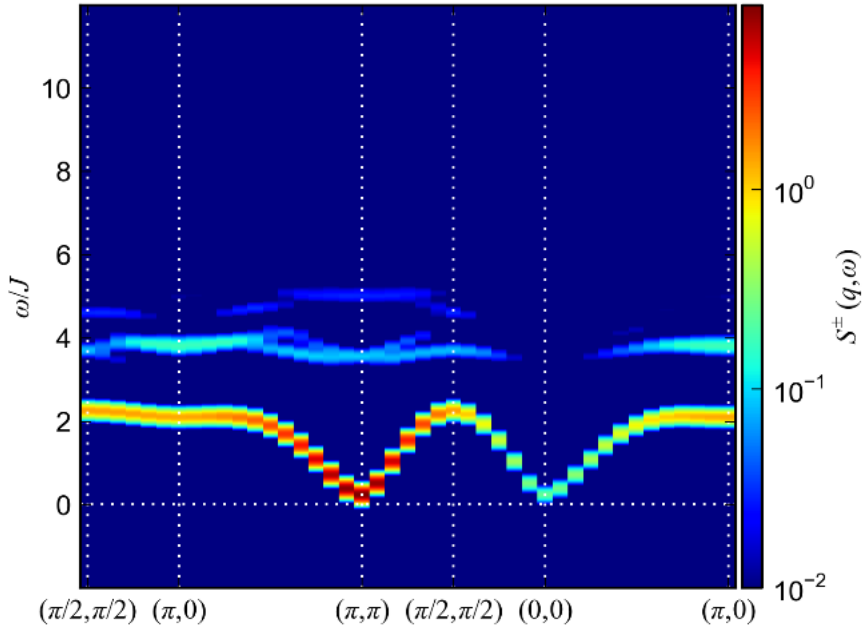


Figure 1.5 – Transverse Dynamic structure factor of SF+N state on a $L = 24 \times 24$ lattice from DallaPiazza et al(2014b).

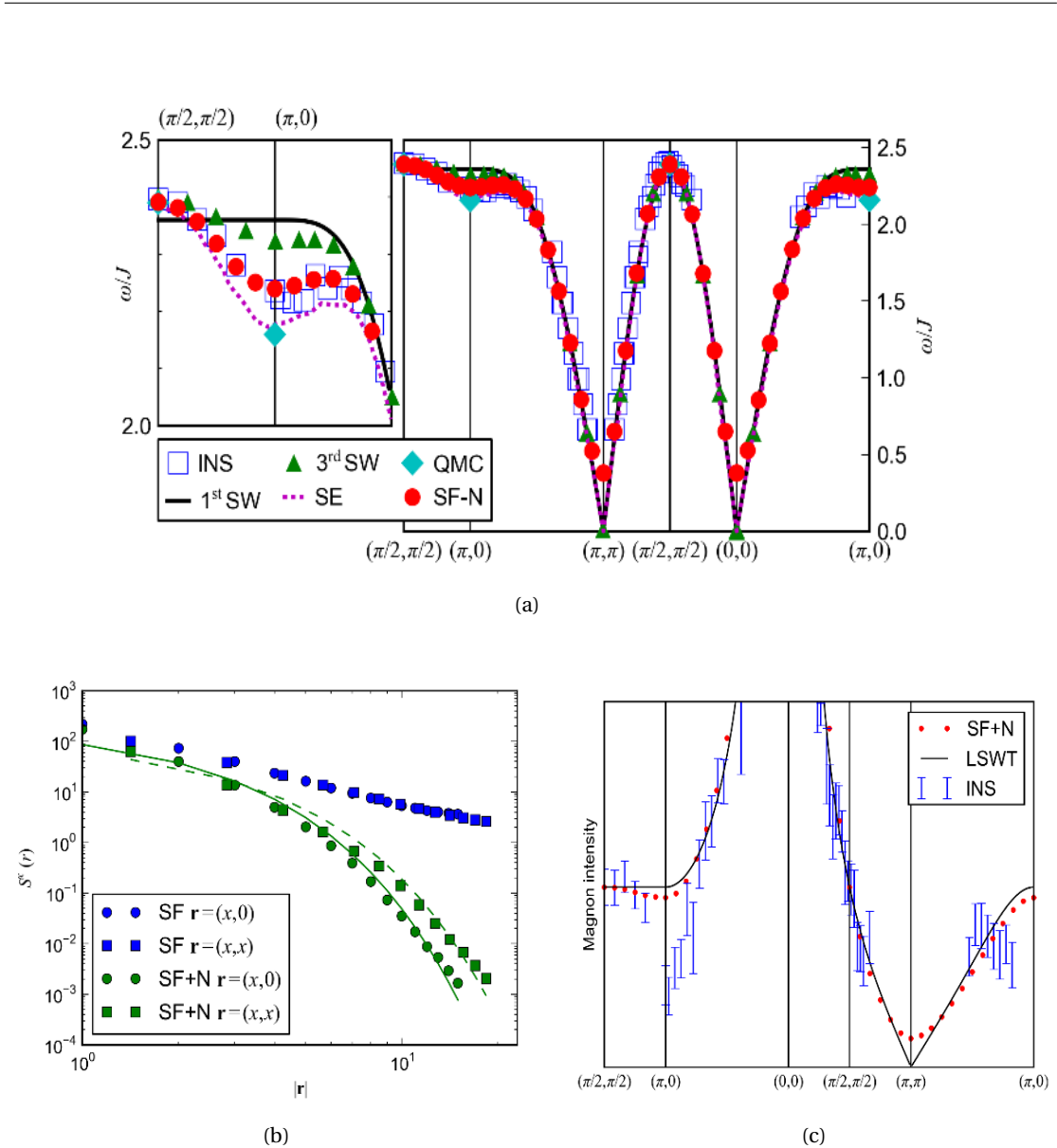


Figure 1.6 – (a) Low energy spin excitation mode from inelastic neutron scattering, and comparisons with results of various numerical methods (b) Instantaneous spin-spin correlation function of SF and SF+N along (1,0) and (1,1) directions. (c) Comparison of INS intensity with estimates from SWT and SF+N. All figures are from Dalla Piazza et al(2014b)

A particularly interesting feature of the SF state is the fact that although the $(\pi, 0)$ mode exhibits a continuum (size dependent discrete mode), the mode at other q vectors $(\pi/2, \pi/2)$ for example exhibit a (size independent) sharp mode that retain a magnon like character (see Fig(1.7)). Calculating a quantity that measures time average of spinon-pair separation, further shows the contrasting nature of excitations at these q-vectors. The spinon pair separation at $(\pi, 0)$ is spread out whereas at $(\pi/2, \pi/2)$ it is fairly localized (Fig(1.8)). This localized spinon pair can be interpreted as magnon like excitation. Hence, the SF wavefunction has a unique

feature of having both confined and deconfined phases of spin excitations.

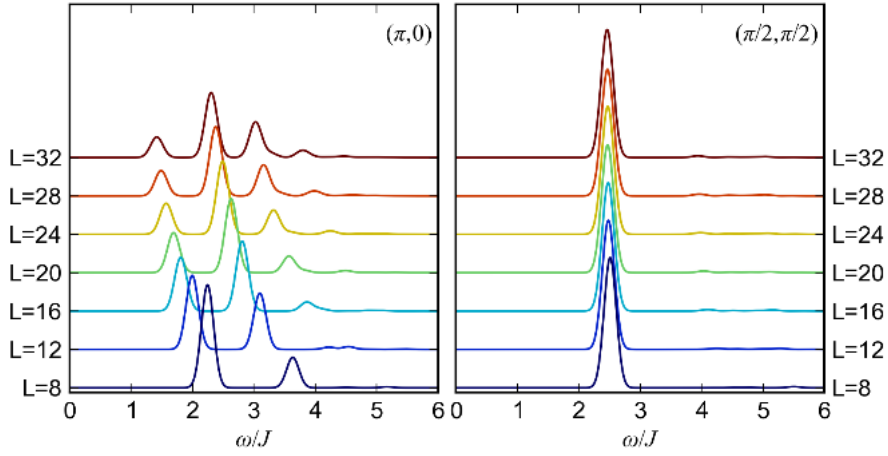


Figure 1.7 – Transverse dynamic structure factor of the SF state at $q = (\pi, 0)$ and $q = (\pi/2, \pi/2)$ for various system sizes(L), from DallaPiazza et al(2014b).

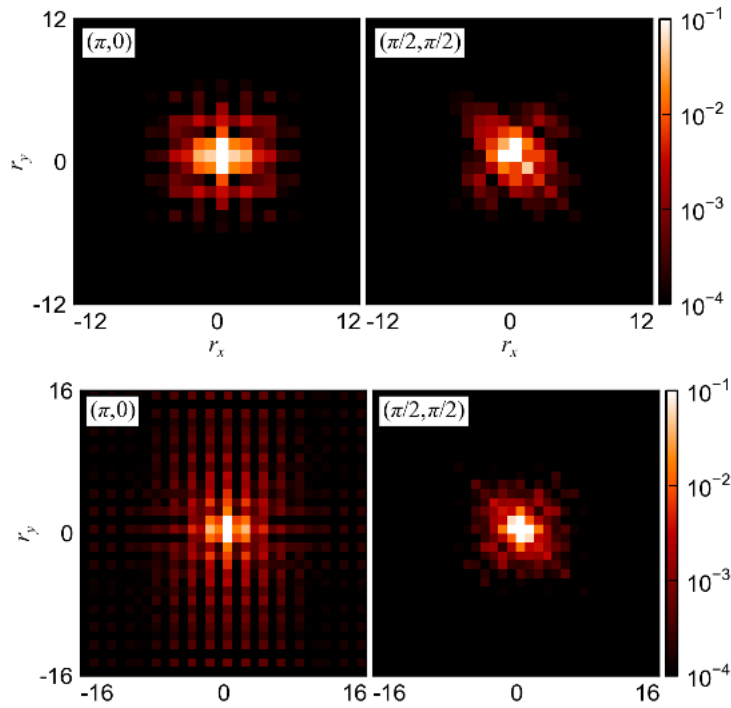


Figure 1.8 – Spinon pair separation at $q = (\pi, 0)$ (left) and $q = (\pi/2, \pi/2)$ (right) for SF+N (top) and SF (bottom) state, from DallaPiazza et al(2014b).

As mentioned earlier free moving spinons are the fundamental excitations on 1D spin chain. It would be interesting to see how the excitation spectrum and the behavior of the disordered

phase gradually evolves as we move from 1D case to a isotropic 2D case. This has been the motivation behind extending the methodology of Dalla Piazza et al to Rectangular Quantum Heisenberg Anti Ferromagnetic (RQHAF) system where by varying $\gamma = J_y/J_x$ we can explore the quasi-1D and 2D regimes.

Outline

The outline of the upcoming chapters:

- **Theoretical Overview-** Starting with the Hubbard model, we briefly present the origins of Heisenberg interaction in strongly correlated materials. We present an overview of Jordan Wigner method in the XY model and discuss the 1D Bethe ansatz solution. In exploring these topics we try to provide an intuitive picture of what ‘spinon’ excitation corresponds to in each of these contexts. Finally, we have a look at other methods like Abelian Bosonization and continuous similarity transformation in the context of the Heisenberg problem. We finish the chapter with a brief discussion on RVB states.
- **Spin wave Theory-** Before moving to the SF solution, we first explore the spin wave method on RQHAF. We first diagonalize the linear component of the spin wave Hamiltonian to obtain the bare magnon dispersion. We then use a Hartree-Fock mean field decoupling to calculate the corrections coming from the next order term. Using these terms we can calculate the renormalized magnon dispersion and the reduction of staggered moment. This method is repeated self-consistently to arrive at a stable solution. In doing so we explore limits at which the self-consistent solution fails. In the region where this method is valid, we provide the results corresponding to staggered moment, groundstate energy, and instantaneous and dynamic transverse spin spin correlation functions.
- **Staggered flux: Groundstate-** Heisenberg Hamiltonian in its fermionic form is diagonalized using a mean field decoupling. Staggered flux wavefunction corresponds to a particular choice of mean fields which are motivated from the d-wave RVB state, and is the exact solution for spins with infinite flavors $n \rightarrow \infty$. The mean fields contain free parameters, which become the variational parameters in our method. The groundstate corresponds to filling the lower band of the diagonalized Hamiltonian. This state has double occupancies which are projected out using a Gutzwiller projector. The Gutzwiller projected wavefunction is used as a variational ansatz and by calculating the expectation value of the (actual) Heisenberg Hamiltonian we find the optimum parameters corresponding to energy minimum. Once we have an optimized wave function we proceed to calculate the instantaneous spin spin correlation function. Finite size effects and effects of various boundary conditions are explored to obtain the estimates for $L \rightarrow \infty$ case. All

Chapter 1. Introduction

the numerical computations corresponding to Gutzwiller projection and calculation of observables is carried out using a Monte Carlo process.

- **Staggered flux: Excited state-** The transverse excitations are induced as particle hole excitations on the SF wave function. The Heisenberg Hamiltonian is diagonalized in the excitation subspace to obtain the eigenenergies and eigenvectors. Transverse dynamic spin structure factor is estimated through this procedure for $L = 24$ system size for various coupling ratios. The results are compared with SWT and Bethe ansatz. By calculating the overlap of the eigenfunctions with a delocalized spin flip state we evaluate a quantity referred to as ‘spinon separation’ that will help us to characterize the nature of the excitations. Finite size effects on dynamic structure factor and spinon separation are analyzed at high symmetry points.
- **Concluding remarks-** This chapter puts together all the relevant conclusions derived from earlier chapters and outlines the key results of our research work.

Chapters 3,4,5 form the main skeleton of this research work. We have made best efforts to make each chapter self-contained to facilitate being read individually. A brief summary is provided at the end of each chapter to help the readers to get a gist of the key observations.

2 Theoretical Overview

In this chapter we discuss the theoretical origins and the analytical treatment of the Heisenberg model. We have a look at the complexity of this simple magnetic model and the rich variety of groundstates it hosts. Starting from the microscopic origin, we gradually proceed to a discussion on a few analytical methods used in the research works related to this domain, that will be relevant for discussion in subsequent chapters. We also have a look at the RVB solutions and their relevance to the Heisenberg model.

Heisenberg Model

Heisenberg exchange interaction is a major type of magnetic interaction in strongly correlated materials. It is perhaps the most commonly observed magnetic interaction besides the dipole-dipole interaction. The interaction manifests itself as a simple dot product between the interacting spins. The most common mechanism by which we obtain a Heisenberg interaction is the super exchange mechanism in strongly correlated materials. The physics of strongly correlated materials in the simplest form can be captured by the Hubbard model:

$$\mathcal{H} = - \underbrace{\sum_{ij\sigma} t_{ij} c_{i\sigma}^\dagger c_{j\sigma}}_T + U \underbrace{\sum_i n_{i\uparrow} n_{i\downarrow}}_V \quad (2.1)$$

where t_{ij} represents the hopping energy between sites i and j and U corresponds to the Coulomb repulsion energy, the cost of having two electrons at the same site. It must be noted that the above model is a single band model, where we assume one state per site. The first term corresponds to the kinetic energy of the hopping electrons, and the magnitude of t_{ij} depends on the bonding strength between the orbitals of site i and j . If one considers $U = 0$ and only nearest neighbor hopping, the Hamiltonian is represented by the kinetic part:

$$\mathcal{H} = - \sum_{ij\sigma} t c_{i\sigma}^\dagger c_{j\sigma} \quad (2.2)$$

Chapter 2. Theoretical Overview

This corresponds to having a electron band of a band width $2t$. The excitations correspond to particle hole excitation in these bands. For small Coulomb repulsion one can introduce the potential term as a perturbation. In such a scenario the systems are well explained in higher dimensions by Landau Fermi liquid theory [Landau (1957a,b, 1959)]. The excitations are rather similar to the free fermions but are dressed with density fluctuations. They acquire an effective mass m^* different from the electron mass and also a finite lifetime τ that depends on the proximity of quasi-particles to Fermi surface. In 1D however, individual motion of excitations is restricted, which leads to the excitations becoming collective and hence the Fermi liquid theory does not work in this regime. The region in which t and U have comparable energies is also a difficult regime to handle and any form of a perturbation theory would generally not work here.

On the other hand, in materials with a very large Coulomb repulsion energy and a small band width, one can consider the potential term to be the main Hamiltonian and introduce the kinetic part as a perturbation. The Coulomb repulsion favors states with one electron per site at half filling. Introducing the kinetic term as a perturbation, we observe that the first order corrections vanish due to the fact that the matrix elements between two different singly occupied states $|\alpha\rangle$ and $|\beta\rangle$ vanishes. This happens because the kinetic term creates a state with double occupancy which has a zero overlap with a singly occupied state.

$$\langle \alpha | T | \beta \rangle = 0$$

The matrix elements that are second order in perturbation theory are given by:

$$\mathcal{H}_{\alpha\beta}^{(2)} = \langle \alpha | \mathcal{H}^{(2)} | \beta \rangle = \sum_{\gamma} \frac{\langle \alpha | T | \gamma \rangle \langle \gamma | T | \beta \rangle}{E_{\alpha} - E_{\gamma}} \quad (2.3)$$

where the states $|\gamma\rangle$ have one double occupancy. Hence these states are higher in energy by U . Both the states $T|\alpha\rangle$ and $T|\beta\rangle$ belong to the subspace of $|\gamma\rangle$. Hence the sum over $|\gamma\rangle$ can be considered as the identity operator in this subspace. The Hamiltonian becomes:

$$\mathcal{H}^{(2)} = -\frac{t^2}{U} \sum_{ij\sigma} \sum_{km\sigma'} c_{i\sigma}^{\dagger} c_{j\sigma} c_{k\sigma'}^{\dagger} c_{m\sigma'} \quad (2.4)$$

The above hamiltonian will have finite matrix elements in space of singly occupied sites only if $m = i$ and $k = j$ which leads to the effective Hamiltonian:

$$\mathcal{H}^{(2)} = -\frac{t^2}{U} \sum_{ij} \sum_{\sigma\sigma'} c_{i\sigma}^{\dagger} c_{j\sigma} c_{j\sigma'}^{\dagger} c_{i\sigma'} \quad (2.5)$$

Considering only the term that corresponds to a specific pair (i, j) in the above Hamiltonian, represented by $\mathcal{H}_{ij}^{(2)}$, we observe that it only acts on the spins at the positions i, j . Within a

subspace $\{|\alpha_{\uparrow\uparrow}\rangle, |\alpha_{\uparrow\downarrow}\rangle, |\alpha_{\downarrow\uparrow}\rangle, |\alpha_{\downarrow\downarrow}\rangle\}$, where only the spins at position i, j are operated on:

$$\mathcal{H}_{ij}^{(2)} = -\frac{t^2}{U} \begin{pmatrix} 0 & 0 & 0 & 0 \\ 0 & 1 & -1 & 0 \\ 0 & -1 & 1 & 0 \\ 0 & 0 & 0 & 0 \end{pmatrix} \quad (2.6)$$

which can be re-written as

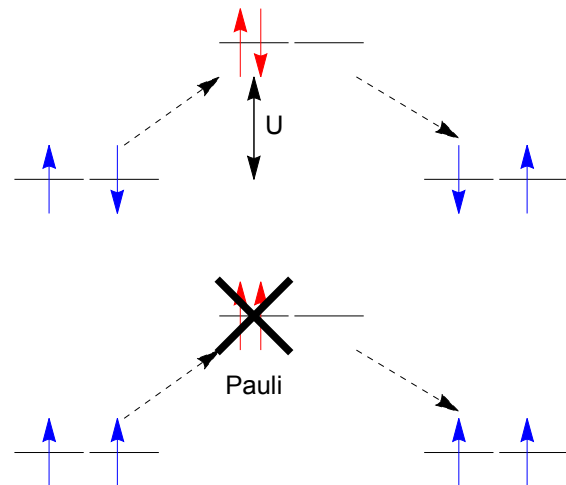
$$\mathcal{H}_{ij}^{(2)} = \frac{2t^2}{U} \left[\begin{pmatrix} \frac{1}{4} & 0 & 0 & 0 \\ 0 & -\frac{1}{4} & \frac{1}{2} & 0 \\ 0 & \frac{1}{2} & \frac{1}{4} & 0 \\ 0 & 0 & 0 & -\frac{1}{4} \end{pmatrix} - \frac{1}{4} \right] = \frac{2t^2}{U} \left(S_i \cdot S_j - \frac{1}{4} \right) \quad (2.7)$$

Hence the overall second order perturbation term becomes:

$$\mathcal{H}^{(2)} = \frac{4t^2}{U} \sum_{\langle i,j \rangle} \left(S_i \cdot S_j - \frac{1}{4} \right) \quad (2.8)$$

The above exercise shows us how adding a small kinetic term to a large on site Coulomb repulsion leads to Heisenberg interaction between the spins. In Fig(2.1) we show an illustration of such process where virtual hoppings that lead to second order perturbation are allowed when neighboring spins are opposite. When the neighbouring spins are same, the hopping process is blocked due to the Pauli exclusion principle. In real materials where Coulomb repulsion is dominant compared to bandwidth, one obtains an insulating phase known as Mott insulator. As expected most of the mott insulators are Anti-Ferromagnets. This process by which a Heisenberg interaction evolves to facilitate free motion of electrons is called a ‘super exchange’.

Figure 2.1 – An illustration of super exchange process where virtual hoppings are allowed for the neighboring up and down spins(top) and are forbidden for neighbouring up spins.



Fermions on Spin Chain

Before moving to the exact solution of Heisenberg chain, it is instructive to have a look at a simpler model, the XY model, where the solution can be written in terms of free moving fermions. The XY Hamiltonian is a special case of the XXZ Hamiltonian:

$$\mathcal{H}_{XXZ} = \sum_i J_{xy} (S_{i+1}^x \cdot S_i^x + S_{i+1}^y \cdot S_i^y) + J_z S_{i+1}^z \cdot S_i^z \quad (2.9)$$

with $J_z = 0$. The commutation relations of spin operators is inconvenient to work with. Hence, we look for a mapping of spin operators to fermionic or bosonic quasi-particles. We start by defining a completely polarized state as vacuum state.

$$|0\rangle = |\uparrow\uparrow \dots \uparrow\rangle \quad (2.10)$$

$$S_i^z |0\rangle = \frac{1}{2} |0\rangle \quad (2.11)$$

The spin flips induced on this state can be considered as quasi-particles. Since we have quantum spins, we cannot create more than one spin flip on each site. If we use a bosonic representation of quasi-particles, then we must pay attention to this constraint which is referred to as a hard-boson mapping. We will deal with this representation in Chapter 3 while studying spin-wave theory. In this section we use a fermionic representation, where by the required constraint inherently exists in the form of Pauli exclusion principle. If we consider the following mapping:

$$\begin{aligned} S_i^+ &= c_i^\dagger \\ S_i^z &= c_i^\dagger c_i - \frac{1}{2} \end{aligned} \quad (2.12)$$

we observe that it fulfills the local spin commutation relations. However, the spin operators on different sites do not commute. To solve this issue one can use the Jordan-Wigner transformation [Jordan and Wigner (1928)].

$$\begin{aligned} S_i^+ &= c_i^\dagger \exp(i\pi\phi_i) \\ S_i^z &= c_i^\dagger c_i - \frac{1}{2} \end{aligned} \quad (2.13)$$

where ϕ_i is the string operator given by:

$$\phi_i = \sum_{m=-\infty}^{i-1} c_m^\dagger c_m \quad (2.14)$$

The XXZ Hamiltonian in this formalism becomes:

$$\mathcal{H}_{XXZ} = \frac{J_{xy}}{2} \sum_i \left[c_{i+1}^\dagger c_i + c_i^\dagger c_{i+1} \right] + J_z \sum_i \left(n_{i+1} - \frac{1}{2} \right) \left(n_i - \frac{1}{2} \right) \quad (2.15)$$

where $n_i = c_i^\dagger c_i$. Using a gauge transformation $c_i \rightarrow (-1)^i c_i$, the Hamiltonian becomes:

$$\mathcal{H}_{XXZ} = -t \sum_i \left[c_{i+1}^\dagger c_i + c_i^\dagger c_{i+1} \right] + V \sum_i \left(n_{i+1} - \frac{1}{2} \right) \left(n_i - \frac{1}{2} \right) \quad (2.16)$$

which describes the spinless fermions hopping with an amplitude $t = J_{XY}/2$ subject to a nearest neighbor repulsion $V = J_z$. Considering the XY model, with $J_z = 0$, the Hamiltonian is quadratic and can be diagonalized in Fourier space:

$$\begin{aligned} \mathcal{H}_{XY} &= \sum_k \epsilon_k c_k^\dagger c_k \\ \epsilon_k &= -2t \cos(ka) \end{aligned} \quad (2.17)$$

which describes a band of free moving fermions on a chain. Since, the Hamiltonian commutes with S_{tot}^z the solutions can be classified into sectors with conserved S_{tot}^z . The ground state at half filling case corresponds to $S_{tot}^z = 0$, where half of the band is filled. The excitations within this sector correspond to particle-hole excitations where one destroys a fermion at a specific k-vector (for e.g $k - q$) and creates one at a different k-vector (for e.g. k) and the difference (q) corresponds to the momentum of the excitation.

$$\begin{aligned} |k, q\rangle &= c_k^\dagger c_{k-q} |GS\rangle \quad \epsilon_{k-q} < \epsilon_F < \epsilon_k \\ |GS\rangle &= \prod_{k_1} c_{k_1}^\dagger |0\rangle \end{aligned} \quad (2.18)$$

where $\epsilon_{k_1} \leq \epsilon_F$. The excitation corresponding to a certain q vector does not have a discrete number of energies. Instead, we have a continuum of excitation at every q vector. If one has a look at the real space version of particle hole excitation induced on a Neel ordered state, as shown in Fig(2.2), we can see that it creates two domain walls that freely propagate on the chain without costing any energy. These domain walls can be identified as spinons in this picture.

Gradually increasing longitudinal coupling J_z would lead to an increasing interaction between spinless fermions and would mix higher order particle-hole excitations. Similar to the case of 1D Hubbard model, perturbatively solving for freely moving fermions with added repulsive interaction becomes intractable in 1D and requires more sophisticated tools. Using this simplistic way of visualizing spinons on a chain as domain walls between two domains, we can also visualize the notion of confinement of spinons. If we consider two coupled XY

Figure 2.2 – A real space representation of spinon on a neel state on quantum 1D XY spin chain. The arrows correspond to the spin representation and plain-hollow dots represent the spinless fermion representation. The particle-hole excitation leads to creating two domain walls, which on application of the Hamiltonian, propagate as free quasi particles

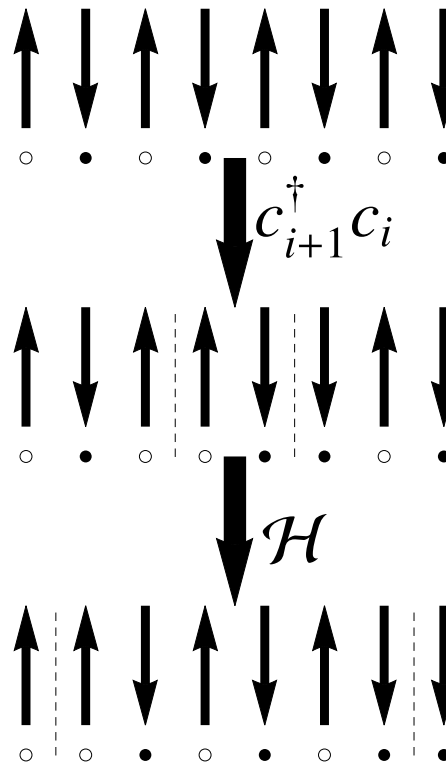
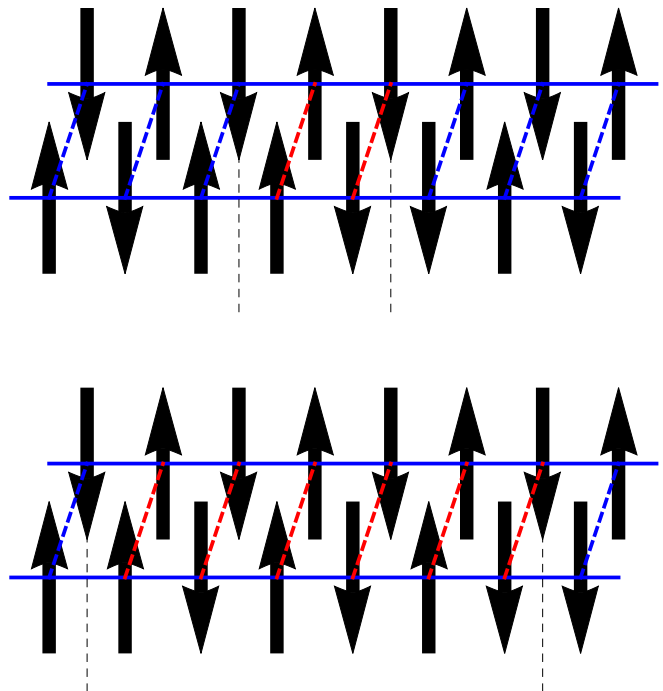


Figure 2.3 – Real space representation of confining nature of excitations when two XY spin chains are coupled. The solid lines represents quantum spin chains and dashed lines represent a weak AFM coupling between the chains. As the domain walls start moving away the misaligned phases lead to the state having high energy (represented in red) due to interaction in between the chain. The energy cost is proportional to the separation between the domain walls.



chains, with AFM interaction for example, separating spinons on one of the Neel aligned chains leads to a corresponding mis-alignment with the neighboring chain. As can be seen from Fig(2.3), this leads to the separation of spinons costing an energy proportional to the distance between them. Although this picture provides us with a visualization of confining interactions in higher dimensions, it must be noted that this is a very primitive way of looking at magnetic interactions. In reality, for Heisenberg chains, we have multiple spinons interacting simultaneously and they cannot be visualized as domain walls between two phases.

Before moving to Heisenberg chains we briefly discuss the boundary conditions these fermions follow. Given a chain of spins which is connected at the ends, the spins would follow a periodic boundary condition.

$$\begin{aligned} S_{i+N}^+ &= S_i^+ \\ \implies c_{i+N}^\dagger \exp(i\pi\phi_{i+N}) &= c_i^\dagger \exp(i\pi\phi_i) \end{aligned} \quad (2.19)$$

where N is the system size. A look at the string operator shows:

$$\phi_{i+N} = \phi_i + \sum_{m=i}^{m=i+N} c_m^\dagger c_m = \phi_i + \sum_{m=i}^{m=i+N} \left(S_m^z + \frac{1}{2} \right) = \phi_i + S_{tot}^z + \frac{N}{2} \quad (2.20)$$

Substituting $S_{tot}^z = 0$ we have:

$$\exp(i\pi\phi_{i+N}) = \exp\left(i\frac{N\pi}{2}\right) \exp(i\pi\phi_i) = \begin{cases} \exp(i\pi\phi_i) & \text{if } N=4n \\ -\exp(i\pi\phi_i) & \text{if } N=4n+2 \end{cases} \quad (2.21)$$

This result leads to the following condition on the fermion operators:

$$c_{i+N}^\dagger = \begin{cases} c_i^\dagger & \text{if } N=4n \\ -c_i^\dagger & \text{if } N=4n+2 \end{cases} \quad (2.22)$$

Hence, the many body fermion wave-function obey different boundary conditions depending on whether $N/2$ is even or odd.

Bethe Ansatz

In this section we explore a few aspects of the exact solution in 1D Heisenberg spin chain that can be obtained via the Bethe ansatz [Bethe (1931)]. Study of Bethe ansatz is a field in itself, and hence we will keep our discussion focused only on the basic aspects of the solution that will be relevant for future discussions. The mathematical formulation in this section is followed from [Karabach et al. (1997); Fradkin (2013)]. For a more detailed and full treatment of Bethe ansatz, interested readers can refer to [Faddeev (1982); Lowenstein (1982)].

Mathematical Structure

We start our discussion through constructing the basis wavefunctions. Since the Heisenberg Hamiltonian conserves total spin along z-axis, we divide the Hilbert space of wave functions into sectors of $S_{tot}^z = N/2 - r$ where the states have r down spins. The case $r = 0$ corresponds to a ferromagnetic state $|F\rangle = |\uparrow\uparrow\uparrow \dots \uparrow\rangle$. Introducing one spin flip at position n we obtain a state labeled as follows:

$$|n\rangle = S_n^- |F\rangle \quad (2.23)$$

An eigenvector in this subspace can be written as superposition of all the basis vectors.

$$|\psi\rangle = \sum_{n=1}^N a(n) |n\rangle \quad (2.24)$$

If eigenvector $|n\rangle$ is an eigenvector of the Heisenberg Hamiltonian then it must satisfy $H|\psi\rangle = E|\psi\rangle$ which leads to the expression:

$$2(E - E_0) = -J(2a(n) - a(n-1) - a(n+1)) \quad (2.25)$$

the coefficients $a(n)$ must satisfy the condition $a(n+N) = a(n)$ if we have periodic boundary conditions. The choice of coefficients that satisfy above equation are N linearly independent solutions:

$$a(n) = e^{ikn}, \quad k = \frac{2\pi}{N}m, \quad m = 0, 1, 2, \dots, N-1. \quad (2.26)$$

The states obtained by using above coefficients, are nothing but magnons states. Moving on to case $r = 2$, we search for solutions of the form:

$$|\psi\rangle = \sum_{1 \leq n_1 < n_2 \leq N} a(n_1, n_2) |n_1, n_2\rangle \quad (2.27)$$

where $|n_1, n_2\rangle = S_{n_1}^- S_{n_2}^- |F\rangle$. It is tempting to use solutions of the form $a(n_1, n_2) = e^{i(k_1 n_1 + k_2 n_2)}$ which are superpositions of magnons. It must be noted that solutions of this form would be a set of $N(N+1)/2$ over complete, non orthogonal, non stationary states. Since our subspace is made up of $N(N-1)/2$ states, and two flipped spins must be on different sites, the superposition states cannot be form the eigenspace of the Heisenberg Hamiltonian. Starting with an ansatz where the coefficients are of the form:

$$a(n_1, n_2) = A_{12} e^{i(k_1 n_1 + k_2 n_2)} + A_{21} e^{i(k_1 n_2 + k_2 n_1)} \quad (2.28)$$

the condition $H|\psi\rangle = E|\psi\rangle$ leads to equations:

$$\begin{aligned} 2(E - E_0) a(n_1, n_2) &= -J(4a(n_1, n_2) - a(n_1 - 1, n_2) - a(n_1, n_2 - 1) \\ &\quad - a(n_1 + 1, n_2) - a(n_1, n_2 + 1)) \quad \text{for } n_2 > n_1 + 1 \quad (2.29a) \\ 2(E - E_0) a(n_1, n_2) &= -J(2a(n_1, n_2) - a(n_1 - 1) - a(n_1, n_2 + 1)) \quad \text{for } n_2 = n_1 + 1 \quad (2.29b) \end{aligned}$$

Equation (2.29a) is automatically satisfied by Equation (2.28) with arbitrary A, A', k_1, k_2 for $n_2 \geq n_1 + 1$ provided the energy depends on k_1, k_2 as follows:

$$E - E_0 = -J \sum_{j=1,2} (1 - \cos k_j) \quad (2.30)$$

To satisfy Eq(2.29b), which are not automatically satisfied by Eq(2.28) we need N additional conditions

$$2a(n_1, n_1 + 1) = a(n_1, n_2) + a(n_1 + 1, n_2 + 1) \quad (2.31)$$

To satisfy this condition we require that the amplitudes in eq(2.28) satisfy:

$$\frac{A_{12}}{A_{21}} = e^{i\theta(k_1, k_2)} = -\frac{e^{i(k_1+k_2)} + 1 - 2e^{ik_1}}{e^{i(k_1+k_2)} + 1 - 2e^{ik_2}} \quad (2.32)$$

Hence the coefficients Eq(2.28) would require additional phase factors that lead to :

$$a(n_1, n_2) = e^{i(k_1 n_1 + k_2 n_2 + \frac{1}{2}\theta(k_1, k_2))} + e^{i(k_1 n_2 + k_2 n_1 + \frac{1}{2}\theta(k_2, k_1))} \quad (2.33)$$

The phase factors $\theta(k_1, k_2)$ are related to the wave vectors k_1, k_2 via the expression

$$2 \cot \frac{\theta(k_1, k_2)}{2} = \cot \frac{k_1}{2} - \cot \frac{k_2}{2} \quad (2.34)$$

The requirement of translational invariance would require $a(n_1, n_2) = a(n_2, n_1 + N)$ which would be satisfied if:

$$Nk_1 = 2\pi\lambda_1 + \theta \quad Nk_2 = 2\pi\lambda_2 - \theta \quad (2.35)$$

The total wavevector is given by the relation.

$$k = 2\pi/N(\lambda_1 + \lambda_2) \quad (2.36)$$

Where $\lambda_1, \lambda_2 \in \{0, 1, \dots, N-1\}$. Eq(2.30) and Eq(2.36) look like the energy and momentum of two superimposed magnons. These magnons are interacting and the interaction is reflected in the phase shift θ . Before moving to a general case, few remarks need to be made here. As can be noticed, the choices of λ_1, λ_2 span a space of $N(N+1)/2$ (reversal of λ_1, λ_2 lead to same

Chapter 2. Theoretical Overview

solution). But the Hilbert space of our states is $N(N-1)/2$ dimensional. It turns out that few of the solutions, particularly the ones where λ_1, λ_2 are equal or differ by one, a set of $2N-3$ states, do not satisfy Eq(2.34). Only a set of $N-3$ complex conjugate pairs constructed out of the $2N-3$ pairs satisfy Eq(2.34).

Moving to a general case with r spins flipped the derivation goes exactly analogous to $r=2$ case. The wavefunction is expected to have a form

$$|\psi\rangle = \sum_{1 < n_1 < n_2 \dots < n_r} a(n_1, n_2 \dots n_r) |n_1, n_2 \dots n_r\rangle$$

Using $H|\psi\rangle = E|\psi\rangle$ we obtain the condition:

$$\frac{E-E_0}{J} a(n_1, \dots, n_r) = -r a(n_1, \dots, n_r) + \frac{1}{2} \sum_{i=1}^r (a(\dots, n_i-1, \dots) + a(\dots, n_i+1, \dots)) \quad (2.37)$$

for cases where all the down spins are isolated $n_i+1 < n_{i+1} \forall i$. For cases with one nearest neighbour pair $n_l+1 = n_{l+1}$ we obtain the relation:

$$\begin{aligned} \frac{E-E_0}{J} a(n_1, \dots, n_r) &= -(r-1) a(n_1, \dots, n_r) + \frac{1}{2} \sum_{i \neq l, l+1}^r (a(\dots, n_i-1, \dots) + a(\dots, n_i+1, \dots)) \\ &+ \frac{1}{2} (a(\dots, n_l-1, n_l+1) + a(\dots, n_l, n_l+2, \dots)) \end{aligned} \quad (2.38)$$

To express Eq(2.38) in the same form as Eq(2.37) the additional constraints that need to be satisfied are:

$$2a(\dots, n_l, n_l+1, \dots) = a(\dots, n_l, n_l, \dots) + a(\dots, n_l+1, n_l+1, \dots) \quad (2.39)$$

Considering a generic form of coefficients motivated by Eq(2.28):

$$a(n_1, n_2 \dots n_r) = \sum_P^{M!} A_P e^{i \sum_{a=1}^r k_{P_a} n_a} \quad (2.40)$$

where P is the set of all permutations of vector $\{1, 2, \dots, r\}$. Substituting Eq(2.40) in Eq(2.39) we obtain:

$$\begin{aligned} 2 \sum_P A_P \left[e^{i \sum_{i \neq l, l+1} k_{P_i} n_i} \right] e^{i k_{P_l} n_l + i k_{P_{l+1}} n_{l+1}} &= \sum_P A_P \left[e^{i \sum_{i \neq l, l+1} k_{P_i} n_i} \right] e^{i k_{P_l} n_l + i k_{P_{l+1}} n_l} \\ &+ \sum_P A_P \left[e^{i \sum_{i \neq l, l+1} k_{P_i} n_i} \right] e^{i k_{P_l} n_{l+1} + i k_{P_{l+1}} n_{l+1}} \end{aligned}$$

where $n_{l+1} = n_l$. The term in square brackets can be cancelled out leading to:

$$2 \sum_P A_P e^{i(k_{P_l} + i k_{P_{l+1}}) n_l} e^{i k_{P_{l+1}}} = \sum_P A_P e^{i(k_{P_l} + k_{P_{l+1}}) n_l} + \sum_P A_P e^{i(k_{P_l} + k_{P_{l+1}})(n_l + 1)}$$

This expression can be further re-written as follows:

$$2 \sum_P A_P e^{i(k_{P_l} + i k_{P_{l+1}}) n_l} e^{i k_{P_{l+1}}} = \sum_P A_P e^{i(k_{P_l} + k_{P_{l+1}}) n_l} + \sum_P A_P e^{i(k_{P_l} + k_{P_{l+1}})(n_l + 1)}$$

Which leads to the final condition on coefficients A_P :

$$\frac{A_P}{A_{P'}} = -e^{i\theta(k_{P_l}, k_{P_{l+1}})} = -\frac{e^{i(k_l + k_{l+1})} + 1 - 2e^{i k_l}}{e^{i(k_l + k_{l+1})} + 1 - 2e^{i k_{l+1}}} \quad (2.41)$$

where the permutation P' is the same as P except the indices $l, l+1$ are reversed such that, $k_{P_l} = k_{P'_{l+1}}$ and $k_{P_{l+1}} = k_{P'_l}$. Using the the same analogy as $r = 2$ case a the amplitude functions look like:

$$A_P = e^{\frac{i}{2} \sum_{1 \leq a < b \leq r} \theta(k_{P_a}, k_{P_b})} \quad (2.42)$$

where the phase $\theta(k_i, k_j)$ follows the constraint:

$$2 \cot \frac{\theta(k_i, k_j)}{2} = \cot \frac{k_i}{2} - \cot \frac{k_j}{2} \quad (2.43)$$

and translational symmetry condition leads to:

$$N k_i = 2\pi \lambda_i + \sum_{j \neq i} \theta_{ij} \quad (2.44)$$

where $\lambda \in \{0, 1, \dots, N-1\}$. The energy and wave number (momentum) of the state are given by the equations:

$$E - E_0 = J \sum_{i=1}^r (1 - \cos(k_i)) \quad (2.45)$$

$$k = \frac{2\pi}{N} \sum_{i=1}^r \lambda_i \quad (2.46)$$

The mathematical formulation so far involves wave numbers k_i and phase factors $\theta(k_i, k_j)$ that show the physical properties of the magnons created on vacuum state $|F\rangle$. This mathematical treatment is convenient for a Ferromagnetic interaction. For an Antiferromagnetic Heisenberg Hamiltonian it would be convenient to start with the groundstate, which corresponds to $r = N/2$ magnons induced on $|F\rangle$, as physical vacuum. For mathematical convenience we

Chapter 2. Theoretical Overview

introduce the following notation:

$$z_i = \cot \frac{k_i}{2} \quad \phi(z_i) = 2 \arctan(z_i) = \pi - k_i \quad (2.47)$$

The function $\theta(k_i, k_j)$ then becomes:

$$\theta(k_i, k_j) = \pi \operatorname{sgn}[\Re(z_i - z_j)] - \phi\left(\frac{z_i - z_j}{2}\right) \quad (2.48)$$

where $\Re(z)$ refers to real part of z . The first term is added to make $\theta(k_i, k_j)$ remain in domain $[-\pi, \pi]$ because the function must satisfy the property $\theta(k_i, k_j) = -\theta(k_j, k_i)$. Rewriting Eq(2.44) using the new variable z finally leads to the Bethe equations:

$$N\phi(z_i) = 2\pi I_i + \sum_{j \neq i} \phi\left(\frac{z_i - z_j}{2}\right) \quad (2.49)$$

where $\{I_i\}$ are called Bethe quantum numbers. The relation between bethe quantum numbers I_i and the corresponding magnon quantum numbers $\{\lambda_i\}$ is given by:

$$I_i = \left(\frac{N}{2} - \lambda_i\right) - \frac{1}{2} \sum_{i \neq j} \operatorname{sgn}(z_i - z_j) \quad (2.50)$$

Expressions for energy and momenta are given by:

$$\frac{E - E_0}{J} = \sum_{i=1}^r \left(\frac{-2}{1 + z_i^2} \right) \quad (2.51)$$

$$k = \sum_{i=1}^r (\pi - \phi(z_i)) = \pi r - \frac{2\pi}{N} \sum_{i=1}^r I_i \quad (2.52)$$

Eq(2.49) and the corresponding energy and momentum relations Eq(2.51) form the essential structure of Bethe Ansatz solution. For some particular choices of Bethe quantum numbers I_i the eigenstates of the Hamiltonian can be constructed. For each choice of Bethe quantum numbers I_i or magnon quantum numbers λ_i , Bethe equations Eq(2.49) can be used self-consistently to derive the energies and momenta for that particular state. Similar solution can be written for a twisted boundary condition as well, with $\psi(L) = e^{i\Phi} \psi(0)$. This corresponds to the Bethe equations being modified as:

$$N\phi(z_i) = 2\pi I_i + \Phi + \sum_{j \neq i} \phi\left(\frac{z_i - z_j}{2}\right) \quad (2.53)$$

In our work we will be dealing with an anti-periodic boundary condition that is equivalent to $\phi = \pm\pi$.

Bethe quantum numbers

Before moving towards determining groundstate and excited state, it is instructive to look at the domain of the Bethe quantum numbers. The Bethe equations impose a few restriction on choices of the quantum numbers. First Eq(2.50) shows that the Bethe quantum numbers must differ only by integers. The quantum numbers I_i can take integer or half integer values. The values of λ 's are distinct for real solutions, we expect the Bethe quantum numbers to be distinct. This condition is not actually true and has been shown to breakdown at large system sizes for $r = 2$. From the Bethe equation we expect in general that $I_i > I_j$ for $z_i > z_j$ (This condition has exceptions and was pointed out by Bethe in his original work).

Considering $\{z_1 < z_2 < \dots z_r\}$ to be a solution in r spin flips sector, we try to find upper bound for I_i by taking $z_r \rightarrow \infty$. This leads to Eq(2.49) becoming:

$$\begin{aligned} N\pi &= 2\pi\tilde{I}_{max} + (r-1)\pi \\ \Rightarrow \tilde{I}_{max} &= \frac{N-r+1}{2} \end{aligned} \quad (2.54)$$

Hence, for finite solutions we have $I_i < \tilde{I}_{max}$. Similar condition for lower bound yields the final result $|I_i| \leq I_{max}$ where $I_{max} = \frac{N-r-1}{2}$. This is an important result which shows that, when $N-r$ is odd(even) the Bethe quantum numbers are (half) integers. The total number of allowed quantum numbers hence is given by $2I_{max} + 1 = N-r$. We have to select r quantum numbers to form a state, hence the total number of states from real solution is given by $\binom{N-r}{r}$. For $r = N/2$ spin flips we have only one choice and hence one state. This turns out to be the ground state. For $r = N/2 - 1$, we have $N(N+1)/8$ choices, these turn out to be the states corresponding to the triplet states for tranverse $S = 1$ excitation.

Ground State

As mentioned previously, for the set of $r = N/2$ real Bethe quantum numbers I_i 's with constraint $|I_i| \leq \frac{N-r-1}{2} = \frac{N-2}{4}$ there is only one choice.

$$\{I_i\} = \left\{ \frac{-N+2}{4}, \frac{-N+6}{4}, \dots, \frac{N-6}{4}, \frac{N-2}{4} \right\} \quad (2.55)$$

This corresponds to the choice of magnon quantum numbers:

$$\{\lambda_j\} = \{1, 3, 5, \dots, N-1\} \quad (2.56)$$

By substituting these quantum numbers, and solving the self-consistency equations we can calculate the groundstate energy. In Fig(2.4) we show the calculation performed at various system sizes for different boundary conditions. As can be seen, the ansatz with anti-periodic boundary condition is higher in energy compared to the one with periodic boundary. As we

increase the system size the energies gradually converge towards the expected value at infinite system size, $E(L = \infty)/J_x = 0.25 - \ln(2)$ represented by the red cross.

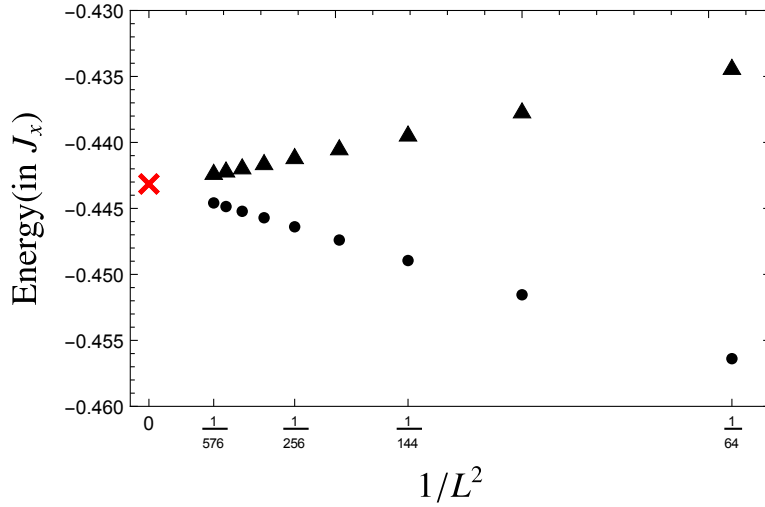


Figure 2.4 – Groundstate energy vs $1/L^2$ calculated by solving Bethe self-consistency equations at different system sizes. Dots(triangles) represent the (anti-)periodic boundary condition. The red cross mark is the exact value ($1/4 - \ln(2)$) at infinite system size.

Transverse Excitations

For inducing a $\Delta S = 1$ excitation we flip one spin down to a spin up, effectively removing one magnon. Hence we would expect our wave function of transverse excitation to be in $r = N/2 - 1$ sector and the longitudinal excitation to be in the $r = N/2$ sector. We restrict ourselves only to the transverse excitation, since the longitudinal and transverse channels are degenerate in Heisenberg case due to $SU(2)$ symmetry. Using the same conditions as previous sections we observe that:

$$I_i \in \left\{ -\frac{N}{4}, -\frac{N}{4} + 1, \dots, \frac{N}{4} - 1, \frac{N}{4} \right\} \quad (2.57)$$

We have a set of $N/2 + 1$ quantum numbers, from which we have to choose $N/2 - 1$ quantum numbers. This leaves two holes in an otherwise regular array of quantum numbers. These holes are what we call spinons. Each hole carries a spin $1/2$ and two holes cannot be on same location and hence behave as ‘fermions’.

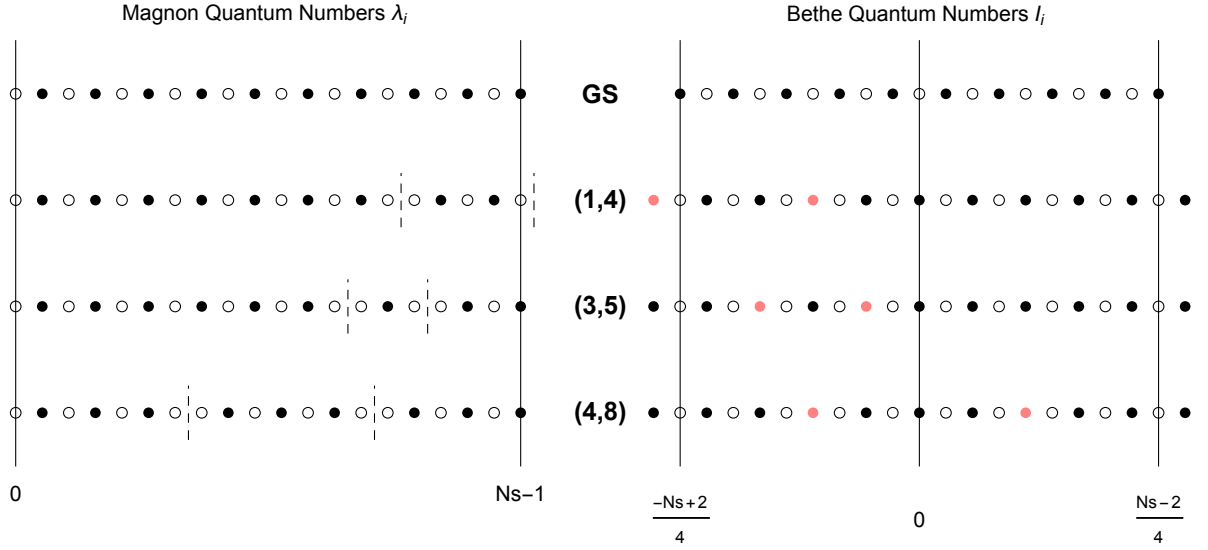


Figure 2.5 – Magnon(left) and Bethe (right) quantum numbers for ground state(GS) and excited states (a, b) where there are two holes at positions a, b .

As can be seen from Fig(2.5) we can see that the excitation spectrum consists of two vacancies or ‘holes’ in otherwise continuous spectrum of Bethe quantum numbers. This equivalently translates to magnon quantum numbers shifting from odd- even-odd values. The positions of the ‘holes’ determine the momenta \bar{k}_1, \bar{k}_2 of the spinons and the total momentum relative to the vacuum state is given by $q = \bar{k}_1 + \bar{k}_2$. Substituting these quantum numbers and solving the bethe equation provides us with the energy spectrum of transverse excitations. In Fig(2.6) we show the transverse excitation spectrum calculated at system size $L = 24$ for both periodic $\Phi = 0$ and anti-periodic $\Phi = \pm\pi$. In case of anti-periodic boundary $\Phi = \pi$ and $\Phi = -\pi$ yield two different solutions that are just related via the symmetry $q \rightarrow \pi - q$. The ‘spinons’ we see here can be interpreted as quantum solitons. Compared to the kink or boundary wall we observe in the XY case, spinons are exponentially decaying kinks. When two solitons collide with each other they emerge preserving their form, except for a phase shift.

The calculation of groundstate energy, excitation energy and related momenta at any given size, can be done via numerically solving Bethe equations. However, due to the complicated form of Bethe wave function calculating the related static or dynamic observables is intractable. A particular technique that can be used to derive these quantities from the solution of Bethe equations is ‘Algebraic Bethe Ansatz’ also known as ‘Quantum Inverse Scattering Model’ developed by the Leningrad school under the leadership of L.D. Faddeev[Faddeev et al. (1980); Takhtajan and Faddeev (1979); Sklyanin (1982)]. We will not derive the full expressions of algebraic Bethe ansatz solution for Heisenberg spin chain here. Instead we take the mathematical expressions corresponding to the dynamic structure factor from the work [Caux et al. (2005)] as a comparative benchmark whenever needed.

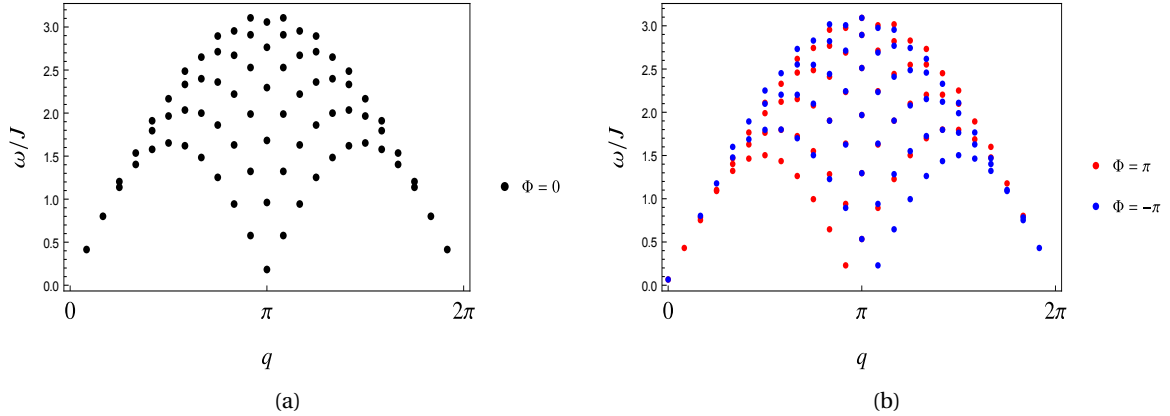


Figure 2.6 – Transverse excitation energies at system size $L = 24$ obtained through Bethe Ansatz. Black dots correspond to periodic boundary with $\Phi = 0$. Red and Blue dots correspond to Anti-periodic boundary condition with $\Phi = \pi$ and $\Phi = -\pi$ respectively, which are related via the symmetry $q \rightarrow \pi - q$.

Other Methods

Although Bethe ansatz provides us with a methodology to exactly solve the Heisenberg model in 1D it is limited to 1D integrable systems and is not generalizable. In this section we briefly discuss other analytical and numerical methods used to study the 1D, quasi-1D and 2D models with Heisenberg or Heisenberg like magnetic interactions. Some of these methods, like bosonization for example, although are specific to 1D are generalizable to higher dimensions.

Abelian Bosonization

Bosonization is a mathematical technique which is very relevant to studying 1D systems. A system of interacting fermions in $(1 + 1)$ dimensions can be transformed into a system of massless non-interacting bosons. The abelian version of this transformation was first discussed by Bloch [Bloch (1933)] and Tomonaga [Tomonaga (1950)] and was later rediscovered and better understood in works of [Mattis and H. Lieb (1965); Coleman (1975); Luther and Peschel (1975); Mandelstam (1975)]. The non-abelian version was developed by Witten [Witten (1984), Polyakov and Wiegmann Polyakov and Wiegmann (1984)]. The underlying principle is that the particle-hole excitations are bosonic in character. This principle however is valid only in 1D as shown by Tomonaga [Sénéchal (2004)]. Here we discuss the abelian bosonization in context of the XXZ model and some relevant aspects at the isotropic point $J_z = J_{xy}$, the Heisenberg model. A more detailed mathematical treatment can be found in a excellent book by Thierry Giamarchi [Giamarchi and Press (2004)].

The starting point of our discussion is the expression Eq(2.15) , where the XXZ Hamiltonian describes spinless fermions hopping with an amplitude $t = J_{xy}/2$ and subject to nearest

neighbor repulsion $V = J_z$. Considering the XY limit, the Hamiltonian yields bands with energy given by $\epsilon_k = 2t \cos(k)$. To describe the low-energy physics of the XY system, one can approximate the bands with a massless 1D system. The low energy physics of free moving fermions in 1D, within the framework of bosonization, can be described by the Hamiltonian given by:

$$\mathcal{H} = \frac{1}{2\pi} \int dx v_F ((\nabla\theta(x))^2 + (\nabla\phi(x))^2) \quad (2.58)$$

where v_F is the Fermi velocity given by $v_F = J_{xy} \sin(k_F)$ ($k_F = \pi/2$) at half filling. The fields $\phi(x), \theta(x)$ are linked to the boson operators that describe the density fluctuations via bosonization rules. The gradient of these fields are linked to the density of right $\rho_R(x)$ movers and left movers $\rho_L(x)$ via the expressions:

$$\nabla\phi(x) = -\pi(\rho_R(x) + \rho_L(x)) \quad (2.59)$$

$$\nabla\theta(x) = \pi(\rho_R(x) - \rho_L(x)) \quad (2.60)$$

which indicates that $\nabla\phi(x)$ represents the $q \sim 0$ component of density fluctuations at a point x and $\nabla\theta(x)$ represents the current operator in this 1D model.

The interaction part of the XXZ model within this framework can be written as:

$$\mathcal{H}_{int} = J_z \int dx \left(\frac{1}{\pi^2} (1 - \cos(2k_F)) (\nabla\phi(x))^2 - \frac{1}{(2\pi\alpha)^2} 2\cos(4\phi(x)) \right) \quad (2.61)$$

where α is a momentum cutoff that regularizes the theory. This finally yields the Hamiltonian:

$$\mathcal{H} = \mathcal{H}_{LL} - \frac{2J_z}{(2\pi\alpha)^2} \int dx \cos(4\phi(x)) \quad (2.62)$$

where \mathcal{H}_{LL} is the Luttinger liquid Hamiltonian:

$$\mathcal{H}_{LL} = \frac{1}{2\pi} \int dx \left(uK(\nabla\theta(x))^2 + \frac{u}{K}(\nabla\phi(x))^2 \right) \quad (2.63)$$

The Luttinger parameters here are given by:

$$\begin{aligned} uK &= v_F = J_{xy} \\ \frac{u}{K} &= v_F \left(1 + \frac{2J_z}{\pi v_F} (1 - \cos(2k_F)) \right) = v_F \left(1 + \frac{4J_z}{\pi J_{xy}} \right) \end{aligned} \quad (2.64)$$

The Hamiltonian Eq(2.62), looks like a Sine-Gordon Hamiltonian where the cosine term is related to the umklapp scattering process. It must be noted that above expressions of Luttinger parameters are valid only in perturbation regime. However, since the exact solution of isotropic

Chapter 2. Theoretical Overview

case via Bethe Ansatz is already known, the Luttinger parameters for this isotropic case can be obtained the analytical expressions of which are given by:

$$\begin{aligned}
 \frac{J_z}{J_{xy}} &= -\cos(\pi\beta^2) \\
 \frac{1}{K} &= 2\beta^2 \\
 u &= \frac{1}{1-\beta^2} \sin(\pi(1-\beta^2)) \frac{J_{xy}}{2}
 \end{aligned} \tag{2.65}$$

A few interesting features can be derived from the above analysis. Firstly, the pure XY regime the umklapp term vanishes, and the low energy physics is described by a Luttinger liquid with parameter $K = 1$. From renormalization group arguments it can be shown that for $K > 1/2$ the umklapp term is irrelevant and the system flows to a system which is Luttinger liquid like. For cases $K < 1/2$ the cosine term is relevant, and the excitations of spin chain develop a gap. Since this phase is dominated by J_z this state corresponds to ising phase along z-direction. From the expressions Eq(2.65), we see that the isotropic point is at $K = 1/2$ a point where the cosine term is marginal. Using this technique one can further estimate the forms of instantaneous spin spin correlation functions. In LL region the instantaneous correlation functions are given by:

$$\begin{aligned}
 \langle S^z(r)S^z(0) \rangle &= C_1 \frac{1}{r^2} + C_2(-1)^r \left(\frac{1}{r}\right)^{2K} \\
 \langle S^+(r)S^-(0) \rangle &= C_3 \left(\frac{1}{r}\right)^{2K+\frac{1}{2K}} + C_4(-1)^r \left(\frac{1}{r}\right)^{\frac{1}{2K}}
 \end{aligned} \tag{2.66}$$

The correlation function exhibit slower decay close to $q \sim 0$ and $q \sim k_F$ points which represent the near ferromagnetic and near Antiferromagnetic correlations respectively. For the XY case with $K = 1$, both the FM and AFM component of longitudinal correlation function decay as $1/x^2$ but the FM part of transverse component exhibits a faster decay. This indicates that the system hosts a AFM ordering in plane. The case $K > 1$ corresponds to attracting fermions that enhances the FM correlation. The case $K < 1$ corresponds to repulsion of spinless fermions that enhances the AFM part of correlation function. At the isotropic case $K = 1/2$, as expected, we can see that the transverse and longitudinal components have the same form of correlation function. Although the AFM part of LL decays as $1/r$, the marginal cosine term additionally yields a logarithmic correction which leads to final expression:

$$\langle S^\alpha(r)s^\alpha(0) \rangle = C_1 \frac{1}{r^2} + C_2(-1)^r \left(\frac{1}{r}\right) \sqrt{\log(r)} \tag{2.67}$$

This result has been derived using field theory by Affleck [Affleck (1998)] and also checked via numerical DMRG calculations by Hallberg et al [Hallberg et al. (1995)]. Hence we see that the abelian bosonization captures many of the essential features of the XXZ model at various

values of J_z/J_{xy} . It provides various insights of the physics in the non-perturbative regime through which the observables for the isotropic case can be estimated. Extending the method of bosonization to 2D is not a trivial process, although various physical properties can be estimated. System of n AFM chains with a strong FM interchain coupling, can be considered as a AFM chain of spins with spin quantum number $S = n/2$ [Timonen and Luther (1985); Schulz (1986)]. This problem has been solved by Haldane, who found a drastic difference for even and odd chains, where the even chains corresponding to integer spins show a spin gap where as the odd chains are gapless [Haldane (1983)], a problem famously known as Haldane conjecture. Similar logic can be used for AFM coupling where the spins along the rung are locked in a singlet configuration. This also yields a state where the even number of chains exhibit a spin gap and odd chains exhibit gapless modes.

The scenario which our work deals with, the coupled spin chains with weak inter-chain coupling, is a difficult problem to solve using bosonization. One can consider different bosonic fields on each chain and express the interaction in terms of these bosonic fields. Based on their analytical forms, irrelevant terms can be dropped. Research works that apply this method on two leg ladders [Timonen and Luther (1985); Schulz (1986); Strong and Millis (1992)] and extending this methodology to large number of legs [Cabra et al. (1998); Kim and Sólyom (1999)] have shown that weakly coupled chains also exhibit the same result as strongly coupled chains where by even chains have a spin gap and odd chains are gapless. Extension of this methodology to infinite chains is highly non-trivial and one must look at more sophisticated methods. Renormalization group arguments on these systems, for example by [Affleck and Halperin (1996)], have indicated that the longrange order should exist all the way to $\gamma = 0$ and that the correlation functions for half-integer spin cases have a powerlaw decay indicating a quasi-longrange order. Exact solutions of Heisenberg quantum spin chain with long-range couplings, known as Haldane-Shastry model [Shastry (1988), Haldane (1988)] are already available. Wavefunctions motivated by the exact solutions to this model can also be used as candidate wavefunctions for solving the nearest neighbor isotropic Heisenberg case.

Continuous similarity transformations

In this subsection we discuss a particular methodology that yields a strictly opposing view to our premise that the high energy features observed in the spectra of CFTD are related to a disordered RVB state. We refer to the work of [Powalski et al. (2015, 2018)]. in which the $(\pi, 0)$ quantum anomaly has been attributed to a multi-magnon interactions. To be more precise, it appears to be related to an attractive interaction that leads to dressed magnons whose excitation spectrum exhibits a relative shift of spectral weight into a high energy continuum and a lowering of the single magnon peak, referred to in their work as the ‘roton minimum’. The procedure starts with expressing the spin operators in terms of magnon excitations using Dyson Maleev representation.

$$\begin{aligned}
 S_i^+ &= \sqrt{2S} \left(a_i - \frac{a_i^\dagger a_i a_i}{2S} \right), & S_i^- &= \sqrt{2S} a_i^\dagger \\
 S_j^+ &= \sqrt{2S} \left(b_j^\dagger - \frac{b_j^\dagger b_j^\dagger b_j}{2S} \right), & S_j^- &= \sqrt{2S} b_j \\
 S_i^z &= S - a_i^\dagger a_i & S_j^z &= -S + b_j^\dagger b_j
 \end{aligned} \tag{2.68}$$

where i, j are different sub-lattices. Dyson Maleev representation has the advantage of having finite terms, at a cost of the hermiticity of the Hamiltonian unlike the Holstien Primakoff representation that requires a $1/S$ expansion. The Hamiltonian under this representation, upon Fourier transformation followed by Bogoliubov transformation, can be written in the following form:

$$\mathcal{H} = \mathcal{H}_{SW} + V^0 + V^+ + V^- \tag{2.69}$$

The first term corresponds to a diagonalized bare magnon term. The term V^0 gives the quartic correction that conserves number of magnons. The term V^+ (V^-) add(removes) magnons. The fundamental idea behind the technique used by Powaski et al., is to convert this Hamiltonian into an effective Hamiltonian that conserves the number of magnons.

$$\mathcal{H}_{eff} = \mathcal{H}_M + \mathcal{V}^0 \tag{2.70}$$

This is achieved through the use of continuous similarity transformation (CST) a method based on continuous unitary transformation CUT. The process involves using a flow equation:

$$\partial_l \mathcal{H}(l) = [\eta(l), \mathcal{H}(l)] \tag{2.71}$$

where l is a continuous variable. The Hamiltonian has same structure as Eq(2.69) but all coefficients depend on l and at $l = 0$ one has the original Hamiltonian in Eq(2.69) and at $l = \infty$ the effective Hamiltonian in Eq(2.70). The term $\eta(l)$ corresponds to the generator $V^+(l) - V^-(l)$. The commutator in Eq(2.71) generates infinite number of terms and a truncation needs to be carried out to perform this calculation numerically. Powalski et al used scaling dimension as their truncation criterion, a criterion typically used to derive the low energy and long wavelength physics via renormalization group methods. The justification of using this choice at short wavelength and high energies is related to the fact that the low edge of the $(\pi, 0)$ anomaly is a single magnon. The high energy continuum at this point is attributed to a three magnon process, where by two of the magnons are close to the gapless $(0, 0)$ point. The two magnon interaction seem to form a ‘Higgs’ resonance corresponding to a longitudinal

magnon. Hence the hybridization of three magnon continuum in this picture, should be strongly influenced by the physics of the long wavelength magnons. The flow equations are solved for finite system sizes and interpolated to $L = \infty$. In Fig(2.7) we show the result obtained from [Powalski et al. (2018)] where they compare their results with dynamical structure factor obtained by [Mourigal (2011)].

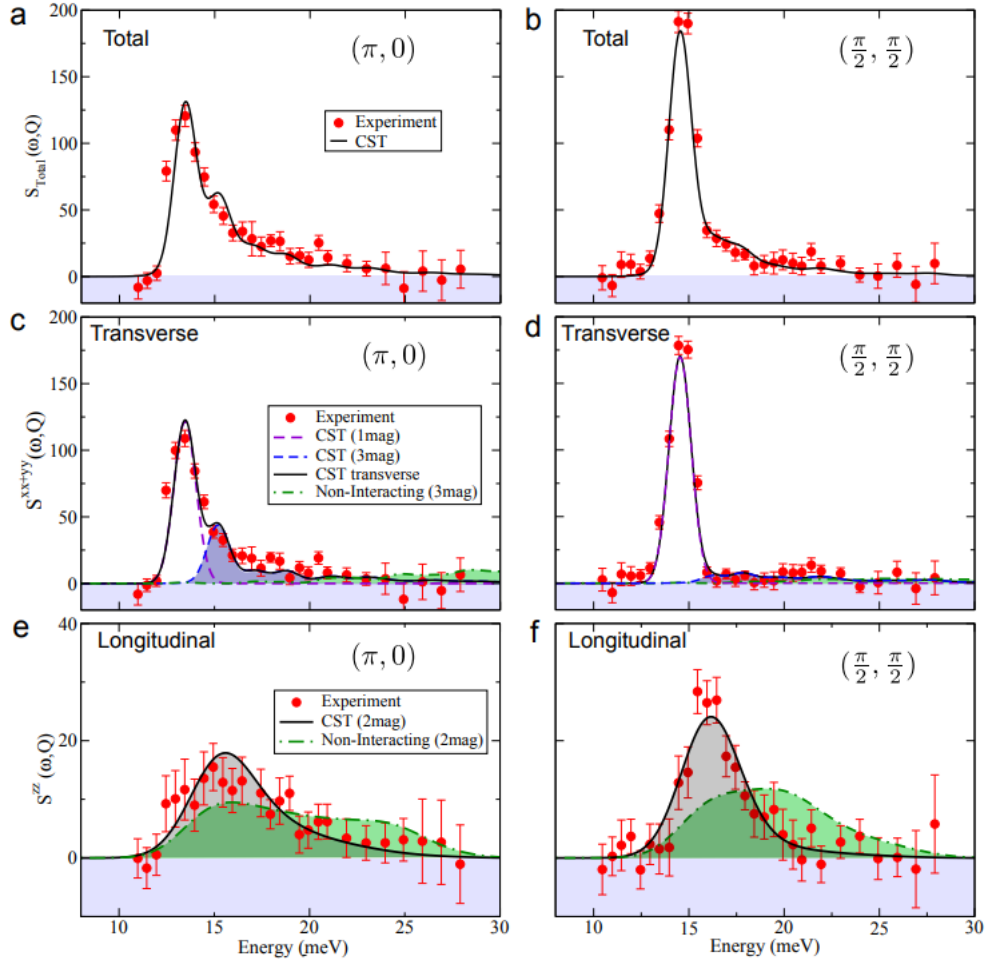
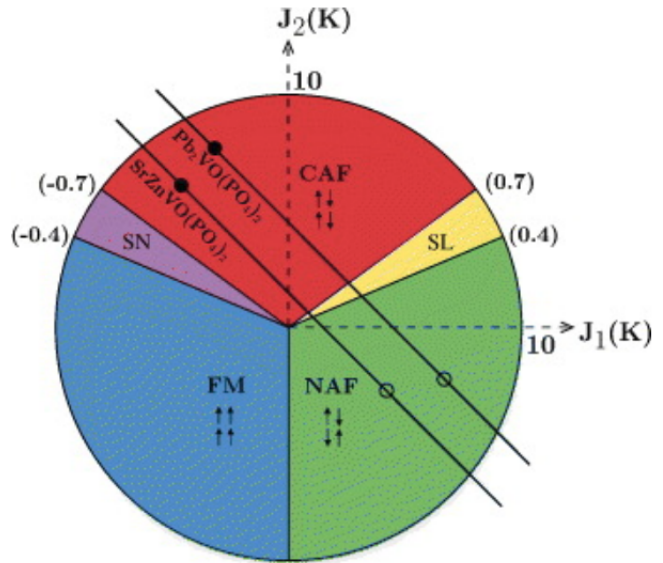


Figure 2.7 – Comparison of Dynamic structure factor data from [Mourigal (2011)] with the CST result by [Powalski et al. (2018)]. Figure taken from Powalski et al(2018).

Quantum spin liquids

In this section we present a short note on the spin liquid solutions on 1D and 2D systems with interacting spins. As mentioned in the introduction, quantum spin liquids are configurations that host massive degeneracy and exhibit a disordered magnetic configuration even at very low temperatures ($T = 0$ in principle). Search for QSL in two dimensions is an ongoing challenge

Figure 2.8 – Phase diagram of the J_1 - J_2 model. Red, green and blue region represent columnar anti ferromagnet, ferromagnet, and Neel anti-ferromagnet respectively. Purple region represents a nematic phase and yellow region is a spin liquid (Figure taken from [Skoulatos et al. (2009)]).



and so far no experimental confirmations have been made. Nevertheless the novelty of this state and its applications to multitude of problems like High Temperature superconductivity, Majorana modes, quantum computation etc. demands a deeper investigation into these states.

A primary driving force behind a QSL state is competing magnetic interactions that lead to frustration. For example in the case of square lattice Heisenberg model, frustration can be induced via the next nearest neighbor coupling J_2 . The state with very small J_2 has Neel ordering and the one with large J_2 a columnar ordering (or Neel state on two inter-penetrating square lattices). For a ferromagnetic J_1 there is a possible state with ising nematic phase [Chandra et al. (1990)]. Near the classical frustrated limit $J_1 = 2J_2$, however, all the above mentioned states become unstable. In this regime, there can be several possibilities. It can be a usual paramagnetic state without long range order and a gap for spin excitations with a unique groundstate. Another possibility one can think of is a state where the spin correlation length becomes very short, and the ground state is described in terms of pairs of spins forming singlets at short distances. These states are called valence bond states. A significant amount of research work has been done on various types of valence bond states like valence bond crystals, Resonating valence bond states with long [Anderson et al. (1987)] and short correlations [Kivelson et al. (1987)] etc. Recent research work by F. Ferrari and F. Becca [Ferrari and Becca (2018)] suggests that close to the critical point $J_2/J_1 = 0.5$ the system transitions from a Neel state to a gapless Z_2 spin liquid state where the dynamic structure factor calculated shows deconfined spinons in the region $0.48 \leq J_2/J_1 \leq 0.6$. The relevance of these RVB states goes beyond the J_1/J_2 model and we would like to present a brief description of these states.

The basic building block of a valence bond state is a singlet pair [Anderson (1973)] that can be

defined as:

$$|i, j\rangle = \frac{1}{\sqrt{2}} (|\uparrow_i \downarrow_j\rangle - |\downarrow_i \uparrow_j\rangle) \quad (2.72)$$

The lattice can be partitioned into all possible sets of pairs. If we assign a singlet to each of these pairs we can define a valance bond state which is a tensor product of these singlets.

$$|VB\rangle = \prod_{\text{pairs}} |i, j\rangle \quad (2.73)$$

It must be noted that each valance bond is odd under exchange of sites and hence a sign convention must be established while creating each pair. Since each pair is a singlet, the total spin of system is equal to zero. A typical wave function can be constructed as a superposition of these states:

$$|\psi\rangle = \sum_P A_P \prod_{\text{pairs}} |i, j\rangle \quad (2.74)$$

where A_P is the amplitude of a particular partition. Although the valance bond states are simple to construct in this way, it must be noted that these states are difficult to work with. A primary reason for this is fact that the valance bond states are not orthogonal and in general cannot be all linearly independent. Hence they form a set of overcomplete states and not generally a good choice for expanding a wavefunction. However, if one wants to construct a variational wave function a popular choice is is the one with factorized amplitude:

$$A(P) = \prod_{\text{pairs}} a(i, j) \quad (2.75)$$

such that the total wave function looks like:

$$|\psi\rangle = \sum_P \prod_{\text{pairs}} a(i, j) |i, j\rangle \quad (2.76)$$

If we make a further assumption that the amplitude $a(i, j)$ is only a function of the distance between the pairs:

$$a(i, j) = a(|r_i - r_j|) \quad (2.77)$$

This choice corresponds to the state known as a Resonating valance bond state [Anderson (1973)] in the sense that all the valance bonds between sites with equal separation, have same amplitude. An extensive study of the Heisenberg model using these states was carried out by Liang, Ducot and Anderson [Liang et al. (1988)] which showed that the physical properties of system depend on how fast the function $a(x)$ decays at infinity. Considering a power-law

ansatz

$$a(|r|) = \frac{c}{|r|^\sigma} \quad (2.78)$$

they found that for $\sigma < 5$ the state exhibits long range Neel order, and for $\sigma \geq 5$ Neel order is limited to a finite correlation length ξ .

Having constructed the basic form of a RVB state an important question one might ask is whether any of these solutions are a good approximates to the groundstate of unfrustrated Heisenberg model. RVB states with short range singlets, have an exponentially decaying spin spin correlation function and must correspond to a groundstate with a finite gap. On the other hand RVB states with long range singlets are closer to a Neel state. Numerical evidence suggest RVB states with sufficiently long range singlets is actually a good approximation to the Neel state [Liang et al. (1988)].

Having constructed the RVB states one might want to have a look at the spin excitations on these states. As mentioned in Chapter 1, a $\Delta S = 1$ excitation excites a singlet into a triplet $|\uparrow\uparrow\rangle$ and each of these up spins propagating in the RVB background at minimal cost can be termed as ‘spinons’. A particular challenge while dealing with spinons is the satisfaction of the no double occupancy constraint when the spinons propagate from one site to another. In case of situations other than half filling one can use the slave-boson approach that lead to RVB theories of [Baskaran et al. (1987)](BZA phase) and [Ruckenstein et al. (1987)]. Basic idea behind this approach is that one considers a constraint:

$$b^\dagger(x)b(x) + f_\alpha^\dagger(x)f_\alpha(x) = 1 \quad (2.79)$$

where the boson operator b^\dagger creates a charge carrying particle called ‘holon’ and the fermion operator f_α^\dagger creates a fermion with flavour α . One could also define the holons to be fermions and ‘spinons’ to be bosons. In case of half filling, the number of holons is zero. In our research work, we use a gutzwiller projector to satisfy the no double occupancy constraint.

In seeking solutions for quantum Heisenberg spin systems a popular methodology is to extned the exact solutions found in a) Large S systems b) $SU(n)$ groups with large n . The first method usually involves some form of spin wave theory which works extremely well in case of classical spins. We would like to discuss a few aspects of the solution of second type found by Marston et al.[Marston and Affleck (1989)], to $SU(n)$ group in large n limit. By studying a $SU(n)$ generalization of Hubbard-Heisenberg model they were able to show that the exact solutions is a dimerized phase in one dimension. In two dimension they found two solutions to be possible candidates, a Peierls phase at exact Heisenberg case and a flux phase for slightly larger t or biquadratic spin terms. Concerning the generalization of $SU(n)$ solution for $n = 2$, in one dimension dimerized phase is not stable and one might require next nearest neighbour coupling to stabilize it. The true ground state must be a gapless phase as required by Lieb-Schultz-Mattis theorem [Lieb et al. (1961)]. In two dimensions, numerical calculations with Gutzwiller projected states suggested that the flux phase might be a better approximation

to the ground state as it has better energy than the Peierls phase. This flux phase shall become the starting point in our work, where instead of a π flux alternating between plaquettes, we consider an arbitrary flux as a variational parameter in constructing our state. In doing so we work with a state that is referred to as the Staggered flux wave function and a Gutzwiller projected version of this state (referred to as SF) shall be used as the groundstate ansatz in our work.

3 Spin Wave Theory

Spin wave theory is by far one of the most successful theories that can accurately explain the spin excitation spectrum of materials with non-frustrated Heisenberg interactions in dimensions $D > 1$. Although there are some limitations in its applicability to quantum spins $S = 1/2$ particularly in lower dimensions, its simplicity makes it an attractive candidate for initial analysis of excitation spectra of various materials. As mentioned in the previous chapters, strict deviations from the spin-wave result ($(\pi, 0)$ quantum anomaly) are the motivation behind searching for alternate methods to describe a the square lattice Heisenberg model. As we move towards 1D case through the rectangular model, it is natural to assume that these deviations would get stronger and the applicability of spin wave result becomes weaker. Nevertheless, it is instructive to use this theory to analyze the RQHAF, to understand its limitations. Furthermore, it could serve as a bench mark against which the staggered flux solution in the subsequent chapters could be compared.

Mathematical Framework

In this chapter we use the spin wave theory to derive groundstate energy, instantaneous and dynamic spin-spin correlation functions of RQHAF. The outline of the procedure is as follows:

- 1) The spin operators are expanded using the Holstien-Primakoff transformation, and the series is truncated to include only terms quartic in boson creation and annihilation operators.
- 2) The linear terms are used to derive the bare values of the observables, and subsequently the fourth order terms are converted to second order using a mean field method. The contribution from the quartic terms provides us with renormalized values for observables.
- 3) Since a mean field method is used, the renormalization procedure is carried out self-consistently to obtain a stable solution. The limitations of the theory would be related to the stability of this self-consistent procedure.

4) Once we have a regime where our spin wave solution is valid we proceed to calculate the groundstate energy, staggered magnetization, and instantaneous and transverse dynamic spin-spin correlation functions.

Operator Expansion

Spin wave theory starts with assuming an ordered state, i.e a Neel state in our case, and introducing fluctuations as $\Delta S = 1$ magnon excitations on it. We assume our Neel state to be ordered along the z-direction. To simplify the formalism we introduce a staggered rotation to make the magnetic ordering ferromagnetic:

$$\begin{aligned} S_i^x &= e^{iQ \cdot R_i} \hat{S}_i^x \\ S_i^y &= \hat{S}_i^y \\ S_i^z &= e^{iQ \cdot R_i} \hat{S}_i^z \end{aligned} \quad (3.1)$$

where $Q = (\pi, \pi)$ and R_i is the position vector (scaled with the lattice constant). A dot product between two spins S_i and $S_{i+\tau}$ separated by vector τ becomes:

$$S_i \cdot S_{i+\tau} = (2\epsilon_\tau - 1) \hat{S}_i^z \hat{S}_{i+\tau}^z + \frac{1}{2} [\epsilon_\tau (\hat{S}_i^+ \hat{S}_{i+\tau}^- + \hat{S}_i^- \hat{S}_{i+\tau}^+) - \bar{\epsilon}_\tau (\hat{S}_i^+ \hat{S}_{i+\tau}^+ + \hat{S}_i^- \hat{S}_{i+\tau}^-)] \quad (3.2)$$

with

$$\epsilon_\tau = \frac{1 + e^{iQ \cdot \tau}}{2} \quad \bar{\epsilon}_\tau = \frac{1 - e^{iQ \cdot \tau}}{2}$$

A local spin flip at site i is induced through bosonic creation(annihilation) operators $a_i^\dagger(a_i)$ via the Holstien-Primakoff transformation [Holstein and Primakoff (1940)] given by:

$$\begin{aligned} \hat{S}_i^z &= S - a_i^\dagger a_i \\ \hat{S}_i^+ &= \sqrt{2S - \hat{n}_i} a_i \\ \hat{S}_i^- &= a_i^\dagger \sqrt{2S - \hat{n}_i} \end{aligned} \quad (3.3)$$

where $\hat{n}_i = a_i^\dagger a_i$. The terms under the square root can be expanded using a binomial expansion:

$$\sqrt{2S - \hat{n}_i} = \sqrt{2S} \sum_{k=0}^{\infty} \frac{1}{2^k k!} \left(\frac{-\hat{n}_i}{2S} \right)^k \quad (3.4)$$

Under the assumption $\hat{n}_i < 2S$ this expression can be sufficiently truncated at some finite and small k . For classical spins i.e large S values this condition is sufficiently satisfied. However, for a quantum spin $S = 1/2$ the series can be truncated only if $\langle \hat{n}_i \rangle < 1$. This equivalent to the 'hard-core' boson condition that requires that the average number of bosons on a single site

cannot be more than one. Assuming a hard core boson condition we substitute Eq(3.4) in Eq(3.2) to obtain:

$$S_i \cdot S_{i+\tau} = S^2 \left[(S_i \cdot S_{i+\tau})^{(0)} + \frac{1}{S} (S_i \cdot S_{i+\tau})^{(1)} + \frac{1}{S^2} (S_i \cdot S_{i+\tau})^{(2)} + \mathcal{O}\left(\frac{1}{S^3}\right) \right] \quad (3.5)$$

where

$$(S_i \cdot S_{i+\tau})^{(0)} = (2\epsilon_\tau - 1) \quad (3.6)$$

$$(S_i \cdot S_{i+\tau})^{(1)} = -(2\epsilon_\tau - 1) \left(a_i^\dagger a_i + a_{i+\tau}^\dagger a_{i+\tau} \right) + \epsilon_\tau \left(a_i a_{i+\tau}^\dagger + a_{i+\tau}^\dagger a_i \right) + \bar{\epsilon}_\tau \left(a_i^\dagger a_{i+\tau}^\dagger + a_i a_{i+\tau} \right) \quad (3.7)$$

$$\begin{aligned} (S_i \cdot S_{i+\tau})^{(2)} &= (2\epsilon_\tau - 1) n_i n_{i+\tau} - \frac{\epsilon_\tau}{4} \left(n_i a_i a_{i+\tau}^\dagger + a_i a_{i+\tau}^\dagger n_{i+\tau} + a_i^\dagger n_i a_{i+\tau} + a_i^\dagger n_{i+\tau} a_{i+\tau} \right) \\ &+ \frac{\bar{\epsilon}_\tau}{4} \left(n_i a_i a_{i+\tau} + a_i n_{i+\tau} a_{i+\tau} + a_i^\dagger n_i a_{i+\tau}^\dagger + a_i^\dagger a_{i+\tau}^\dagger n_{i+\tau} \right) \end{aligned} \quad (3.8)$$

In our present work, we consider the terms only till the order $1/S^2$ in square brackets of Eq(3.5).

Linear Terms

The zero order term is nothing but the Neel state energy. The first order term, which is quadratic in boson operators, is the quantized manifestation of fluctuations away from Neel state. Using the following Fourier transform:

$$\begin{aligned} a_i &= \frac{1}{\sqrt{N}} \sum_q e^{iq \cdot R_i} a_q \\ a_i^\dagger &= \frac{1}{\sqrt{N}} \sum_q e^{-iq \cdot R_i} a_q^\dagger \end{aligned}$$

Summation over the quadratic part over all lattice sites turns out to be:

$$\sum_i (S_i \cdot S_{i+\tau})^{(1)} = \sum_k A_k^\tau a_k^\dagger a_k + \frac{1}{2} B_k^\tau \left(a_k^\dagger a_{-k}^\dagger + a_k a_{-k} \right) \quad (3.9)$$

where:

$$\begin{aligned} A_k^\tau &= (1 - 2\epsilon_\tau) + 2\epsilon_\tau \cos(k \cdot \tau) \\ B_k^\tau &= -2\bar{\epsilon}_\tau \cos(k \cdot \tau) \end{aligned} \quad (3.10)$$

Chapter 3. Spin Wave Theory

The final contribution of these terms to Heisenberg Hamiltonian is given by:

$$\mathcal{H}_{SW}^{(2)} = \sum_k A_k a_k^\dagger a_k + \frac{1}{2} B_k (a_k^\dagger a_{-k}^\dagger + a_k a_{-k}) \quad (3.11)$$

where

$$A_k = \sum_\tau J_\tau S A_k^\tau \quad B_k = \sum_\tau J_\tau S B_k^\tau \quad (3.12)$$

Apart from containing a diagonalized part, the Hamiltonian Eq(3.11) contains non-diagonal ($a^\dagger a^\dagger$) and (aa) like terms. To diagonalize Eq(3.11), we utilize a Bogoliubov transformation. Defining the following quasi particle operators:

$$b_k = u_k a_k + v_k a_{-k}^\dagger \quad (3.13)$$

the diagonalized Hamiltonian is expected to have the following form:

$$\mathcal{H}_{SW}^{(2)} = \sum_k \omega_k b_k^\dagger b_k + \sum_k \frac{1}{2} \omega_k - \frac{1}{2} \sum_k A_k \quad (3.14)$$

The first term corresponds to bosonic excitations and the second and third term reflect the zero-point energy of the vacuum state. Eq(3.14) must satisfy:

$$\left[\mathcal{H}_{SW}^{(2)}, b_k \right] = -\omega_k b_k \quad (3.15)$$

which leads to the eigenvalue problem:

$$\begin{pmatrix} A_k & -B_k \\ B_k & -A_k \end{pmatrix} \begin{pmatrix} u_k \\ v_k \end{pmatrix} = \omega_k \begin{pmatrix} u_k \\ v_k \end{pmatrix} \quad (3.16)$$

Solving the eigenvalue problem leads to :

$$\omega_k = \sqrt{A_k^2 - B_k^2} \quad (3.17)$$

with

$$u_k = \sqrt{\frac{1}{2} \left(\frac{A_k}{\omega_k} + 1 \right)}, \quad v_k = \text{sign}(B_k) \sqrt{\frac{1}{2} \left(\frac{A_k}{\omega_k} - 1 \right)} \quad (3.18)$$

For case of rectangular lattice the bare magnon energy is given by:

$$\omega(k_x, k_y) = \sqrt{(J_x + J_y)^2 - (J_x \cos k_x + J_y \cos k_y)^2} \quad (3.19)$$

Before moving to further, it is instructive to look at some symmetries in coefficients u_k, v_k . Both of them are real and have inversion symmetry $u_k = u_{-k}, v_k = v_{-k}$. Apart from inversion

symmetry they also exhibit the symmetry, $u_{k\pm Q} = u_k$ and $v_{k\pm Q} = -v_k$.

First Quantum Correction

In this section we treat the first correction containing terms quartic in fermion operators which is given by Eq(3.8). These terms represent the magnon-magnon interactions. To convert them into quadratic form, first we divide the product of a pair of boson operators A, B as below:

$$AB = \overline{AB} + :AB: \quad (3.20)$$

where \overline{AB} is called the contraction and $:AB:$ is called the normal ordering. Using Wick's theorem, a product of four operators A, B, C, D can be written as:

$$\begin{aligned} ABCD &= :ABCD: + \sum_{pairs} \overline{AB} :CD: + \sum_{pairs} \overline{AB} \overline{CD} \\ ABCD &= :ABCD: + \sum_{pairs} \overline{AB}(CD - \overline{CD}) + \sum_{pairs} \overline{AB} \overline{CD} \\ ABCD &= :ABCD: + \sum_{pairs} \overline{AB}CD - \sum_{pairs} \overline{AB} \overline{CD} \end{aligned} \quad (3.21)$$

The first term has zero expectation value for ground state and hence ignored. Here we make an assumption where the pair-wise contraction \overline{AB} is replaced by a mean field $\langle AB \rangle$. This is analogous to Hartree-Fock method in quantum many body problem. If the mean field is derived through an iterative process it is called 'Self-consistent' mean field method. The second term contributes to the dispersion spectrum and the third term contributes to the ground state energy. We first define the following mean fields:

$$\begin{aligned} n &= \langle a_i^\dagger a_i \rangle \\ \delta &= \langle a_i a_i \rangle = \langle a_i^\dagger a_i^\dagger \rangle \\ t_\tau &= \langle a_i^\dagger a_{i+\tau} \rangle = \langle a_i a_{i+\tau}^\dagger \rangle \\ \Delta_\tau &= \langle a_i a_{i+\tau} \rangle = \langle a_i^\dagger a_{i+\tau}^\dagger \rangle \end{aligned}$$

Using these mean fields one could decouple the quartic bosonic terms to quadratic form. For example considering quartic part of the first term in Eq(3.8):

$$\begin{aligned} \sum_i n_i n_{i+\tau} &= \sum_i a_i^\dagger a_i a_{i+\tau}^\dagger a_{i+\tau} \\ &= \sum_i \left[n \left(a_i^\dagger a_i + a_{i+\tau}^\dagger a_{i+\tau} \right) + \Delta_\tau \left(a_i a_{i+\tau} + a_i^\dagger a_{i+\tau}^\dagger \right) + t_\tau \left(a_i a_{i+\tau}^\dagger + a_i^\dagger a_{i+\tau} \right) \right] \end{aligned} \quad (3.22)$$

Chapter 3. Spin Wave Theory

Using the fourier transform of the bosonic operators:

$$\sum_i n_i n_{i+\tau} = \sum_k \left[2(n + t_\tau \cos(k \cdot \tau)) a_k^\dagger a_k + \Delta_\tau \cos(k \cdot \tau) (a_q^\dagger a_{-q}^\dagger + a_q a_{-q}) \right] \quad (3.23)$$

This expression looks similar to Eq(3.9). Adding all the contributions from Eq(3.8) we obtain:

$$\sum_i (S_i \cdot S_{i+\tau})^{(2)} = \sum_k dA_k^\tau a_k^\dagger a_k + \frac{1}{2} dB_k^\tau (a_k^\dagger a_{-k}^\dagger + a_k a_{-k}) \quad (3.24)$$

where

$$\begin{aligned} dA_k^\tau &= 2\epsilon_\tau (1 - \cos(k \cdot \tau)) (n - t_\tau) + 2\bar{\epsilon}_\tau \left(\Delta_\tau - n + \left(\frac{\delta}{2} - t_\tau \right) \cos(k \cdot \tau) \right) \\ dB_k^\tau &= 2\epsilon_\tau \left(\left(\Delta_\tau - \frac{\delta}{2} \right) \cos(k \cdot \tau) - \frac{\Delta_\tau}{2} \right) + 2\bar{\epsilon}_\tau \left(\frac{t_\tau}{2} + (n - \Delta_\tau) \cos(k \cdot \tau) \right) \end{aligned} \quad (3.25)$$

Adding these terms to the bare Hamiltonian would provide us with an expression similar to Eq(3.11) with modified amplitudes:

$$A'_k = A_k + dA_k \quad B'_k = B_k + dB_k \quad (3.26)$$

where

$$dA_k = \sum_\tau J_\tau dA_k^\tau \quad dB_k = \sum_\tau J_\tau dB_k^\tau \quad (3.27)$$

Calculating the mean fields from the groundstate of diagonalized Hamiltonian Eq(3.14) we obtain:

$$\begin{aligned} n &= \frac{1}{N} \sum_k v_k^2 = \frac{1}{(2\pi)^2} \int_0^{2\pi} dk_x \int_0^{2\pi} dk_y v_k^2 \\ \delta &= -\frac{1}{N} \sum_k u_k v_k = -\frac{1}{(2\pi)^2} \int_0^{2\pi} dk_x \int_0^{2\pi} dk_y u_k v_k \\ t_\tau &= \frac{1}{N} \sum_k \cos(k \cdot \tau) v_k^2 = \frac{1}{(2\pi)^2} \int_0^{2\pi} dk_x \int_0^{2\pi} dk_y \cos(k \cdot \tau) v_k^2 \\ \Delta_\tau &= -\frac{1}{N} \sum_k \cos(k \cdot \tau) u_k v_k = -\frac{1}{(2\pi)^2} \int_0^{2\pi} dk_x \int_0^{2\pi} dk_y \cos(k \cdot \tau) u_k v_k \end{aligned} \quad (3.28)$$

Using the symmetry $u_{k\pm Q} = u_k$ and $v_{k\pm Q} = -v_k$, we observe integrals of the term δ evaluates to zero. Since we have only nearest neighbor interactions with $\tau = \hat{e}_x, \hat{e}_y$, we observe that the

terms t_τ also vanish. Hence the terms in Eq(3.25) can be simplified as:

$$\begin{aligned} dA_k^\tau &= 2(\Delta_\tau - n) \\ dB_k^\tau &= 2(n - \Delta_\tau) \cos(k \cdot \tau) \end{aligned} \quad (3.29)$$

By calculating the mean fields we can estimate the corrections dA_k, dB_k and calculate the renormalized dispersion from which we can obtain the new estimates for the mean fields. This process can be done self-consistently until we achieve required accuracy. However, there are a few challenges pertaining to carrying out this procedure on rectangular Heisenberg systems, particularly at low couplings.

Instability at low Coupling

Taking a look at the mean field n that gives average number of bosons on a site:

$$n = \frac{1}{(2\pi)^d} \int d^d k v_k^2 = \frac{1}{(2\pi)^d} \int d^d k \frac{1}{2} \left(\frac{A_k}{\omega_k} - 1 \right) \quad (3.30)$$

where d is the dimension. In 1D case this mean field becomes:

$$n = \frac{1}{2\pi} \int_0^\pi dk \left(\frac{1}{\sqrt{1 - \cos^2(k)}} - 1 \right) \quad (3.31)$$

The integrand diverges at $k = 0$. Rewriting the integral as follows:

$$n = \int_\delta^\pi \frac{dk}{2\pi} \left(\frac{1}{\sqrt{1 - \cos^2(k)}} - 1 \right) + \int_0^\delta \frac{dk}{2\pi} \left(\frac{1}{\sqrt{1 - \cos^2(k)}} - 1 \right) \quad (3.32)$$

where δ is a small number. The first part of the integral is finite and can be numerically evaluated The second term at small k can be expanded as follows:

$$\int_0^\delta \frac{dk}{2\pi} \left(\frac{\sqrt{2}}{k} - 1 \right) = \frac{\sqrt{2}}{2\pi} \log k \Big|_0^\delta - \frac{\delta}{2\pi} \quad (3.33)$$

Hence we observe that the mean field has a logarithmic divergence and has no finite value. Hence, even at zero temperature the 1D chain does not exhibit a long range order. The quantum fluctuations are strong enough to destroy the longrange order and hence the groundstate is a disordered phase. When we move into 2D case with a square lattice carrying out the same procedure will lead to the second term being(cutoff is a circle around $(0, 0)$):

$$\int_0^\delta dk \int_0^{2\pi} d\phi \frac{k}{(2\pi)^2} \left(\frac{\sqrt{2}}{k} - 1 \right) = \frac{\sqrt{2}\delta}{2\pi} - \frac{\delta^2}{4\pi} \quad (3.34)$$

which is finite and vanishes as $\delta \rightarrow 0$. Hence 2D case hosts long range order at least at $T = 0$. In rectangular lattices, reducing the coupling J_y towards zero, gradually brings us towards a case where the divergence at $k = 0$ plays a significant role and hence the estimate of n becomes increasingly large. In applying the self-consistency criterion, apart from the stability of the mean fields, we must pay attention to the constraints on our mean fields. Previously we have mentioned the hard core boson constraint $n_i < 1$. Apart from this we have a much stronger constraint $n < 1/2$, which comes from the fact that as n gets close to $1/2$ the staggered magnetization $\langle (-1)^i S_i^z \rangle = 1/2 - n$ goes to zero. If $n > 1/2$ then our initial assumption of ordered state (FM lattice \hat{S}_i ordered along +z direction with reduced moment) fails. In the subsequent sections we provide a more clear argument for this constraint.

Correlation functions

To estimate the static and dynamic correlation functions we have to establish their mathematical forms. Following the same procedure as in previous sections we obtain the following forms for correlation functions.

$$\begin{aligned} \langle S_i^x \cdot S_{i+\tau}^x \rangle &= \frac{e^{iQ \cdot R_i}}{2} (1 - 2n) (\Delta_\tau + t_\tau) \\ \langle S_i^y \cdot S_{i+\tau}^y \rangle &= \frac{1}{2} (1 - 2n) (t_\tau - \Delta_\tau) \\ \langle S_i^z \cdot S_{i+\tau}^z \rangle &= e^{iQ \cdot R_i} \left(\frac{1}{4} - n + n^2 + \Delta_\tau^2 + t_\tau^2 \right) \end{aligned} \quad (3.35)$$

We have used the fact that $\delta = 0$ in our case while deriving the above equations. At $\tau = 0$ we have $t_\tau = n, \Delta_\tau = 0$ which leads to the result $\langle S_i^x \cdot S_{i+\tau}^x \rangle = \langle S_i^y \cdot S_{i+\tau}^y \rangle = n/2 - n^2$ and $\langle S_i^z \cdot S_{i+\tau}^z \rangle = 1/4 - n + 2n^2$ leading to $\langle S_i^z \rangle = 1/4$ which is different from the expected result $\langle S_i^z \rangle = 3/4$. This is due to the fact that the operators for S_i^x and S_i^y are truncated and to first order, carry only the contributions from the fluctuations away from Neel state. As one would expect a non negative value for $\langle S_i^z \rangle$ we obtain the constraint $n < 1/2$. At finite τ , from above expressions, it is clear that the x and z components of the correlation functions are staggered. Although it is not clearly evident from above expressions, applying the symmetry $k \rightarrow k + Q$ in Eq(3.28), we observe that on even sublattice $\Delta_\tau = 0$ and on odd sublattice $t_\tau = 0$. This renders the x and y components of the correlation function to be equal, as expected.

The Dynamic(transverse) spin correlation function on other hand is given by the equation:

$$S^{+-}(q, \omega) = \sum_{\lambda} \langle 0 | S_q^+ | \lambda \rangle \langle \lambda | S_q^- | 0 \rangle \delta(\omega + E_{GS} - E_{\lambda}) \quad (3.36)$$

where $|0\rangle$ is the ground state i.e the vacuum state of operators b, b^\dagger and $|\lambda\rangle$ are all possible intermediate states. In principle they contain both single magnon and multi-magnon contributions. In this work we only consider the contribution of the states corresponding to single

magnon excitations, $|\lambda\rangle = b_k^\dagger |0\rangle$. Substituting this result and performing a few mathematical calculations leads to the final expression

$$S^{+-}(q, \omega) = 2(1 - n)(u_k + v_k)^2 \delta(\omega + E_{GS} - E_\lambda) \quad (3.37)$$

where the factor $(1 - n)$ comes from the quantum corrections.

Results

In this section we present the results corresponding to our self-consistent mean field calculations. Values of the mean fields have been determined by using numerical integration. While performing the numerical integration we assume a finite cutoff $\delta = \pi/1000$ around the points $(0, 0)$ and (π, π) where $\omega_k = 0$. We assume that the contribution from the omitted part to be minimal which may not be true very close to $J_y = 0$.

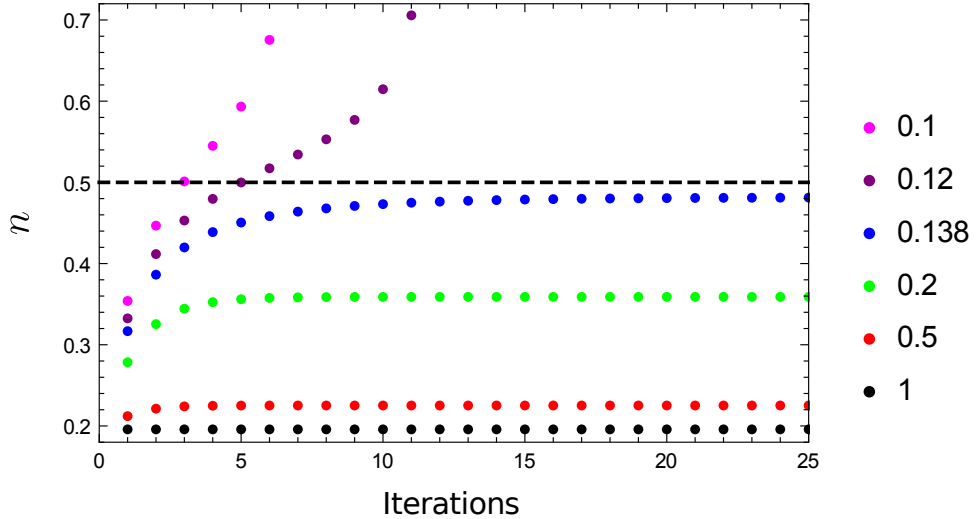


Figure 3.1 – Values of Meanfield n vs iterations for various γ in a self-consistent calculation. The dashed line indicates the limit corresponding to the constraint $n < 1/2$.

For the moment, we focus our attention on the fulfillment of the self consistency criterion and the constraint $n < 1/2$. In Fig(3.1) we show the value of mean field n for the first 25 iterations in the self consistency calculation. As one can see within a few steps, we achieve a good convergence for values $J_y/J_x \geq 0.138$. However for $J_y/J_x < 0.138$ we observe the self-consistency criterion failing and the value of n going beyond $1/2$. $J_y/J_x = 0.138$ appears to be the limiting value where Linear spin-wave theory with first order correction works. This also happens to be close to 0.1356 , the value proposed by [Miyazaki et al. (1995)] using Schwinger boson mean field technique. However this by no means is a proof that long range order is destroyed at this coupling. This might just be the effect of mean field wavefunction and this has been expressed by Miyazaki et al. as well. In Fig(3.2) we show the final values of mean

fields obtained using the self-consistency procedure. In Fig(3.2)(a), we show the staggered magnetization given by $\langle e^{iQ \cdot R} S_i^z(R) \rangle = 1/2 - n$. The staggered magnetization has a reduced value 0.304 at symmetric case which gradually goes to 0 around $\gamma = 0.138$. We also show the values of functions Δ_τ for $\tau = \hat{e}_x, \hat{e}_y$ which represents the nearest neighbor (staggered)spin-spin correlation function(xx and yy components to first order) as can be seen from Eq(3.35). The nearest-neighbor correlation(till first order) decreases in y-direction while it increases in x direction as we decrease γ .

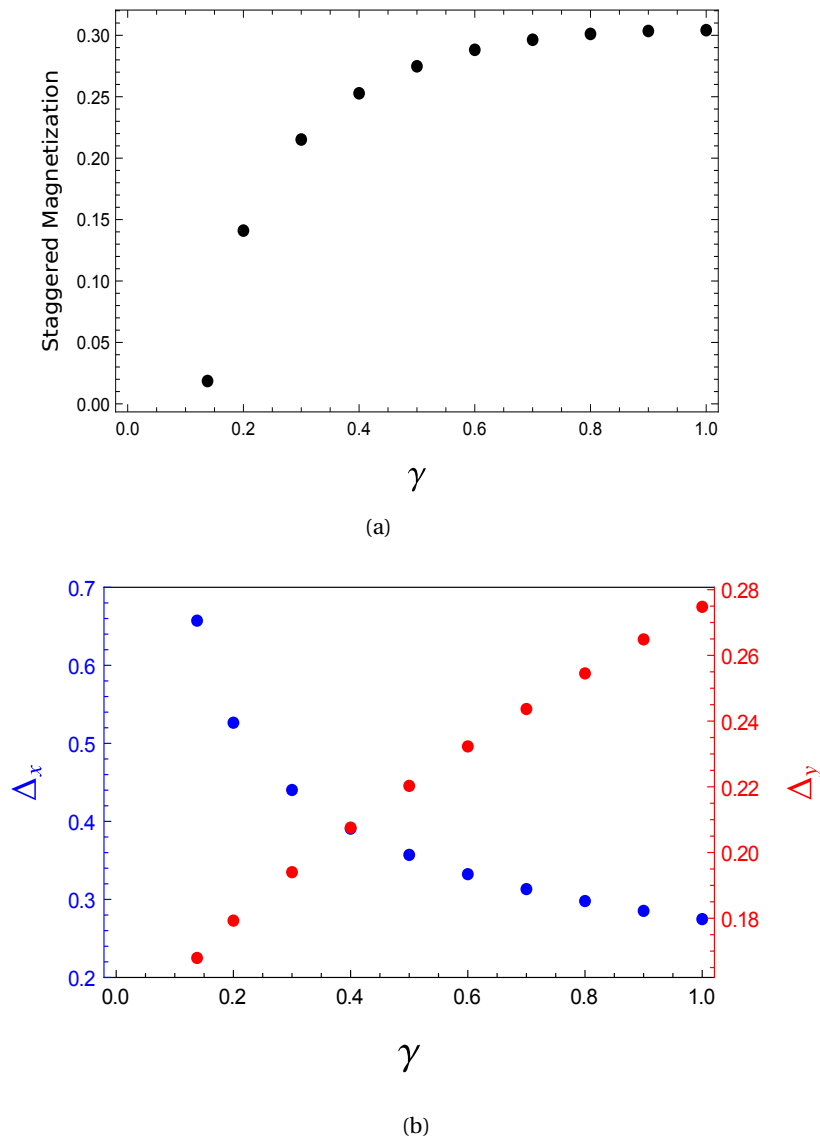


Figure 3.2 – (a) Staggered magnetization and the (b) mean field Δ_τ for $\tau = x(\hat{e}_x), y(\hat{e}_y)$ represented with blue and red dots respectively vs coupling ratio γ .

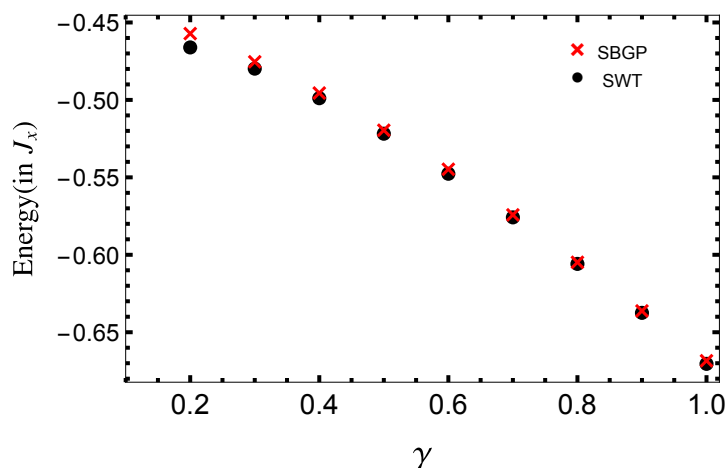


Figure 3.3 – Ground state energy obtained from spin wave theory(SWT) and a comparison with Gutzwiller projected Schwinger boson result from Miyazaki et al.

The ground state energy can be estimated via the nearest neighbor spin-spin correlation function expressions in Eq(3.35) using the expression.

$$\begin{aligned}
 E_{GS} &= \sum_{\tau} J_{\tau} \langle 0 | S_{i+\tau} S_i | 0 \rangle \\
 &= \sum_{\tau} J_{\tau} \left[\left(-\frac{1}{4} \right) + (n - \Delta_{\tau}) - (n - \Delta_{\tau})^2 \right]
 \end{aligned} \tag{3.38}$$

where we use the expressions from Eq(3.35) and we substitute $t_{\tau} = 0$ for nearest neighbors. The first term in square brackets is the energy from Neel term. Through some mathematical calculations it can be shown that the second term, if considered to first order, is exactly equal to the zero point energy in Eq(3.14). The third term provides the next order corrections to this zero-point energy. In Fig(3.3) we show the groundstate energies for $\gamma \geq 0.2$ obtained from this procedure. We compare this result with the results from Miyazaki et al, where they use Gutzwiller projected ordered state as ground state ansatz. The excitations induced in their work are Schwinger bosons, and the Gutzwiller projector is used to impose the hard core boson condition. The result obtained from our self-consistent procedure seems to have better groundstate estimates compared to their work. Moreover our groundstate estimate in symmetric case $\gamma = 1$ is -0.6704 J which is better than the current best numerical estimate -0.6692 J obtained via Greens function Monte Carlo by [Trivedi and Ceperley (1989); Runge (1992); Calandra Buonaura and Sorella (1998)]. However, since we use a mean field method and our Hamiltonian is not exact(is truncated), there is a possibility that our groundstate wavefunction might over estimate the ground state energy.

A look at the instantaneous spin-spin correlation function shows us that the functions exhibit a power-law decay(at least at long distances) in the xx and yy components. In Fig(3.4(a))

we show the Log-Log plot of the correlation function along x-direction at selected γ values. Fitting these functions with power law decay at large x values shows that they decay as A_x/x^{e_x} with $e_x \sim 1(= 1.04)$. Hence, we plot the function $xS^{(xx)}(x)$ in Fig(3.4(b)), which shows that the correlation functions at large x are more or less constant. The amplitude of the decay however does not follow a monotonous relation with γ . Initially we observe an increase in the amplitude with decreasing γ . However, at $\gamma = 0.2$ we observe a sudden decrease in overall correlation function. One can see the origin of this effect if we look at the expressions of correlation functions given in Eq(3.35) along with the symmetry arguments that lead to:

$$\langle S_i^x \cdot S_{i+\tau}^x \rangle = \begin{cases} \frac{1}{2}(1-2n)t_\tau & \tau \in E \\ -\frac{1}{2}(1-2n)\Delta_\tau & \tau \in O \end{cases} \quad (3.39)$$

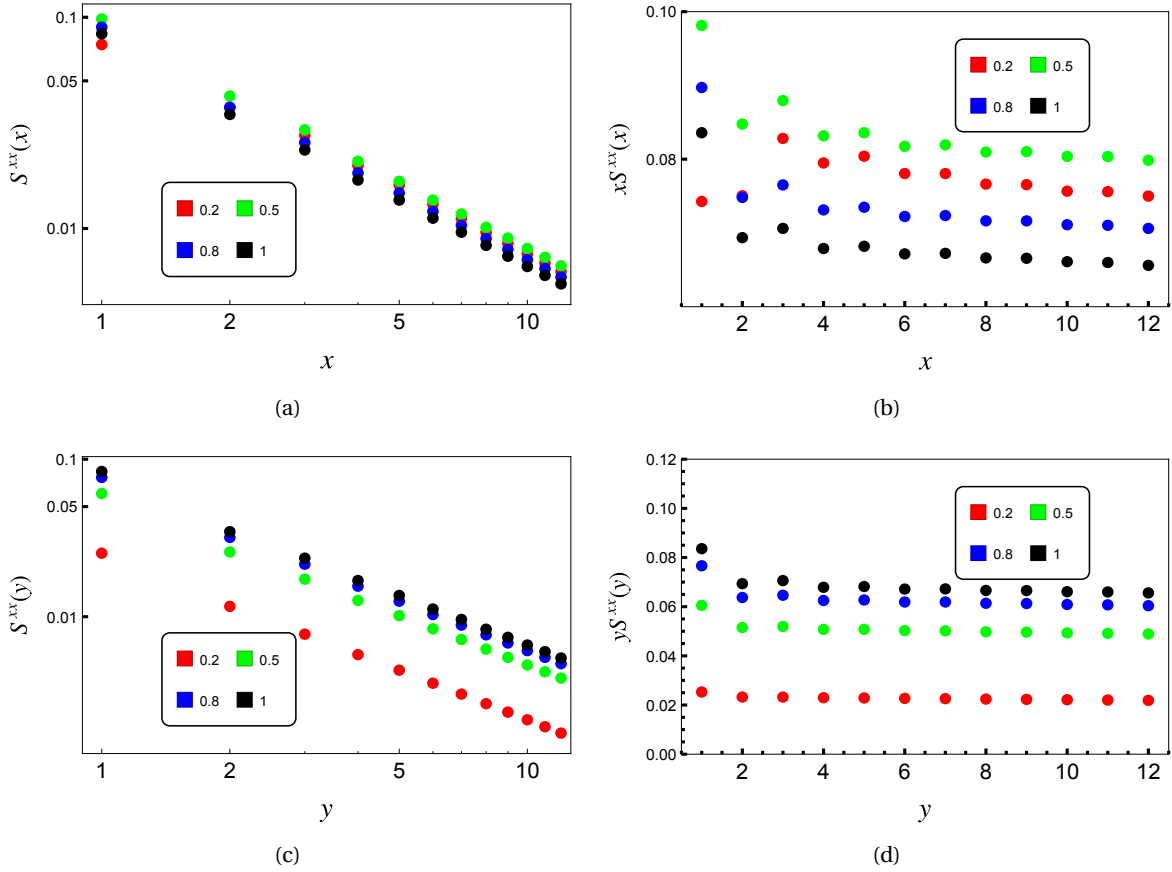


Figure 3.4 – Spin-spin correlation function $S^{xx}(r)$ (left) and the product $rS^{xx}(r)$ (right) in for $r = x$ (top) and $r = y$ (bottom) directions for couplings $\gamma = 0.2$ (red), 0.5 (green), 0.7 (blue) and 1 (black).

Without the $(1 - 2n)$ term we would observe a monotonously increasing behaviour of the correlation function. At $\gamma = 0.2$ the increase in t_x, Δ_x is overpowered by decrease in $(1 - 2n)$

which leads to the observed effect. Moving to y -direction, we observe a similar power-law decay A/y^{e_y} with $e_y \sim 1$ albeit with an amplitude that decreases with decreasing γ . As can be seen from Fig(3.4(c,d)) we observe an abrupt decrease of the correlation function. This is also due to the factor $(1 - 2n)$ in the above equations, which adds to the already decreasing first order correlation functions t_y, Δ_y (for even and odd sublattices).

Moving on to the zz component of the correlation function from the expressions in Eq(3.35) along with the symmetry conditions lead to:

$$\langle S_i^z \cdot S_{i+\tau}^z \rangle = \begin{cases} \frac{1}{4} - n + n^2 + t_\tau^2 & \tau \in E \\ -\frac{1}{4} + n - n^2 - \Delta_\tau^2 & \tau \in O \end{cases} \quad (3.40)$$

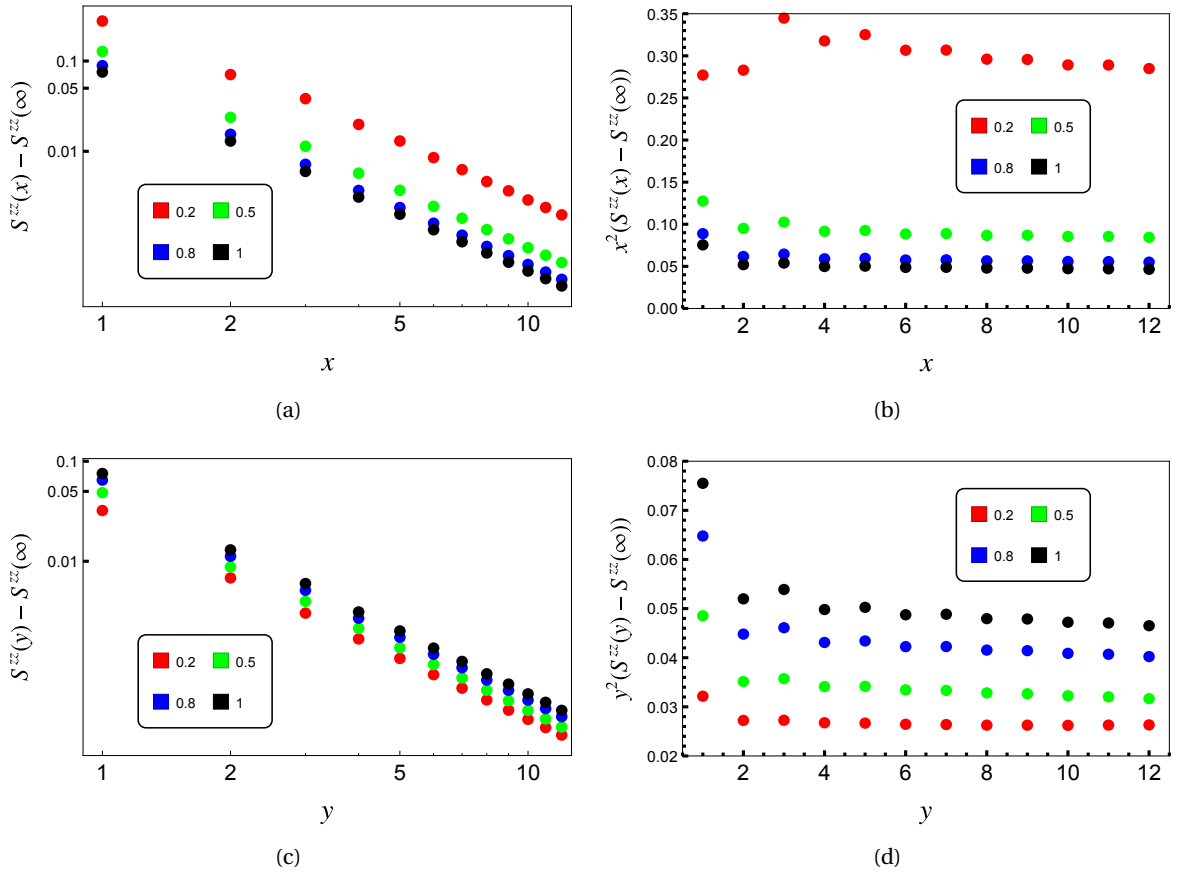


Figure 3.5 – Difference between spin spin correlation function $S^{zz}(r)$ at $r = 0$ and $r = \infty$ (left) and the product of this function with z^2 (right) in x (top) and y (bottom) directions for couplings $\gamma = 0.2$ (red), 0.5 (green), 0.7 (blue) and 1 (black).

The τ independent part $(1/2 - n)^2$ reflects the contribution coming from the long range order. Subtracting this part from the staggered correlation function we observe that it is given by $\{t_\tau^2, \Delta_\tau^2\}$ for $\tau \in \{E, O\}$. Hence it is just the square of the first order component of xx correlation

Chapter 3. Spin Wave Theory

function and hence follows a power-law decay as can be seen from Fig(3.5(a),(c)), and multiplying with $x^2(y^2)$ in x(y)-direction we observe the functions being constant at large distances. Fitting a powerlaw function, as expected gives an exponent of e_x, e_y 2(= 2.08). The amplitude increases(decreases) monotonically with decreasing coupling along x(y)-direction.

Once we have the correction terms dA_k and dB_k the and the renormalization of bare magnon energy can be calculated as:

$$\omega_k = \sqrt{(A_k + dA_k)^2 + (B_k + dB_k)^2} \quad (3.41)$$

$$Z_k = \frac{\sqrt{(A_k + dA_k)^2 + (B_k + dB_k)^2}}{\sqrt{A_k^2 + B_k^2}} \quad (3.42)$$

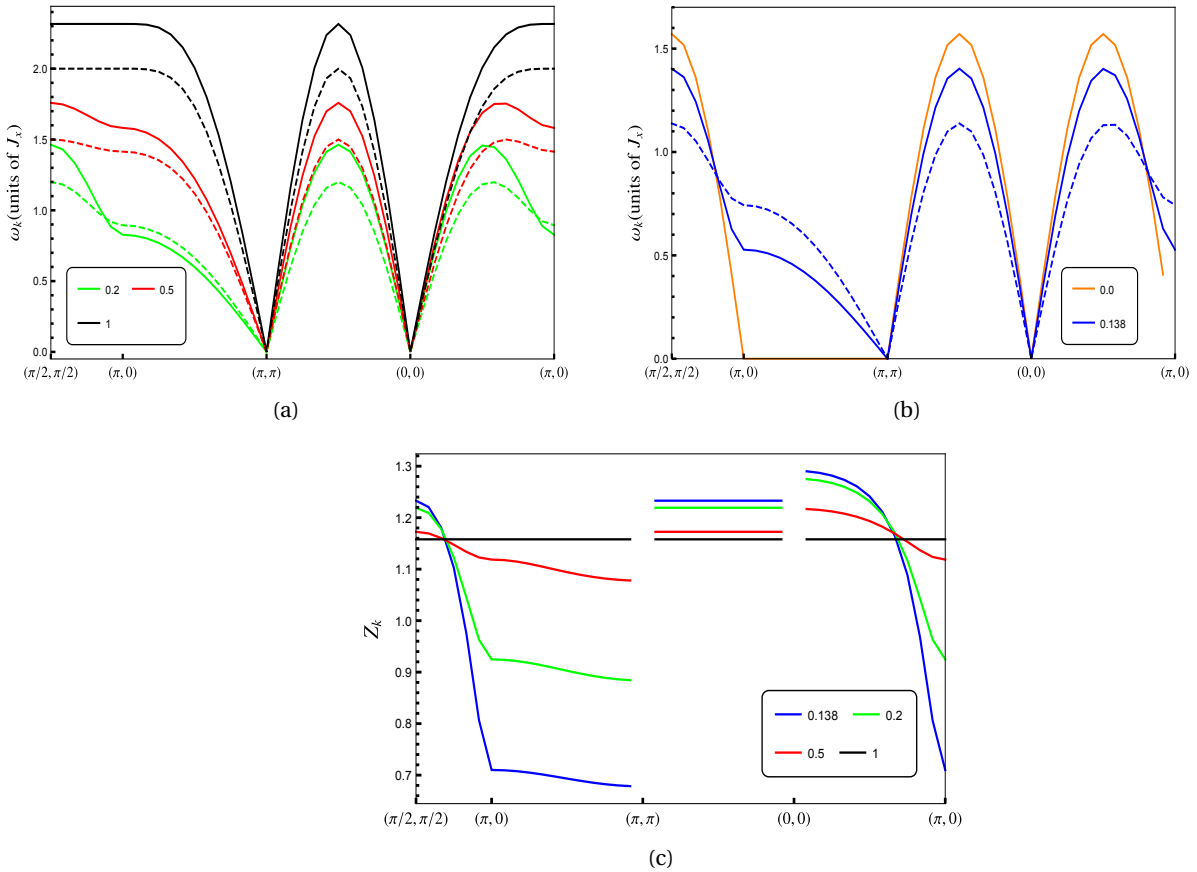


Figure 3.6 – (a) Renormalized dispersion(bold) and bare(dashed) magnon dispersion at $\gamma = 0.2, 0.5, 1$ indicated by green, red and black. b) Comparison of the limiting case $\gamma = 0.138$ (blue) with lower limit of Bethe Ansatz(orange) (chain along x-direction) (c) Renormalization factors in (a) and (b).

In Fig(3.6(a)), we show the calculated spin wave dispersion for values of $\gamma = 0.2, 0.5, 1$ and in Fig(3.6(b)), we show the dispersion corresponding to the limiting value $\gamma = 0.138$ and the lower limit of Bethe ansatz solution i.e $\omega_k = \frac{\pi}{2} \sin k$. The dashed lines indicate the bare dispersion from linear component and the solid lines show the renormalized dispersion. The spin wave solutions shows gapless goldstone modes at $(0, 0)$ and (π, π) that appear due to spontaneously broken spin rotational symmetry. As can be observed Fig(3.6(c)) renormalization factors are not k-dependent for square lattice and has value of $Z(q) = 1.158$. As we move towards smaller couplings we progressively see a larger k-dependence and the overall magnitude of the renormalization also increases. This is a result of increasing quantum fluctuations that would eventually destabilize the Neel state for 1D case. As can be seen from Fig(3.6(b)), the limiting case falls a bit short in terms of energy compared to the Bethe ansatz. This is due to the fact that at the limiting case since $n \sim 0.5$, and the next order correction in the spin wave expansion Eq(3.5) would contribute to higher renormalization. If we assume the lower limit of Bethe Ansatz as a representation of magnon mode then the renormalization factor is $\pi/2 = 1.57$ a value larger than the renormalization at our limiting case 1.25, and indication that our truncated Hamiltonian barely captures the full renormalization.

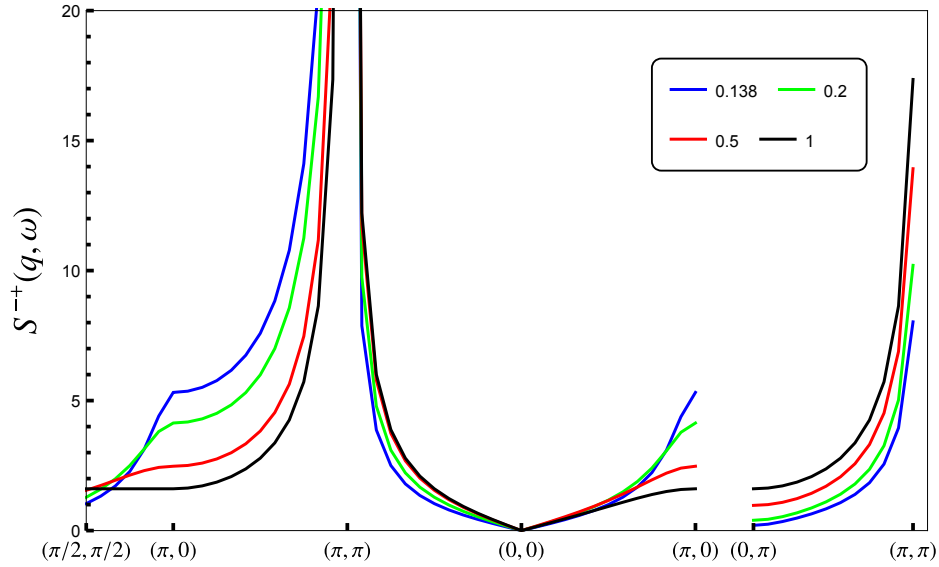


Figure 3.7 – Transverse dynamical spin-spin correlation function, along a selected k-path, for $\gamma = 0.138, 0.2, 0.5, 1$ represented by blue, green, red and black.

Finally, Fig(3.7) shows the evolution of dynamic spin spin correlation functions at various γ along the selected k-path. As can be seen the structure factor vanishes at $(0, 0)$ point, and diverges at (π, π) . The spectral weight at $(\pi, 0)$ symmetry point increases with decreasing coupling. We additionally added the k-path along $(0, \pi) \rightarrow (\pi, \pi)$ where we see the correlation function decreasing at point $(0, \pi)$ with decreasing γ . This is an expected as the spectral weight of excitations with momenta along y-direction should get weaker as we move towards 1D.

Summary

Summarizing the spin wave calculations performed on RQHAF for various coupling ratios γ , we have the following results:

1) The Heisenberg Hamiltonian expanded using Holstien-Primakoff transformation is truncated, to only include terms up to fourth order in bosonic operators. The quadratic components lead to linear spin wave theory which yields the bare value of the observables. The quartic components through a self-consistent mean field method, yield the renormalized values. This method yields a stable solution, with constraint $n < 1/2$, only for the coupling ratios $\gamma \geq 0.138$.

2) Calculated ground state energies match (are slightly better than) the result from Gutzwiller projected Schwinger boson wave function by Miyazaki et al. and Green's function Monte Carlo result at symmetric case $\gamma = 1$. However, since we are not working with the true Hamiltonian, there is a possibility that our results might be overestimated.

3) Transverse components of the instantaneous spin-spin correlation functions $\langle S^x S^x \rangle$ exhibit a power law decay both in x and y directions following the relation $\sim A/r$. Along x-direction the correlation function increases with decreasing coupling, except at $\gamma = 0.2$ where the second order correction seems to lead to an overall decrease in correlation function amplitude. Along y-direction we observe the amplitude decreasing with decreasing coupling.

4) The longitudinal component of the correlation function $\langle S^z S^z \rangle$ contains, in addition to a power-law decaying part, an added factor related to the long-range order (correlation function between two infinitely separated points). Subtracting this factor from correlation functions shows that the resulting expression is just the square of the transverse correlation function (to first order).

5) The renormalization of the magnon dispersion increases in magnitude as we approach lower couplings. The q-dependence also increases with decreasing coupling. A look at the transverse dynamic correlation function shows an increase in spectral weight at $(\pi, 0)$ point and a decrease at $(0, \pi)$ as we decrease the coupling which reflects the fact that we approach a 1D case.

4 Staggered flux:Ground state

In this chapter we explore the Gutzwiller projected staggered flux variational wavefunction (denoted as SF) as a ground state approximation on a Rectangular Quantum Heisenberg AntiFerromagnetic (RQHAF) lattice. By gradually varying the coupling ratio $\gamma = J_y/J_x$, we investigate the evolution of groundstate properties of this wavefunction. As explained in the introduction, the interest in this state comes primarily from the fact that it exhibits stark deviations from spin wave theory, which qualitatively explain the observed experimental effects in square lattices. Furthermore, the wavefunction at specific q vectors that exhibit these deviations, appear to host de-confined fractional excitations which are 2D analogues of ‘spinons’. Although this state lacks long-range order and is slightly higher in energy, these interesting features motivate further investigation into this wavefunction. The interest in a non ordered quantum spin liquid solution comes also from the fact that in high temperature superconductors, cuprates for example, upon introducing a small doping the AFM ordering of the parent compound is destroyed. In this scenario, the Resonating Valance Bond state has been proposed by Anderson [Anderson et al. (1987); Anderson (1973)] as a prototypical state to explain High temperature superconductivity, a problem that still lacks a universally accepted solution.

Mathematical Framework

In this section we introduce the theoretical framework used to construct the SF wavefunction and the methodology used to calculate the observables. The basic outline of this procedure is as follows:

- 1) Heisenberg Hamiltonian is expressed in fermionic form by representing the spin operators in fermion creation and annihilation operators. Since the Hamiltonian is quartic we use mean field decoupling, to convert it to a quadratic form.
- 2) A particular choice of mean fields defines our staggered flux Hamiltonian which upon diagonalization yields two bands which are gappless at k -points $(\pm \frac{\pi}{2}, \pm \frac{\pi}{2})$. Filling the lower

band with up and down spins yields our staggered flux wave function which ends up being dependent on two variational parameters α and θ (to be defined).

3) Since the staggered flux state hosts double occupancies we introduce a Gutzwiller projection to project them out. Thus the Gutzwiller projected staggered flux state becomes our variational ansatz.

4) Once we have a variational ansatz, values of various observables are estimated by calculating the expectation values of the corresponding operators. Calculation of observables on this Gutzwiller projected state is performed numerically by using a Montecarlo process.

Fermionized Heisenberg Hamiltonian

As described in the previous chapters, in most of the existing formalisms, the diagonalization of the Heisenberg Hamiltonian is carried out through the introduction of excitations on an ordered state. These excitations could be bosonic or fermionic depending on the formalism. Since, the bosonic excitations restrict the possibility of having fractional $S = 1/2$ excitations, a natural choice is to turn to a fermionic version of the Hamiltonian. The notion of spinless fermions seems to be the first choice in this regard, since it provides us with an exact solution for the XY model in 1D. However, the complexity of string operator renders this to be impractical. Hence we turn to the simple way of expressing the spin operators via the creation and annihilation operators of $S = 1/2$ fermions.

$$S_i^k = \sum_{\alpha\alpha'} c_{i\alpha}^\dagger (S_i^k)_{\alpha\alpha'} c_{i\alpha'} \quad (4.1)$$

where $k \in \{x, y, z\}$, $\alpha \in \{\uparrow, \downarrow\}$ and $(S_i^k)_{\alpha\alpha'}$ corresponds to the matrix elements of the spin operator S_i^k . Using this operator the Heisenberg Hamiltonian becomes:

$$\begin{aligned} \mathcal{H} &= \sum_{\langle i,j \rangle} J_{ij} \sum_k \sum_{1234} c_{i\alpha_1}^\dagger (S_i^k)_{\alpha_1\alpha_2} c_{i\alpha_2} c_{i\alpha_3}^\dagger (S_j^k)_{\alpha_3\alpha_4} c_{i\alpha_4} \\ &= \sum_{\langle i,j \rangle} \sum_\alpha \frac{J_{ij}}{4} \left(n_{i\alpha} n_{j\alpha} - n_{i\alpha} n_{j\bar{\alpha}} + 2c_{i\alpha}^\dagger c_{i\bar{\alpha}} c_{j\bar{\alpha}}^\dagger c_{j\alpha} \right) \text{ where } n_{i\alpha} = c_{i\alpha}^\dagger c_{i\alpha}, \bar{\alpha} = \uparrow (\downarrow) \text{ if } \alpha = \downarrow (\uparrow) \\ &= \sum_{\langle i,j \rangle} \frac{-J_{ij}}{2} \left[n_i \left(\frac{n_j}{2} - 1 \right) + \sum_{\alpha\beta} c_{i\alpha}^\dagger c_{j\alpha} c_{j\beta}^\dagger c_{i\beta} \right] \end{aligned} \quad (4.2)$$

where sum over $\langle \rangle$ implies summation over pairs, $n_i = \sum_\alpha n_{i\alpha} = \sum_\alpha c_{i\alpha}^\dagger c_{i\alpha}$, $\bar{\alpha} = \uparrow (\downarrow)$ if $\alpha = \downarrow (\uparrow)$ and in last expression $\alpha, \beta \in \{\uparrow, \downarrow\}$. It must be noted that, unlike the Heisenberg Hamiltonian, the hilbert space of Eq(4.2) contains double occupancies and empty sites. The equivalence exists only in the subspace corresponding to the states, where we have all the sites occupied by a single spin. The wavefunctions that diagonalize the Heisenberg Hamiltonian are expected

to be in this subspace. The unphysical wavefunctions, not belonging to this subspace, will be projected out using a Gutzwiller projector. Since the groundstate belongs to the sector $S_{tot}^z = 0$, at half filling we have $N_\uparrow = N_\downarrow = N/2$. A state with an induced transverse excitation would belong to the sector $S_{tot}^z = 1$ and hence has $N_\uparrow = N/2 + 1, N_\downarrow = N/2 - 1$.

Mean Field decoupling

Starting with the second part of Eq(4.2), we use a mean field decoupling(similar to chapter 3) to reduce the terms quartic in creation/annihilation operators to a quadratic form .

$$\begin{aligned} \mathcal{H}_{MF} = & -\frac{1}{2} \sum_{\langle i,j \rangle} J_{ij} \sum_{\alpha\beta} \left(\langle c_{i\alpha}^\dagger c_{j\alpha} \rangle c_{i\beta}^\dagger c_{j\beta} + \langle c_{j\beta}^\dagger c_{i\beta} \rangle c_{i\alpha} c_{j\alpha} + \langle c_{i\alpha}^\dagger c_{j\beta} \rangle c_{i\beta} c_{j\alpha} \right. \\ & \left. + \langle c_{i\beta} c_{j\alpha} \rangle c_{i\alpha}^\dagger c_{j\beta}^\dagger + \langle c_{i\alpha}^\dagger c_{i\beta} \rangle c_{j\alpha} c_{j\beta}^\dagger + \langle c_{j\alpha} c_{j\beta}^\dagger \rangle c_{i\alpha}^\dagger c_{i\beta} \right) \end{aligned}$$

Defining the mean fields with the following notation:

$$2 \langle c_{i\sigma}^\dagger c_{j\sigma} \rangle = \chi_{ij}, \quad \langle c_{i\uparrow} c_{j\downarrow} \rangle = \Delta_{ij}, \quad \langle c_{i\sigma}^\dagger c_{i\sigma} \rangle = h_{i\sigma}$$

The Mean field Hamiltonian becomes,

$$\mathcal{H}_{MF} = \sum_{\alpha} \left(\chi_{ij} c_{j\alpha}^\dagger c_{i\alpha} + \epsilon_{\alpha\bar{\alpha}} \Delta_{ij} c_{i\bar{\alpha}}^\dagger c_{j\alpha}^\dagger + h_{i\alpha} c_{j\alpha} c_{j\alpha}^\dagger \right) + h.c. \quad (4.3)$$

where $\epsilon_{\uparrow\downarrow} = -\epsilon_{\downarrow\uparrow} = 1$. In our formulation we set $h_{i\sigma} = 0$ as we are interested in a disordered state. The choice for the remaining two fields χ_{ij}, Δ_{ij} we use is:

$$\chi_{ij} = \begin{cases} t_x e^{i\theta_{ij}}, & \theta_{ij} = \theta_x (-1)^{i_x + j_y} \quad \text{for } j = i \pm \hat{e}_x \\ t_y e^{i\theta_{ij}}, & \theta_{ij} = \theta_y (-1)^{i_x + j_y} \quad \text{for } j = i \pm \hat{e}_y \end{cases}, \quad \Delta_{ij} = 0 \quad (4.4)$$

It can be shown that this choice is related to an asymmetric d-wave RVB ansatz given by:

$$\chi_{ij} = \begin{cases} \chi_x & \text{for } j = i \pm \hat{e}_x \\ \chi_y & \text{for } j = i \pm \hat{e}_y \end{cases}, \quad \Delta_{ij} = \begin{cases} \Delta_x & \text{for } j = i \pm \hat{e}_x \\ -\Delta_y & \text{for } j = i \pm \hat{e}_y \end{cases} \quad (4.5)$$

via an $SU(2)$ transformation that relates the parameters via the expressions, $t_i = \sqrt{\chi_i^2 + \Delta_i^2}$, $\theta_0 = \tan^{-1}(\Delta_i / \chi_i)$ for $i=x,y$. The d-wave ansatz is inspired by the Bardeen-Cooper-Schrieffer mean-field [Bardeen et al. (1957)] decoupling of the electron-phonon interaction Hamiltonian, which is responsible for the conventional super conductivity. The staggered flux on other-hand, has been introduced by Affleck and Marston for symmetric case [Affleck et al. (1988)], which turns out to be one of the two exact solutions for $SU(n)$ Hubbard-Heisenberg model in two dimensions with $n \rightarrow \infty$ [Marston and Affleck (1989)](see chapter 2). The resulting spin liquid state is described as the so called π -flux phase with total flux obtained by a fermion by circulating around a plaquette being π . This choice of flux preserves the time reversal

symmetry. In the work of Dallapiazza et al., the flux parameter is considered to be a variational parameter, whose optimum value turned out to be $\theta_x = \theta_y = 0.075\pi$ and hence the name ‘staggered-flux’. This choice breaks time-reversal symmetry. The parameter t on other-hand sets the energy scale and has no real significance in the symmetric case. In rectangular lattices however, where we induce an asymmetric staggered flux state, we shall see that the ratio t_y/t_x and $\theta = \theta_x + \theta_y$ both play a role in deciding the groundstate energy of the wavefunction.

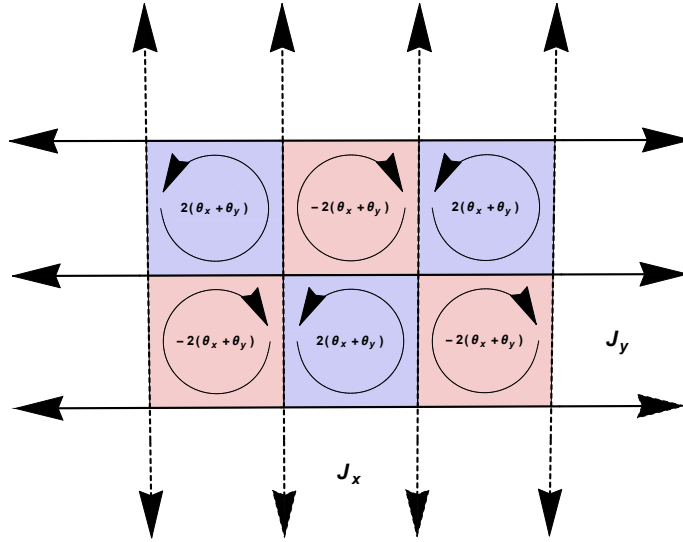


Figure 4.1 – An illustration of staggered flux state with anisotropic couplings, represented as flux of magnitude $2(\theta_x + \theta_y)$ threading the lattice in a staggered manner.

Staggered Flux Hamiltonian

Using the choice of mean fields Eq(4.4), the mean field Hamiltonian Eq (4.3) becomes the staggered flux hamiltonian:

$$\begin{aligned} \mathcal{H}_{SF} = & \sum_{i \text{ even}, \sigma} \left(-\frac{J_x t_x}{2} e^{-i\theta_x} c_{i\sigma}^\dagger c_{i+x\sigma} - \frac{J_y t_y}{2} e^{i\theta_y} c_{i\sigma}^\dagger c_{i+y\sigma} + h.c \right) \\ & + \sum_{i \text{ odd}, \sigma} \left(-\frac{J_x t_x}{2} e^{i\theta_x} c_{i\sigma}^\dagger c_{i+x\sigma} - \frac{J_y t_y}{2} e^{-i\theta_y} c_{i\sigma}^\dagger c_{i+y\sigma} + h.c \right) \end{aligned} \quad (4.6)$$

Using the Fourier transform and expressing the creation and annihilation operators on even(e) and odd(o) sublattices in k space as,

$$e_{k\sigma} = \frac{c_{k\sigma} + c_{k+Q\sigma}}{\sqrt{2}}, \quad o_{k\sigma} = \frac{c_{k\sigma} - c_{k+Q\sigma}}{\sqrt{2}}, \quad (4.7)$$

with $k \in MBZ$ i.e Magnetic Brillouin zone and $Q = (\pi, \pi)$. The staggered Flux Hamiltonian can be written as:

$$\mathcal{H}_{SF} = -J_x t_x \sum_k \begin{pmatrix} e_{k\sigma}^\dagger & o_{k\sigma}^\dagger \end{pmatrix} \begin{pmatrix} 0 & \Delta_k^* \\ \Delta_k & 0 \end{pmatrix} \begin{pmatrix} e_{k\sigma} \\ o_{k\sigma} \end{pmatrix} \quad (4.8)$$

where

$$\Delta_k = \frac{1}{2} \left(e^{i\theta_x} \cos k_x + \alpha e^{-i\theta_y} \cos k_y \right) \quad (4.9)$$

where we define $\alpha = J_y t_y / J_x t_x$. To diagonalize the Hamiltonian we require a unitary transformation $U_{k\sigma}$ such that:

$$\Omega_{k\sigma} = U_{k\sigma}^{-1} \begin{pmatrix} 0 & \Delta_k^* \\ \Delta_k & 0 \end{pmatrix} U_{k\sigma} \quad (4.10)$$

is a diagonal matrix. Defining the unitary transformation as:

$$U_{k\sigma} = \begin{pmatrix} u_{k\sigma-} & u_{k\sigma+} \\ v_{k\sigma-} & v_{k\sigma+} \end{pmatrix} \quad (4.11)$$

the diagonalization can be achieved through the following choice:

$$u_{k\sigma-} = v_{k\sigma+} = \sqrt{\frac{1}{2}}, \quad v_{k\sigma-} = -u_{k\sigma+}^* = \frac{\Delta_k}{\sqrt{2}|\Delta_k|} \quad (4.12)$$

which finally leads to a diagonalized hamiltonian:

$$\Omega_{k\sigma} = \begin{pmatrix} -J_x t_x |\Delta_k| & 0 \\ 0 & J_x t_x |\Delta_k| \end{pmatrix} \quad (4.13)$$

We have two bands with energies, $\omega = -J_x t_x |\Delta_k|$ and $\omega = J_x t_x |\Delta_k|$ which we will shall refer from here on as $'-'$ and $'+'$ respectively. A look at these bands for selected parameters from Fig(4.2) shows that the bands are gapless with nodes at $(\pm \frac{\pi}{2}, \pm \frac{\pi}{2})$. These k -points are problematic for numerical calculations, as the phase of Δ_k is ill defined at these points. To circumvent this problem we shall work with different boundary conditions as will be explained more clearly in later sections. The-quasi particle creation and annihilation operators in the

diagonalized space, are related to the fermion creation and annihilation operators through:

$$\begin{pmatrix} d_{k\sigma-} \\ d_{k\sigma+} \end{pmatrix} = \begin{pmatrix} u_{k\sigma-} & v_{k\sigma-}^* \\ u_{k\sigma+}^* & v_{k\sigma+} \end{pmatrix} \begin{pmatrix} e_{k\sigma} \\ o_{k\sigma} \end{pmatrix} \quad (4.14)$$

The real space fermion operators are related to the quasi particle operators via the expression:

$$c_{i\sigma} = \sqrt{2} \sum_{k \in MBZ} e^{ikR_i} [(\epsilon_{R_i} u_{k\sigma-} + \bar{\epsilon}_{R_i} v_{k\sigma-}) d_{k\sigma-} + (\epsilon_{R_i} u_{k\sigma+} + \bar{\epsilon}_{R_i} v_{k\sigma+}) d_{k\sigma+}] \quad (4.15)$$

where ϵ_{R_i} and $\bar{\epsilon}_{R_i}$ determine if site i is even or odd via:

$$\epsilon_{R_i} = \frac{1 + e^{iQR_i}}{2}, \quad \bar{\epsilon}_{R_i} = \frac{1 - e^{iQR_i}}{2} \quad (4.16)$$

The groundstate of the SF Hamiltonian is obtained by completely filling the lower band with spin up and spin down quasi-particles:

$$|\psi_{GS}\rangle = \prod_{k \in MBZ} d_{k\uparrow-}^\dagger d_{k\downarrow-}^\dagger |0\rangle \quad (4.17)$$

Since, the quasi particle operators are dependent only on the phase of the function Δ_k our ground state wave function depends only on parameters α, θ_x and θ_y . A look at the definition of the quasi-particle operators shows that the staggered flux ground state, has double occupancies. In order to get rid of these, we use a Gutzwiller projected state as our variational ground state.

$$|GS\rangle = P_G |\psi_{GS}\rangle \quad (4.18)$$

Staggered flux as the superposition of singlets

At this point, it is instructive to look at how the SF wave function, looks in the physical space. The staggered flux state is created through filling the lower band with up and down spins. The creation operator $d_{k\sigma-}^\dagger$ is related to the spin creation operators through:

$$d_{k\sigma-}^\dagger = u_{k\sigma-}^* e_{k\sigma}^\dagger + v_{k\sigma} o_{k\sigma}^\dagger = \frac{1}{\sqrt{2}} e_{k\sigma}^\dagger + \frac{e^{i\phi_k}}{\sqrt{2}} o_{k\sigma}^\dagger \quad (4.19)$$

where ϕ_k is the phase of function Δ_k and depends on the parameters $\alpha, \theta_x, \theta_y$. Using these definitions:

$$d_{k\uparrow-}^\dagger d_{k\downarrow-}^\dagger = \frac{1}{2} \left[e_{k\uparrow}^\dagger e_{k\downarrow}^\dagger + e^{i\phi_k} \left(e_{k\uparrow}^\dagger o_{k\downarrow}^\dagger + o_{k\uparrow}^\dagger e_{k\downarrow}^\dagger \right) + e^{2i\phi_k} o_{k\uparrow}^\dagger o_{k\downarrow}^\dagger \right] \quad (4.20)$$

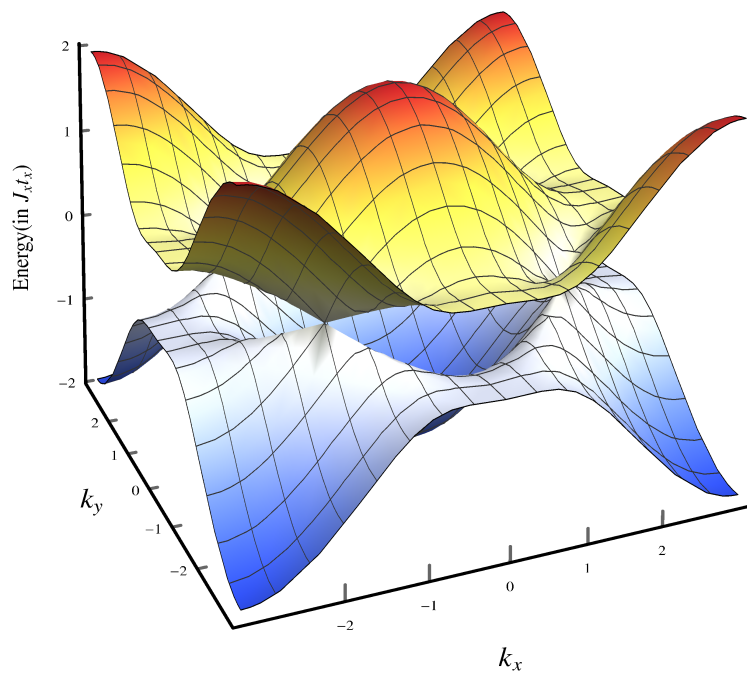
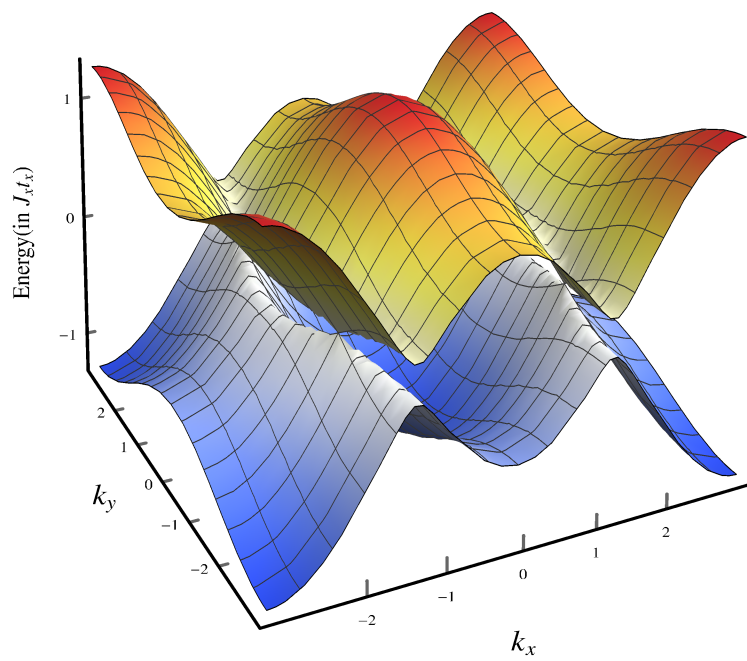
(a) $\alpha = 1, \theta = 0.15\pi$ (b) $\alpha = 0.3, \theta = 0.15\pi$

Figure 4.2 – Quasi particle bands of staggered flux Hamiltonian for selected parameters.

Expanding the first term in square brackets in real space:

$$e_{k\uparrow}^\dagger e_{k\downarrow}^\dagger = \frac{1}{N} \sum_{i \in E} \sum_{j \in E} e^{-ik \cdot (R_i + R_j)} c_{i\uparrow}^\dagger c_{j\downarrow}^\dagger \quad (4.21)$$

where E represents the even sublattice and O represents the odd sublattice. Since, the terms corresponding to $i = j$ will be projected out by the Gutzwiller projector considering only the contribution from $i \neq j$:

$$\begin{aligned} e_{k\uparrow}^\dagger e_{k\downarrow}^\dagger &= \frac{1}{N} \sum_{\langle i,j \rangle \in E} e^{-ik \cdot (R_i + R_j)} \left(c_{i\uparrow}^\dagger c_{j\downarrow}^\dagger + c_{j\uparrow}^\dagger c_{i\downarrow}^\dagger \right) \\ &= \frac{1}{N} \sum_{\langle i,j \rangle \in E} e^{-ik \cdot (R_i + R_j)} \left(c_{i\uparrow}^\dagger c_{j\downarrow}^\dagger - c_{i\downarrow}^\dagger c_{j\uparrow}^\dagger \right) \end{aligned} \quad (4.22)$$

where $\langle i, j \rangle$ refers to the pair i, j . As can be seen, the term in parenthesis creates a singlet on the pair i, j with both i and j belonging to even sublattice. Similarly, one can show that the other terms in Eq(4.20) each creates singlets in similar fashion (on even-odd, odd-odd sublattices). Hence the staggered flux state upon Gutzwiller projection, will lead to a state that is superposition of various singlet configurations as shown in Fig(4.3). While creating each singlet we have establish a overall sign convention to have a proper sign (for example spins on bottom right are created first). Once this is done, one does not have to worry about the sign convention while filling the states as superposition singlets in this manner, because the singlet creation operator term in parentheses in Eq(4.22) is quadratic in fermion operators and hence they can be exchanged without changing the overall sign of the wave function.

In Fig(4.3), we show an illustration of this state. The wavefunction $|\psi_{GS}\rangle$ with filled lower band, as mentioned above, is made up of states that contain double occupancies and empty sites and singly occupied states that can be written as superposition of pair-wise singlets. The coefficients of these states are linked to the fourier factors and the phase ϕ_k as shown above. The Gutzwiller projector projects out all the states that are not singly occupied, leaving us with a linear combination of states made up of superposition of pairwise singlet states. Although the superposed pairwise singlet states provide us with an intuitive picture, they do not function as good wavefunction vectors as they are not orthonormal. Nevertheless they provide us with an intuitive picture of the underlying states and it shall be used while exploring the spinon separation in next chapter.

$$P_G |\psi_{GS}\rangle = P_G \left(\dots + \sum_m D_m \left| \begin{array}{c} \text{Diagram 1} \\ \text{Diagram 2} \end{array} \right\rangle + \dots + \sum_m A_m \left| \begin{array}{c} \text{Diagram 3} \\ \text{Diagram 4} \end{array} \right\rangle + \dots \right)$$

$$= \sum_m A_m \left| \begin{array}{c} \text{Diagram 5} \\ \text{Diagram 6} \end{array} \right\rangle$$

Figure 4.3 – An illustration of staggered flux state as a sum of states made up of superposition of singlets. The double arrow represents the double occupancies and the open circle represents an empty site. The Gutzwiller projector projects out states that are not singly occupied and yields a state that is sum of states with superposed singlets occupying all sites.

Boundary Conditions

We come back to the problem associated with the special k points $(\pm \frac{\pi}{2}, \pm \frac{\pi}{2})$ where the quasi particle spectrum Fig(4.2) is gapless and the phase of the function Δ_k is ill-defined. Since we work on a finite lattices for our numerical computations where we consider lattices of size $L \times L$ with L being even. If we have periodic boundary condition, our k space is made up of points $(\frac{2\pi n_x}{L}, \frac{2\pi n_y}{L})$. For systems of size $L = 4n$ we observe that k -space contains $(\frac{\pi}{2}, \frac{\pi}{2})$. To get around this, one could slightly tilt the k -space that will lead to the nodal points being avoided [Gros (1989)]. However, this would break some lattice symmetries like four fold rotational symmetry. Another way of doing this is to consider Anti-periodic boundary conditions. Considering anti-periodic boundary conditions in direction i leads to following relations wavefunctions with translational symmetry:

$$\begin{aligned}
 \psi_k(r + m\hat{i}) &= e^{ik_i m} \psi(r) \\
 \psi_k(r + L\hat{i}) &= -\psi_k(r)
 \end{aligned} \tag{4.23}$$

which leads to the definition of wavevectors:

$$k_i = \left(n_i + \frac{1}{2} \right) \frac{2\pi}{L} \tag{4.24}$$

Hence we have 3 possible choices that we can employ for system sizes $L = 4n$, anti-periodic in both directions ($ABC - ABC$), anti-periodic in x and periodic in y ($ABC - PBC$), periodic in x and anti-periodic in y (PBC, ABC). The k-space corresponding to these choices is shown in Fig(4.4). Similarly, for systems of size $L = 4n + 2$, we have the choices ($PBC - PBC$), ($PBC - ABC$), ($ABC - PBC$). Ideally a single choice would be enough for our purpose, but as will be shown in next section, the values of observables at small γ strongly depend on the system size. Looking at the finite size effects along with different boundary conditions would provide us with additional information that would be helpful to establish the $L \rightarrow \infty$ values of the observables.

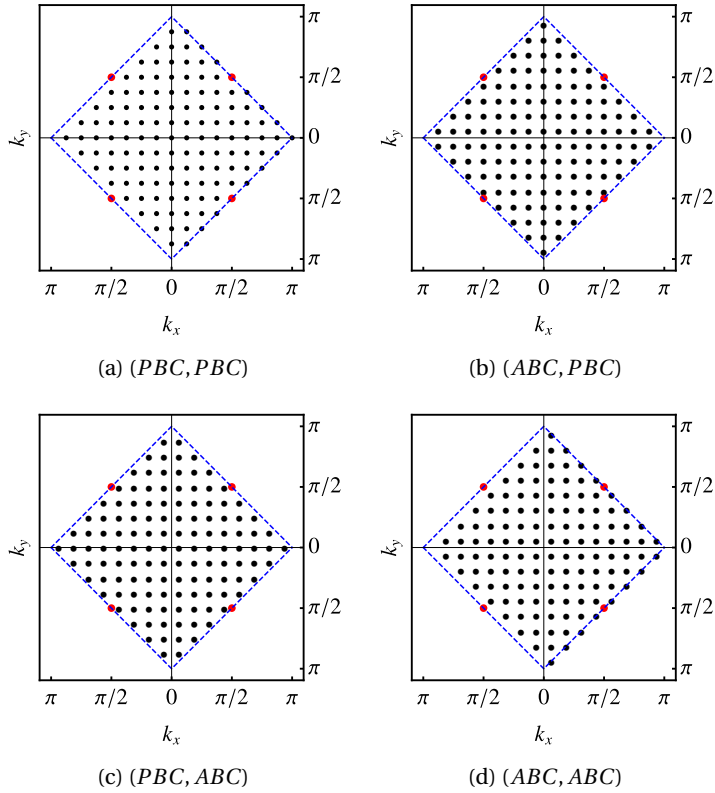


Figure 4.4 – k space corresponding to MBZ for various choices of Boundary conditions for system size $L = 16$. The nodal points are indicated by red dots.

Calculation of observables

Once we have established our k-points we can proceed to constructing the staggered flux wave function. To optimize our groundstate wave function we need to minimize the groundstate

energy given by:

$$E_{GS} = \frac{\langle GS | \mathcal{H} | GS \rangle}{\langle GS | GS \rangle} = \frac{\langle \psi_{GS} | P_G \mathcal{H} P_G | \psi_{GS} \rangle}{\langle \psi_{GS} | P_G | \psi_{GS} \rangle} \quad (4.25)$$

where \mathcal{H} is the exact Heisenberg Hamiltonian. This would yield the optimum values for our variational parameters $\alpha, \theta_x, \theta_y$. Once such a state is found we can proceed to calculate the relevant observables necessary to study the wave function. For this purpose we need a way to evaluate the expectation values of a given observable O :

$$\langle O \rangle = \frac{\langle GS | O | GS \rangle}{\langle GS | GS \rangle} = \frac{\langle \psi_{GS} | P_G O P_G | \psi_{GS} \rangle}{\langle \psi_{GS} | P_G | \psi_{GS} \rangle} \quad (4.26)$$

Due to the complexity of the projector, it is difficult to carry out computation in Eq(4.26) analytically. One can use the Gutzwiller approximation [Gros (1989)]. In our work we try to do it exactly by defining the Gutzwiller projection on a finite lattice via the operator:

$$P_G = \sum_{\beta} |\beta\rangle \langle \beta| \quad (4.27)$$

where the space $\{|\beta\rangle\}$ corresponds to the space of singly occupied sites. Due to the enormous size of this space, carrying out this calculation exactly is not feasible for large system sizes. Hence we use a numerical method based on Monte Carlo Algorithm [Gros (1989); Foulkes et al. (2001)] which can be derived as follows. We start by rewriting Eq(4.26) along with the projector in Eq(4.27), which after a few mathematical steps becomes:

$$\langle O \rangle = \sum_{\beta} \underbrace{\frac{|\langle \beta | \psi_{GS} \rangle|^2}{\sum_{\beta} |\langle \beta | \psi_{GS} \rangle|^2}}_{\rho(\beta)} \underbrace{\left(\sum_{\gamma} \langle \beta | O | \gamma \rangle \frac{\langle \gamma | \psi_{GS} \rangle}{\langle \beta | \psi_{GS} \rangle} \right)}_{f(\beta)} \quad (4.28)$$

where the space $\{|\gamma\rangle\} = \{|\beta\rangle\}$. Equation (4.28) has the form of a weighted average where the weight:

$$\rho(\beta) = \frac{|\langle \beta | \psi_{GS} \rangle|^2}{\sum_{\beta} |\langle \beta | \psi_{GS} \rangle|^2} \quad (4.29)$$

is the normalized probability distribution for the quantity

$$f(\beta) = \left(\sum_{\gamma} \langle \beta | O | \gamma \rangle \frac{\langle \gamma | \psi_{GS} \rangle}{\langle \beta | \psi_{GS} \rangle} \right) \quad (4.30)$$

Hence a numerical estimate for the value of the observable can be obtained by using a Monte Carlo algorithm. The relevant quantities to be calculated are the overlap functions $\langle \alpha | \psi_{GS} \rangle$, which are Slater determinants due to the fermionic nature of $|\psi_{GS}\rangle$. The basic definition of our staggered flux wave function involved three variational parameters $\alpha, \theta_x, \theta_y$ which enter the

matrix elements of the Slater determinant matrix through the function Δ_k in Eq(4.9). Taking out the factor $e^{i\theta_y}$ just leads to a phase change of this function that in turn leads to just a phase change in $|\psi_{GS}\rangle$. Due to the form of Eq(4.28), overall constant phase change of the any Slater determinant $\langle\alpha|\psi_{GS}\rangle$ does not impact the observable and hence the physics of our wavefunction depends only on two parameters α and $\theta = \theta_x + \theta_y$.

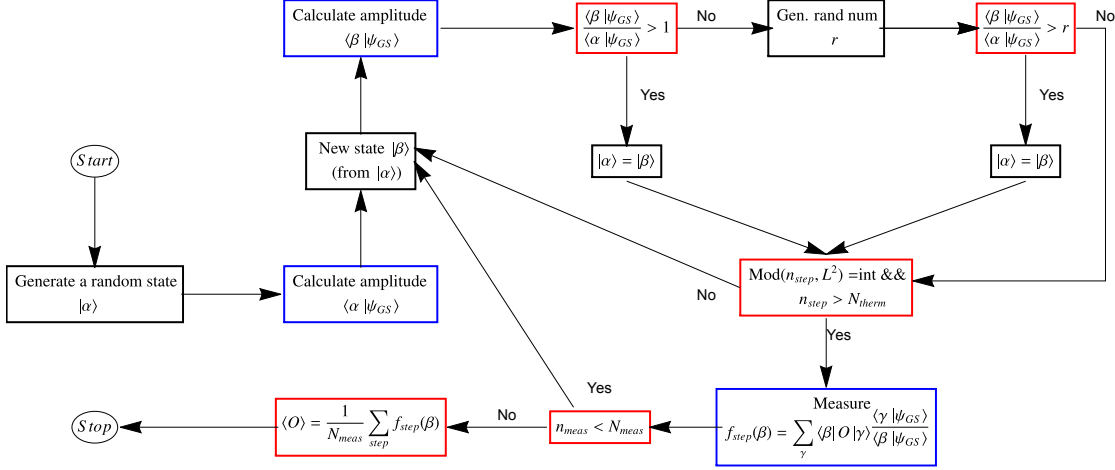


Figure 4.5 – A flow chart describing the Monte Carlo Algorithm used to calculate the numerical estimates of an observable O . The blue boxes correspond to calculations, red boxes are conditions and black boxes are regular operations. N_{therm} and N_{meas} are required number of thermalization steps and required number of measurements.

Montecaro Algorithm

Montecarlo Algorithm or more specifically Metropolis-Hastings algorithm [Hastings (1970); Metropolis et al. (1953)], involves the use of a Markov chain. At each step a new state $|\beta\rangle$ is generated from the current state $|\alpha\rangle$, and is added to the chain only if the acceptance ratio $\rho(\beta)/\rho(\alpha)$ is greater than a randomly generated number $r \in [0, 1)$. The states we work with are single occupancy states and each new state is derived by exchanging a pair of randomly selected nearest neighbor spins that are pointing in opposite directions. In Fig(4.5), we show the flow chart of our algorithm. We start with a randomly generated state and start constructing our markov chain based on previously mentioned criteria. To avoid the bias that might be caused by a randomly chosen state far away from the equilibrium, we thermalize our state for N_{therm} steps. After this we start calculating the value of $f(\beta)$ that shall be averaged at the end. Measurement of $f(\beta)$ is made at every L^2 steps to make the samples independent. After we have sufficient statistics N_{meas} , we average the values of $f(\beta)$ to obtain the numerical estimate of $\langle O \rangle$. It must be noted that, although calculation of $f(\beta)$ seems to require the summation over the full space of singly occupied states $\{|\gamma\rangle\}$, the observables we evaluate i.e groundstate energy and instantaneous spin spin correlation function, have only few states in $\{|\gamma\rangle\}$ such that $\langle\beta|O|\gamma\rangle$ is finite. Major part of the computation revolves around estimating the overlaps $\langle\alpha|\psi_{GS}\rangle$. Details on the procedure in estimating this quantity, the computational complexity

and resulting statistical errors can be found in the Appendices.

Results

In this section we present the results corresponding to the optimization of variational parameters, calculation of the groundstate energy and instantaneous spin-spin correlation functions. Since we perform our calculations on finite system sizes, we also have a close look at the finite size effects on our calculations. Only the figures and data relevant for the discussion are provided here. Additional figures are provided in the Appendices.

Optimization of parameters

As established in our theoretical framework, the staggered flux wave function and the related observables depend on two variational parameters α, θ . Hence our first step is to accurately estimate the values of these parameters as a function of γ . For this purpose we compute the Energy maps $E(\alpha, \theta)$ on a finite grid in α and θ space. We start with the symmetric case $\gamma = 1$ at system size $L = 8$ to establish the location of the Energy minimum. Once this is known, we progressively proceed towards smaller coupling ratio in steps of 0.1 till we reach $\gamma = 0.1$. The region of (α, θ) space upon which the computations are performed, is chosen from previous calculations. At every step we make sure that the Energy minimum is well contained in the computed region. The Energy maps corresponding to $\gamma = 0.1, 0.5, 0.2, 0.1$ are provided in Fig(4.6) which capture the essential features of energy dependence on the parameters. Firstly, we observe well defined minima in all the energy maps. At the symmetric case $\gamma = 1$, as expected we observe the energy minima at $\alpha = 1$ and the corresponding θ at 0.15π coinciding with the work of Dalla Piazza et al. Close to the symmetric case we observe the energy strongly depending of variational parameters as shown by the clear minima. However, as we go towards smaller coupling ratio, we observe a weak dependence of energy with the variational parameters, particularly θ . This is not surprising, since as we approach 1D the flux in a closed loop is an ill-defined parameter. Since our data is subject to numerical errors, to have a proper estimate of the variational parameters, we fit the lower part of energy minima with a second degree polynomial in α, θ and use the minima of the polynomial. The fitting function is given by:

$$E(\alpha, \theta) = a(\theta - \theta_0)^2 + b(\theta - \theta_0)(\alpha - \alpha_0) + c(\alpha - \alpha_0)^2 + E_{GS} \quad (4.31)$$

where (θ_0, α_0) is the location of the parabolic minimum and E_{GS} is the energy at this minimum. More details on this fitting procedure are presented in the Appendices.

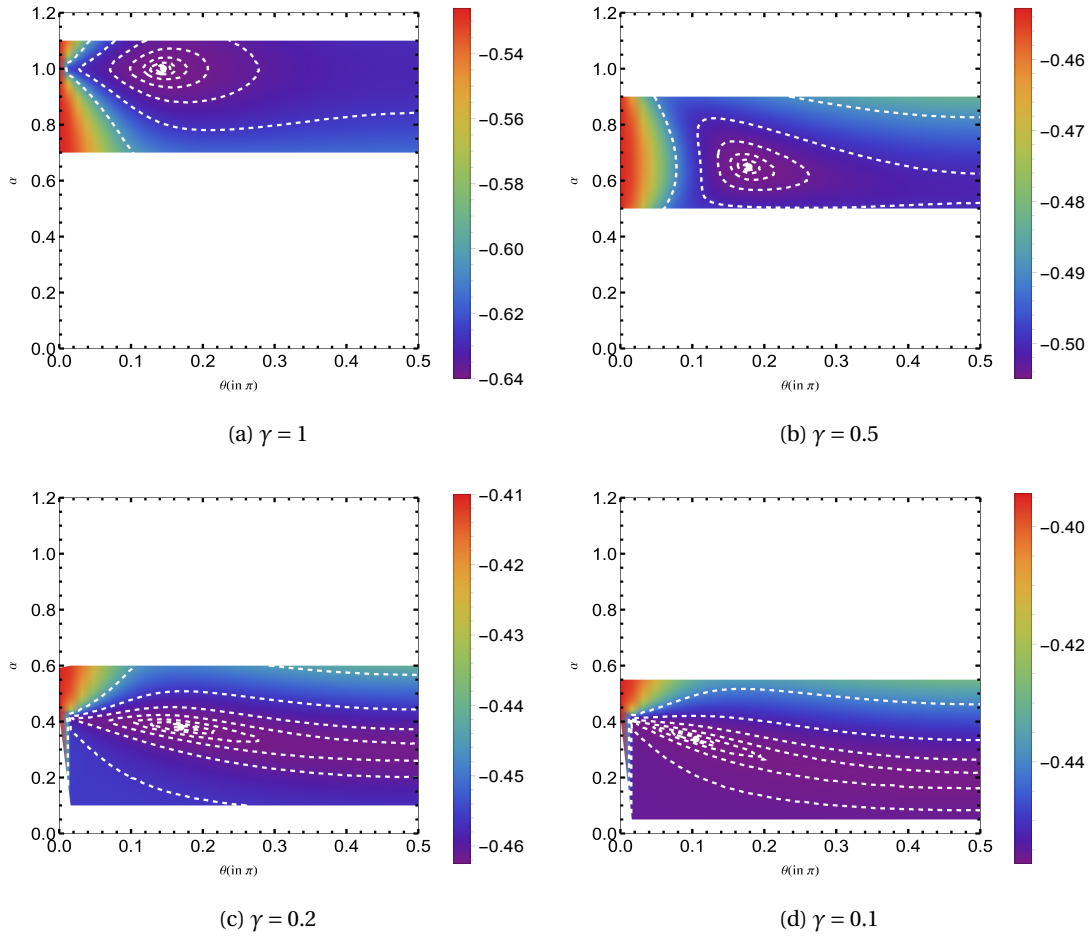


Figure 4.6 – Ground state Energy maps of systems with size $L=8$ for various coupling ratios. The white contours(dot) indicate the points corresponding to same energy(minima).

Finite size effects

A particular concern while working on small system sizes are the finite size effects. The resulting values of variational parameters and energy would make sense only if the solution is stable with respect to different system sizes or converges while increasing the size. If the solution converges to some value as we increase system size, we should reliably be able to estimate the groundstate energies at $L = \infty$ limit. A particular technique that is useful to us in this regards is the use of different boundary conditions. Since the effect of the boundary becomes irrelevant as one approaches $L = \infty$, by looking at results from different boundary conditions one can get additional piece of information about the limiting values.

All the computations carried out for $L = 8$, were repeated for different boundary conditions and for different system sizes $L = 12, 16, 20, 24$. Due to computational time limitations these calculations were performed with smaller grid sizes, making sure at each step that the minima

is well contained within the grid. The resulting energies are presented in Fig(4.7a). Our initial calculations showed us that the effects of boundary conditions are dominant only at small coupling ratios. Moreover they appear to be depending only on the Boundary condition along the strong coupling direction. Hence we present the data corresponding to only two choices of boundary conditions ($ABC - ABC$) and ($PBC - ABC$), which we refer to from here on as ABC and PBC indicating the boundary condition along x-direction. We also present the energy corresponding to Bethe ansatz solutions obtained by solving the Bethe self consistency equations at various system sizes. As can be seen the 1D Bethe ansatz solution, at finite system sizes, also has different energies for periodic and anti-periodic boundary conditions which progressively converge towards the $L = \infty$ value. This is the same situation we observe for staggered flux solutions where we observe that the energy difference between different boundary conditions decreases with increase in system size. This difference, as mentioned before, is dominant at small coupling ratios and progressively gets smaller as we move towards symmetric case.

So far we have considered only system sizes of the type $L = 4n$. To have a complete picture, we extend our analysis to system sizes of type $4n + 2$. As noted before for these systems the possible boundary conditions are ($PBC - PBC$), ($ABC - PBC$), ($PBC - ABC$). Similar to the case of $L = 4n$ we consider only two boundary conditions ($PBC - PBC$), ($ABC - PBC$) and refer to them as PBC and ABC denoting the boundary condition along strong coupling direction. It must be noted here that, due to computational time constraints, unlike the optimization of variational parameters for $L = 4n$ systems, the paramters for $L = 4n + 2$ were obtained through an interpolation of $L = 4n$ data. The result of these calculations are shown in Fig(4.7b). Comparing with 1D Bethe ansatz solutions, a particular interesting feature that we observe here is that for system sizes of type $L = 4n$, there is a reversal of energies with respect to the boundary conditions i.e Bethe ansatz energies of PBC boundary conditions are closer to the ABC boundary conditions of Staggered-flux state and vice-versa. For system sizes of type $4n + 2$ we observe equivalence of boundary conditions. This effect seems to be related to the fermionic nature of our wavefunction. Within the formalism of Bethe ansatz solution the wavefunction vectors are made up of spin flips induced on a FM state. Since they are bosonic in nature one does not consider the order in which these spin flips are induced. However, if one considers a fermionic spin flip instead(Jordan Wigner for example), the phase factor attained by shifting the lattice by single unit will not be the same as the phase factor of Bethe ansatz solution. It will have a sign difference induced through the sign convention which is given by $(-1)^{L/2-1}$. Hence, for $L = 4n$ we have an additional sign (-1) and for $L = 4n + 2$ we have equivalence with Bethe ansatz. This is exactly what we observe in Fig(4.7) and relates to the discussion from fermions on XY model from chapter 2.

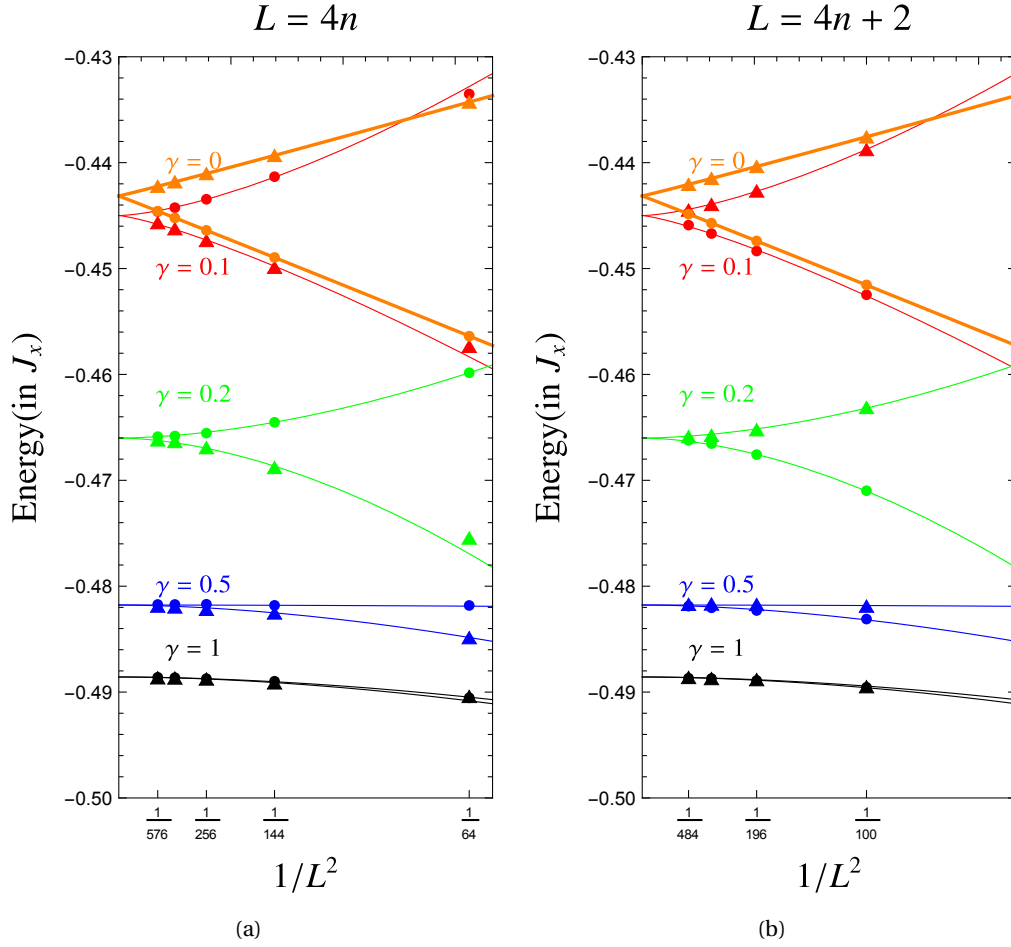


Figure 4.7 – Ground state energies for various system sizes of form $L = 4n$ (a) and $L = 4n + 2$ (b), for various coupling ratios, along with the corresponding fits. The dots (triangles) correspond to the boundary condition ABC(PBC). Red, Green, Blue and Black correspond to $\gamma = 0.1, 0.2, 0.5, 1$ respectively and Orange corresponds to Bethe ansatz. The energies corresponding to $\gamma = 0.2, 0.5, 0.1$ are offset by $-0.013, 0.02, 0.15$ respectively for better visualization.

Assuming that the energy values converge at large system sizes, we fit the data with an expression algebraic in inverse system size. Unfortunately, a similar scaling could not be observed in the variational parameters. This is partly due to the fact that the variational parameters were extracted by fitting the energy maps with a second order equation in (α, θ) space given by Eq(4.31). This procedure is susceptible not only from the errors corresponding to the fitting, but also from the fact that the energy maps do not contain an exactly parabolic minima like the fit function used. As can be seen from Fig(4.8), although we could not see an exact scaling relation, we observe a qualitative convergence of the variational parameters, with increasing system size.

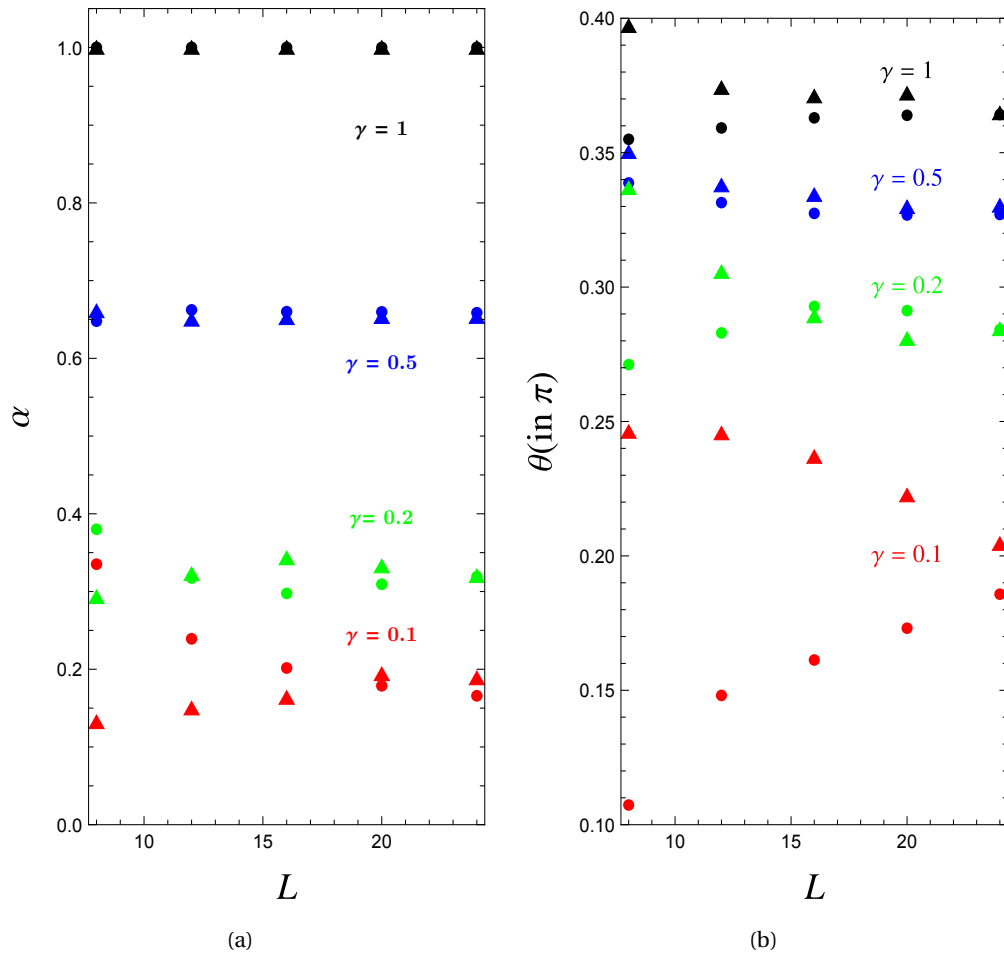


Figure 4.8 – Optimized variational parameters α and θ for system sizes $L = 4n$. Similar to Fig(4.7) the dots (triangles) correspond to the boundary condition ABC(PBC). Red, Green, Blue and Black correspond to $\gamma = 0.1, 0.2, 0.5, 1$ respectively. For better visibility the parameter θ corresponding to $\gamma = 0.1, 0.5, 1$ are offset by $0.1\pi, 0.16\pi, 0.21\pi$ respectively

Optimized Parameters

Here we have a closer look at the final results from our optimization procedure and Finite size analysis. In Fig(4.9)(at L=24) we show the evolution of groundstate energy and in Fig(4.10) corresponding variational parameters (at $L = 24$), with the coupling ratio. As the coupling ratio γ is reduced, as expected we observe that the ground state energy progressively increases and approaches the value corresponding to the Bethe ansatz. For a comparison we present the data corresponding to the Gutzwiller projected Schwinger boson wave functions calculation by Miyazaki et al Miyazaki et al. (1995). and the self-consistent spin wave result from chapter 3.

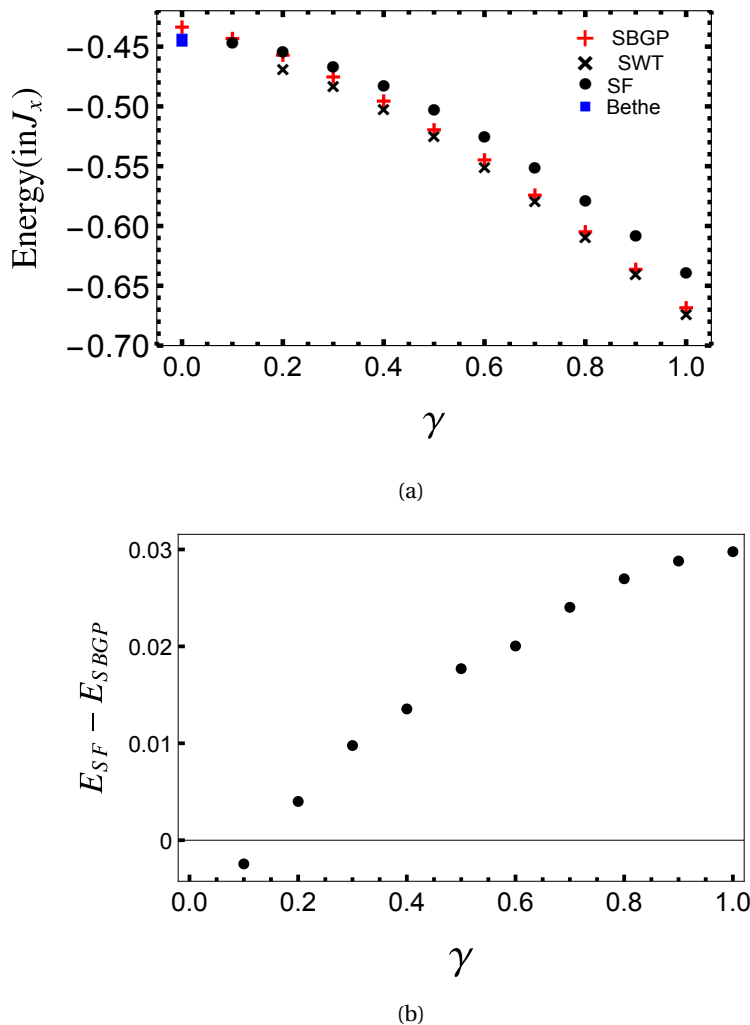
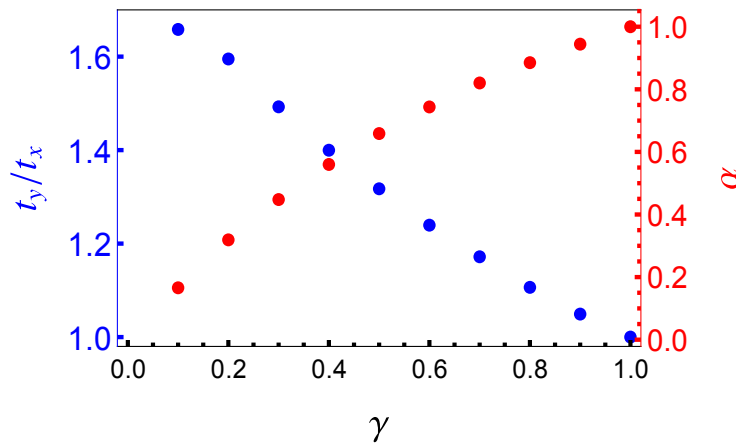
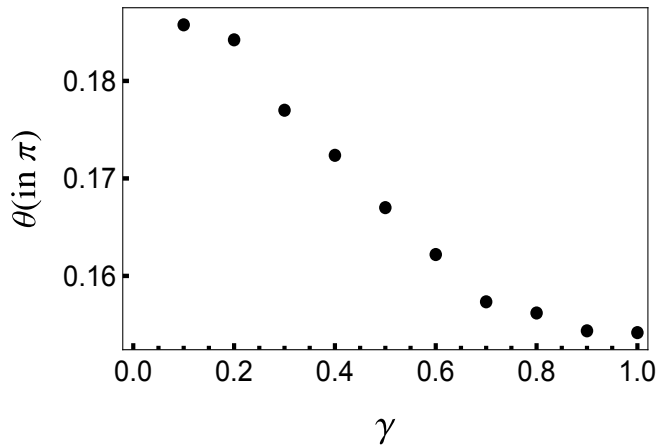


Figure 4.9 – (a) A comparison of groundstate energy at L=24 from our staggered flux wave function (SF), Gutzwiller projected Schwinger boson wavefunction from Miyazaki et. al(SBGP), and Linear spin wave theory(LSWT) from chapter 3. The solution corresponding to Bethe ansatz is indicated by blue dot. (b) Difference between energies from SF and SBGP results.

The comparison of ground state energies shows that close to the symmetric case, the disordered staggered flux state is worse compared to the ordered state. But as we move progressively towards $\gamma = 0$ we observe the difference gets smaller. In work of Miyazaki et al., it has been mentioned that below $\gamma = 0.1356$ they have a disordered state. Hence it comes as no surprise that we have almost the same energy as their work. We cannot calculate the ground state energy at exact 1D case $\gamma = 0$ using our procedure. Nevertheless, we could consider a small finite value of $\alpha = 0.05$, and fix $\gamma = 0$ on this wavefunction to calculate the nearest estimate. This is the same procedure used by Miyazaki et al. to obtain an estimate of $E(\gamma = 0) = -0.4337$. Using this procedure we end up getting a value $E(\gamma = 0) = -0.4436$ a result much closer to the exact Bethe ansatz value at $L = 24$ of $E(\gamma = 0) = -0.4445$.



(a)



(b)

Figure 4.10 – (a) Optimized variational parameter α and the mean field ratio t_y/t_x vs γ . (b) Optimized variational parameter θ vs γ . All above parameters correspond to the system size $L=24$

Moving to the variational parameters, we observe that the staggered flux parameter θ appears

to increase slightly as we move towards smaller coupling ratio. However, it must be noted that the energy is weakly dependent on θ at small coupling ratios and hence the estimates of θ at smaller coupling ratios is not strictly reliable. On the other hand the parameter α decreases with γ . This is logical since $\alpha = J_y t_y / J_x t_x$, but the surprising aspect is that the ratio t_y / t_x increases as we decrease the coupling ratio. The physical significance of this result is still not clear to us. In Table 4.1, we present the optimized values of α and θ for system size $L = 24$, and the corresponding ground state energy. These are the values used in Fig(4.10). We also present the values of $L = \infty$ estimates obtained from the algebraic fit in Figure 4.7.

γ	0.1	0.2	0.3	0.4	0.5	0.6	0.7	0.8	0.9	1
$\theta(\text{in } \pi)$	0.186	0.184	0.177	0.172	0.167	0.162	0.157	0.156	0.154	0.154
α	0.166	0.319	0.448	0.560	0.659	0.74	0.820	0.885	0.944	1
$E(L = 24)$	-0.446	-0.453	-0.466	-0.482	-0.502	-0.525	-0.550	-0.578	-0.607	-0.639
$E(L = \infty)$	-0.4450	-0.4530	-0.4654	-0.4819	-0.5018	-0.5246	-0.5501	-0.5778	-0.6074	-0.6385

Table 4.1 – Optimized variational parameters and corresponding Energy at $L = 24$. and estimates at $L = \infty$ for different values of γ

Instantaneous spin correlation

The instantaneous spin spin correlation function is an important observable that can be derived from the ground state wave function. A spin-spin correlation function estimates how the value of a spin measurement at position R and time t influences a subsequent measurement at positions $R + r$ and time t . Instantaneous spin spin correlation function is the static component of this function with $t = 0$. At zero temperature $T = 0$ it is calculated as:

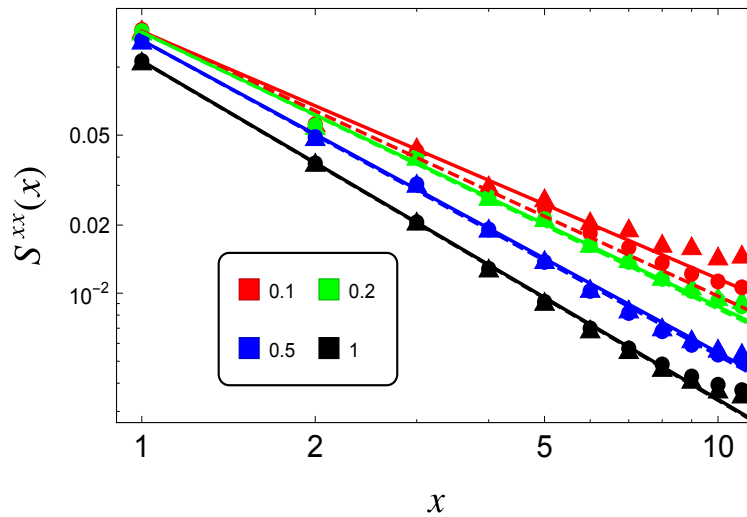
$$\mathbf{S}^{\alpha\alpha}(r) = \frac{1}{N} \sum_R \frac{\langle \text{GS} | S^\alpha(R+r) S^\alpha(R) | \text{GS} \rangle}{\langle \text{GS} | \text{GS} \rangle} \quad (4.32)$$

where $\alpha \in x, y, z$. Since we are working on a system with AFM coupling $J_x, J_y > 0$ we expect a staggered correlation function. Hence for convenience we work a staggered version of the correlation function.

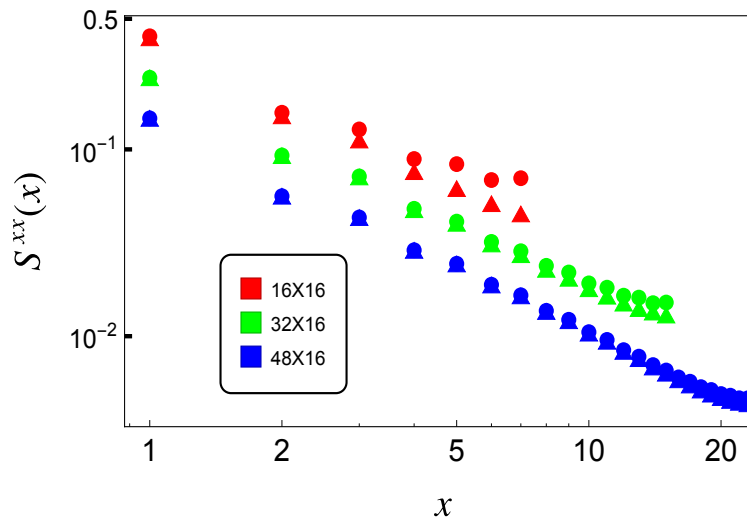
$$S^{\alpha\alpha} = e^{iQ \cdot r} \mathbf{S}^{\alpha\alpha} \quad (4.33)$$

As shown in the previous chapter, spin wave theory exhibits a power law decay of spin-spin correlation functions. This exactly what is observed in the staggered flux state in the symmetric case from the work of Bastien et al., and is also one of the positive features of the staggered flux state compared to a (Neel)state with broken symmetry. Since our state has SU(2) symmetry the components $S^{xx}(r), S^{yy}(r), S^{zz}(r)$ should be equal at a given r . This is exactly what we observe and additionally we also observe that the transverse components have smaller statistical errors compared to longitudinal component(see appendix on error analysis). Hence we present the data corresponding to $S^{xx}(r) = \langle S^x(r) S^x(0) \rangle$ only. Also, we restrict our discussion to the

correlation function along x and y directions, which capture the relevant aspects on a 2D lattice.



(a)



(b)

Figure 4.11 – a) Instantaneous spin correlation function, along x -direction along with fits corresponding to power-law decay A_x/x^{e_x} , for system size $L = 24$ at $\gamma = 1, 0.5, 0.2, 0.1$ represented with Black, Blue, Green and Red. b) Instantaneous spin correlation function along x -direction at $\gamma = 0.1$ for rectangular system sizes $L_x \times 16$ with $L_x = 16, 32, 48$ indicated by Red, Green and Blue. For better visualization, the correlation functions for $L_x = 16, 32$ in (b) have been multiplied by \sqrt{e}, e to offset. In both figures, triangles represent ABC boundary conditions and dot represent PBC boundary conditions. For Fig(a) solid line corresponds to the ABC boundary condition and dashed lines corresponds to the PBC boundary condition.

In Fig(4.11a) we show the correlation functions along the strong coupling (x) direction for both ABC(triangles) and PBC(circles). We observe that as we decrease the coupling ratio γ , the correlation function keeps exhibiting a power law decay. The decay exponent appears to be decreasing with a decreasing coupling ratio. Similar to the ground state energies, one can observe a difference between the PBC and ABC cases. The difference appears to be dominating at small coupling ratios. To see if this is just a finite size effect we need to increase the system size. Unfortunately, due to computational limitations we could only go till $L = 28$. To get around this, we perform additional calculations where we consider a rectangular system size $L_x \times L_y$, where we limit the size of our system in y direction to $L_y = 16$. This allows us to increase the system size in x-direction L_x . In Fig(4.11(b)) we show the correlation function at $\gamma = 0.1$ for $L_x = 16, 32, 48$, and as one can see the difference between both boundary conditions becomes smaller at large system sizes.

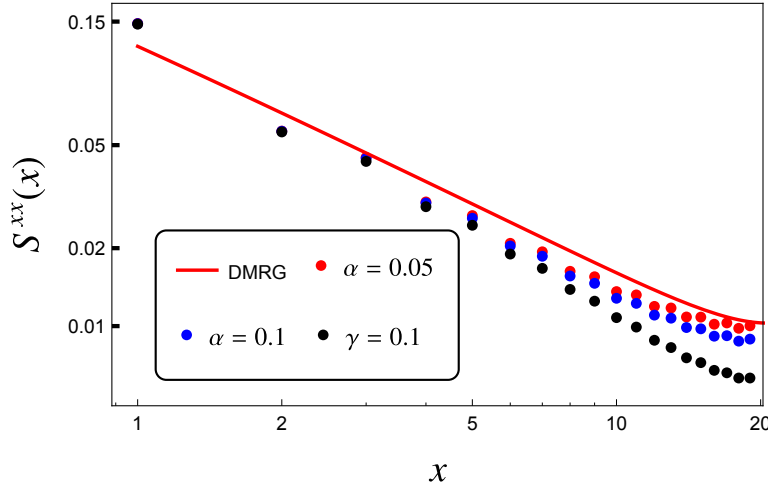
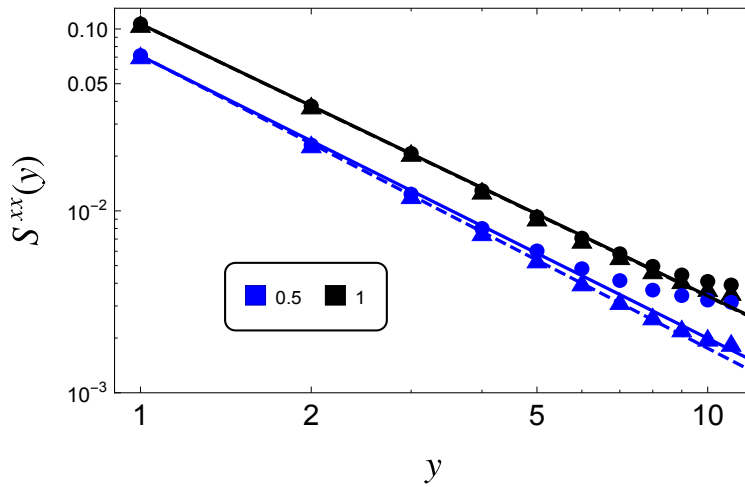


Figure 4.12 – Instantaneous spin correlation function close to 1D. The solid line corresponds to the analytic expression provided by Hallberg et al by fitting the DMRG data. Black dots correspond to optimized case for $\gamma = 0.1$. Blue and red dots correspond to $\alpha = 0.05, 0.1$ with $\theta = 0.175\pi$.

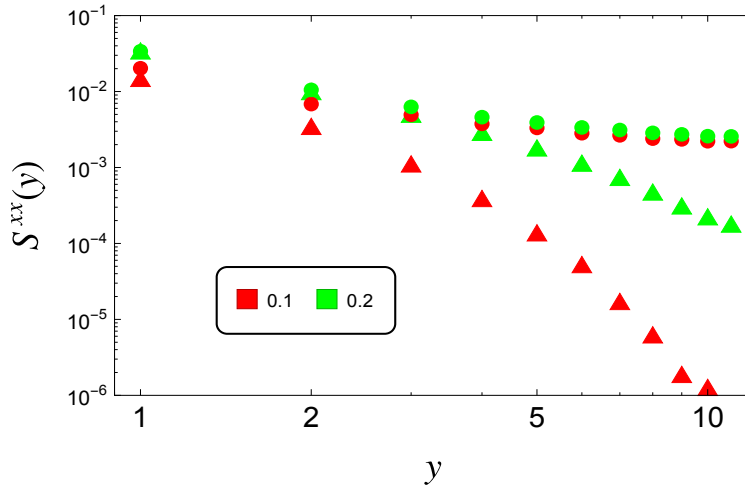
As mentioned in chapter 2 the bosonization technique shows that the mathematical form of the correlation function for 1D case at infinite system size and large r is known to be decaying algebraically with a logarithmic correction $\frac{C}{r} \sqrt{\ln r}$. From field theory the value of the coefficient is obtained as $1/(2\pi)^{3/2}$. Unfortunately, this expression does not work well at small r . Hence, for a comparison at 1D we look for other numerical methods involving finite system sizes. The research work we use is the result by Hallberg et al, where they use numerical renormalization group methods (currently called DMRG) to derive the correlation function at finite system sizes. They provide an analytic expression that fits the numerical data obtained at $L = 20$. We use this expression as a benchmark for the comparison at 1D limit.

Since our method does not work at $\gamma = 0$ we compare the coupling ratios very close to this limit.

A particular difficulty with making this comparison is the fact that, as we go closer to $\gamma = 0$, the energy maps become extremely flat. Hence, estimating the optimum values of α and θ becomes challenging. Since, we observe that the physical properties are weakly dependent on θ , instead of optimizing we fix $\theta = 0.175\pi$ and calculate correlation functions at very small α . As can be seen from Fig(4.12), the calculated correlation functions are gradually converging towards the DMRG result as we go towards smaller coupling ratios. Although the value of anisotropy γ corresponding to α is not known, if we assume $\alpha > \gamma$ (as observed at almost all coupling ratios) is satisfied close to 1D limit then we can safely assume that we are at a coupling ratio $\gamma < 0.05$.



(a)



(b)

Figure 4.13 – a) Instantaneous spin correlation function along y -direction, along with fits corresponding to power-law decay A_y/x^{e_y} , for system sizes $L = 24$ at $\gamma = 1, 0.5$ represented with Blue, Green and Red. b) For Fig(a) solid line corresponds to the ABC boundary condition and dashed lines corresponds to the PBC boundary condition.

Moving on to the y-direction, as can be seen from Fig(4.13a) at large γ we observe that the correlation functions continue have a power-law decay but the decay exponent increases only slightly with decreasing γ (see Table(4.2)). At low coupling ratios however, for ABC boundary conditions we observe a exponential decay, as can be seen in Fig(4.13b). However, for PBC boundary conditions we observe a power-law decay. To evaluate if this is just a finite size effect, similar to the case of x-direction, we calculate the correlation function for rectangular system sizes fixing $L_y = 16$. Increasing system size in x-direction, we observe that the correlation functions gradually converge indicating that the exponential decay was just a finite size effect. This particular observation throws into question the exponential decay observed in staggered flux state with Neel field $SF + N$ in work of DallaPiazza et. al. One must revisit this state and perform a detailed finite size analysis to see if the observed exponential decay is only a Finite size effect.

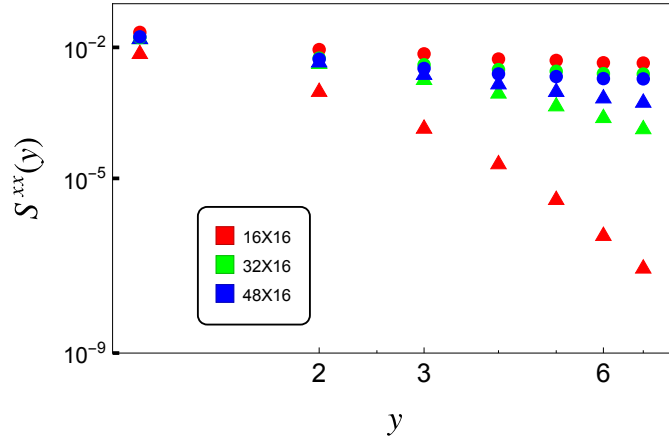


Figure 4.14 – Instantaneous spin correlation function along y-direction at $\gamma = 0.1$ for rectangular system sizes $L_x \times 16$ with $L_x = 16, 32, 48$ indicated by Red, Green and Blue. In both figures, triangles represent ABC boundary conditions and dot represent PBC. boundary conditions.

In table, we present our estimates of decay exponents. For $\gamma > 0.6$, where the boundary effects are minimal, they are obtained by fitting $L = 24$ data with expressions b_x/e^{e_x} and b_y/e^{e_y} along x and y-directions respectively. For coupling ratios $\gamma \leq 0.6$ we fit the data obtained from the largest rectangular system size which we could achieve i.e. $L_x \times L_y = 56 \times 16$, where we observe the boundary effects to be minimal.

γ	0.1	0.2	0.3	0.4	0.5	0.6	0.7	0.8	0.9	1
e_x	1.16	1.26	1.33	1.39	1.42	1.45	1.48	1.50	1.50	1.50
e_y	1.72	1.63	1.61	1.59	1.56	1.54	1.51	1.50	1.50	1.50

Table 4.2 – Decay exponents obtained for different γ .

Summary

1) Heisenberg Hamiltonian of RQHAF, in its fermionic form is diagonalized by using a mean field decoupling. A particular choice of these mean fields yields us the staggered flux wavefunction, which can be obtained by filling the lower band of the diagonalized Hamiltonian. Staggered flux state contains double occupancies, and hence cannot be considered as true physical groundstate. Hence, a Gutzwiller projection of this state is considered to be the ground state. This wavefunction is parameterized by two parameters α, θ . The parameters are optimized through numerical evaluation, where the calculation of observables is carried out through a Montecarlo process. To avoid nodal points $(\pi/2, \pi/2)$, we consider various boundary conditions.

2) Energy maps on the (α, θ) space at $L = 8$ reveal clearly visible energy minima. At large coupling ratios we see the energy strongly depending on parameters and hence the minima being well defined. At small coupling ratios the energy minima are extremely flat, particularly in θ space. To find the exact position of minima, the lower part of energy maps are fitted with second order polynomial in α, θ . This procedure is repeated with various system sizes with different boundary conditions.

3) Finite size calculations show that the energies and parameters are strongly dependent on system size L only at small coupling ratios. This is not surprising as Bethe ansatz also shows similar finite size dependence. Calculations for system sizes $L = 4n$, show that the results for different boundary conditions (along strong coupling direction) converge as we increase system size. Using this, we estimate the $L \rightarrow \infty$ values of energy. A peculiar observation is the similarity between Bethe ansatz solution with anti-periodic boundary condition and staggered flux solution with periodic boundary condition (and vice versa). This is reversed for systems of sizes $L = 4n + 2$. This is related to the fact that our wavefunction is made up of fermions. Scaling relations for optimized parameters, similar to groundstate energy, could not be obtained to determine the $L \rightarrow \infty$ value of these parameters. Nevertheless, a qualitative convergence is observed. A look at the optimized parameters at $L = 24$, reveals that the parameter θ increases slightly as we move towards smaller coupling ratios. As expected parameter α decreases as we move towards smaller coupling ratios, but surprisingly the ratio t_y/t_x increases. The origin of this is still not clear.

4) The instantaneous spin correlation (xx component) function along x-direction shows power-law behavior. It is observed that the correlation function for small coupling ratios at large distances depends strongly on boundary conditions. Since our computational capacity is limited, to determine accurate form of correlation function at large system sizes and small coupling ratios, we consider rectangular system sizes $L_x \times L_y$ with $L_y = 16$ and L_x going upto $L_x = 56$. We observe the boundary effects becoming minimal as we increase L_x . By fitting the correlation function with a power-law decay we estimate the decay exponents. Contrary to the spin wave case, where (along x-direction) we observe decay exponent of $e_x = 1 (\sim 1.04)$ (for

all γ , we observe that the decay exponent decreases with decreasing γ .

5)The instantaneous spin correlation function along y-direction exhibited a power-law decay at large coupling ratios. At small coupling ratios, it showed an exponential decay for Anti-periodic boundary conditions and a power-law decay for periodic. Similar to previous case, working with rectangular system sizes with large L_x we were able to show that the correlation function converges to a power law decay. Fitting the correlation function with power-law decay shows that the decay exponent increases with decreasing γ , opposite of the result in x-direction. This is also different from the spin wave result where the correlation function had same exponent $e_y = 1(\sim 1.04)$ and a decreasing amplitude with decreasing γ .

5 Staggered flux:Excited State

In this chapter we study the transverse spin excitations induced on a staggered flux ansatz on a RQHAF. Transverse $\Delta S = 1$ excitation is constructed from the Gutzwiller projected state, as a particle-hole excitations on the optimized wave function derived in chapter 4. By studying the dynamic spin structure factor as function of coupling ratios $\gamma = J_y/J_x$, we analyze the gradual evolution of the spin excitations on this RVB state. As mentioned in work of [Dalla Piazza et al. (2014a); Dalla Piazza (2014b)], the excitation spectrum in the symmetric (square lattice) case, manages to capture various qualitative features of the observed $(\pi, 0)$ quantum anomaly (see chapter 1). However, it also hosts some un-physical features that make this state un-fit to be the true ground state of the 2D Heisenberg model, particularly at long wavelengths. The most notable feature is the un-physical negative energies observed at (π, π) , which is a result of our assumed ground state lacking long-range order. A staggered flux state with induced Neel field, on the other hand, has a Goldstone mode at (π, π) point and a good groundstate energy. However, it does not manage to capture all the features of the $(\pi, 0)$ anomaly.

Repairing the staggered flux wave function by artificially inducing long range correlations should be possible. Methods like Jastrow factor optimization [Jastrow (1955)] have been proposed for this purpose, but they require optimization of a large number of variational parameters. Repairing the staggered flux wave function, although is a top priority, is not the focus of our research work. We carry on our analysis assuming this imperfect state to be the ground state, and focus our attention to the high energy features of the excitation spectrum, which the staggered flux state manages to capture qualitatively. We hope that a future research work to induce long wavelength correlations would be carried out, that would lead to a more reliable wave function. As mentioned in chapter 2, different explanations for the $(\pi, 0)$ quantum anomaly are available in literature, notably the work of [Powalski et al. (2015, 2018)] using continuous similarity transformations on spin wave induced states. Although these research works bring into question the validity of a deconfined spinon excitations in 2D, they do not entirely exclude the possibility that a staggered flux state with sufficiently long range correlations could be a good approximation to the ground state of the 2D model. In such a scenario, multi-magnon and deconfined spinon excitations might serve as two

different pictures of the same spin excitation spectrum. Other works that are inclined towards a deconfined spinon picture also exist in the literature [Shao et al. (2017); Ghioldi et al. (2016)]. Other research works involving the use of a Gutzwiller projected states with long range order also exist. A recent work by F. Ferrari and E. Becca [Ferrari and Becca (2018)] deals with RQHAF using a Gutzwiller projected fermionic wave function along with a AFM parameter Δ_{AF} which is zero at $\gamma = 0$ and has a finite value as soon as J_y is turned on. This wavefunction in principle should be equivalent to $SF + N$ wave function used by Dalla Piazza et al. and exhibits an excitation spectrum quite similar to their work at symmetry point $\gamma = 1$.

This research work, although motivated from the explanation of the $(\pi, 0)$ quantum anomaly, does not anchor itself towards explaining the experimental features or deriving the exact numerical values of a RQHAF. It instead focuses on the novel aspect of the staggered flux state, notably the spinon excitations and their evolution as we traverse the 1D to 2D regime by varying γ . All the numerical results provided here describe the qualitative aspects of the spin spectra of the staggered flux state.

Mathematical Framework

In this section we provide the mathematical framework used for calculating the dynamical quantities corresponding to our wave function. The basic outline of this procedure is as follows:

- 1) A vector space of particle-hole excitation states $|k, q\rangle$, is created by destroying a down spin at $k - q$ in the lower band of SF state and creating a up spin at k in the upper band of the SF state.
- 2) A transverse spin excitation of momentum q induced on the SF state, can be expressed as a linear combination of the particle-hole states $|k, q\rangle$. The coefficients can be calculated from the relation between the quasi-particle fermion operators $\gamma_k^\dagger, \gamma_k$ and original fermionic operators c_k^\dagger, c_k from Eq(4.15) from chapter 4.
- 3) To obtain the excitation spectrum at a specific q vector, the Heisenberg Hamiltonian can be diagonalized in the excitation subspace $\{|k_1, q\rangle, |k_2, q\rangle \dots |k_n, q\rangle\}$. Since the particle-hole states $|k, q\rangle$ are not orthogonal we have to solve a generalized eigenvalue problem.
- 4) The numerical quantities that need to be evaluated are the matrix elements $H_{kk'}^q$ of the Hamiltonian and the matrix elements $O_{kk'}^q$ of the overlap matrix. A numerical Monte Carlo method, similar to chapter4, is developed to evaluate this quantities that are subject to Gutzwiller projection.
- 5) Once we have estimated the matrix elements of the Hamiltonian and the overlap matrix, we carry out a generalized diagonalization of the Hamiltonian to derive the eigenvalues

and eigenvectors. These quantities shall further be used to calculate the dynamical quantities.

Transverse dynamic spin structure factor

Our main focus would be on calculating the dynamic spin structure factor, a quantity of high relevance in quantum magnetism. Being related to one of the simplest dynamical quantities, the spin-spin correlation function in time and space, the dynamical structure factor is the key quantity measured in inelastic neutron scattering experiments. Its mathematical form is given by:

$$S^{\alpha\beta}(q, \omega) = \int dt \sum_{R,r} e^{iqr+i\omega t} \langle S_{R+r}^{\alpha}(t) S_R^{\beta}(0) \rangle \quad (5.1)$$

Transverse dynamic spin structure factor (TDSF) corresponds to $(\alpha, \beta) = (x, x)$ and longitudinal dynamical structure factor corresponds to $(\alpha, \beta) = (z, z)$. Since we work on a disordered state (SU(2) symmetric), the longitudinal structure factor is expected to be the same as the transverse component. Hence, in this work we focus only on the TDSF in our work. For mathematical convenience, we work with the $S^{-+}(q, \omega)$ which is just twice the xx component. For Performing a few elementary calculations at $T = 0$ this quantity can be re-written as:

$$S^{-+}(q, \omega) = \sum_{\lambda} \left| \langle \lambda | S_q^+ | GS \rangle \right|^2 \delta(\omega - E_{\lambda} + E_{GS}) \quad (5.2)$$

where $\{|\lambda\rangle\}$ are the eigenstates of the excitation subspace. It must be noted that the eigenstates $|\lambda\rangle$ must be complete i.e $|\lambda\rangle\langle\lambda| = \mathbb{1}$ where $\mathbb{1}$ is the identity matrix in the Hilbert space of transverse excitation subspace, which is larger than single particle-hole excitation space. One has to include multiple particle-hole excitations to have the complete Hilbert space. In this work we assume that multiple particle-hole excitations have a very small contribution to TDSF and we restrict ourselves to the single particle hole excitations. This claim might be challenged, given that at 1D two-spinon excitations capture only 73% of the excitation spectrum [Karbach et al. (1997)] and including four spinon terms capture 98% of the excitation spectrum [Caux and Hagemans (2006)]. But carrying out calculations to multiple particle-hole excitations is numerically intractable. Hence, we concern ourselves only with single particle excitations (one magnon or two spinon).

Transverse Excitation Subspace

We start by defining an excitation with momentum q as:

$$|q\rangle = S_q^+ P_{D=0} |\psi_{GS}\rangle \quad (5.3)$$

Chapter 5. Staggered flux:Excited State

In terms of fermionic operators S_q^+ can be written as

$$S_q^+ = \sum_k c_{k\uparrow}^\dagger c_{k-q\downarrow} \quad (5.4)$$

Using Eq(4.15) (from chapter 4) this can be converted in terms of the quasi particle operators as:

$$|q\rangle = P_{D=0} \sum_k \phi_k^q d_{k\uparrow}^\dagger d_{\bar{k}-q\downarrow} |\psi_{GS}\rangle \quad (5.5)$$

where we have used the fact that $[S_q^+, P_{D=0}] = 0$. \bar{k} implies that k has been folded into magnetic brillouin zone. The coefficients ϕ_k^q are given by

$$\phi_k^q = u_{k\uparrow}^* u_{k-q\downarrow} + v_{k\uparrow}^* v_{k-q\downarrow} \quad (5.6)$$

Hence, the excited state becomes a linear combination of particle-hole excitation states defined as:

$$|k, q\rangle = P_{D=0} d_{k\uparrow}^\dagger d_{\bar{k}-q\downarrow} |\psi_{GS}\rangle \quad (5.7)$$

In Fig(5.1) we show an illustration of a particle-hole excitation on an un projected staggered flux state. The bands are represented by their density of states which is evaluated as $D(\omega) = \sum_{k \in MBZ} D(\omega, k)$ at parameters $\alpha = 1, 0.3$ and $\theta = 0.15\pi$. Since $|k, q\rangle$ are the vectors of excitation subspace, the excitation eigenstates $|\lambda\rangle = |n, q\rangle$ can be written as:

$$|n, q\rangle = \sum_k \phi_{kn}^q |k, q\rangle \quad (5.8)$$

The coefficients ϕ_{kn}^q have to be determined by diagonalizing the Hamiltonian in the excitation subspace. If the states $|n, q\rangle$ are eigenstate of the Hamiltonian they must satisfy the condition:

$$\langle n, q | \mathcal{H} | n, q \rangle = E_n^q \langle n, q | n, q \rangle \quad (5.9)$$

$$\langle n', q | n, q \rangle = \delta_{nn'} \quad (5.10)$$

This leads to the generalized eigen value problem:

$$\sum_{k, k'} \phi_{k'n}^q * H_{k'k}^q \phi_{kn}^q = E_n^q \sum_{kk'} \phi_{k'n}^q * O_{k'k}^q \phi_{kn}^q \quad (5.11)$$

where

$$\begin{aligned} H_{kk'}^q &= \langle k, q | \mathcal{H} | k', q \rangle \\ O_{kk'}^q &= \langle k, q | k', q \rangle \end{aligned} \quad (5.12)$$

The dynamical quantities that we want to estimate depend entirely on the eigenvalues E_n^q and eigenvectors $|n, q\rangle$. Hence we need to devise a numerical methodology to estimate the matrix elements in Eq(5.12). Although the equations Eq(5.12) do not have the same form as calculation of a given observable on the groundstate (Eq(4.26) in chapter 4), it will be shown in the subsequent sections on how to apply a Monte Carlo process to calculate this quantity.

Monte Carlo Method

Similar to the case of ground state, the Gutzwiller projector is constructed using the single particle states $\{|\alpha\rangle\}$ except that, compared to ground state, the states $|\alpha\rangle$ have $(N + 1)/2$ up spins and $(N - 1)/2$ downspins. The matrix elements in Eq(5.12) can be written as:

$$H_{kk'}^q = \sum_{\alpha\beta} \langle k, q | \alpha \rangle \langle \alpha | \mathcal{H} | \beta \rangle \langle \beta | k', q \rangle \quad (5.13)$$

This equation can be rewritten as:

$$\frac{H_{kk'}^q}{\langle k, q | k, q \rangle} = \sum_{\alpha} \underbrace{\frac{|\langle k, q | \alpha \rangle|^2}{\langle k, q | k, q \rangle}}_{\rho(\alpha)} \underbrace{\sum_{\beta} \langle \alpha | \mathcal{H} | \beta \rangle \frac{\langle \beta | k', q \rangle}{\langle \alpha | k, q \rangle}}_{f(\alpha)} \quad (5.14)$$

If we construct a Monte Carlo process following the above equation, then we obtain the matrix elements $H_{kk'}^q$ along with a k dependent factor $\langle k, q | k, q \rangle$. If one wants to calculate all the matrix elements $H_{kk'}^q$ then one can pick an arbitrary state $|k_0, q\rangle$ and rewrite the above equation as:

$$\frac{H_{kk'}^q}{\langle k_0, q | k_0, q \rangle} = \sum_{\alpha} \underbrace{\frac{|\langle k_0, q | \alpha \rangle|^2}{\langle k_0, q | k_0, q \rangle}}_{\rho(\alpha)} \underbrace{\sum_{\beta} \frac{\langle k, q | \alpha \rangle}{\langle k_0, q | \alpha \rangle} \langle \alpha | \mathcal{H} | \beta \rangle \frac{\langle \beta | k', q \rangle}{\langle \alpha | k_0, q \rangle}}_{f(\alpha)} \quad (5.15)$$

This formulation is unstable due to the fact that if $\langle \alpha | k_0, q \rangle \rightarrow 0$ then $f(\beta) \rightarrow \infty$. This would render the Monte Carlo sampling impossible. To solve this Li and Yang [Li and Yang (2010)] introduced a re-weighting technique where the matrix elements are re-define as weighted sum:

$$\frac{H_{k,k'}^q}{W_q} = \sum_{\alpha} \underbrace{\frac{W_q(\alpha)}{W_q}}_{\rho(\alpha)} \underbrace{\sum_{\beta} \frac{\langle k, q | \alpha \rangle \langle \alpha | \mathcal{H} | \beta \rangle \langle \beta | k', q \rangle}{W_q(\alpha)}}_{f(\alpha)} \quad (5.16)$$

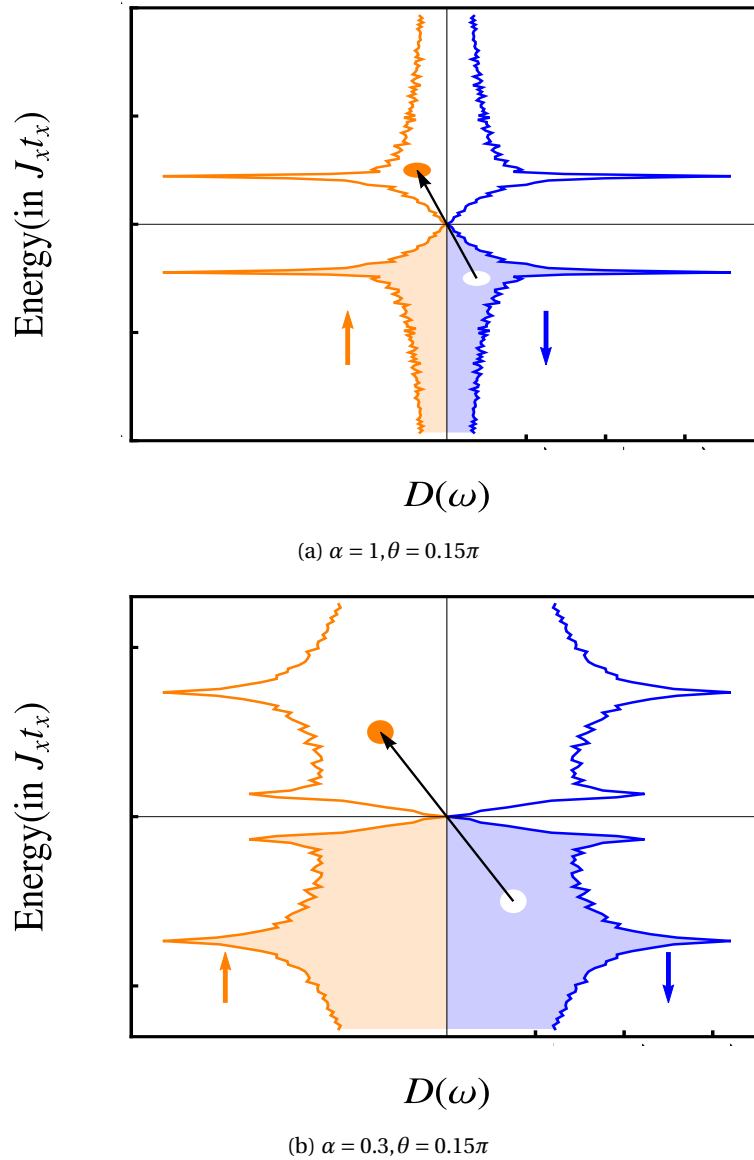


Figure 5.1 – Transverse spin excitation represented as particle-hole pair excitation. Bands corresponding to staggered flux state with selected parameters $\alpha = 1, \theta = 0.15\pi$ (a) and $\alpha = 0.3, \theta = 0.15\pi$ (b). A spin \downarrow (blue) is taken from lower band flipped, and filled in upper band as a \uparrow (orange). The density of states is calculated as $D(\omega) = \sum_{k \in MBZ} D(\omega, k)$ and the density of states corresponding to $\uparrow(\downarrow)$ is represented on negative(positive) x-axis.

where

$$W_q(\alpha) = \sum_k |\langle \alpha | k, q \rangle|^2 \quad (5.17)$$

$$W_q = \sum_\alpha W_q(\alpha) \quad (5.18)$$

Similarly, to calculate the elements $O_{kk'}^q$ in the overlap matrix we have the equation:

$$\frac{O_{k,k'}^q}{W_q} = \sum_\alpha \underbrace{\frac{W_q(\alpha)}{W_q}}_{\rho(\alpha)} \underbrace{\frac{\langle k, q | \alpha \rangle \langle \alpha | k', q \rangle}{W_q(\alpha)}}_{f(\alpha)} \quad (5.19)$$

To numerically estimate of the matrix elements, we can follow the same procedure as developed for the ground state. Analogous to calculating the amplitude $|\langle \alpha | GS \rangle|^2$ in the groundstate, we have to calculate the weight $W_q(\alpha) = \sum_k |\langle \alpha | k, q \rangle|^2$ over the entire space $k \in \text{MBZ}$. The details on the algorithm to efficiently calculate this quantity and the associated computational difficulty are provided in the Appendices.

Dynamical structure factor

Once we manage to calculate the matrix elements in Eq(5.12), we are in a position to evaluate the dynamical structure factor. We have to make the following substitutions in Eq(5.2):

$$|\lambda\rangle = |n, q\rangle \quad (5.20)$$

$$S_q^+ |GS\rangle = |q\rangle \quad (5.21)$$

and the dynamical structure factor becomes:

$$S^{-+}(q, \omega) = \sum_n |\langle n, q | q \rangle|^2 \delta(\omega - E_n^q + E_{GS}) \quad (5.22)$$

Expanding $|n, q\rangle$ and $|q\rangle$ using Eq(5.5) and Eq(5.7) we obtain:

$$\frac{S^{-+}(q, \omega)}{W_q^2} = \sum_n \left| \sum_{kk'} \phi_{kn}^q * \frac{O_{kk'}^q}{W_q} \phi_{k'}^q \right|^2 \delta(\omega - E_n^q + E_{GS}) \quad (5.23)$$

As we can see, our formalism explicitly contains the q-dependent normalization weight W_q^2 . This makes comparison of the structure factor across various q values challenging. Here utilize the fact that the sum rules over dynamical structure factor is related to the instantaneous

structure factor via:

$$\int d\omega S^{-+}(q, \omega) = \langle S_q^- S_q^+ \rangle \quad (5.24)$$

Using the property:

$$\sum_{nk} \phi_{nk_1}^q * O_{k_2k} * \phi_{nk}^q = \delta_{k_1k_2} \quad (5.25)$$

we can get:

$$\begin{aligned} \int d\omega \frac{S^{-+}(q, \omega)}{W_q^2} &= \sum_n \left| \sum_{kk'} \phi_{kn}^q * \frac{O_{kk'}^q}{W_q} \phi_{k'}^q \right|^2 \\ \frac{\langle S_q^- S_q^+ \rangle}{W_q^2} &= \sum_{kk'} \phi_k^q \frac{O_{kk'}^q}{W_q} \phi_{k'}^q = \langle S_q^- S_q^+ \rangle_{\Omega_q} \end{aligned} \quad (5.26)$$

The quantity $\langle S_q^- S_q^+ \rangle_{\Omega_q}$ can be estimated from the matrix elements is $O_{kk'}^q / W_q$ that we actually calculate in our Monte Carlo process. We also know the value of instantaneous spin-spin correlation function $\langle S_q^- S_q^+ \rangle$ from the Groundstate calculations. Hence the relation:

$$W_q = \sqrt{\frac{\langle S_q^- S_q^+ \rangle}{\langle S_q^- S_q^+ \rangle_{\Omega_q}}} \quad (5.27)$$

gives us the q-dependent scaling factor W_q .

Spinon pair separation distribution

Apart from calculating the dynamic structure factor, the knowledge of eigenenergies and eigenvectors of the Hamiltonian in the particle-hole basis can be used to further scrutinize the nature of the observed excitations. A particularly important distinction to be made here is if the excitations are 'magnon' like or 'spinon' like. We understand magnons as Fourier sums of localized spin flips on an ordered lattices, and spinons as delocalized 'solitons' moving freely on a Heisenberg chain or de-localized boundaries on a XY-chain. As explained in chapter 1, 'spinons' on RVB state (transverse excitation) can be understood as two up spins from a broken singlet that move on the spin liquid background. Hence, to quantify the nature of an excitation, one must evaluate the degree of delocalization of the induced spin flip on the corresponding eigenvector. We use the methodology developed in [Dalla Piazza et al. (2014a); Dalla Piazza (2014b)] for this purpose. We start by defining a de-localized spin flip in the real

space given by:

$$|R, r\rangle = P_G c_{R+r\uparrow}^\dagger c_{R\downarrow} |\psi_{GS}\rangle \quad (5.28)$$

where we annihilate a down spin at position R and create an up-spin at position $R + r$ on the lattice. Here we define r as the spinon-pair separation distribution. It must be noted that, unlike a localized spin flip S_i^+ , the delocalized spin flip does not commute with the Gutzwiller projector (except when $r = 0$). Hence, it can only be applied on the unprojected staggered flux wave function. The physical interpretation of this state shall be explained soon. Since, we are working on a translational invariant system it would be convenient to work in crystal momentum space. Hence we define the following state:

$$|r, q\rangle = P_G \sum_R e^{iqR} c_{R+r\uparrow}^\dagger c_{R\downarrow} |\psi_{GS}\rangle \quad (5.29)$$

which can be understood as a spinon pair separated by r and propagating with momentum q . In this representation a localized spin flip S_q^+ is nothing but a local transvers spinon pair with zero separation.

$$P_G S_q^+ |\psi_{GS}\rangle = |0, q\rangle \quad (5.30)$$

By expanding the fermion operators in quasi particle operators via Eq(4.15), we can relate the spinon pair wave function to the particle-hole excitations through the equations:

$$|r, q\rangle = \sum_k \phi_k^q(r) |k, q\rangle \quad (5.31)$$

where

$$\phi_k^q(r) = e^{ikr} \left[\epsilon_r \left(u_{k\uparrow+}^* u_{k-q\downarrow-} + v_{k\uparrow+}^* v_{k-q\downarrow-} \right) + \bar{\epsilon}_r \left(v_{k\uparrow+}^* u_{k-q\downarrow-} + u_{k\uparrow+}^* v_{k-q\downarrow-} \right) \right] \quad (5.32)$$

and

$$\epsilon_r = \frac{1}{2} \left(e^{iQ \cdot r} + 1 \right), \quad \bar{\epsilon}_r = \frac{1}{2} \left(e^{iQ \cdot r} - 1 \right) \quad (5.33)$$

It can be seen that the space $\{|r, q\rangle\}$ has twice the number of states that the particle-hole basis $\{|k, q\rangle\}$ has, and hence cannot be a basis of the excitation subspace. This happens because the definition of $|r, q\rangle$ in eq(5.31) is not inversion symmetric ($r \rightarrow -r$). One could work with a symmetric definition:

$$|r, q\rangle' = \frac{1}{\sqrt{2}} (|r, q\rangle + |-r, q\rangle) \quad (5.34)$$

Chapter 5. Staggered flux:Excited State

The new basis $\{|r, q\rangle\}$ can form a basis in projected particle-hole excitation space where r is considered only in the positive half plane ($r_x > 0$ for example). We nonetheless work with the basis $\{|r, q\rangle\}$ as we observe that the results are essentially the same for both formulations.

Having defined the delocalized spin-flip state $|r, q\rangle$ we now turn to establish the quantities one could calculate using these states. First we have to define what a 'magnon' like state would look like in our formulations. Similar to case of ordered lattices we can imagine a magnon to be the Fourier sum of localized spin flips induced on the ground state. Considering the same interpretation, we have:

$$\sum_R e^{iqR_i} S_{R_i}^+ |GS\rangle = |r=0, q\rangle \quad (5.35)$$

which indicates that a 'magnon' in our context is nothing but a spinon pair with zero separation. The overlap of this state with an eigenstate measures how much the eigenstate is magnon like. Hence, to determine the nature of the excitation, we are interested in the quantity:

$$P^q(r, n) = |\langle r, q | n, q \rangle|^2 \quad (5.36)$$

Since there are about $L^2/2$ eigen energies at each q vector, we would like a quantity that can characterize overall spectrum at a given q vector. The choice used by Dalla Piazza et al in their work is:

$$\tilde{\rho}^q(r) = \sum_n |\langle r, q | n, q \rangle \langle n, q | r=0, q \rangle|^2 \quad (5.37)$$

which is normalized such that $\sum_r \tilde{\rho}^q(r) = 1$. The weight $|\langle n, q | r=0, q \rangle|^2$ is nothing but the contribution of the mode $|n, q\rangle$ to the dynamic structure factor. Hence, the contribution of each eigen state is weighted according to its intensity. The interest in this quantity also comes from the fact that it represents the time averaged spinon pair separation distribution. This comes from the fact that a local spin flip S_q^+ caused by by probing a neutron for instance, delocalizes into extended spinons, the dynamics of which are given by:

$$\tilde{\rho}^q(r, t) = |\langle r, q | e^{-i\mathcal{H}t} | r=0, q \rangle|^2 \quad (5.38)$$

Resolving the time evolution operator by introducing the eigenstate propagator $|n, q\rangle \langle n, q|$ we observe that :

$$\lim_{T \rightarrow \infty} \frac{1}{T} \int_0^T \tilde{\rho}^q(r, t) dt = \lim_{T \rightarrow \infty} \frac{1}{T} \int_0^T \left| \sum_n \langle r, q | n, q \rangle \langle n, q | r=0, q \rangle e^{-iE_n t} \right|^2 dt \quad (5.39)$$

$$= \sum_n |\langle r, q | n, q \rangle \langle n, q | r=0, q \rangle|^2 = \tilde{\rho}^q(r) \quad (5.40)$$

Hence the quantity $\rho^q(r)$ can be interpreted as the time-averaged spinon pair separation dis-

tribution of the spin -flip state $|r = 0, q\rangle$. $\rho^q(r)$ is the quantity we are interested in, and by comparing this quantity as a function of r one can evaluate the degree of spinon de-localization. Since, we are comparing the spinon pair separation distribution for different r we feel that it is more appropriate to calculate the overlap with normalized states $|r, q\rangle / \sqrt{\langle r, q | r, q\rangle}$. Hence we redefine our spinon pair separation distribution density as:

$$\rho^q(r) = \sum_n \frac{|\langle r, q | n, q\rangle \langle n, q | r = 0, q\rangle|^2}{\langle r, q | r, q\rangle} \quad (5.41)$$

This is the final quantity we evaluate at various q for systems of different γ to characterize the nature of excitations. It must be noted here that a delocalized spin flip is not a quantized observable. Hence the notion of normalization does not have a solid reasoning and is completely an optional exercise.

Real space picture

Similar to the chapter 4, where we expressed the groundstate as a superposition of singlets, within the same picture, it is instructive to have a look at the what a delocalized spin flip state in Eq(5.28) and its overlap with eigenstates in Eq(5.36) correspond to. We start by looking at the state corresponding to a 'localized spin' flip induced at position i on the groundstate. In Fig(5.2) we show an illustration of such a state. The spin flip breaks the singlets seperated by τ_i , into a $|\uparrow\uparrow\rangle$ state where the up spins are separated by τ_i and we refer to them as individual 'spinons'. The coefficients A_m, A_n corresponding to τ_m, τ_n depend on the ground state wave function. We can work with a translational invariant version of this state that is induced through S_q^+ , but for simplicity lets stick to the position representation.

$$\begin{aligned}
 S_i^+ P_G |\psi_{GS}\rangle &= S_i^+ \left(\dots + A_m \left[\text{Diagram 1} \right] + \dots + A_n \left[\text{Diagram 2} \right] + \dots \right) \\
 &= \left(\dots + A_m \left[\text{Diagram 3} \right] + \dots + A_n \left[\text{Diagram 4} \right] + \dots \right)
 \end{aligned}$$

Figure 5.2 – An illustration of a localized transverse spin excitation S_i^+ induced at position i on the staggered flux ground state. The spin-liquid background is represented by blue dots.

Once a pair of spinons is created on a RVB background, they are free to move. The energy cost of the movement is dictated by the Heisenberg interaction. Each eigenvector of the Heisenberg Hamiltonian in the space of the Gutzwiller projected particle hole excitations, with a conserved energy and momentum, corresponds to a stable configuration of these separated spinons with a different RVB background and amplitudes. In Fig(5.3), we show an illustration of an eigen-state $|n, q\rangle$. Here as well, we ignore the translational symmetry of the system for illustrative purposes. The coefficients K_m are decided by the dynamics of the Hamiltonian.

$$|n, q\rangle = \left(\dots + K_m \left[\text{Diagram 1} \right] + \dots + K_n \left[\text{Diagram 2} \right] + \dots \right)$$

Figure 5.3 – An illustration of eigen-state $|n, q\rangle$ in particle-hole basis. To distinguish from a transverse excitation in Fig(5.2) the spin-liquid singlet background is represented by purple dots.

On the other hand if we have a look at a delocalized spin flip of separation τ_m , as can be seen from Fig(5.4), upon Gutzwiller projector we have a state where the spinons are separated by the specific vector τ_m . It originates from the part of the unprojected staggered flux wave function, that had a single double occupancy. Hence, the quantity $\langle i, \tau_m | n, q \rangle$ or its translational invariant Fourier component $\langle \tau_m, q | n, q \rangle$ 'roughly' estimates the contribution coming from a specific separation τ_m . We emphasize that it is a 'rough' estimate because the state $|i, \tau_m\rangle$ has a finite overlap with states having different spinon separation $\tau_n \neq \tau_m$, on account of the singlet background being non orthogonal. Since the RVB wavefunctions are non-orthogonal they are not a convenient representation to establish specific observables that would accurately determine the spinon-separation. Nevertheless, as shall be seen in subsequent sections the spinon separation distribution defined in Eq(5.41) adequately captures the qualitative features of a magnon to spinon transition. This exercise is provided only for illustrative purposes to motivate the utility of a delocalized spin flip state in estimating the spinon separation distribution.

$$|i, \tau_m\rangle = P_G c_{i+\tau_m}^\dagger c_{i\downarrow} \left(\sum_m A_m \left(\text{Diagram 1} \right) + \sum_m D_m \left(\text{Diagram 2} \right) + \dots \right)$$

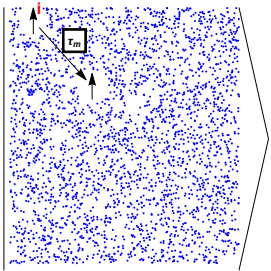
$= D_m$


Figure 5.4 – An illustration of delocalized spin flip induced on the Staggered flux state. After Gutzwiller projection, the delocalized spin flip yields a state with two up spins (spinons) on an RVB background. This state was derived from a state that contained a single double occupancy and a empty site in the staggered flux state.

Results

In this section, we present the results from numerical calculations on the excited state with induced transverse $\Delta S = 1$ excitations. Due to computational limitations we cannot carry

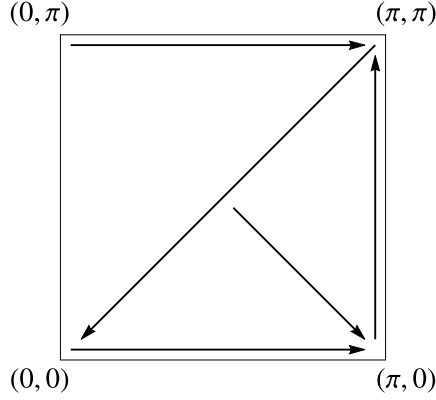


Figure 5.5 – The path in k-space along which the dynamical quantities are calculated.

out the calculations over the entire k-space. Hence, we perform our computations along the selected k-path $(\pi/2, \pi/2) \rightarrow (\pi, 0) \rightarrow (\pi, \pi) \rightarrow (0, 0) \rightarrow (\pi, 0)$ and $(0, \pi) \rightarrow (\pi, \pi)$ as illustrated in Fig(5.5). In the symmetric case the path $(\pi, 0) \rightarrow (\pi, \pi)$ is same as $(0, \pi) \rightarrow (\pi, \pi)$ due to mirror symmetry via the plane $(1, 1)$. In the asymmetric case however these two paths have different features. In all the upcoming figures where data is plotted along this k-path, the points $(\pi, 0)$ and $(0, \pi)$ have been separated by an empty region to avoid confusion.

As mentioned in previous sections, the eigen energies are derived by diagonalizing the Heisenberg Hamiltonian in the excitation subspace via Eq(5.11). Its intensity is related to the overlap of the corresponding eigenvector with a state that has S_q^+ excitation induced on the ground state ($S_q^+ |GS\rangle$). The dimension of the subspace for a given q vector is $L^2/2$, the number of k points in the MBZ. Hence we have $L^2/2$ energies at every q vector. We start by looking at the Density of states along the selected k-path which is given by:

$$\begin{aligned}
 D(q, \omega) &= \sum_n \delta(\omega - E_n^q + E_{GS}) \\
 &\simeq \sum_n \frac{1}{\sqrt{2\pi\sigma^2}} \exp \left[-\frac{1}{2} \left(\frac{\omega - E_n^q + E_{GS}}{\sigma} \right)^2 \right]
 \end{aligned} \tag{5.42}$$

where the delta function here, and in all the subsequent plots, has been approximated by a Gaussian function with a variance of $\sigma = 0.1J_x$. Starting from the symmetric case, as can be seen from Fig(5.6)(a), we have a continuous distribution of energies all the way up to $10J_x$ (and slightly beyond). At (π, π) and $(0, 0)$ we observe the un-physical negative energies. As we decrease the coupling ratio γ we observe that the upper bound of the energy distribution is lowered. At coupling ratio $\gamma = 0.1$, however, this trend is broken and we observe the energies being distributed all the way up to $10J_x$ and a large number of eigenstates with negative energies all over the q space. This particularly concerning feature turned out just to be a finite size effect (linked to the boundary condition), as the corresponding density of states

for a periodic boundary condition(PBC-ABC) in Fig(5.7), shows a well contained energy distribution. It must be noted that the eigen energies in themselves are not the representation of the dynamical features, and one has to have a look at the spectral weight (or intensity) and as will be shown in later sections, most of the high energy modes do not carry any spectral weight.

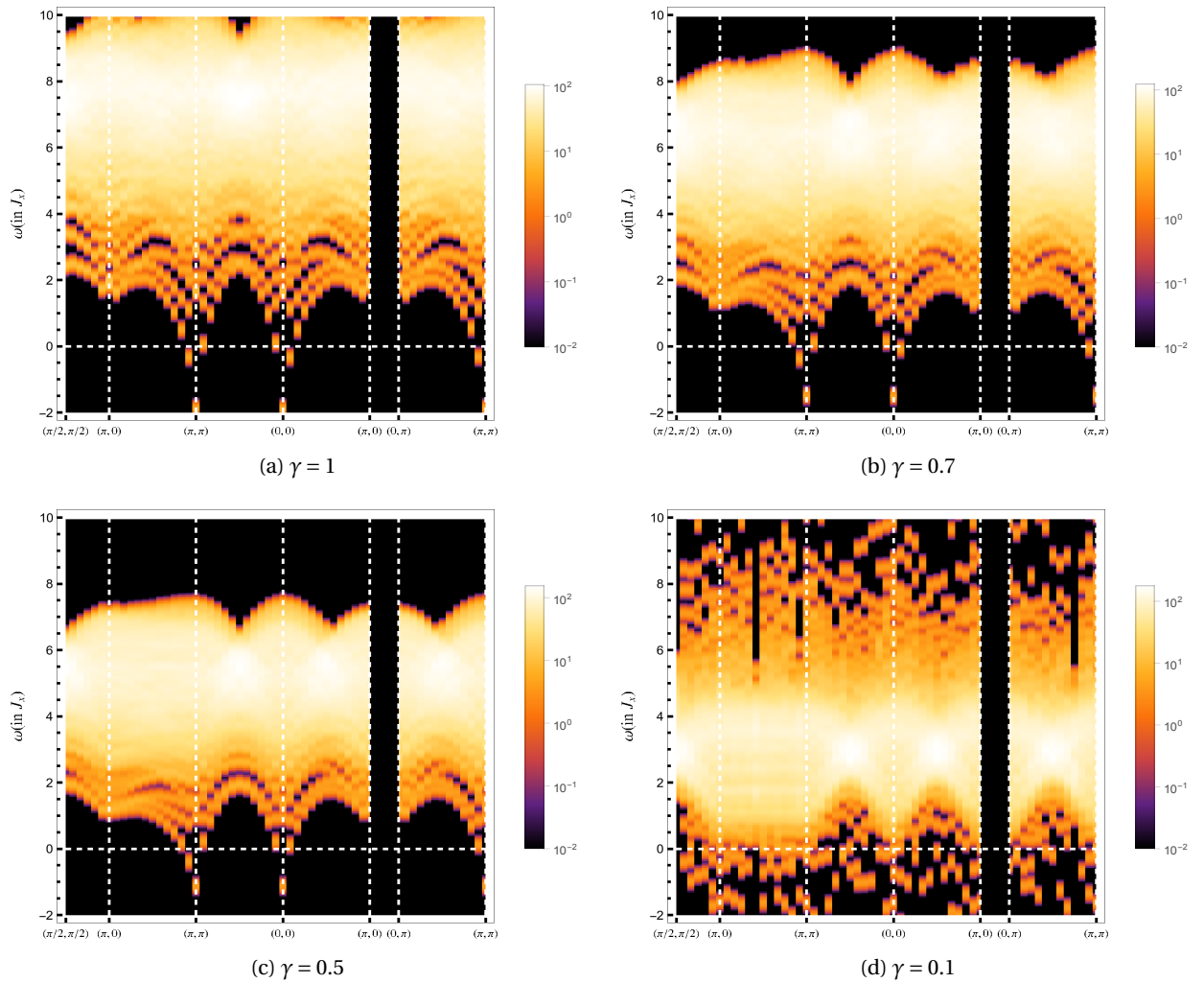


Figure 5.6 – Density of states $D(q, \omega)$ as defined in Eq(5.42) at different γ values for Anti-periodic boundary condition.

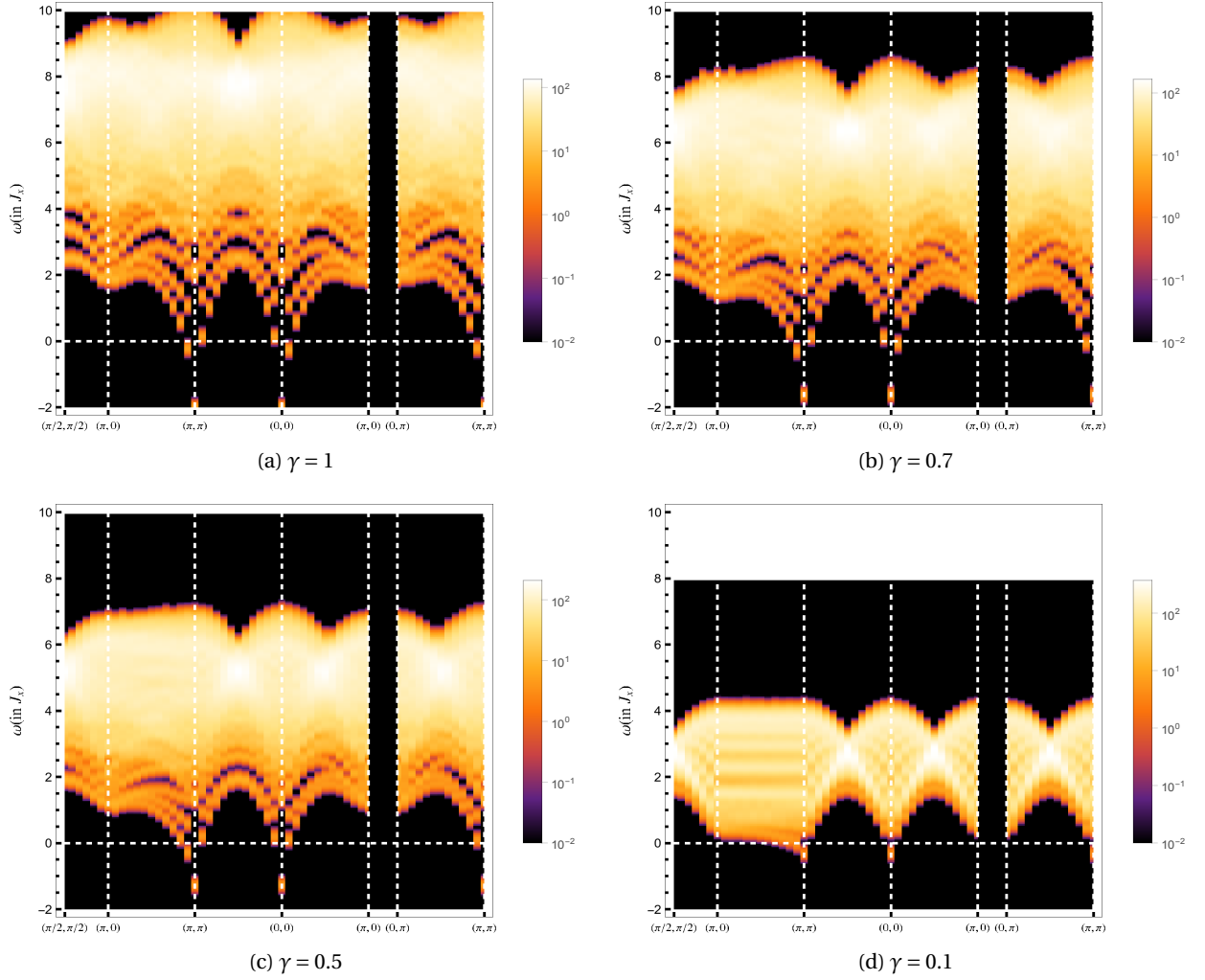


Figure 5.7 – Density of states $D(q, \omega)$ as defined in Eq(5.42) at different γ values for Periodic boundary conditions.

Quasi-1D

To have a clear picture close to 1D, apart from the coupling ratios $\gamma = 0.1 - 1$ in steps of 0.1, we performed additional calculations for TDSF at $L = 24$ and $\gamma = 0.05, 0.15$. We start our discussion by having a look at the lowest coupling ratio in our analysis $\gamma = 0.05$. At system size $L = 24$, we compare the q-sector in the x-direction (at $k_y = 0$) with the corresponding result from the Bethe ansatz. The eigen energies and corresponding q-vectors can be calculated via solving the Bethe self-consistency equations as described in chapter 2. These are the two spinon contributions. To estimate the TDSF for Bethe ansatz we use Algebraic Bethe ansatz with mathematical expressions taken from the work of [Caux et al. (2005)].

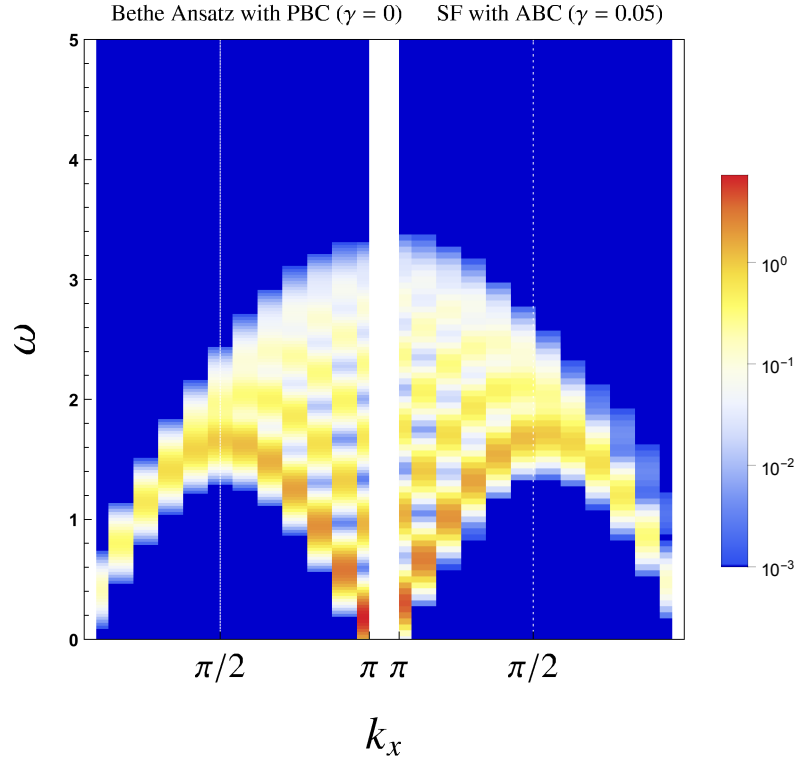


Figure 5.8 – TDSF at $\gamma = 0$ from Algebraic Bethe ansatz (with PBC) (left) and $\gamma = 0.05$ (right) obtained from the simulation of the staggered flux state (with ABC). The structure factor from Algebraic Bethe ansatz has been normalized such that $\int \frac{dk}{N} \int d\omega S^{-+}(q, \omega) = \frac{1}{2}$.

As can be seen from Fig(5.8), we observe that the excitation spectra at $\gamma = 0.05$ closely resemble the 1D TDSF calculated from Algebraic Bethe ansatz. The overall spectrum is slightly higher in energy owing to a finite γ . A few observable features include, a small visible continuum evolving particularly close to $k_x = 0$ and a small loss in spectral weight in the low energy mode near $k_x = \pi$. These features are more clearly visible in Fig(5.10).

Fig(5.9) shows the full spectrum along the selected k path for $\gamma = 0.05, 0.1, 0.15, 0.2$ which we refer to as the 'quasi-1D' region. At $\gamma = 0, 0.15, 0.2$ we also show the renormalized spin wave spectrum obtained from chapter 3. We observe a gradual evolution of the structure factor as we increase the coupling ratio. Except for the low energy mode, the structure factor along the y direction $(\pi, 0) \rightarrow (\pi, \pi)$ is almost dispersion less indicating that the high energy modes are roughly 1D. We also observe that the low energy mode in this direction gradually evolves towards the unphysical negative energy at (π, π) , previously observed in the symmetric case.

Restricting ourselves to the spectrum along the x direction i.e $k_x = 0 \rightarrow \pi$ for $k_y = 0$, we observe that at q -points $k_x \sim 0, \pi$ the spectral weight is redistributed to higher energies whereas at other q -points we observe the high energy modes gradually losing the spectral weight. These effects are clearly visible in Fig(5.10) where we show the evolution of energy cuts at fixed q_x

values $q_x = \pi/12, \pi/2, \pi$ for $q_y = 0$ with increasing γ . We also plot the corresponding energy cuts at $\gamma = 0$ obtained from algebraic Bethe ansatz. Also shown(right column) are the energy cuts at same q_x points but with $q_y = \pi$.

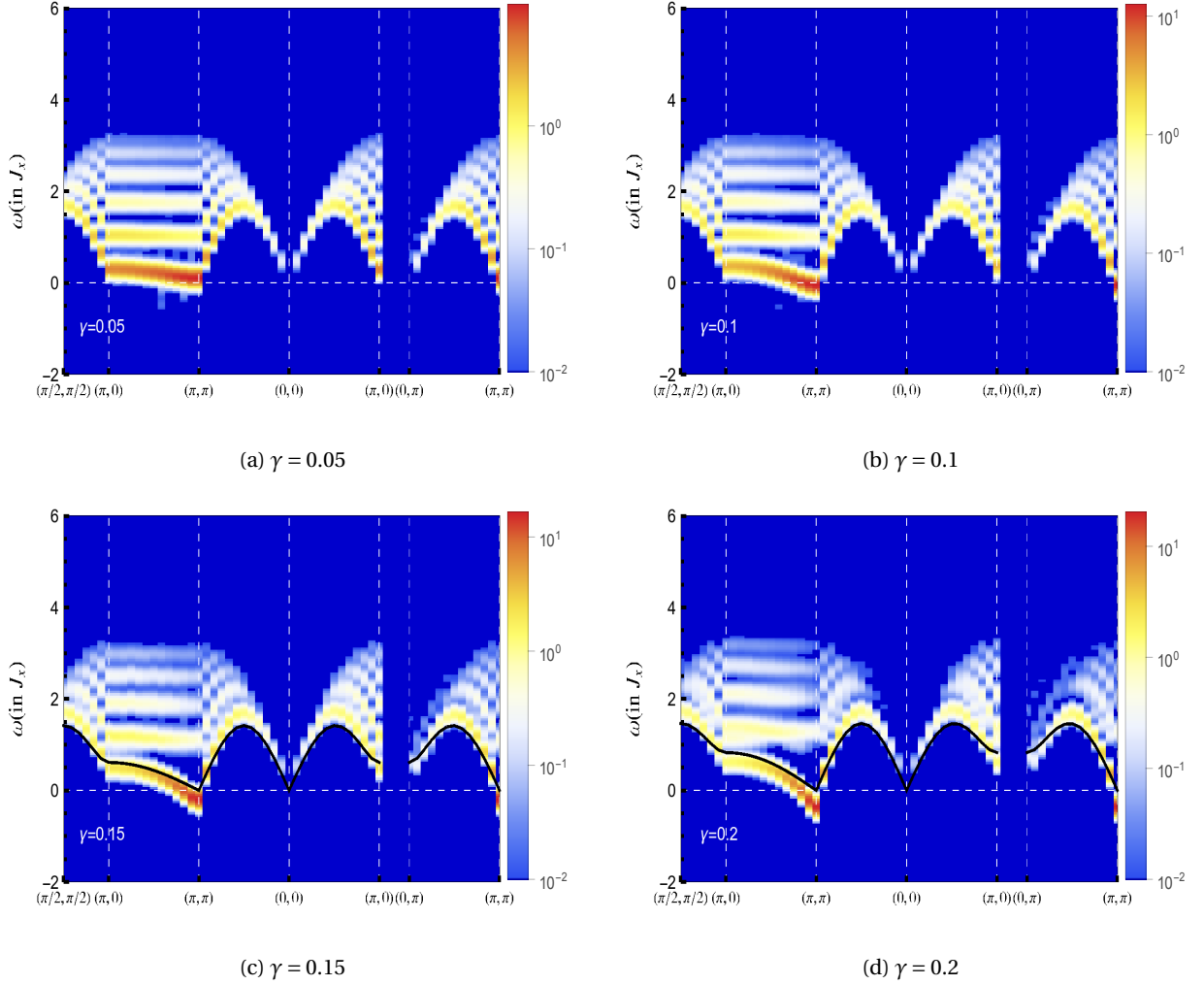


Figure 5.9 – TDSF of staggered flux state (with ABC)for different gamma values $\gamma = 0.05, 0.1, 0.15, 0.2$ corresponding to the quasi-1D region. At $\gamma = 0.15, 0.2$ the black line represents the self-consistent spin wave result obtained from chapter 3.

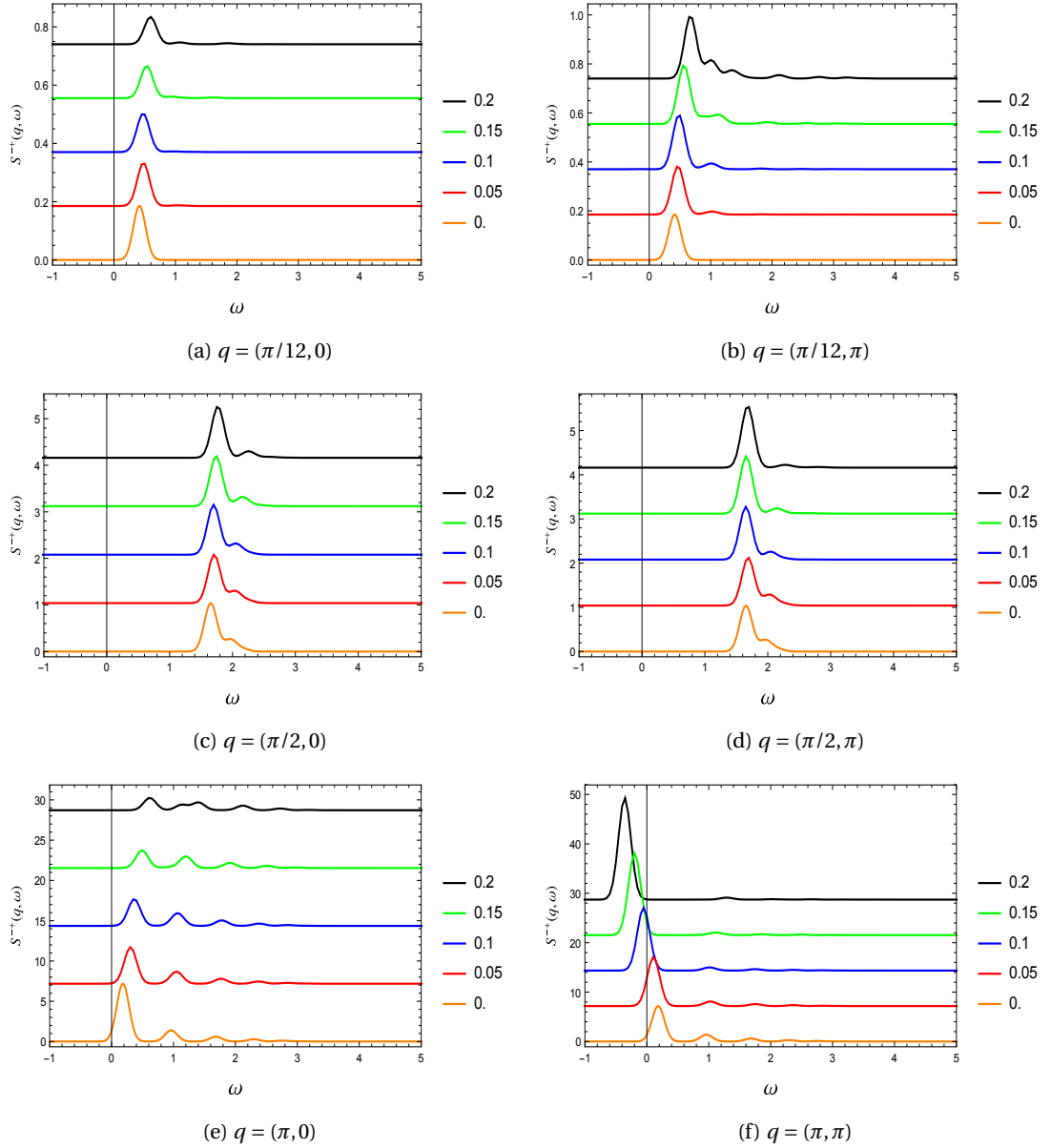


Figure 5.10 – TDSF of staggered flux state (with ABC) at k-points $k_x = \pi/6$ (top), $\pi/2$ (middle), π (bottom) at $q_y = 0$ (left), π (right) for $\gamma = 0.05, 0.1, 0.15, 0.2$, corresponding to quasi-1D region.

The main focus of our research revolves around the distinction between magnon and spinon features in the excitation spectrum. Magnon excitations are characterized by sharp modes whereas spinons exhibit a continuum. Since we expect our excitation spectrum to evolve from a continuum to sharp modes as we increase γ , one feature we can focus on is the gain/loss of the spectral weight from the peak with highest intensity. This of course underlies an assumption that the peak with the highest intensity becomes the magnon mode. Looking at Fig(5.10), at least at small coupling ratios, this appears to be a valid assumption. The peak

with highest intensity is also the one with lowest energy (also the closest to the spin wave estimate at $\gamma = 0.15, 0.2$).

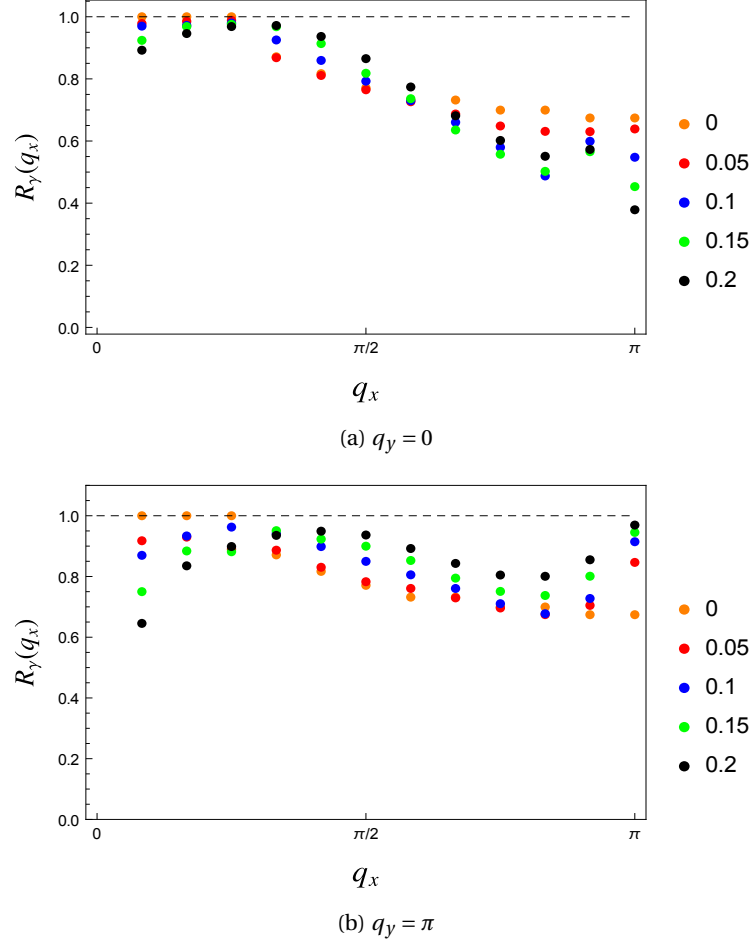


Figure 5.11 – Proportion of spectral weight in the low energy mode as defined in Eq(5.43) vs q points along x-direction $q_x = 0 \rightarrow \pi$ for $q_y = 0$ (top), π (bottom), for coupling ratios $\gamma = 0.05, 0.1, 0.15, 0.2$ corresponding to the quasi-1D region for ABC.

To accurately quantify the gain/loss in spectral weight we first define a quantity that calculates the proportion of spectral weight in the lowest energy mode

$$R_\gamma(q_x) = \frac{\sum_{\omega_0 - \delta < \omega_n < \omega_0 + \delta} S^-(q_x, \omega_n)}{\sum_n S^-(q_x, \omega_n)} \quad (5.43)$$

where ω_0 is the energy corresponding to the eigenvector with highest intensity and we include the intensities of eigenvector with energies in a neighborhood of $\delta = 0.1J$ around ω_0 . In Fig(5.11a) we plot this ratio at $k_y = 0$ as a function of k_x in the quasi-1D region. We also plot the values obtained from algebraic Bethe ansatz. The proportion of spectral weight of the low energy mode gradually decreases as we move from $q_x = 0$ to $q_x = \pi$. This is an obvious result

as proportion of continuum gets larger as we move towards $q = \pi$ in the 1D solution, and we expect to see similar pattern at small coupling ratios. On the other hand the trend of evolution shows that close to $q_x = \pi/2$ proportion of spectral weight in the low energy peak starts to increase indicating that the excitations around this point start to become more magnon like. The points around $q_x = 0, \pi$, however, exhibit a larger proportion of spectral weight being shifted into the high energy peaks as we increase coupling ratio. The trend at $q_x = \pi$ is not surprising as we expect to see this continuum evolving towards the $(\pi, 0)$ anomaly. The trend near $q_x = 0$, however is a new observation and as shall be seen while analyzing the spinon separation we observe similar features. At $q_y = \pi$ we observe a quite different pattern. The points close to $q_x = 0$ exhibit a similar trend and a greater shift of spectral weight from low energy mode to high energies. This is expected as it would gradually evolve into the $(0, \pi)$ anomaly. The point $q_x = \pi/2$ exhibits a similar pattern as well, with low energy peaks gaining spectral weight. However, $q_x = \pi$ shows an increase in spectral weight of the low energy peak quite different from the observation at $(0, 0)$. It must be remembered that $q = (\pi, \pi)$ is the point where we observe the unphysical negative energies and our wavefunction fails. Hence we do not pay serious attention to the trend at this point.

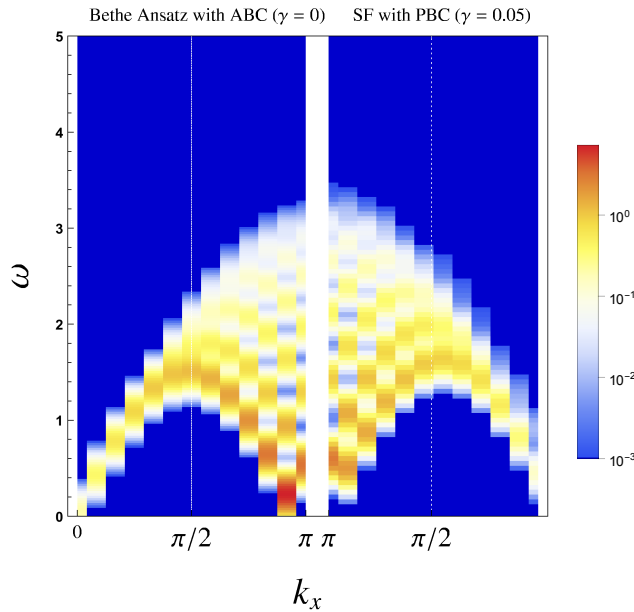


Figure 5.12 – TDSF at $\gamma = 0$ from Algebraic Bethe ansatz (with ABC) (left) and $\gamma = 0.05$ (right) obtained from the simulation of the staggered flux state (with PBC). The structure factor from Algebraic Bethe ansatz has been normalized such that $\int \frac{dk_x}{N} \int d\omega S^{-+}(q, \omega) = \frac{1}{2}$.

So far, for the analysis at small coupling ratios, we have made the comparison of Bethe ansatz with periodic boundary condition, and staggered flux with Anti-periodic boundary condition which we have seen to be equivalent from chapter 4. From chapter 4, we also know that the staggered flux with periodic boundary condition is comparable to the Bethe ansatz with Anti-periodic boundary conditions. Assuming this equivalence, we perform a similar analysis

as above, in case of the periodic boundary. The results are shown in Fig(5.12),Fig(5.13) and Fig(5.14). The lowest coupling ratio $\gamma = 0.05$ as shown in Fig(5.12) has a TDSF quite similar to the Bethe ansatz with ABC. It even captures the feature where lowest energy mode is slightly shifted away from $q_x = \pi$. All the major features mentioned in the ABC case are also seen in the PBC case.

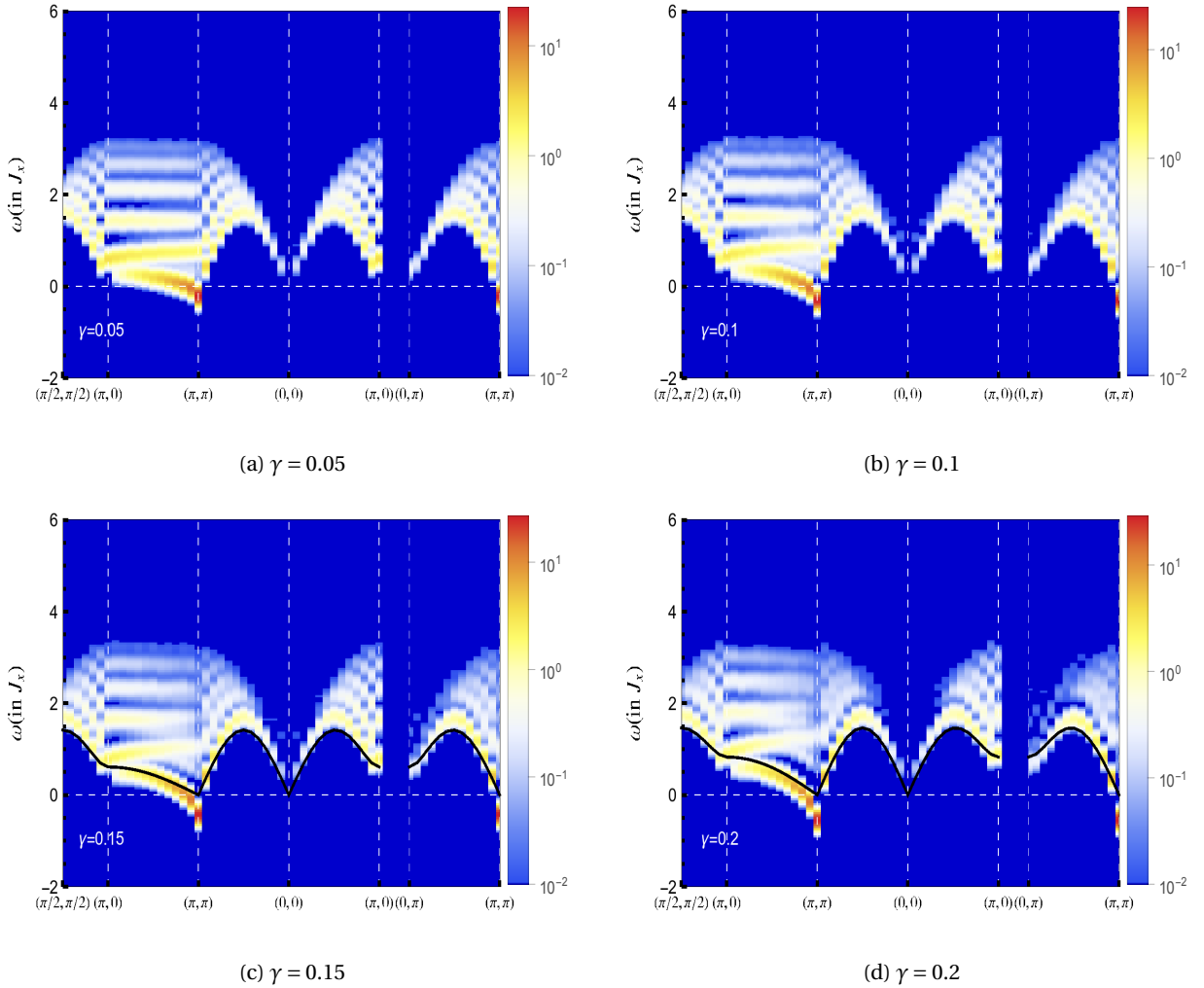


Figure 5.13 – TDSF of staggered flux state with PBC for different gamma values $\gamma = 0.05, 0.1, 0.15, 0.2$ corresponding to the quasi-1D region. At $\gamma = 0.15, 0.2$ the black line represents the self-consistent spin wave result obtained from chapter 3.

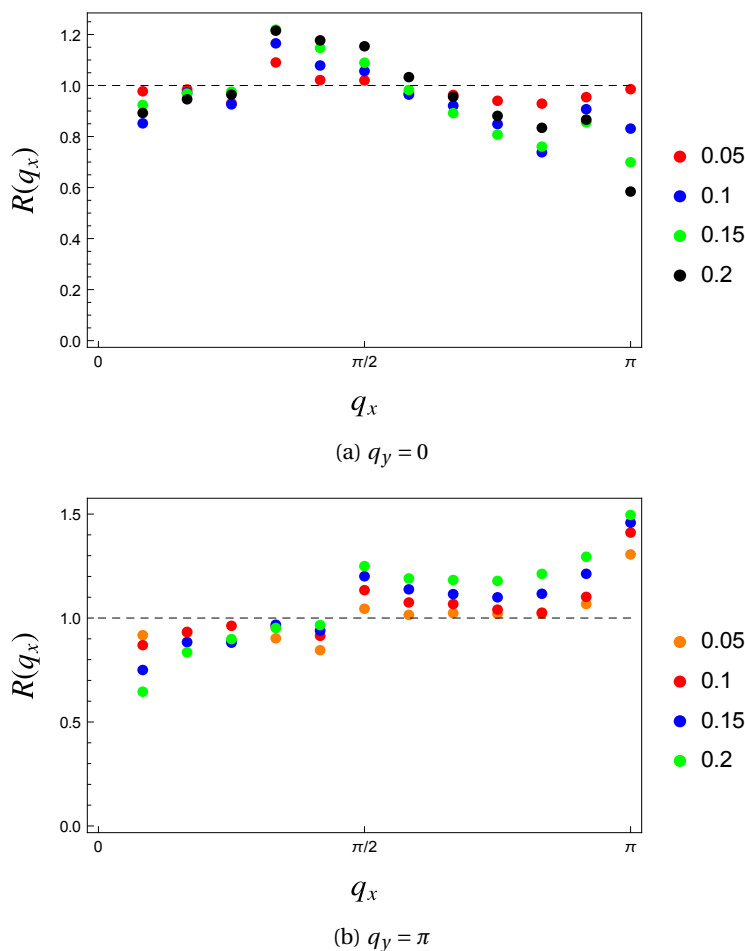


Figure 5.14 – Proportion of spectral weight in the low energy mode as defined in Eq(5.43) vs q points along x-direction $q_x = 0 \rightarrow \pi$ for $q_y = 0$ (top), π (bottom), for coupling ratios $\gamma = 0.05, 0.1, 0.15, 0.2$ corresponding to the quasi-1D region for PBC.

Rectangular lattice

Moving on to larger coupling ratios, we proceed to calculate the structure factor for coupling ratios $\gamma = 0.3 - 1$ in steps of 0.1 for both boundary conditions. In Fig (5.15) we show the data corresponding to coupling ratios $\gamma = 0.3, 0.5, 0.8, 1$ for staggered flux with ABC. We observe that the gap between the main magnon like peak and the high energy modes gradually increases as we move towards the symmetric case. This happens everywhere in the q space, except near the $(\pi, 0)$ and $(0, \pi)$ symmetry points, where the high energy modes lie closer to the magnon peak. We also observe that the spectral weight of the high energy modes gradually decreases with increase in coupling ratio. Also, we see a good agreement between the re-normalized spin wave dispersion (from chapter 3) and the lowest energy mode. Sizable deviations are observed near $(\pi, 0)$ point, where the continuum of excitations still exhibits a significant spectral weight and the (π, π) zone where the negative energies are observed. As mentioned previously the

Chapter 5. Staggered flux:Excited State

(π, π) anomaly is linked to the fact that our assumed groundstate ansatz is not be the exact ground state. The feature observed at $(\pi, 0)$ or $(0, \pi)$ is rather interesting where we observe a significant departure from the ordinary spin wave result. This is the exact feature, which in the symmetric case, Dalla Piazza et al linked to the experimentally observed continuum from the experiments of Ronnow et al. The extension of the Staggered flux solution to rectangular lattices provides us with a smooth gradual evolution of the transverse structure factor from isotropic($\gamma = 1$) to 1D($\gamma = 0$) case. We also present the structure factor corresponding to the periodic boundary condition in Fig(5.16), which shows similar features as its anti-periodic counterpart with a few minor deviations, that shall become clear in finite size analysis.

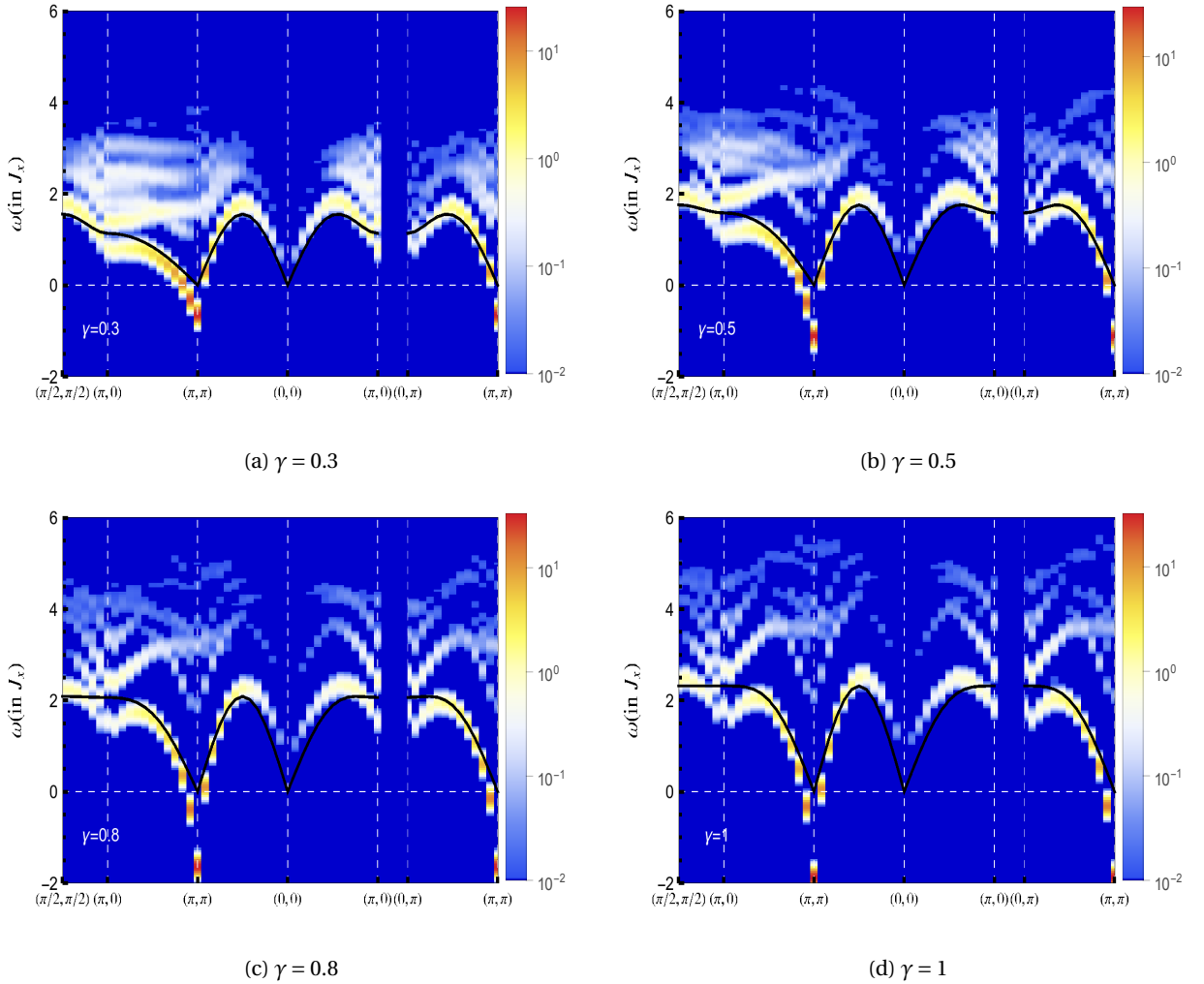


Figure 5.15 – TDSF of staggered flux state(with ABC) for different gamma values $\gamma = 0.3, 0.5, 0.8, 1$. The self consistent spin-wave result from chapter 3 is indicated by the black line.

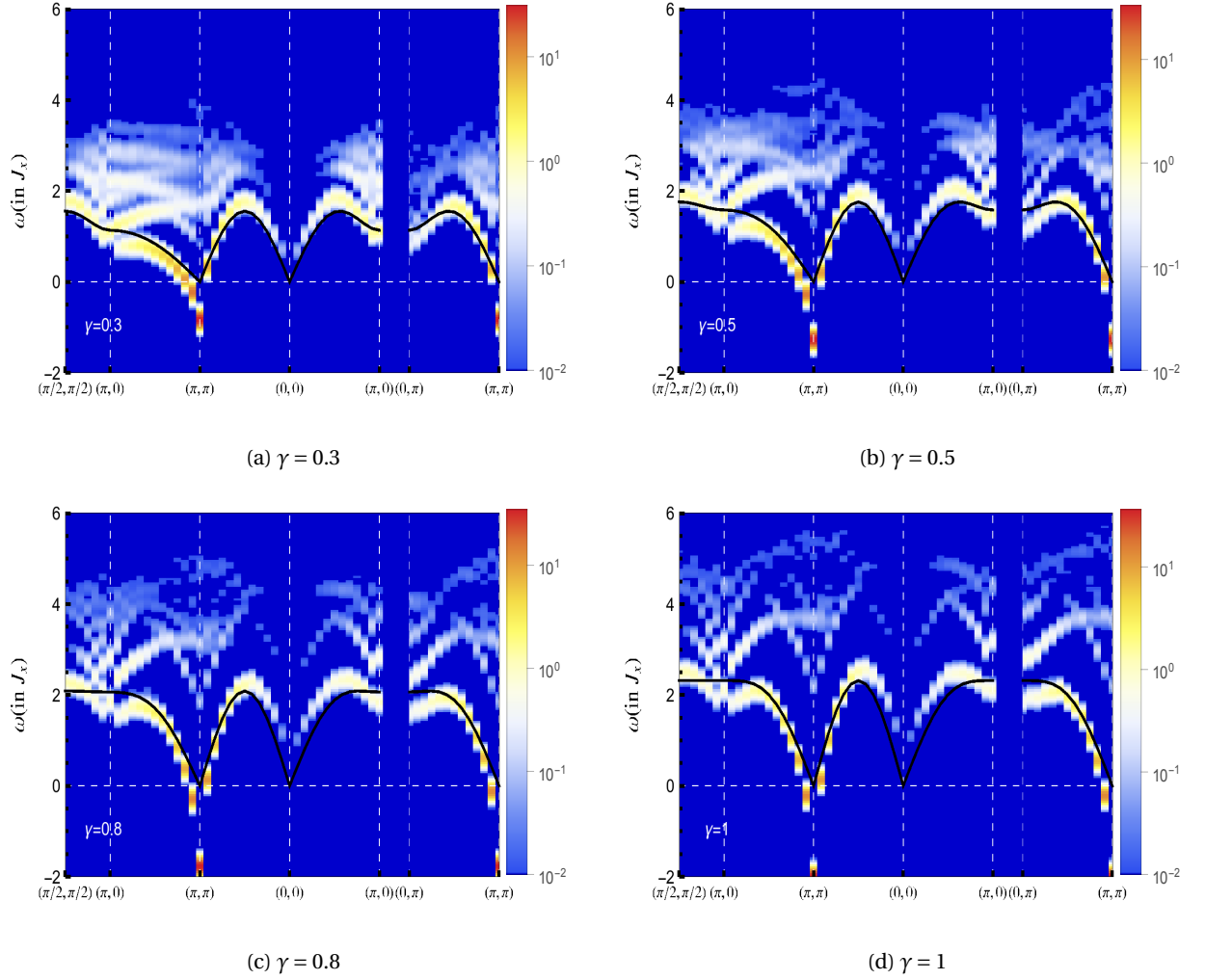


Figure 5.16 – TDSF of staggered flux state (with PBC) for different gamma values $\gamma = 0.3, 0.5, 0.8, 1$. The self consistent spin-wave result from chapter 3 is indicated by the black line.

Finite size analysis

Since we work on finite system sizes, the expected continuum at higher energies appears as a set of discrete modes. Hence, it is instructive to observe the gradual evolution of the TDSF with increasing system size. Unlike the case of the groundstate energy, through the finite size analysis, we do not aim to estimate a converging $L = \infty$ values of a single observable. Instead, we look for the trend where by we observe additional modes as we increase the system size L , which eventually is expected to become a continuum of excitations. We also have a look at both PBC and ABC boundary conditions to look for convergence in the low energy peak. Due to computational limitations we performed our calculations only at high symmetry points $(\pi, 0), (0, \pi)$ and $(\pi/2, \pi/2)$ which should be able to capture the overall trend of the spectrum. The highest system size we work with is $L = 28$.

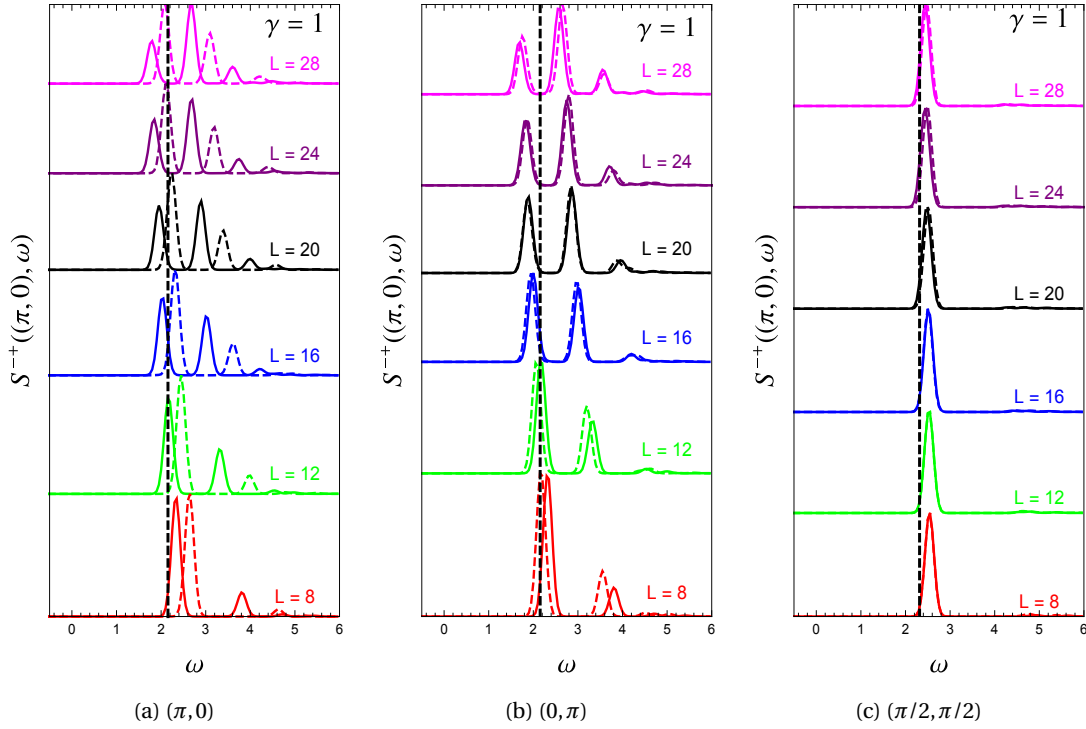


Figure 5.17 – Evolution of TDSF for $\gamma = 1$, at q-points $(\pi, 0)$ (a), $(0, \pi)$ (b) and $(\pi/2, \pi/2)$ (c) as we increase system size. The solid line represents ABC and dashed line represents the PBC. The dashed vertical line indicates the energy of the self-consistent spin wave result from chapter 3 along with a 7% reduction at $(\pi, 0)$ and $(0, \pi)$.

Starting with the symmetric case $\gamma = 1$ in Fig(5.17), we observe that the spectrum at $(\pi, 0)$ and $(0, \pi)$ is very similar for ABC boundary condition (solid lines) (ignoring statistical errors). For PBC (dashed lines) boundary condition (PBC-ABC), however, we see a different spectrum compared to ABC for $(\pi, 0)$ but not for $(0, \pi)$. As we increase system size we gradually observe additional modes at high energies for both boundary conditions. This is quite different from the point $(\pi/2, \pi/2)$ where we observe essentially only a single mode for all system sizes. For comparison, we also show the energy corresponding to the spin wave theory (from chapter 3) indicated by the dashed line, along with the expected 7% energy reduction at $(\pi, 0)$ and $(0, \pi)$. As can be seen, the lowest peak of $(\pi, 0)$ and $(0, \pi)$ modes at ABC approach the expected value at $L = 12$ but undergoes further reduction at higher system size. It also starts losing the spectral weight and the next peak gains spectral weight. This effect was noted by Dalla Piazza et al. as well, and they propose that following the trend as we move to higher system sizes the first peak should lose all the spectral weight and the second peak should approach the expected result. Thanks to the PBC result we have a further validity of this proposal as the PBC result does not show this peak reversal and the low energy peak is reasonably close to the expected result. Hence, the low energy peak observed in ABC case is just an effect of the boundary condition and is expected to vanish as the system size increases.

Moving to smaller coupling ratios we continue to observe a similar pattern, where number of additional modes at high energies increases with system size. At $\gamma = 0.5$ (Fig 5.18), for example both ABC and PBC spectra show that the $(\pi, 0)$ and $(0, \pi)$ modes exhibit more and more high energy modes and the $(\pi/2, \pi/2)$ still exhibits a single peak and a very good convergence between ABC and PBC results. Contrary to the $\gamma = 1$ case, both ABC and PBC spectra show different spectra at $(\pi, 0)$ compared to $(0, \pi)$. This is not a surprising result as we are in an asymmetric situation and $(\pi, 0)$ and $(0, \pi)$ are expected to exhibit different spectra. The surprising aspect is the difference between ABC and PBC spectra at each of these points. Along $(\pi, 0)$, for example, the ABC spectrum and PBC spectrum both show similar effect as $\gamma = 1$. At $(0, \pi)$, however, we do not see a similar spectrum, as observed at $\gamma = 1$. The PBC spectrum undergoes the same transition as the $\gamma = 1$ case. The ABC spectrum on the other hand does not show the peak reversal like the PBC counterpart. We cannot conclusively say if the ABC spectrum is just lagging behind in terms of the peak reversal compared to the PBC result, but the general trend seems to suggest this.

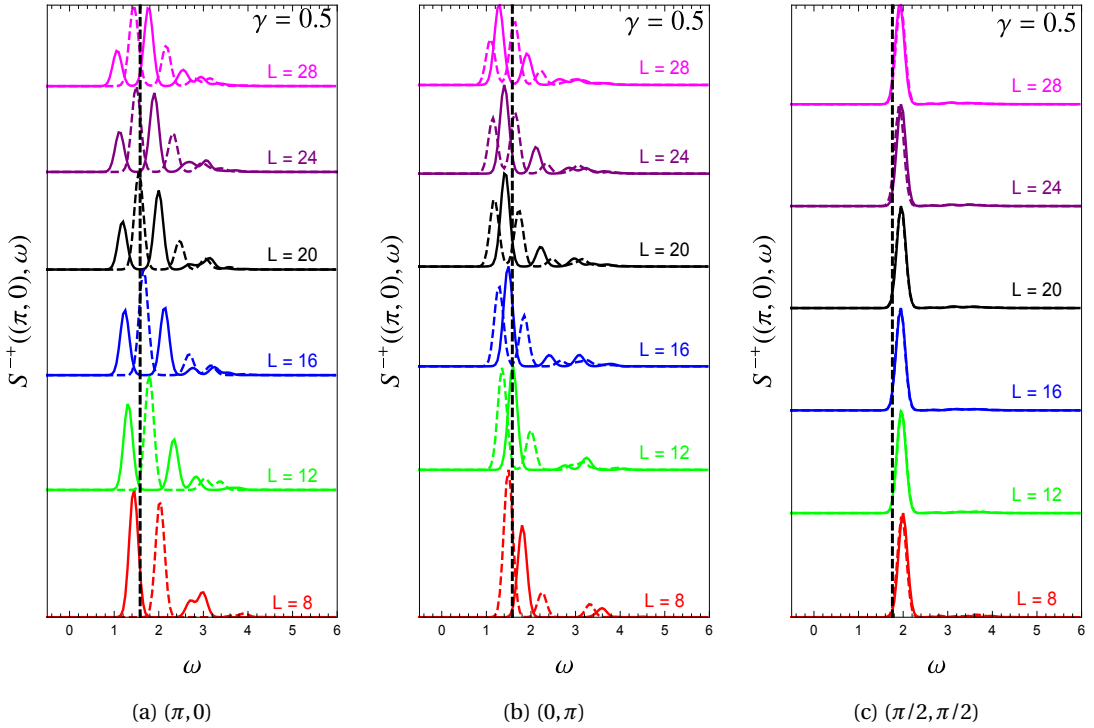


Figure 5.18 – Evolution of TDSF(solid lines) for $\gamma = 0.5$, at q-points $(\pi, 0)$ (a), $(0, \pi)$ (b) and $(\pi/2, \pi/2)$ (c) as we increase system size. The solid line represents ABC and dashed line represents the PBC. The dashed vertical line indicates the energy of the self-consistent spin wave result from chapter 3.

In case of $\gamma = 0.1$ as shown in Fig(5.19), we progressively see more and more energies at large system size and low energy mode getting closer at $(\pi, 0)$ an expected trend that is similar to what Bethe ansatz shows. At $(0, \pi)$ we see a single mode that gets slightly closer to zero energy

Chapter 5. Staggered flux:Excited State

as we increase the system size. The trend seen in the intensity is the consequence of the effect we saw in Chapter 4, where the ABC chains exhibited weak correlations compared to *PBC* chains at small system sizes which progressively get stronger large system size. The $(\pi/2, \pi/2)$ has a small continuum apart from a sharp mode indicating the emergence of spinons.

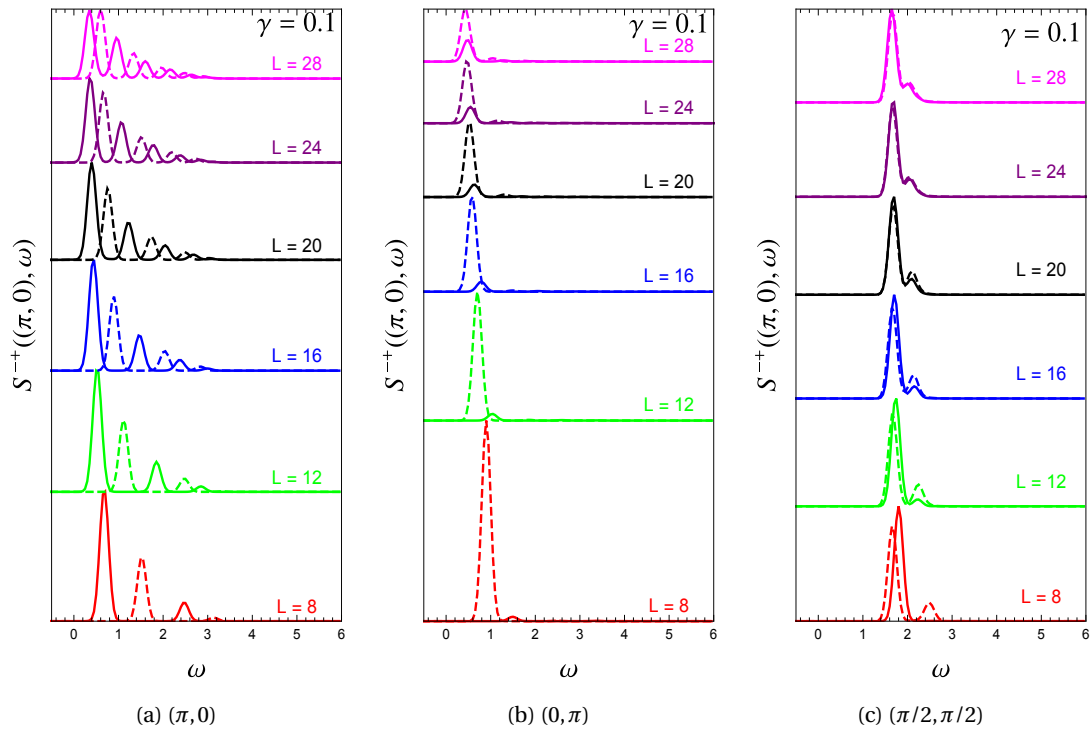


Figure 5.19 – Evolution of TDSF(solid lines) for $\gamma = 0.1$, at q-points $(\pi, 0)$ (a), $(0, \pi)$ (b) and $(\pi/2, \pi/2)$ (c) as we increase system size. The solid line represents ABC and dashed line represents the PBC.

In Fig(5.20) and Fig(5.21), we show the evolution of TDSF at $(\pi, 0), (0, \pi)$ and $(\pi/2, \pi/2)$ for ABC and PBC, as we decrease γ at $L = 28$. At point $(\pi, 0)$ we see the low energy mode and the subsequent continuum moving to higher energies. If we ignore the lowest energy mode in the ABC that is expected to vanish at large system size, we see that the magnon like mode has around half of the total spectral weight at this q point for all γ , indicating that the continuum does not loose any spectral weight and just moves to higher energies. The overall intensity of the spectrum is decreasing as we increase the coupling ratio γ . This just reflects the shift of the spectral weight from a predominantly one dimensional spectrum at $\gamma \sim 0$ to a two dimensional spectrum at $\gamma \sim 1$ and qualitatively similar to the result from SWT. As expected we see an inverse effect at the $(0, \pi)$ point, where the overall intensity of the spectrum increases with increase in γ . Along with the gain in overall spectral weight, we gradually see a larger continuum as well. At the point $(\pi/2, \pi/2)$ apart from the low energy mode, we see a small additional mode near $\gamma = 0.1$ which initially moves towards higher energies, but gradually loses spectral weight, making the spectrum magnon like.

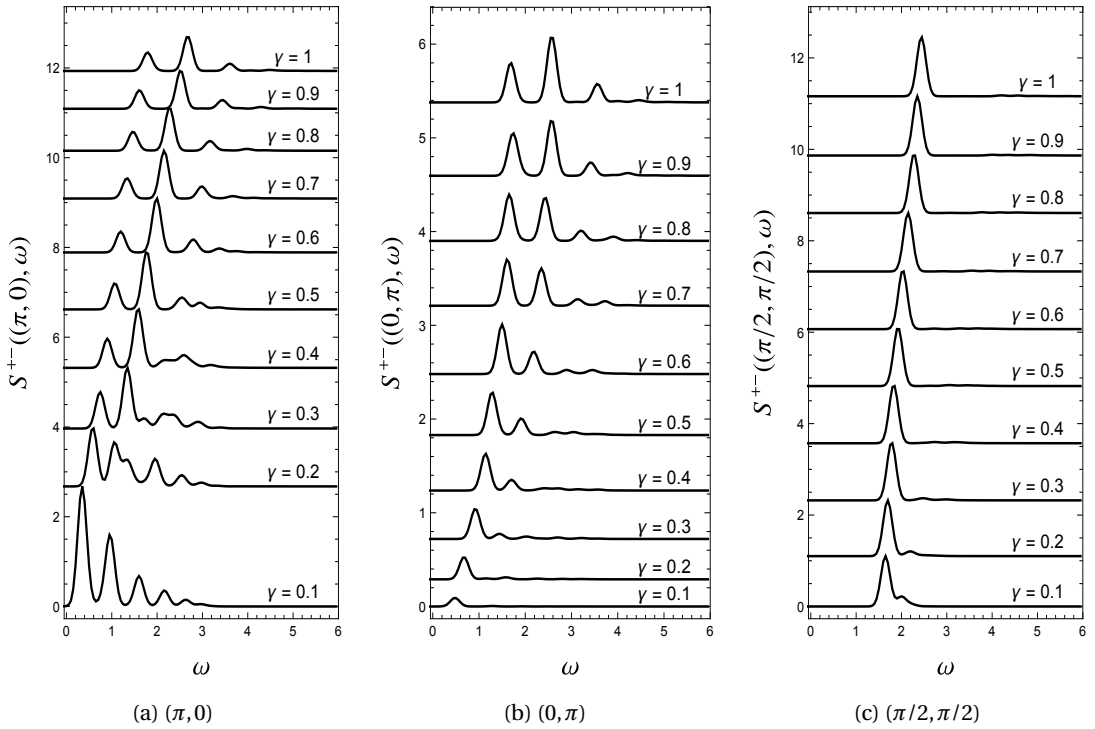


Figure 5.20 – Evolution of TDSF of staggered flux state (with ABC) with γ , for system size $L = 28$, at q -points $(\pi, 0)$ (left), $(0, \pi)$ (center) and $(\pi/2, \pi/2)$ (right)

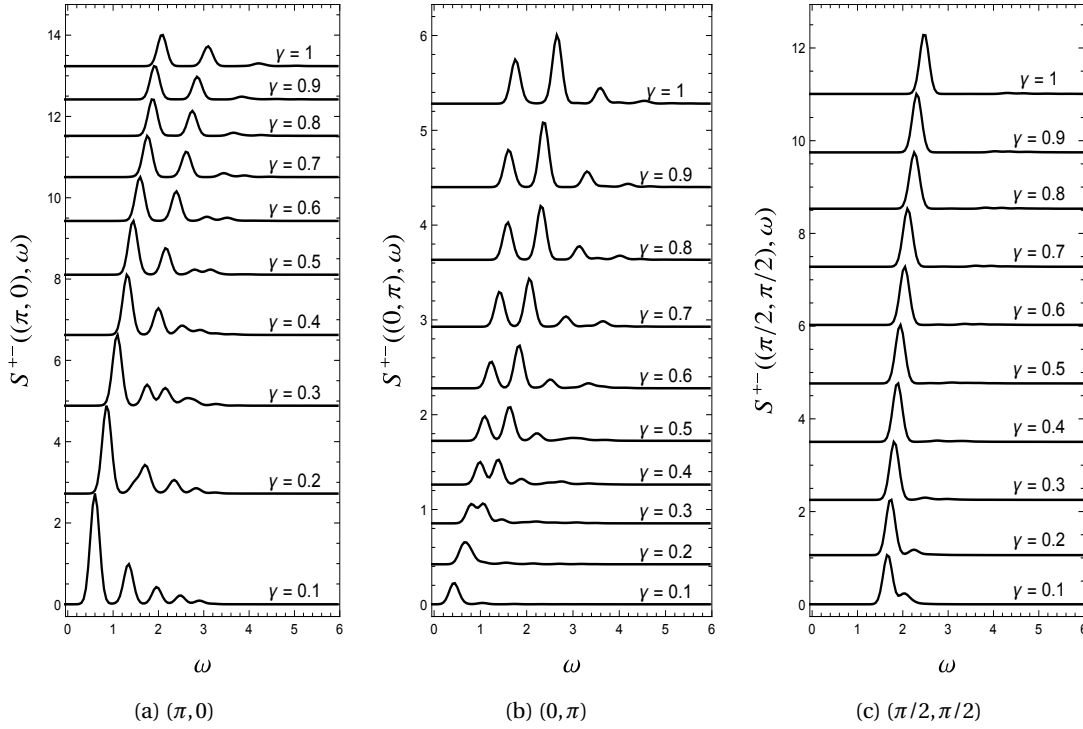


Figure 5.21 – Evolution of TDSF of staggered flux state (with PBC) with γ , for system size $L = 28$, at q-points $(\pi, 0)$ (left), $(0, \pi)$ (center) and $(\pi/2, \pi/2)$ (right)

Spinon pair separation

As mentioned in the theoretical framework, the quantity we estimate to understand the nature of excitations is the spinon-separation distribution given by:

$$\rho^q(r) = \frac{1}{\rho_0^q} \sum_n \frac{|\langle r, q | n, q \rangle \langle n, q | 0, q \rangle|^2}{\langle r, q | r, q \rangle} \quad (5.44)$$

where ρ_0 represents the normalization on a grid of $r_x, r_y \in \{-L/2, L/2\}, [-L/2, L/2]$ such that:

$$\sum_r \rho^q(r) = 1 \quad (5.45)$$

Compared to work of Dalla Piazza et al, this parameter has been normalized at each r (through denominator $\langle r, q | r, q \rangle$), not to be confused with normalization on a grid ρ_0^q . Starting with the symmetric case, in Fig (5.22) we show the map of $\rho^q(r)$ at two points $(\pi, 0)$ and $(\pi/2, \pi/2)$. As can be seen, the spinon pair separation distribution is more localized near the $(\pi/2, \pi/2)$ compared to the $(\pi, 0)$ point an indication of the more 'magnon' like character of the excitations at $(\pi/2, \pi/2)$ and 'spinon' like character of $(\pi, 0)$ excitations where the continuum is observed.

We also show the un-normalized distribution in Fig (5.22)(c,d). In the reminder of this section, we present the results corresponding to the normalized distributions.

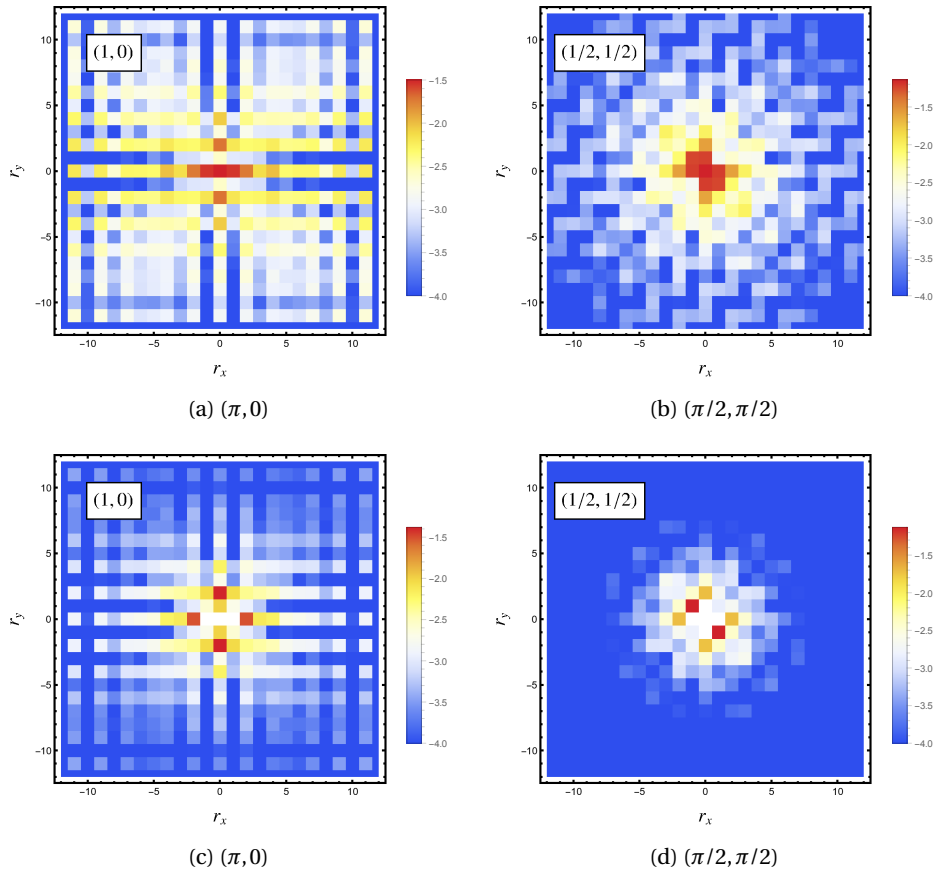


Figure 5.22 – Spinon pair separation distribution on a 24×24 grid in position space at q -points $(\pi, 0)$ (left) and $(\pi/2, \pi/2)$ (right). The normalized value is plotted in top row and the un-normalized quantity, presented in Dalla Piazza et al. is plotted in the bottom row.

A look at $\rho^q(r)$ for different boundary conditions also shows a few interesting features. As observed while calculating the instantaneous correlation function in chapter 4, for small coupling ratios, the PBC exhibited the chains to be strongly coupled compared to the ABC. This effect is evident in Fig(5.23) where we plot the spinon separation distribution $\rho^q(r)$ at $\gamma = 0.1$ for two points $(\pi, 0)$ and $(\pi/2, \pi/2)$. As can be seen, the distribution is fairly localized in y -direction for ABC compared to the PBC.

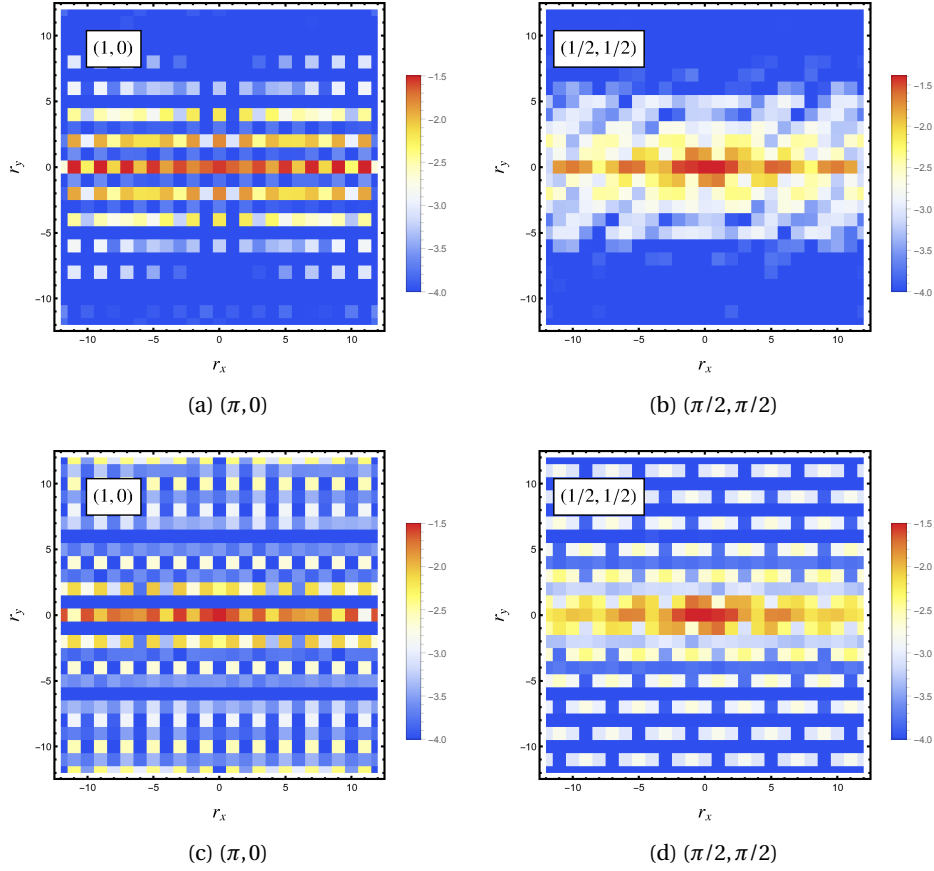


Figure 5.23 – Spinon pair separation distribution on a 24×24 grid in position space at q-points $(\pi, 0)$ (left) and $(\pi/2, \pi/2)$ (right). Top row corresponds to Anti-periodic and bottom corresponds to a system with periodic boundary.

To compare at various q we need a single quantity that parameterizes the distribution $\rho^q(r)$. An obvious choice would be the root mean square (RMS) spinon separation given by:

$$M(q) = \sqrt{\sum_r \rho^q(r)} \quad (5.46)$$

In Fig(5.24) we show the RMS spinon separation along the selected k-path for $\gamma = 1, 0.8, 0.3, 0.1$ for both boundary conditions. Starting with the symmetric case, $\gamma = 1$, we observe that the RMS separation has peaks around the high symmetry points $(\pi, 0)$, $(0, \pi)$, $(\pi/2, \pi/2)$. At $(0, 0)$, due to lack of finite intensity in TDSF, we could not estimate the spinon separation. The increase of spinon separation at $(\pi, 0)$, $(0, \pi)$ is not surprising as it was already mentioned in the work of Dalla Piazza et. al. The surprising aspect is the large spinon separation around $(0, 0)$ which is almost the same or greater than the RMS spinon separation at $(\pi, 0)$. This effect could be visualized in parallel to the comparison of TDSF at small coupling ratio with Bethe

ansatz in Fig(5.11), where spectral loss in the low energy peak was observed both at $q_x = 0$ and $q_x = \pi$ points. The spinon separation also exhibits a peak at (π, π) , but we abstain from discussing this q-point, since the TDSF exhibits unphysical negative energies here.

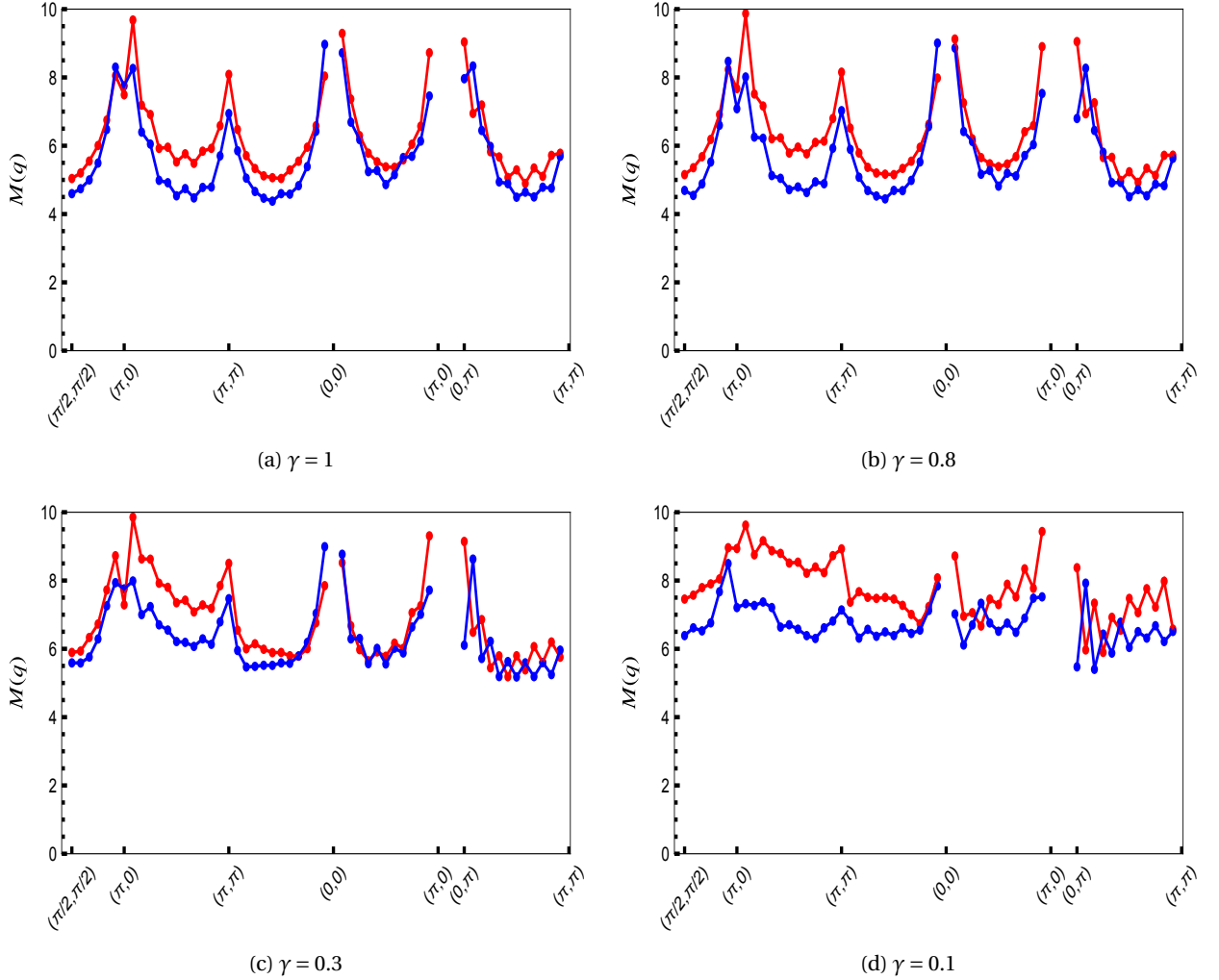


Figure 5.24 – Root mean square separation as defined in Eq(5.46) at various γ values. Anti-periodic boundary condition is represented by blue dots and Periodic boundary is represented by red dots.

As we move towards smaller coupling ratios we observe that the spinon separation at other q-points slowly starts moving towards the peak value. The spinon separation at $\gamma = 0.1$ is almost constant. This is not surprising since we expect the spinons to be well separated on average as we move towards 1D. This result provides validity for our notion of confined/de-confined spinon states existing at different q-points in the staggered flux solution. Comparison of results at different boundary conditions shows that there exists some difference between ABC and PBC results and the difference gets larger particularly at small coupling ratios. This is

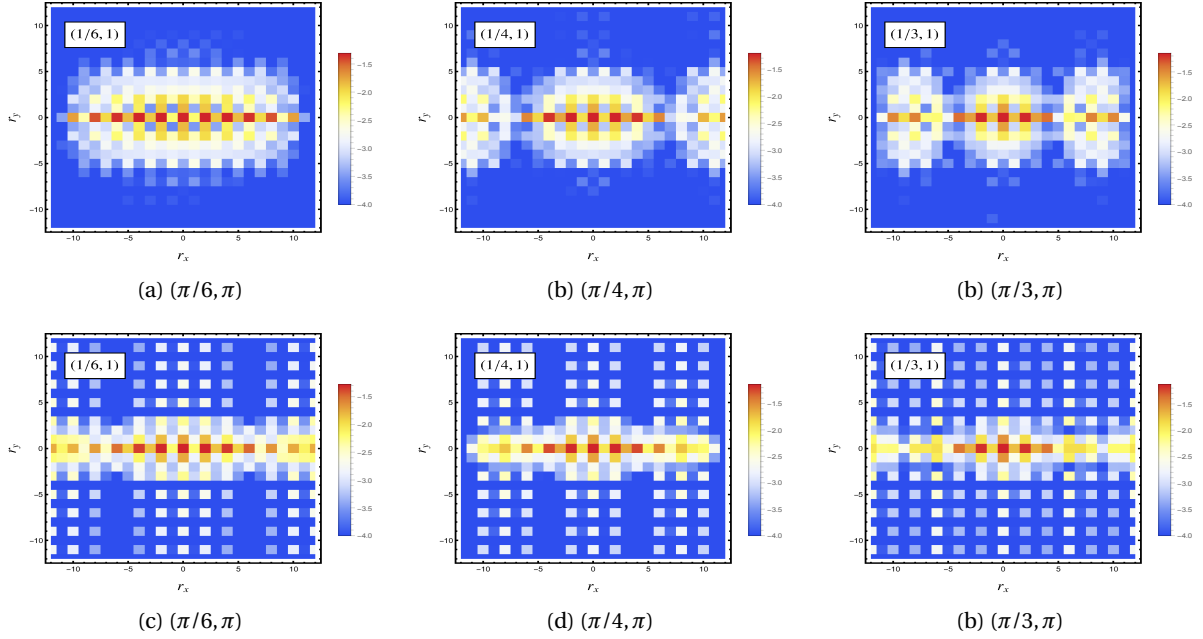


Figure 5.25 – Spinon separation at three neighboring q points $(\pi/6, \pi)$ (left), $(\pi/4, \pi)$ (middle), $(\pi/3, \pi)$ (right) for system with coupling ratio $\gamma = 0.1$. Top row corresponds to Anti Periodic boundary condition, and bottom corresponds to periodic boundary. The value at the boundary alternates between finite and zero ($< 10^{-4}$) as we move from one point to other which leads to the zig-zag pattern in RMS value. The trend is reversed for periodic boundary condition.

expected, since for finite system size we already observed the small coupling ratios to have significant difference between different boundary conditions. A peculiar feature of the RMS plot is the zig-zag like behavior observed at various places (for example $(0, \pi) \rightarrow (\pi, \pi)$). This is related to the r at the boundary which has significant contribution to the RMS value, and which hosts large spinon separation at at some alternating q -points as can be observed in Fig(5.25)(a). What is more interesting is that pattern along $q_y = 0 \rightarrow \pi$ for $q_x = 0$ follows the same pattern for both boundary conditions, but for $q_x = \pi$ we observe a reversal of the zig-zag pattern Fig(5.25)(b).

Although RMS spinon separation captures the essence of the magnon/spinon behavior at various q -values, in terms of magnitude(due to limited system size) it does not show a drastic difference between symmetric case and near-1D case. It is also heavily influenced by the r points at the boundary. For these reasons, we have a look at a different measure of the spinon separation which is the cumulative distribution function (CDF) of $\rho^q(r)$ in a disk of radius $r = L/2$ which is given by:

$$R_q(r) = \sum_{|r'| \leq r} \bar{\rho}^q(r') \quad (5.47)$$

where $\bar{\rho}^q(r')$ is $\rho^q(r)$ normalized such that:

$$\sum_{|r'| \leq L/2} \bar{\rho}^q(r') = 1 \quad (5.48)$$

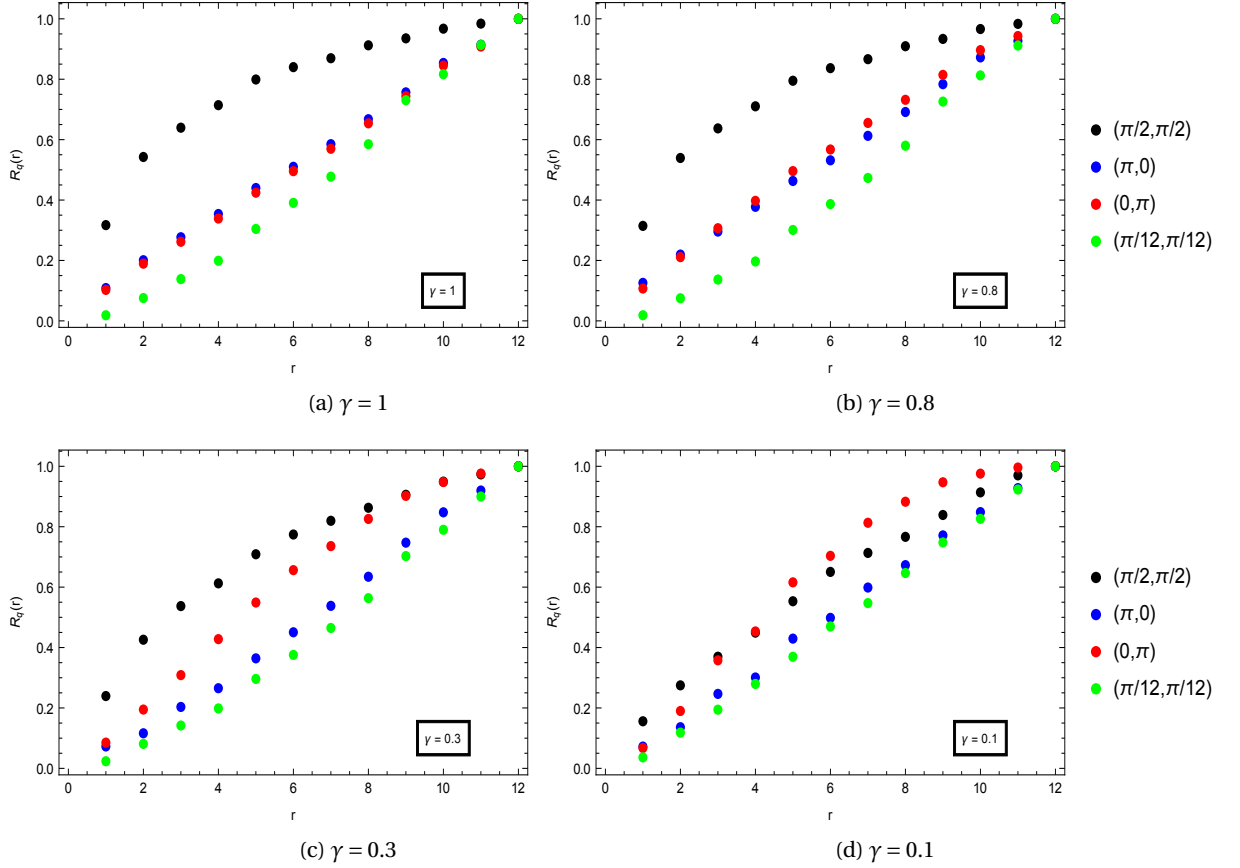


Figure 5.26 – CDF of spinon separation at q points $(\pi/2, \pi/2)$ (black), $(\pi, 0)$ (blue), $(0, \pi)$ (red), $(\pi/12, \pi/12)$ (green) for $\gamma = 1$ (top-left), $\gamma = 0.8$ (top-right), $\gamma = 0.3$ (bottom-left), $\gamma = 0.1$ (bottom-right) for a system with ABC.

A look at Fig (5.26) shows the CDF at high symmetry points. Since we cannot calculate spinon separation exactly at $(0, 0)$, we instead have a look at the closest point in the $(1, 1)$ direction i.e $(\pi/12, \pi/12)$. The comparison across various γ show that the points $(\pi, 0)$, $(0, \pi)$, $(\pi/12, \pi/12)$ have a more or less a linear CDF indicating that spread of the spinon-separation is nearly constant for any given r or that given a spinon at $r = 0$ probability of finding a spinon at distance r is proportional to $1/r$. At $(\pi/2, \pi/2)$ however, the distribution transitions from a linear dependance on r for $\gamma = 0.1$ to a more localized distribution for $\gamma = 1$ which clearly evidences a more magnon like behavior at this point as we increase the coupling ratio. Similar effects are seen in PBC as well (Fig(5.27)).

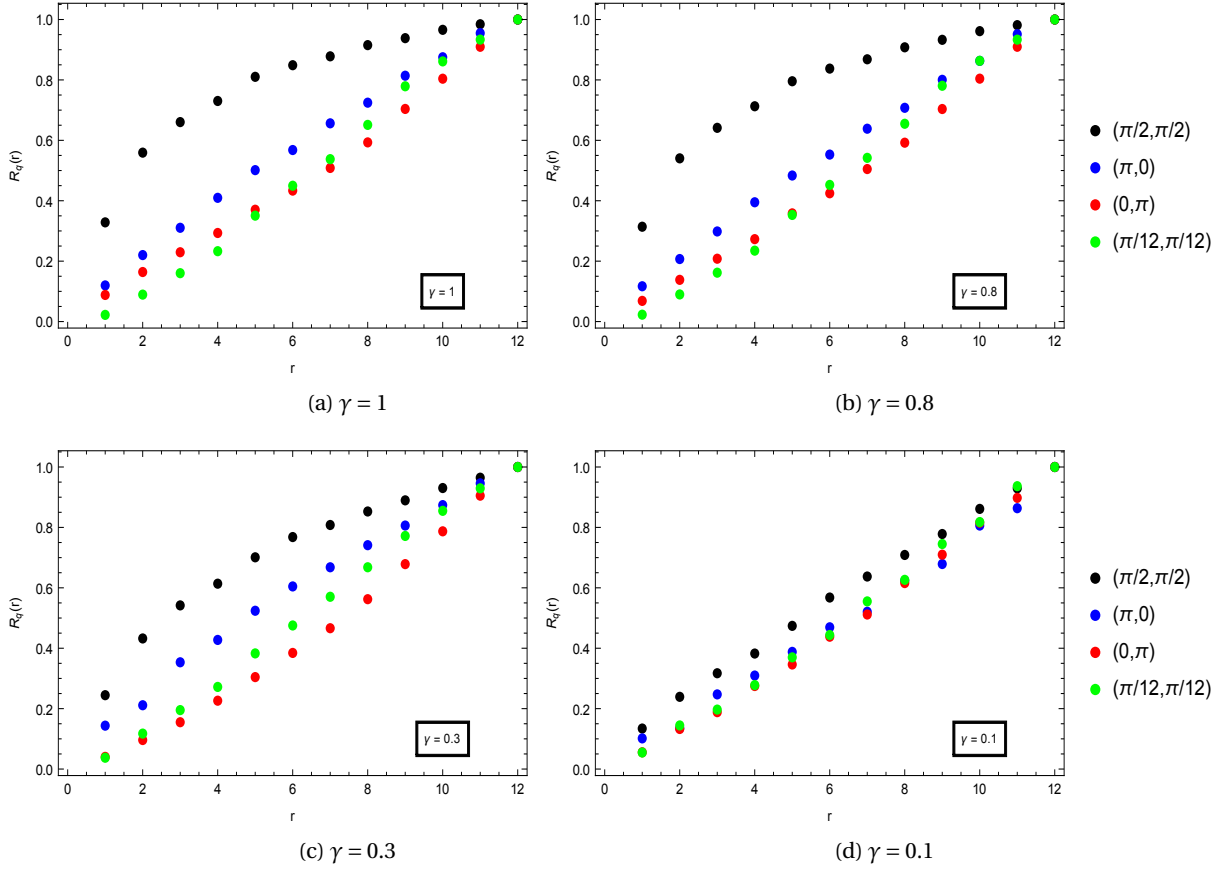


Figure 5.27 – CDF of spinon separation at q points $(\pi/2, \pi/2)$ (black), $(\pi, 0)$ (blue), $(0, \pi)$ (red), $(\pi/12, \pi/12)$ (green) for $\gamma = 1$ (top-left), $\gamma = 0.8$ (top-right), $\gamma = 0.3$ (bottom-left), $\gamma = 0.1$ (bottom-right) for a system with PBC.

The CDF of spinon separation shows the distinguishing features of spinon and magnon like behavior of spin excitations more clearly (compared to RMS). Although differences between different boundary conditions do exist, indicating the dependence on finite size, these differences are rather small and qualitatively do not impact the conclusions drawn. However, the validity of these conclusions should extend to $L \rightarrow \infty$ and should not be just a artifact of small system sizes. To ensure that the conclusions drawn extend to infinite system sizes, we analyze the data corresponding to different system sizes at high symmetry points previously calculated. In Fig(5.28) we show the CDF at $(\pi, 0)$ for different system sizes at different coupling ratios. As can be seen the distribution remains linear at all system sizes and all coupling ratios indicating that the spin excitations retain their 'spinon' like behavior at all coupling ratios even at large system sizes. A look at $(0, \pi)$ symmetry point, in Fig(5.29), shows a linear behavior at high coupling ratios and a slightly localized behavior at small coupling ratios for all system sizes. The spinon separation at $(\pi/2, \pi/2)$ on other hand, as shown in Fig(5.30) has a linear behavior at $\gamma = 0.1$ which progressively becomes localized at $\gamma = 1$ and this happens at all system sizes.

In Fig(5.31),Fig(5.32),Fig(5.32) we show the corresponding data for PBC boundary conditions where we observe similar features as the ABC case.

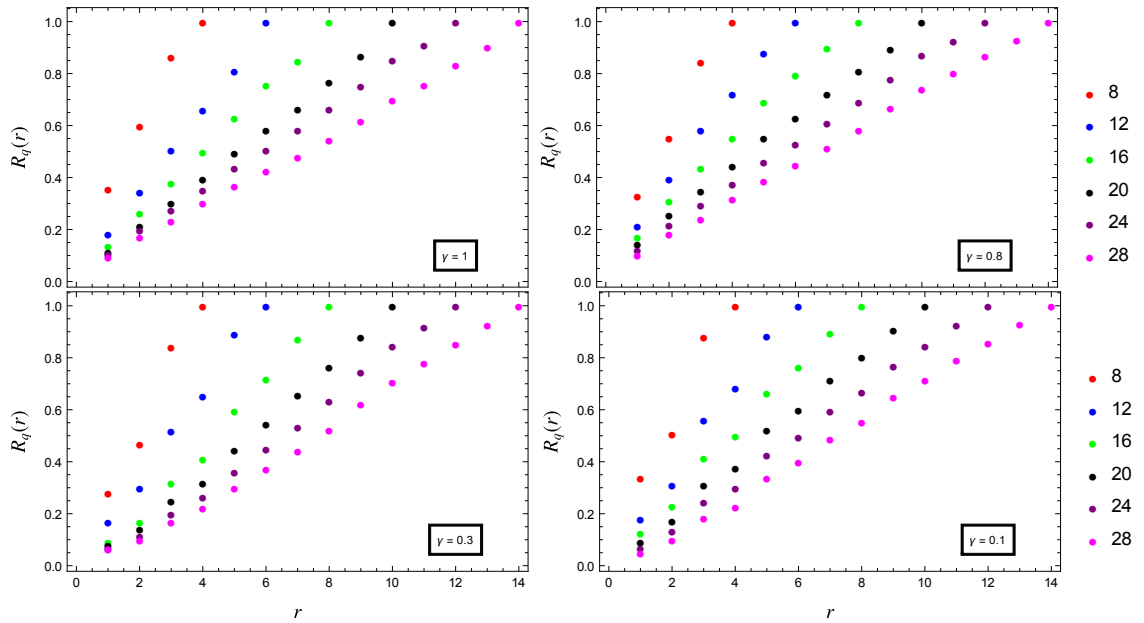


Figure 5.28 – CDF of spinon separation at $(\pi, 0)$ for various system sizes $L = 8, 12, 16, 20, 24, 28$ represented by red, blue, green, black, brown and magenta respectively. Top-left(right) corresponds to $\gamma = 1(0.8)$ and bottom-left(right) corresponds to $\gamma = 0.3(0.1)$. The system has ABC.

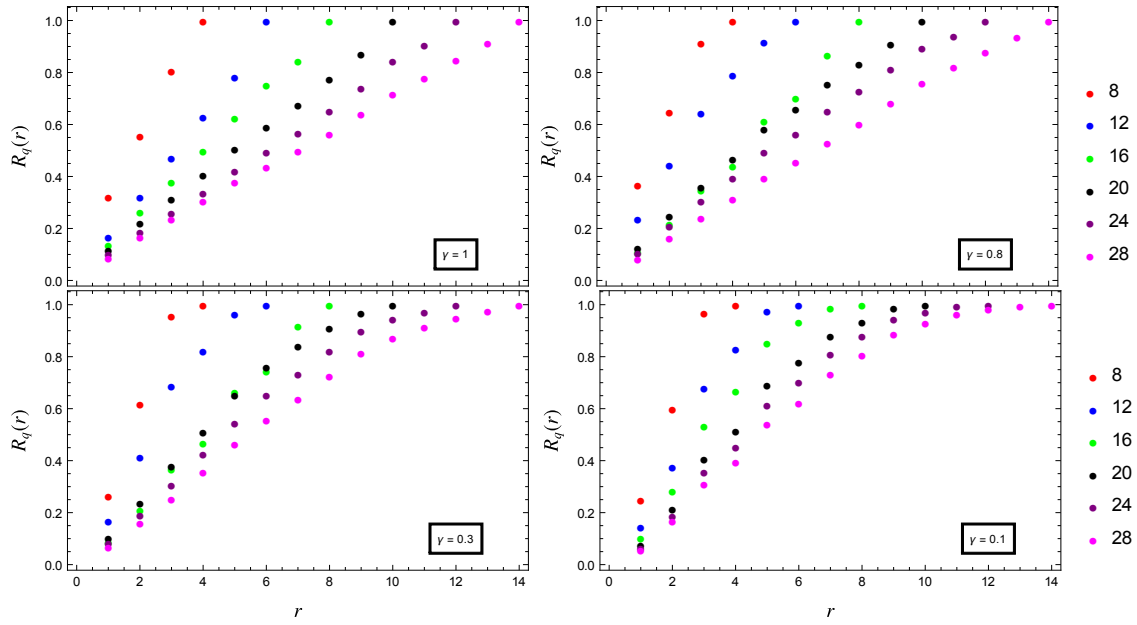


Figure 5.29 – CDF of spinon separation at $(0, \pi)$ for various system sizes $L = 8, 12, 16, 20, 24, 28$ represented by red, blue, green, black, brown and magenta respectively. Top-left(right) corresponds to $\gamma = 1(0.8)$ and bottom-left(right) corresponds to $\gamma = 0.3(0.1)$. The system has ABC.

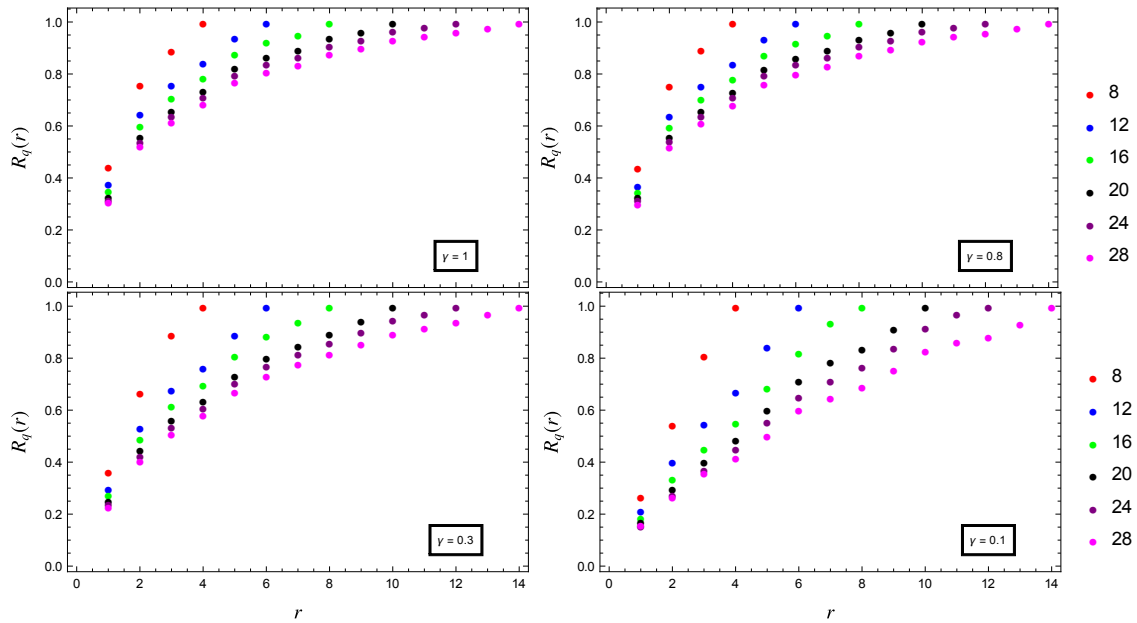


Figure 5.30 – CDF of spinon separation at $(\pi/2, \pi/2)$ for various system sizes $L = 8, 12, 16, 20, 24, 28$ represented by red, blue, green, black, brown and magenta respectively. Top-left(right) corresponds to $\gamma = 1(0.8)$ and bottom-left(right) corresponds to $\gamma = 0.3(0.1)$. The system has ABC.

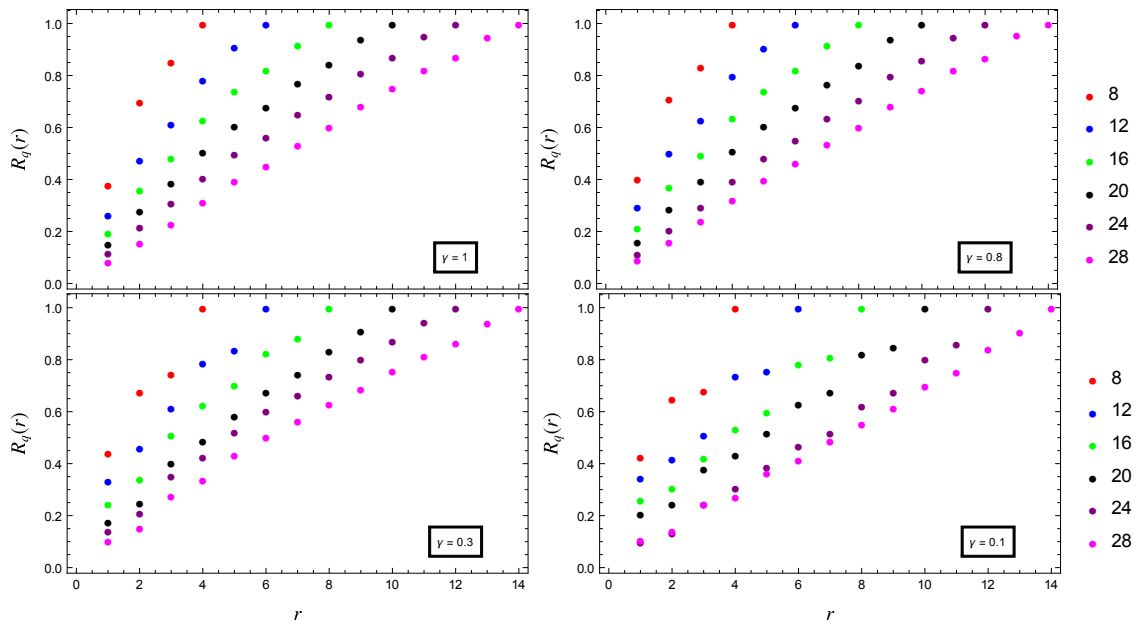


Figure 5.31 – CDF of spinon separation at $(\pi, 0)$ for various system sizes $L = 8, 12, 16, 20, 24, 28$ represented by red, blue, green, black, brown and magenta respectively. Top-left(right) corresponds to $\gamma = 1(0.8)$ and bottom-left(right) corresponds to $\gamma = 0.3(0.1)$. The system has PBC.

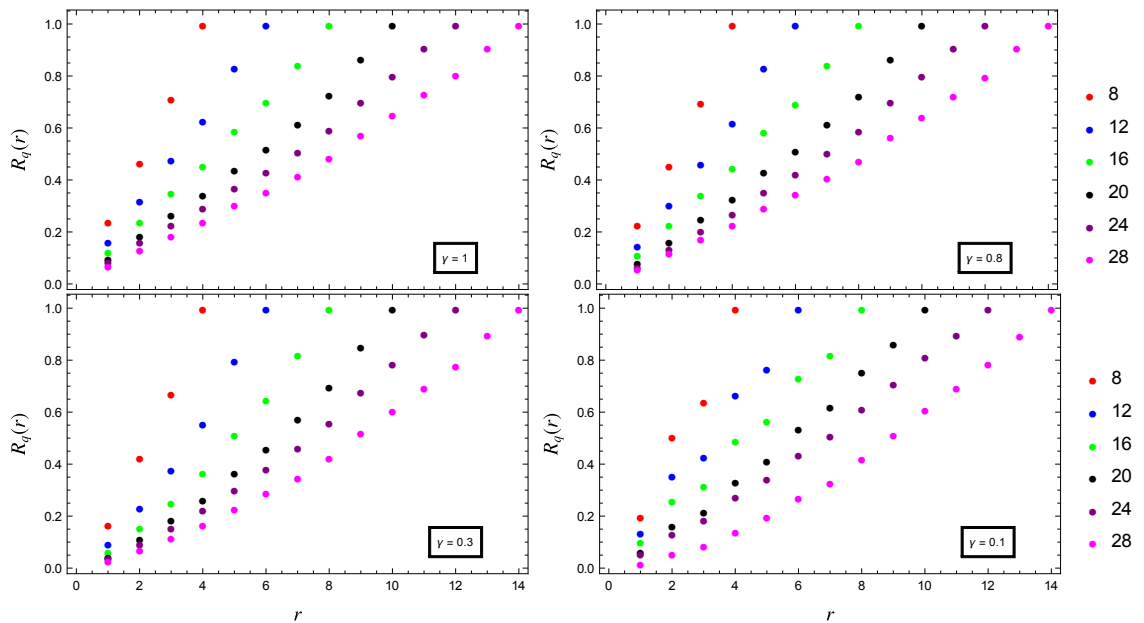


Figure 5.32 – CDF of spinon separation at $(0, \pi)$ for various system sizes $L = 8, 12, 16, 20, 24, 28$ represented by red, blue, green, black, brown and magenta respectively. Top-left(right) corresponds to $\gamma = 1(0.8)$ and bottom-left(right) corresponds to $\gamma = 0.3(0.1)$. The system has PBC.

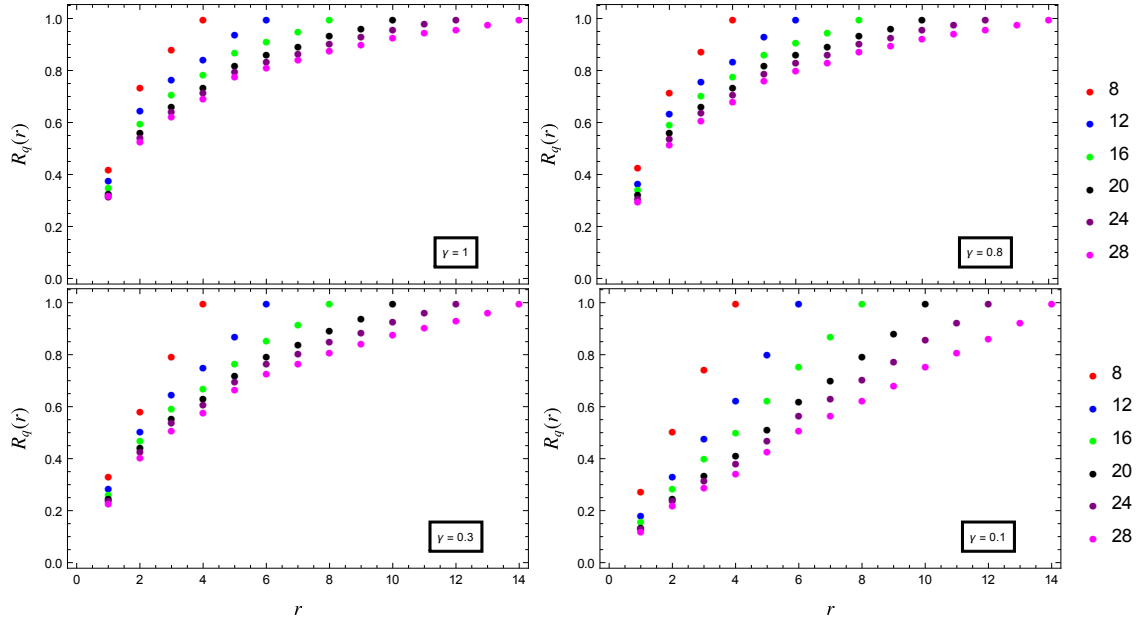


Figure 5.33 – CDF of spinon separation at $(\pi/2, \pi/2)$ for various system sizes $L = 8, 12, 16, 20, 24, 28$ represented by red, blue, green, black, brown and magenta respectively. Top-left(right) corresponds to $\gamma = 1(0.8)$ and bottom-left(right) corresponds to $\gamma = 0.3(0.1)$. The system has PBC.

Summary

The previous sections were dedicated to elaborating various features of the Transverse dynamical spin structure factor on a Rectangular Heisenberg system, by comparing it with Bethe ansatz at small coupling ratios and spin wave theory elsewhere. We also had a look at the nature of the spin excitations by calculating the evolution of spinon separation with γ . These analysis were extended to different system sizes at high-symmetry points to study the finite size effects. Here we outline the main observations and conclusions derived through our analysis.

1) A comparison of TDSF along $(0, 0) \rightarrow (\pi, 0)$ at $\gamma = 0.05$ (with ABC) with the $\gamma = 0$ estimate from Algebraic Bethe ansatz shows a good equivalence between both the spectra (Fig(5.8)) with the energies at $\gamma = 0.05$ being slightly shifted. A similar comparison of staggered flux state with PBC and Bethe ansatz with ABC shows similar equivalence.

2) Assuming the physics to be marginally one dimensional, we compare the evolution of the spectral weight in the low energy mode as we increase the coupling ratio γ from 0.05 to 0.2. We observe that close to points $(\pi, 0)$, $(0, \pi)$ and $(0, 0)$, the low energy peak loses spectral weight which is transferred to the high energy excitations (Fig(5.11)). Simultaneously these points in our spinon-separation analysis start to show a large RMS spinon separation, indi-

cating that the excitations close to these symmetry points preserve a ‘spinon’ like behavior. At points close to $(\pi/2, 0)$ and $(\pi/2, \pi)$ we see the low energy mode gaining spectral weight and gradually evolving towards a ‘magnon’ like excitation. The same effect is observed in corresponding spinon separation analysis. The (π, π) symmetry point on other hand starts to show un-physical negative energies from $\gamma = 0.1$, which we shall ignore in our further analysis.

3) As we move towards higher coupling ratios, we observe the high energy modes gradually loosing spectral weight everywhere except at $(\pi, 0)$ and $(0, \pi)$, (Fig(5.15)) which continue to show a significant number of contributing high energy modes. This gradual evolution suggests that the 2D version of ‘spinons’ on an RVB state are linked to the corresponding 1D analogues. A comparison of low energy modes with the self-consistent spin wave result, shows a good agreement in most of the k-space except at the $(\pi, 0)$ and $(0, \pi)$ points where we observe a sharp dip and loss of peak intensity into high energy modes. Similar effects are observed for PBC case as well (Fig(5.16)).

4) To observe the finite size effects on our calculations, we calculate the TDSF at high symmetry points $(\pi, 0)$, $(0, \pi)$ and $(\pi/2, \pi/2)$ for system sizes $L = 8, 12, 16, 20, 24, 28$. At $(\pi, 0)$, for all coupling ratios, we progressively observe large number of modes as we increase the system size indicating that the high energy modes will gradually become a continuum. A comparison with the spin wave result at $\gamma = 1$ (Fig(5.17)) shows that the low energy mode that closely matches with the spin wave estimate at small system sizes, actually loses spectral weight and exhibits a much larger reduction than the expected 7% reduction. The second peak subsequently gains spectral weight and moves closer to the expected result. Dalla Piazza et al. have speculated that this eventually becomes the magnon like peak at larger system sizes. By looking at the corresponding PBC result at $(\pi, 0)$ we were able to conclude that this is indeed true, and the low energy mode observed in ABC case is just a finite size effect. We continue to observe this effect at $(\pi, 0)$ for smaller coupling ratios as well.

5) At $(0, \pi)$ in the symmetric case, we see same spectra for both boundary conditions which show the low energy mode loosing spectral weight. At low coupling ratios, for example $\gamma = 0.5$ (Fig(5.18)), we see only the PBC showing this effect strongly whereas the ABC shows a weaker trend. At $(\pi/2, \pi/2)$, for large coupling ratios we observe a sharp peak that matches well with the spin wave result. At low coupling ratios, for e.g. $\gamma = 0.1$ in Fig(5.19), we observe small additional peaks at $(\pi/2, \pi/2)$ indicating that the spin excitations slowly become ‘spinon’ like. A look at the spectrum at high symmetry points at $L = 28$ in Fig(5.20) and Fig(5.21), shows the $(\pi, 0)$ mode gradually losing spectral weight and $(0, \pi)$ mode gradually gaining spectral weight as we increase γ . Both points continue to show significant high energy excitations at large γ containing around 50% spectral weight at all couplings. The spectrum at $(\pi/2, \pi/2)$ shows a small additional peak at small coupling ratios, which subsequently moves to higher energies and loses spectral weight as γ is increased.

6) So far, from TDSF data, we have speculated that the sharp modes are magnon like and

the modes with continuum are spinon like. To put this picture on a stronger footing, for an excitation with momentum q , we evaluate the spinon separation on a real space grid. In the symmetric case as already noted by Dalla Piazza et al. the spinon separation is localized at $(\pi/2, \pi/2)$ and spread out in position space at $(\pi, 0)$ (Fig(5.22)). A look at the evolution of RMS separation with coupling ratio (Fig(5.24)) shows that, small coupling ratios we have more or less a constant RMS spinon separation, gradually exhibits a decreasing RMS separation with increasing γ at all q-points except in regions close to $(\pi, 0), (0, \pi)$ and $(0, 0)$. A look at the CDF of spinon separation (Fig(5.26)) also shows the same effect, where the CDF behaves linearly with distance for all coupling ratios at $(\pi, 0)$ and $(\pi/12, \pi/12)$, but the CDF at $(\pi/2, \pi/2)$ gradually evolves from a linear at $\gamma = 0.1$ to being localized at $\gamma = 1$. The spinon like behavior of excitations near $(\pi, 0)$ and $(0, \pi)$ is not a new result, but the spinon like behavior close to $(0, 0)$ is a new observation.

7) The spinon-magnon like behavior of excitations should extend to large system sizes as well and should not be a artifact of a finite size calculation. Hence, we analyze the CDF at symmetry points $(0, \pi), (\pi, 0)$ and $(\pi/2, \pi/2)$ as we increase system size, that shows that the $(\pi, 0)$ symmetry point (Fig(5.28)) continues to show a linear behavior with distance, for all system sizes and all coupling ratios. The $(\pi/2, \pi/2)$ (Fig(5.30)) shows a gradual localization as we increase the coupling ratio which happens at all system sizes. The PBC data also shows the same features (Fig(5.31), Fig(5.32), Fig(5.33)). Thus at infinite system size we expect the spinons at $(0, \pi)$ and $(\pi, 0)$ to be widely distributed on the lattice, where as the spinons at $(\pi/2, \pi/2)$ gradually get localized with increasing γ as we move from 1D to 2D.

6 Conclusion

Our interest in the SF state on RQHAF began with a prospect of being able to study the evolution of its physics as the dimensionality of the system passes through quasi-1D towards a 2D regime. The underlying motivation was the fractionalization of ‘magnon’ excitations into ‘spinons’, particularly in an unfrustrated system. Mermin-Wagner theorem allows for breaking of continuous symmetry in 2D systems only at $T = 0$, and as plethora of experimental, theoretical and numerical evidence suggests, the groundstate of a 2D AFM Heisenberg systems appears to be a state with a broken symmetry the Neel state. As seen in the example of coupled XY chains, conventional wisdom would dictate that in cases where there is a ordered state, finding free spinons would be improbable and hence one needs frustration to acquire a quantum spin liquid state, where the spinons would be able to propagate freely. The merit of the SF state on a square lattice was related to its capability to qualitatively explain the experimentally observed $(\pi, 0)$ quantum anomaly. New research work involving continuous similarity transformation provide an alternate view point, where the quantum anomaly can be explained within the framework of multi-magnon excitations. Given all these arguments, one might wonder on why we consider a disordered state on an unfrustrated system, which is known not to be the groundstate, and study spinons on such a state. But the spirit of research and scientific enquiry lies in exploring all the possibilities, despite a few caveats here and there. This is necessary to create a wholesome picture of the underlying physics behind these systems. The novelty of a spin liquid state, fractionalization and their possible role in explaining High T_c superconductivity and their relevance to topological quantum computing motivate a requirement for a deeper understanding into these states.

As we move forward in this research work a few relevant questions we ask ourselves were:

- 1) Is the $(\pi, 0)$ quantum anomaly fully explained by the SF state ?
- 2) Are the fractional excitations termed as ‘spinons’, that qualitatively reproduced the $(\pi, 0)$ quantum anomaly in 2D, linked to the 1D spinons found through the Bethe ansatz solution ?

Chapter 6. Conclusion

3) If a link is found, is it a gradual evolution ? or does there exist a phase transition or a crossover ?

4) Could a disordered RVB solutions or RVB solutions with sufficiently long range correlations, be a better ground state for the 2D model at $T = 0$ compared to a symmetry broken state ?

5) What happens to spinons on SF state as we turn on and increase the coupling along y direction ?

Considering the first question, one of the de-merits of the SF state, in the work of Dalla Piazza et al., was that the zone boundary dispersion of the SF state was too pronounced. Through a finite size analysis Dalla Piazza et al. speculated that the low energy peak of the TDSF at $(\pi, 0)$, that is gradually seen to be loosing weight, would disappear at infinite system size. In this scenario the subsequent peak would become the low edge of the continuum, which would be in agreement with the experimental observation. In this thesis, by using different boundary conditions, we were able to show that this is indeed the case and the low energy peak is just an artefact of the anti-periodic boundary condition. This result shows the utility of using different boundary conditions when we are working with Finite size systems.

Moving on to the second and third questions, it appears that the 2D ‘spinons’ are gradually linked to their 1D counterparts. The qualitative equivalence of the $\gamma = 0.05$ TDSF with the Bethe Ansatz solution for both boundary conditions, and the observed evolution of the excitation spectrum without any striking anomaly seems to indicate that the evolution is gradual. The self-consistent spin wave theory result indicates that below $\gamma = 0.138$ the long-range order vanishes, a result that coincides with the work of Miyazaki et al. Consequently we observe a good agreement between the SF groundstate energy and the Gutzwiller projected Schwinger boson result by Miyazaki et al., both of which are disordered states. However, this is not an indication that Neel order would vanish around this region particularly given that we observe unphysical negative energies at (π, π) all the way down to $\gamma = 0.05$. Hence it cannot be conclusively said from our data, if there exists a crossover region. One must have a more detailed look around $\gamma = 0.1 - 0.2$ region to see if the SF state shows signatures of a possible crossover.

As far as the much debated fourth question goes, unfortunately we do not have a conclusive answer. Continued existence of the negative energy at (π, π) point all the way down to $\gamma = 0.05$ seems to indicate that the true ground state might have long range order all the way down to (except at) $\gamma = 0$. Although the SF state shows a power-law decay of the correlation functions the decay exponent is higher than the spin wave result. This indicates that if at all there is a RVB state that could be the groundstate of the 2D model without breaking the continuous symmetry, it needs to have larger correlations than the SF state. Hence, we believe that the answer lies in experimenting with a SF state with artificially induced long range correlations. We believe that this would repair the long wavelength and low energy discrepancies observed in our work, without qualitatively changing the high energy short wavelength aspects.

Coming to the last question, although spinons are confined in the symmetry broken state, like the Neel state, explicit symmetry breaking does not seem to be a necessary condition for confinement of spinons into 'magnons'. It must be noted here that, since we work at finite system sizes, it is hard to classify an exactly confined/de-confined phases. Hence, when we say confined(de-confined) it means that the excitations are strongly(weakly) confined. In the quasi-1D regime, we saw the points away from $(\pi, 0)$, $(0, \pi)$, $(0, 0)$ gradually becoming magnon like as we increase γ . This is indicated by the gradual shift of spectral weight of the continuum, towards a single peak. The points close to $(\pi, 0)$, $(0, \pi)$, $(0, 0)$ on the other show a gradual loss of spectral weight from the low energy mode. Parallely the decrease of spinon-pair separation at all the k-points except near $(\pi, 0)$, $(0, \pi)$, $(0, 0)$ with increase of coupling ratio γ all the way till the symmetric case, indicates confinement occuring even without the Neel order. The points close to $(\pi, 0)$, $(0, \pi)$, $(0, 0)$ continue to show significant spinon-pair separation. The existence of fractional excitations at $(\pi, 0)$ and $(0, \pi)$ is not a new result. The large spinon separation at (close to) $(0, 0)$ is a new observation not noticed by Dalla Piazza et al. Due to the lack of proper density of states and the proximity to long wavelengths, it is doubtful if this feature, if at all exists, could be captured by an experiment.

This discussion provides the concluding arguments from our research work. We hope that it motivates further research into Gutzwiller projected states and makes a small contribution to the field of quantum magnetism.

A Simulation details

Metropolis MonteCarlo

As discussed in chapter 4, the core process of our simulation is a Metropolis MonteCarlo Algorithm [Metropolis et al. (1953)], where a Markov chain is created in the single particle basis. The Metropolis Monte Carlo is a numerical method we use to provide an estimated for a weighted average Q of a quantity $f(\alpha)$ subject to a probability distribution $\rho(\alpha)$:

$$Q = \sum_{\alpha} \rho(\alpha) f(\alpha) \quad (\text{A.1})$$

where α parameterizes a space too large to be included in a finite numerical calculation. It provides a simple way to estimate Q by summing contributions $f(\alpha)$ where α states are generated through a random walk following a probability distribution $\rho(\alpha)$. The construction of a Markov chain involves defining a proposal function $\mathcal{P}(\alpha'|\alpha_n)$ that generates a state $|\alpha'\rangle$ given a state $|\alpha_n\rangle$ at the n 'th step of the Montecarlo process. We can then move on to define the acceptance ratio or the transition probability:

$$A(\alpha'|\alpha_n) = \text{Max} \left[1, \frac{\mathcal{P}(\alpha_n|\alpha')\rho(\alpha')}{\mathcal{P}(\alpha'|\alpha_n)\rho(\alpha_n)} \right] \quad (\text{A.2})$$

Once we have chosen a proposal function and defined the acceptance ratio a random walk is generated as follows:

Step 1: A new state $|\alpha'\rangle$ is generated by the proposal function $\mathcal{P}(\alpha'|\alpha_n)$.

Step 2: A random number $r \in [0, 1)$ is drawn and if $r < A(\alpha'|\alpha_n)$ then the new state is accepted such that $|\alpha_{n+1}\rangle = |\alpha'\rangle$. Else the new state is rejected such that $|\alpha_{n+1}\rangle = |\alpha_n\rangle$.

Step 3: Go back to step 1.

The conditional probability in this random walk becomes:

$$P(\alpha_{n+1}|\alpha_n) = \begin{cases} A(\alpha_{n+1}|\alpha_n)\mathcal{P}(\alpha_{n+1}|\alpha_n) & |\alpha_{n+1}\rangle \neq |\alpha_n\rangle \\ 1 - \sum_{\alpha'} A(\alpha'|\alpha_n)\mathcal{P}(\alpha'|\alpha_n) & |\alpha_{n+1}\rangle = |\alpha_n\rangle \end{cases} \quad (\text{A.3})$$

Appendix A. Simulation details

which satisfies the condition of detailed balance(or time reversibility):

$$P(\alpha'|\alpha)\rho(\alpha) = P(\alpha|\alpha')\rho(\alpha) \quad (\text{A.4})$$

that guarantees that the sample states $|\alpha_n\rangle$ drawn in our random walk satisfy a steady probability distribution $\rho(\alpha)$. We have a great freedom in choosing the proposal function $\mathcal{P}(\alpha'|\alpha)$. To keep things simple the proposal function we use to generate a new state in a single particle basis is to randomly pick a spin and then randomly pick its neighbor and generate a new state by exchanging the spins if they are anti-aligned. This renders the proposal density to be symmetric $\mathcal{P}(\alpha'|\alpha) = \mathcal{P}(\alpha|\alpha')$ rendering our acceptance ratio to simply be $A(\alpha'|\alpha) = \text{Max}([1, \rho(\alpha')/\rho(\alpha)])$. To be able to estimate the uncertainty in the values of our measured observables, one runs into a difficulty that our samples are not sufficiently random on a Markov chain. To get around this we make measurement at sufficiently spaced intervals (L^2 where L is the system size).

Overlap Amplitudes

As described in earlier section, the primary quantity of concern to us is the overlap amplitude $\rho(\alpha) = |\langle \alpha | \psi \rangle|^2$ where $|\psi\rangle = |\psi_{GS}\rangle$ for ground state and $|\psi\rangle = |k, q\rangle$ in the case of excited state. The wave function $|\psi\rangle$ is created via filling particles in the momentum space where as the single particle basis $|\alpha\rangle$ is in the position basis. Since we are dealing with fermions and our wave function needs to be anti-symmetric with respect to exchange of particles, the overlap $\langle \alpha | \psi \rangle$ must be calculated as a slater determinant. We first start by defining a general single particle wave function written in terms of single particle basis:

$$|\alpha\rangle = |R_1, \sigma_1\rangle \otimes |R_2, \sigma_2\rangle \otimes \dots |R_N, \sigma_N\rangle \quad R_i \neq R_j \forall i, j \quad (\text{A.5})$$

where R_i is the position of spin σ_n . It must be noted that while deriving a new state α' from this state, the fermionic sign convention must be included. In the same spirit we construct the staggered flux wave function, that must be antisymmetrized with respect to exchange of two spins. This state can be represented as a slater determinant:

$$|\psi\rangle = \frac{1}{\sqrt{N!}} \begin{vmatrix} |k_1, \sigma_1, b_1\rangle & |k_2, \sigma_1, b_2\rangle & \dots & \dots & |k_n, \sigma_1, b_n\rangle \\ |k_1, \sigma_2, b_1\rangle & |k_2, \sigma_2, b_2\rangle & \dots & \dots & |k_n, \sigma_2, b_n\rangle \\ \vdots & \vdots & \vdots & \vdots & \vdots \\ \vdots & \vdots & \vdots & \vdots & \vdots \\ |k_1, \sigma_n, b_1\rangle & |k_2, \sigma_n, b_2\rangle & \dots & \dots & |k_n, \sigma_n, b_n\rangle \end{vmatrix} \quad (\text{A.6})$$

where b_n is the band index of the k point k_n . We can ignore the normalization value $1/\sqrt{N!}$ since we only require the ratios between different overlap amplitude. Hence within our

construction the overlap amplitudes become:

$$\langle \alpha | \psi \rangle = \text{Det}_{ij} \langle R_i, \sigma_i | k_j, \sigma_j, b_j \rangle \quad (\text{A.7})$$

where $\langle R_i, \sigma_i | k_j, \sigma_j, b_j \rangle$ is the single particle amplitude. Since S_{tot}^z is a good quantum number, the determinant can be further split into two components as:

$$\langle \alpha | \psi \rangle = \text{Det}_{i \uparrow j \uparrow} \langle R_{i \uparrow}, \uparrow | k_{j \uparrow}, \uparrow, b_{j \uparrow} \rangle \text{Det}_{i \downarrow j \downarrow} \langle R_{i \downarrow}, \downarrow | k_{j \downarrow}, \downarrow, b_{j \downarrow} \rangle \quad (\text{A.8})$$

Determinant Update Algorithms

Calculating determinant of a $N \times N$ matrix has a complexity of $\mathcal{O}(N^3)$. In our calculation each new state $|\alpha_{n+1}\rangle$ is derived from a previous state $|\alpha_n\rangle$ in our Markov chain. Since, the previous amplitude $\langle \alpha_n | \psi \rangle$ is already known we can reduce the complexity of the problem by updating the previously calculated amplitude with respect to the changes introduced. To do this, first we must understand what each operation while generating a new state does to the slater determinant. In our Markov chain a new state $|\alpha_{n+1}\rangle$ is generated via exchanging two randomly selected neighboring spins if they are anti-aligned. This is equivalent to change of a single column each in the slater determinant matrix of the up spin and down spin. If one remembers the formula for calculating the inverse of a matrix:

$$A^{-1} = \frac{1}{\text{Det}(A)} \text{cof}(A)^T \quad (\text{A.9})$$

where the i, j element of the cofactor matrix is nothing but the determinant of a matrix obtained by removing the row i and column j of matrix A . Using these considerations one can show that:

$$\frac{\text{Det}(A')}{\text{Det}(A)} = \sum_j A'_{kj} A_{jk}^{-1} \quad (\text{A.10})$$

where the matrix A' is obtained by changing the column k of matrix A . A similar formula for the update of the inverse matrix (A'^{-1}) can also be obtained in the same spirit. Thus we reduce a calculation of complexity $\mathcal{O}(N^3)$ to a $\mathcal{O}(N)$ complexity. A general case of obtaining these update formulas is as follows. Assume A is a $N \times N$ matrix, U a $N \times m$ matrix and V a $m \times N$ matrix. If a rank- m modification of matrix A is defined as:

$$A' = A + UV \quad (\text{A.11})$$

The resulting updates for the determinant and inverse are given by[Brookes (2011)]:

$$\text{Det}(A') = \text{Det}(A) \text{Det}(I_{m \times m} + VA^{-1}U) \quad (\text{A.12})$$

Appendix A. Simulation details

$$(A')^{-1} = A^{-1} - A^{-1}U(I_{m \times m} + VA^{-1}U)^{-1}VA^{-1} \quad (\text{A.13})$$

where it is assumed that the term in parenthesis is invertible. Using this method, we would like to construct a general algorithm that would work for a simultaneous update of m_r rows and m_c columns. The reason for this will become clear in the next section. We start by defining the matrices of new rows and columns as R and C that are matrices of dimensions $m_r \times N$ and $N \times m_c$. We let r_1, r_2, \dots, r_{m_r} to be the indices of rows to be changed and c_1, c_2, \dots, c_{m_c} the indices of columns to be changed. Also we define the unit column vectors \hat{e}_i where only non zero element is $(\hat{e}_i)_i = 1$. Using this construction, one can show that the following U and V define a simultaneous change of the r_i th rows and c_j th columns of A by i th rows of R and j th rows of columns of C:

$$U = \begin{pmatrix} C' & E_r \end{pmatrix} \quad (\text{A.14})$$

$$V = \begin{pmatrix} E_c \\ R' \end{pmatrix} \quad (\text{A.15})$$

with E_r and E_c defined as:

$$E_r = \begin{pmatrix} \hat{e}_{r_1} & \hat{e}_{r_2} & \dots & \hat{e}_{r_{m_r}} \end{pmatrix} \quad (\text{A.16})$$

$$E_c = \begin{pmatrix} \hat{e}_{c_1} & \hat{e}_{c_2} & \dots & \hat{e}_{c_{m_c}} \end{pmatrix}^T \quad (\text{A.17})$$

and R', C' defined as

$$C' = (1 - E_r E_r^T)(C - A E_c^T) \quad (\text{A.18})$$

$$R' = R - E_r^T A \quad (\text{A.19})$$

The matrix $K = I_{m \times m} + VA^{-1}U$, where $m = m_r + m_c$ has the block form:

$$K = \left(\begin{array}{c|c} E_c A^{-1} C - E_c A^{-1} E_r E_r^T C + E_c A^{-1} E_r E_r^T A E_c^T & E_c A^{-1} E_r \\ \hline R A^{-1} C - R A^{-1} E_r E_r^T C - R E_c^T + R A^{-1} E_r E_r^T A E_c^T & R A^{-1} E_r \end{array} \right) \quad (\text{A.20})$$

Let us analyze the computational complexity of calculating each block assuming $m_r \ll N$ and $m_c \ll N$ which implies that major calculations are related to multiplication of $N \times N$ matrices. Starting with the upper left block of dimensionality $m_c \times m_c$, we see that it requires a multiplication of two $N \times N$ matrices, which requires $\mathcal{O}(N)$ operations. The lower left block of $m_r \times m_c$ elements involves multiplication of three $N \times N$ matrices, which has computational complexity of $\mathcal{O}(N^2)$. The top right block does not have any large matrix multiplication and

hence requires $\mathcal{O}(N^0)$ operations. The bottom right block has multiplication of two $N \times N$ matrices, that require $\mathcal{O}(N)$ operations. Hence in total the evaluation of this matrix has $\mathcal{O}(N^2)$ complexity. When there are no row changes or no column changes, the above formulas will be simplified yielding:

$$K = E_c A^{-1} C \quad \text{for no row changes} \quad (\text{A.21})$$

$$K = R A^{-1} E_r \quad \text{for no column changes} \quad (\text{A.22})$$

which are of complexity $\mathcal{O}(N)$. Once we have the K matrix the determinant update can be obtained From Eq(A.12). The calculation of inverse of K does not cost much (assuming m_r, m_c to be very small), however the update of the inverse matrix through Eq(A.13) would require additional multiplication of two $N \times N$ matrices that requires an additional \mathcal{O} operations. Hence, in total to evaluate determinant and inverse update, the above algorithm yields a worst case $\mathcal{O}(N^2)$ computations in the case of only rows or only column updates

Computational details

In this section we provide the details on the basic structure of the algorithms used, and the computational cost at each step. Starting with the groundstate calculation, the staggered flux is initialized with given variational parameters. A random single particle state is generated (through a random seed) and the overlap amplitude is calculated. This implies calculating the determinant and inverse of the overlap matrix a step that typically requires $\mathcal{O}(N^3)$ steps (through LU decomposition and Gauss-Jordan elimination). If the overlap amplitude is too small, a new state is initialized and this process is repeated a few times until we have a random initial state, that has a finite overlap amplitude. Once such a initial state is found new states in the Markov chain are generated by exchanging randomly selected spins. At each step the determinant is updated and if the state is selected the inverse matrix is also updated. Since exchanging two spins merely corresponds to changing a single column of the slater determinant matrix, thanks to the algorithm developed in previous section, this step typically requires $\mathcal{O}(N)$ for determinant update and $\mathcal{O}(N^2)$ for inverse matrix update. Hence each random step in total has a complexity $\mathcal{O}(N^2)$.

The Hamiltonian operator has sum over $2N$ pairs and since it has off diagonal elements that exchange spins on neighboring sites, the complexity of computation of energy on each pair is $\mathcal{O}(N)$, which makes the total complexity to be $\mathcal{O}(N)$. The instantaneous longitudinal correlation function is diagonal and the computation of correlation on each pair does not cost much. However, since it has a double sum which involves $N^2/2$ pairs, the overall complexity of calculating instantaneous longitudinal correlation function is $\mathcal{O}(N^2)$. The instantaneous transverse correlation function, apart from having a double sum has also off-diagonal terms. Hence it has a computational complexity of $\mathcal{O}(N^3)$. To eliminate the bias from a initial random state that could be far away from equilibrium, we carryout sufficient thermalization steps

Appendix A. Simulation details

before starting the measurements. Dalla Piazza et. al. showed that a good equilibrium is reached within $20L^2$ steps. However, to be on the safe side we carry out a $200L^2$ thermalization steps since they do not cost much. To make the samples sufficiently independent, the measurements are made once every L^2 steps.

Moving on to the excited state simulation, at the beginning of each simulation the particle-hole excitation states $|k, q\rangle$ are initialized. The quantity we need to calculate at each random step is $W(\alpha) = \sum_k |\langle \alpha | k, q \rangle|^2$. Hence one might think that for a given $|\alpha\rangle$ we need to evaluate $\langle \alpha | k, q \rangle$ with all the k values. This is not required since given a particular Slater determinant $\langle \alpha | k, q \rangle$, a Slater determinant corresponding to a different k' i.e $\langle \alpha | k', q \rangle$ could be obtained by exchanging the particle at k to k' . This corresponds to just a column change in a Slater determinant matrix. Also, given a Slater determinant $\langle \alpha | k, q \rangle$ calculating $\langle \beta | k', q \rangle$ just requires considering the simultaneous row and column changes for which the algorithm in previous section has been built. Having all these considerations in mind, following the similar logic as the ground state calculations we can see that the random steps have $\mathcal{O}(N^2)$, and the measurement of transverse structure factor has $\mathcal{O}(N^3)$ complexity. Similar to groundstate calculations, we carry out thermalization for $200L^2$ steps.

So far, we have discussed the scaling of computational effort required with system size in each of the above simulations. We would also like to provide a few details on the real time computational cost and necessary statistics for this overall project. As Dalla Piazza et al mentioned in their work, a million measurements should suffice to minimize the statistical error. We started with this estimate and carried out our calculations of groundstate optimization and instantaneous structure factor calculation (with ABC) for coupling ratios $\gamma = 0.1 - 1$ in steps of 0.1. We also carried out the TDSF calculations at few coupling ratios $\gamma = 0.1, 0.2, 0.5$ with a million statistics for each individual simulation. However, as we realized that we need to consider effects of alternate boundary conditions as well, we decided to reduce the statistics to 0.25×10^6 measurements due to computational limitations. This corresponds to a certain trade off of statistical error which we shall discuss in the next section. Providing individual computational costs of each run for different types of observations, system sizes, couplings, boundary conditions etc would be cumbersome. Hence we provide the total estimate of our computational cost for this project that accounted for more than 2.5×10^6 cpu hours. Almost all of this computation has been performed on a local Quantum Wolf cluster that has of 320 cpus. This amounts to about nearly 8000 hours of cluster utilization over a period of 2 and a half years of handling this project.

B Error Analysis

Since most of our results are derived from a simulation of a Monte Carlo process the discussion would be incomplete without a detailed analysis of the possible numerical errors. There are two kinds of errors that creep into the final results that we obtain from our analysis. The first kind are related to the statistical errors coming from the limited sampling of the measurement of observables. The second kind are the fitting errors related to fits performed to derive numerical estimates from the simulation data.

Statistical Errors

Starting with the groundstate observables ground state energy and instantaneous spin spin correlation function, we estimate a single observable for every simulation. Hence the numerical error in this context is simply the standard error corresponding to the sampling. For example, if N measurements are made for estimating an observable O then the expectation value of this observable is given by:

$$\langle O \rangle = \frac{1}{N-1} \sum_N O_N \quad (\text{B.1})$$

where O_N is the N 'th measurement. The variance of this measurement is:

$$\sigma_O^2 = \frac{1}{N-1} \sum_N (O_N - \langle O \rangle)^2 \quad (\text{B.2})$$

The standard error is given by

$$E(O) = \frac{\sigma_O}{\sqrt{N}} \quad (\text{B.3})$$

Most of our simulations are performed on 320 computer nodes with 3000 measurements on each node (10^6 statistics). However, storing a million numbers per each simulation would cost a lot of memory. Hence the algorithms are designed to evaluate the average on each node

Appendix B. Error Analysis

which in the end gives us 320 samples. To obtain the standard error corresponding to our sampling, we use the binning procedure where the sample space is divided into N bins and the mean of each bin is taken to be the representative observation of that bin. Considering each bin as a single sample, we evaluate the standard error as function of number of bins. In Fig(B.1), we plot the standard deviation and the standard error of a randomly selected groundstate energy measurement, as function of number of bins. As can be seen, for a large number of bins we observe approximately constant standard error which is in the range of 1.4×10^{-5} . For almost all of the ground state measurements our standard error is in the range of $10^{-4} - 10^{-5}$. Hence the first three digits after the decimal point are accurate and the fourth digit can have a small error corresponding to the uncertainty in subsequent digits.

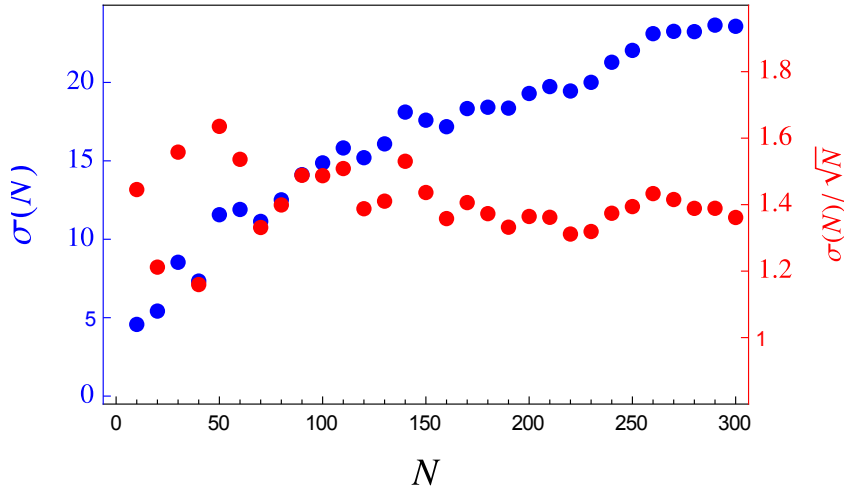


Figure B.1 – Standard deviation and standard error vs number of bins of a randomly selected simulation of groundstate energy measurement.

A second quantity that we measure from the ground state wave function is the instantaneous spin spin correlation. We expect $\langle S^x(r)S^x(0) \rangle$ to be the same as $\langle S^z(r)S^z(0) \rangle$ because of the $SU(2)$ symmetry of our wave function. We observe that this to be satisfied in almost all the data sets. A few exceptions were noticed while calculating the correlation function in y-direction at extremely low couplings. In this region, the numerical values of the correlation function are of the order 10^{-5} and it was found that the statistical errors were quite large in the zz component of the correlation function but not the xx component. In Fig(B.2) we plot the correlation function at $\alpha = 0.1$ for ABC boundary conditions. As can be seen in x-direction the xx and zz components coincide where as in y-direction the zz component is slightly shifted with large standard error.

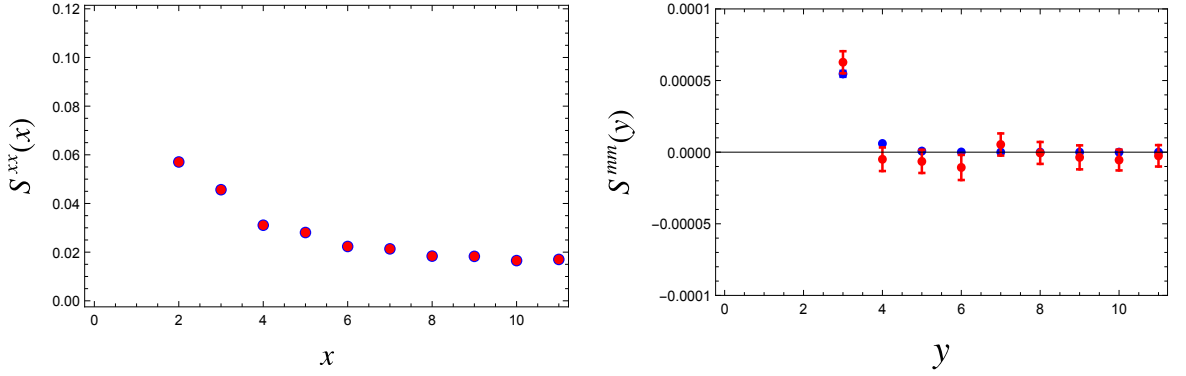


Figure B.2 – Instantaneous spin spin correlation function along with the standard error along x(left) and y directions(right) for simulation at $\alpha = 0.1$. The blue color corresponds to the xx component ($m = x$) and the red color corresponds to the zz component ($m = z$)

A hint of why this is happening could be understood by having a look at the expression we use to calculate an observable of our Gutzwiller projected state:

$$\langle O \rangle = \sum_{\beta} \frac{|\langle \beta | \psi_{GS} \rangle|^2}{\sum_{\beta} |\langle \beta | \psi_{GS} \rangle|^2} \underbrace{\left(\sum_{\gamma} \langle \beta | O | \gamma \rangle \frac{\langle \gamma | \psi_{GS} \rangle}{\langle \beta | \psi_{GS} \rangle} \right)}_{f(\beta)} \quad (\text{B.4})$$

When $O = S^z(r)S^z(0)$ the function $f(\beta)$ has constant values $+1/4$ or $-1/4$ depending on whether the spin at r in $|\beta\rangle$ is aligned or anti-aligned with respect to spin at $r = 0$. When $O = S^+(r)S^-(0)$ (relating to xx component) we have $f(\beta)$ depends not only on state $|\beta\rangle$ but also on the state $|\gamma\rangle = O|\beta\rangle$. Hence, calculation of the xx component involves a larger subspace of the single particle basis compared to the zz state. This is the reason why xx component exhibits a better statistical convergence for the limited statistics we have.

Moving on to the excited state calculations, determining the statistical errors is highly non-trivial. This is due to the fact that the measurements we make while simulating the excited states are the matrix elements H_{kk}^q and the final quantity we try to calculate is linked to the eigenvalues and eigenvectors of this matrix. The propagation of errors from matrix elements to eigenvector and eigenvalues, cannot be estimated without the knowledge of the actual matrix. Instead we just have a look at the TDSF samples at $q = (\pi, 0)$ and $\gamma = 0.5$ obtained via binning the matrix data into $N = 5$ bins. In Fig(B.3) we show the resulting spectra(convoluted by gaussians of $0.1J_x$), where the data from individual bins has been plotted in black lines and the average in Red. This data set contained a million observations which have been grouped into bins of 0.2 million. The overall error in x direction seems to be in the order of $0.1J_x$. Hence by taking 0.25 million statistics in most of our data sets we are sacrificing an accuracy in the range of $0.1J_x$

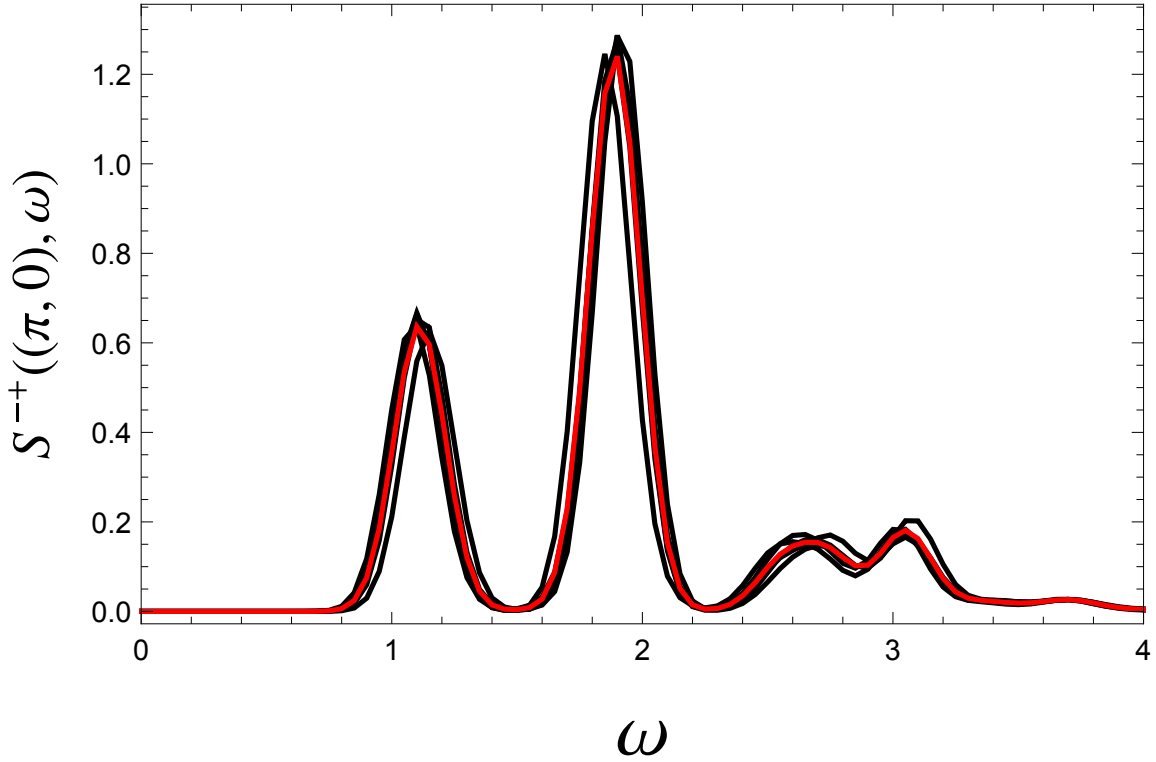


Figure B.3 – TDSF simulation of a randomly selected data set with 10^6 statistics binned into $N = 5$ bins. The black lines represent the TDSF from each bin, and the red line is the average.

Fitting Errors

In this section we discuss the fitting procedures used for estimating various numerical estimates obtained in the thesis, and the corresponding error estimates. We start our discussion with the fitting of Energymaps from section(4.2.1), where the lower part of the energy maps $E(\theta, \alpha)$ is fit with a function biquadratic in α and θ to estimate the position of the optimum parameters corresponding to the energy minimum. The function is given by:

$$E(\alpha, \theta) = a(\theta - \theta_0)^2 + b(\theta - \theta_0)(\alpha - \alpha_0) + c(\alpha - \alpha_0)^2 + E_{GS} \quad (\text{B.5})$$

This function has six free parameters $a, b, c, d, \theta_0, \alpha_0$. Fitting routine from Mathematica ‘Non-LinearModelFit’ has been used for fitting the energy minima with this function. Apart from the values of the ‘Best fit parameters’ we also obtain the corresponding standard error of these estimates. A particular problem encountered while fitting the discrete data, particularly at low couplings, is that if we consider only the points closest to the minimum energy the numerical errors and the lack of curvature could make the fit unstable. On the other hand if we consider points farther away as well, then they might influence the fit leading to wrong estimates of the minima. One solution to this problem is to give more weight to the points closer to the minima.

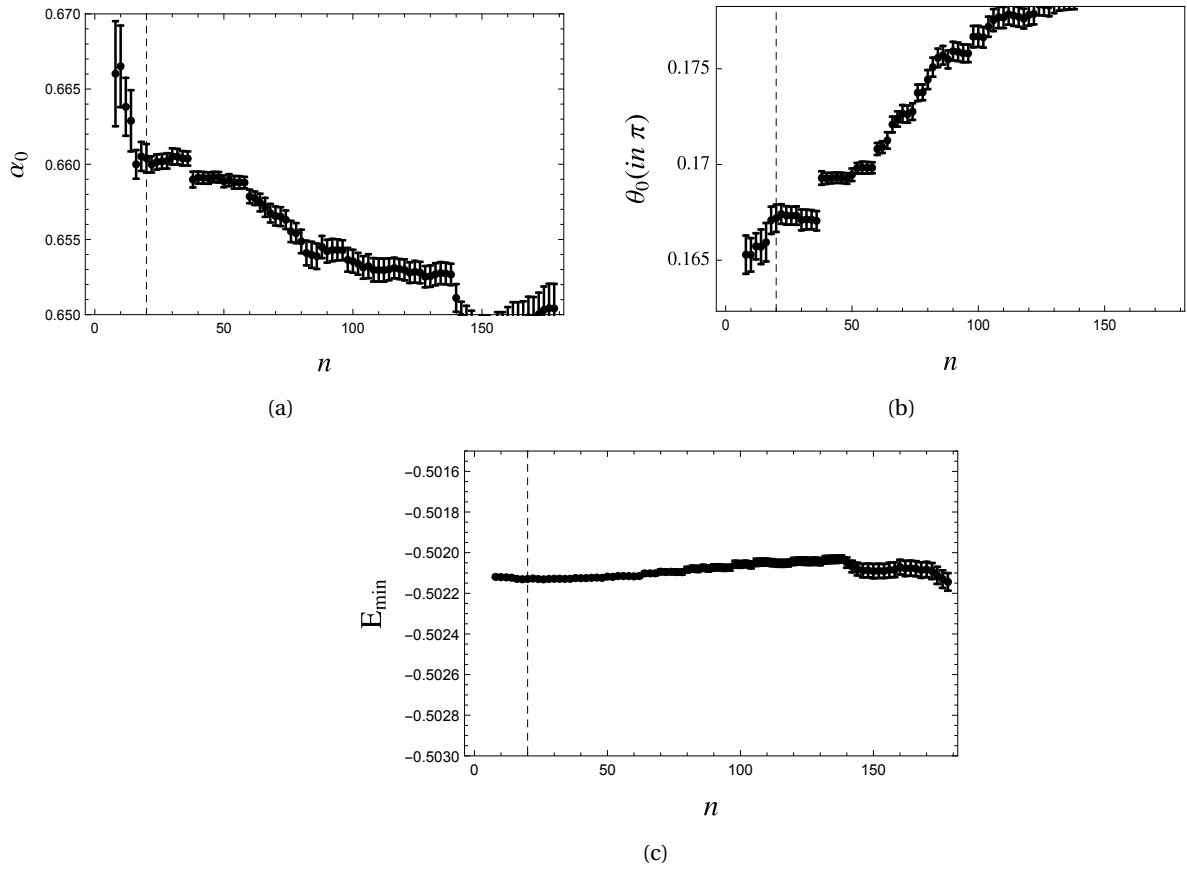


Figure B.4 – Fitted parameters $\alpha_0, \theta_0, E_{min}$ of the energy maps at $\gamma = 0.5$ and $L=16$ along with their fitting errors as a function of number of points (in ascending order of their energy) close to global minima used for fitting.

Another solution is to start the fit with a few points lowest in energy, and progressively add more and more points. Once we have included all the points we can pick out the fit parameters that are estimated from lowest number of points, but also with a reasonably small standard error. We choose the later procedure.

For an illustration in Fig(B.4) we show the result of such a process at $\gamma = 0.5$ for $L = 16$. As can be seen, the ground state energy estimate has a very small standard error. The parameter α_0 exhibits large standard error when only few points are taken and subsequently shows small standard error when lowest 20 points are taken. We select the optimum parameters and groundstate energy here, which is indicated by the dashed line. Similar procedure is repeated for all coupling ratios at different system sizes. Although standard error can be estimated in this fashion, it does not provide us with overall uncertainty of our optimal parameters. This is due to the fact that the function $Eg(B.5)$ assumes a parabolic minima, whereas the minima of our energy maps are not necessarily parabolic. Hence we cannot directly determine the numerical accuracy of the extracted optimal parameters without a more detailed mapping of

Appendix B. Error Analysis

the groundstate energy.

C Additional figures

Only figures that capture the relevant conclusions, have been presented in the main part of the thesis. Here we present the additional figures for completeness.

Energy maps

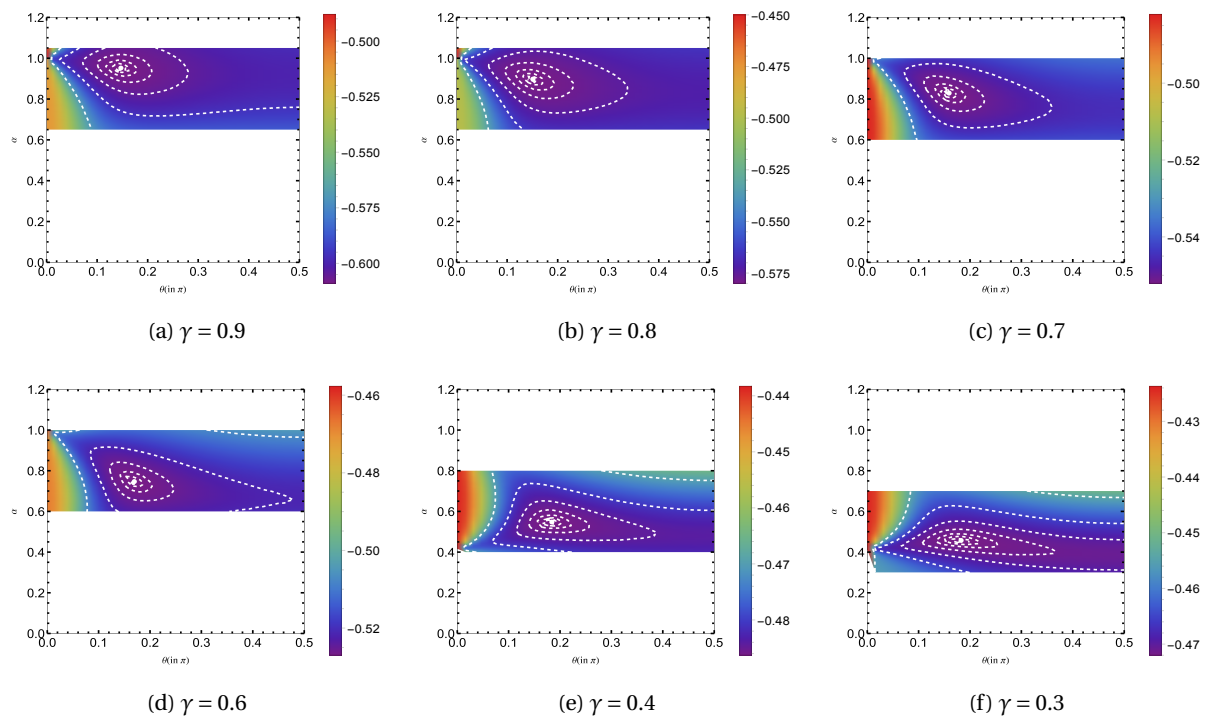


Figure C.1 – Ground state Energy maps of systems with size $L=8$ for various coupling ratios. The white contours(dot) indicate the points corresponding to same energy(minima).

Density of States (ABC)

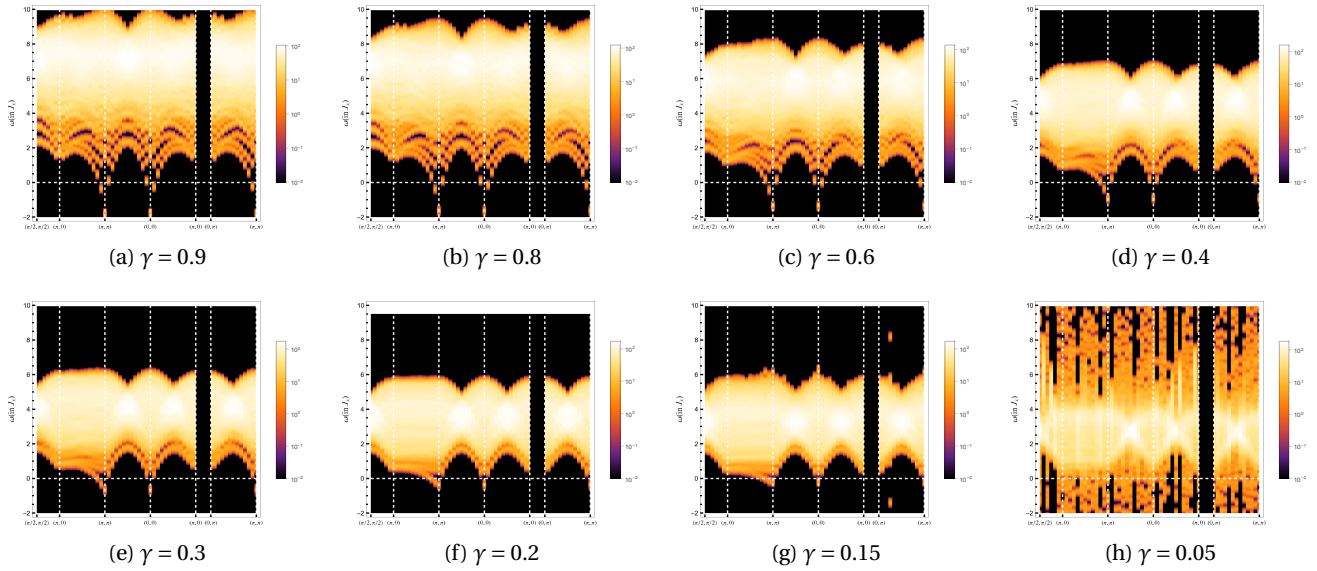


Figure C.2 – Density of states $D(q, \omega)$ as defined in Eq(5.42) at different γ values for anti-periodic boundary condition.

Density of States (PBC)

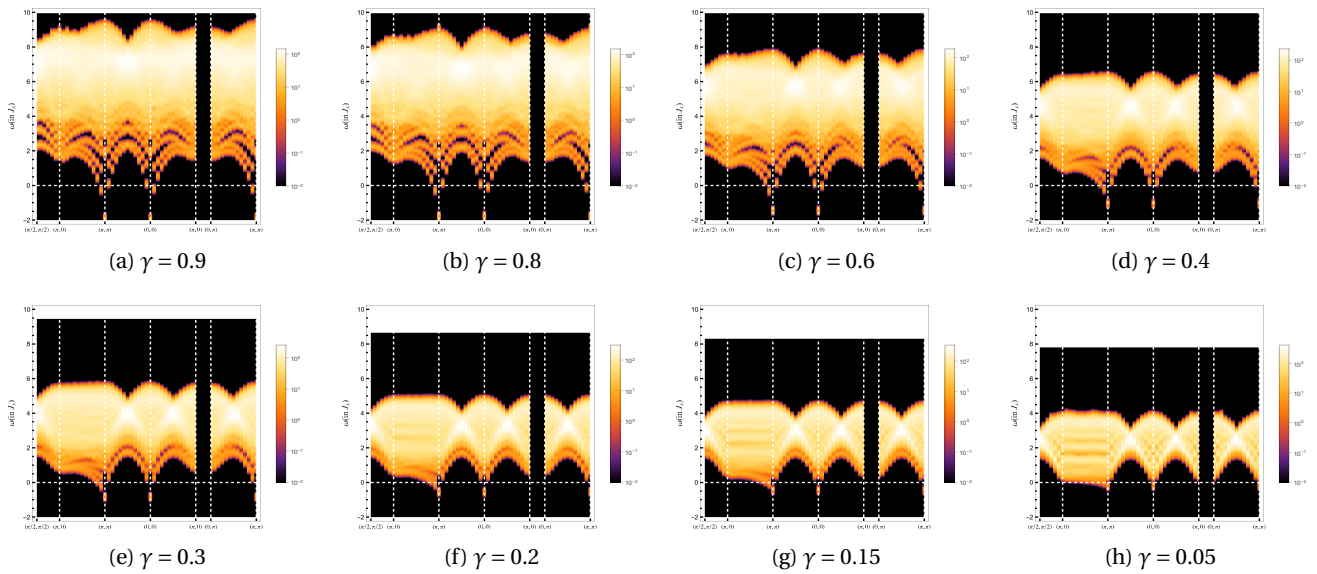


Figure C.3 – Density of states $D(q, \omega)$ as defined in Eq(5.42) at different γ values for periodic boundary condition.

TDSF (ABC)

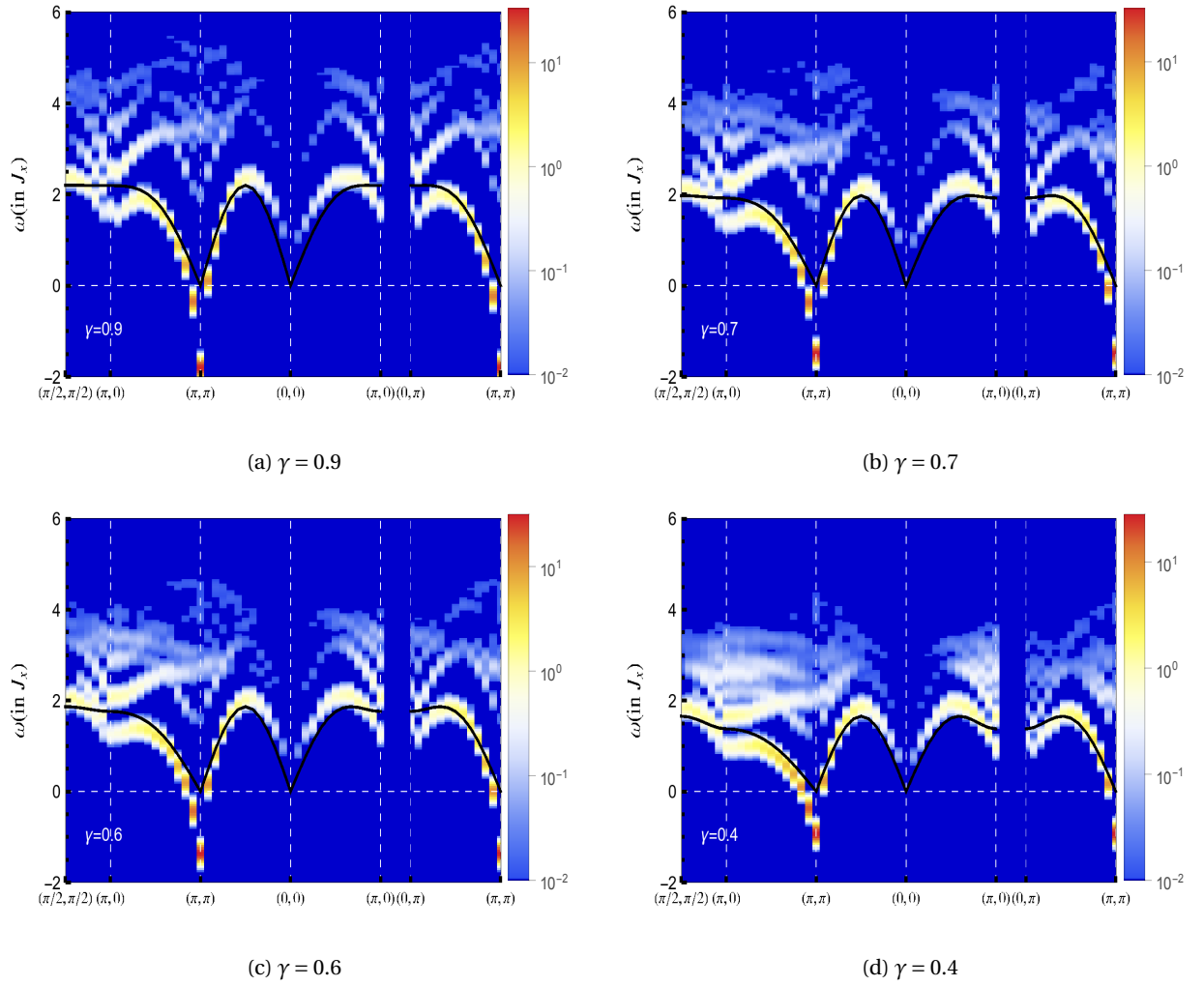
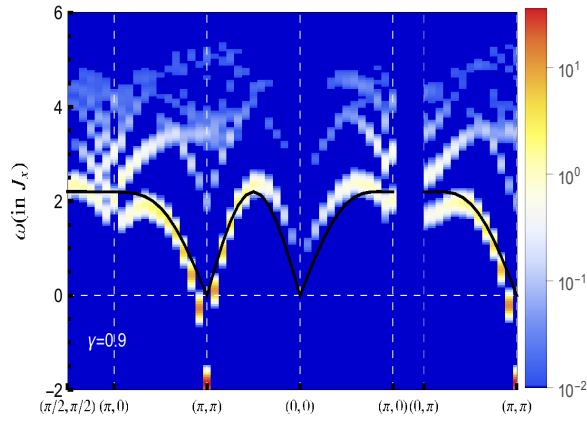
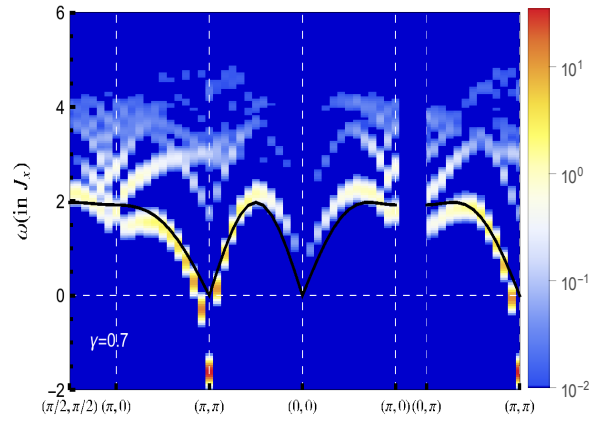


Figure C.4 – TDSF of staggered flux state (with ABC) for different γ values. The black line represents the self-consistent spin wave result obtained from chapter 3.

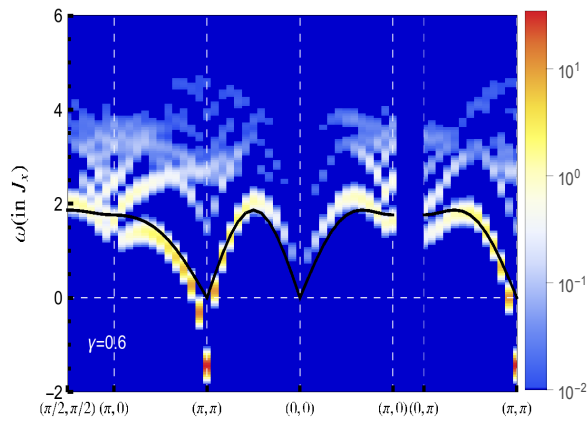
TDSF (PBC)



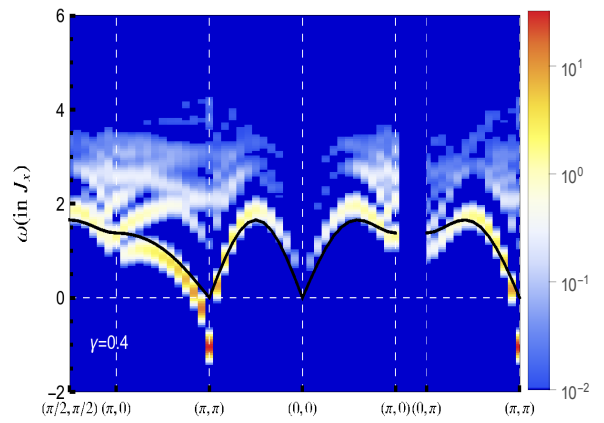
(a) $\gamma = 0.9$



(b) $\gamma = 0.7$



(c) $\gamma = 0.6$



(d) $\gamma = 0.4$

Figure C.5 – TDSF of staggered flux state (with PBC) for different γ values. The black line represents the self-consistent spin wave result obtained from chapter 3.

TDSF at different system sizes

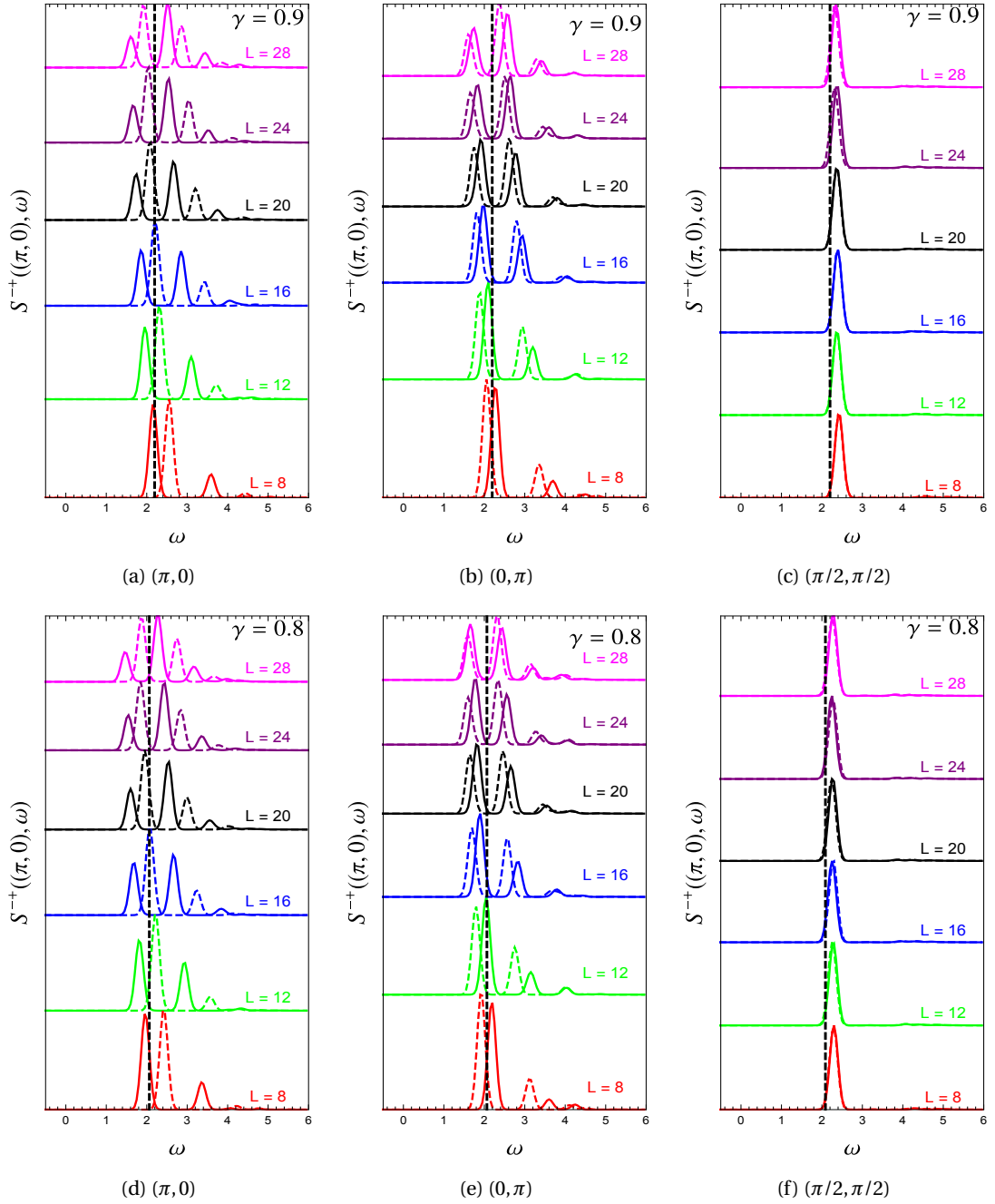


Figure C.6 – Evolution of TDSF for $\gamma = 0.9$ (top) and $\gamma = 0.8$ (bottom), at q-points $(\pi, 0)$ (left), $(0, \pi)$ (center) and $(\pi/2, \pi/2)$ (right) as we increase system size. The solid line represents ABC and dashed line represents the PBC. The dashed vertical line indicates the energy of the self-consistent spin wave result from chapter 3.

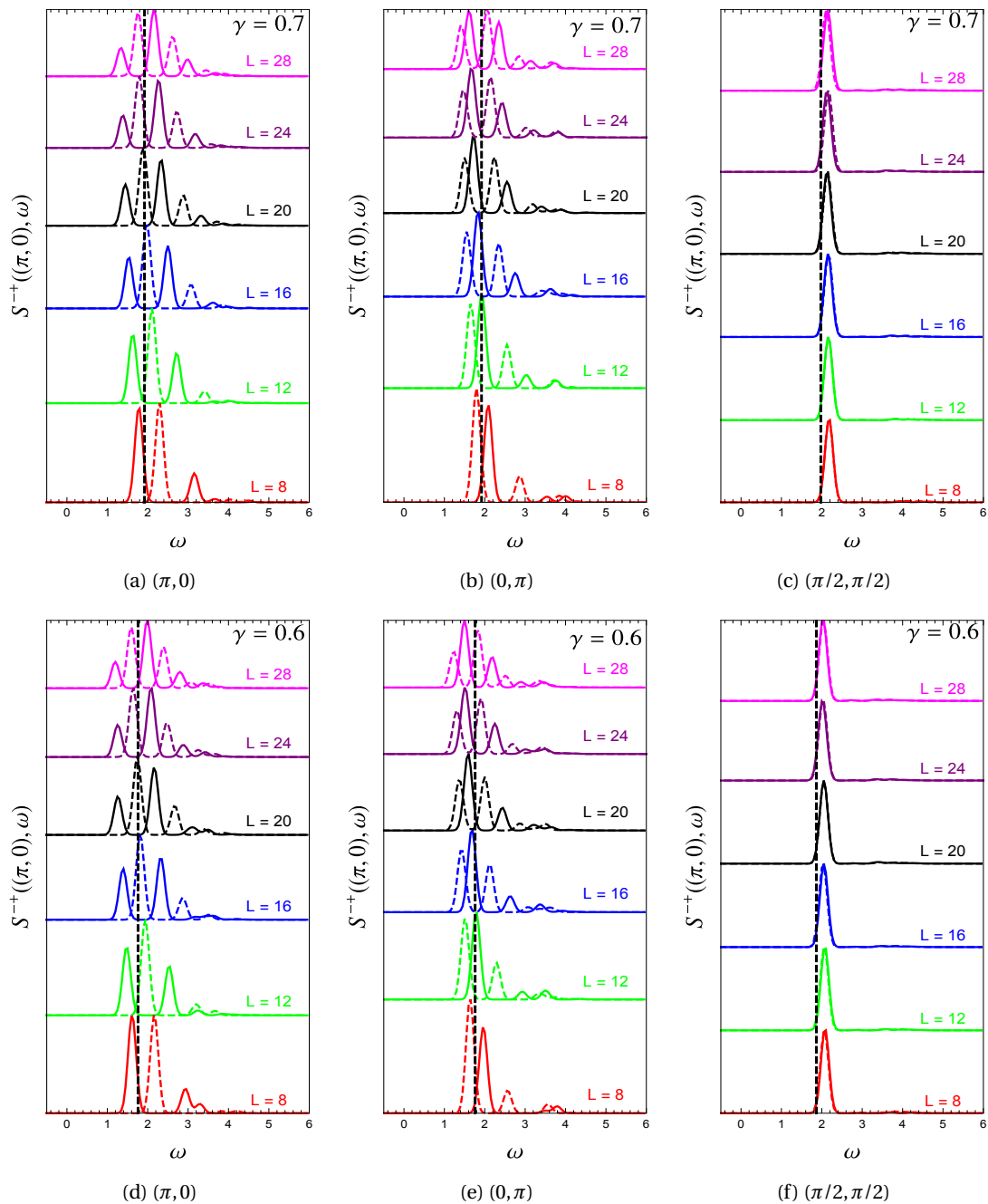


Figure C.7 – Evolution of TDSF for $\gamma = 0.7$ (top) and $\gamma = 0.6$ (bottom), at q-points $(\pi, 0)$ (left), $(0, \pi)$ (center) and $(\pi/2, \pi/2)$ (right) as we increase system size. The solid line represents ABC and dashed line represents the PBC. The dashed vertical line indicates the energy of the self-consistent spin wave result from chapter 3.

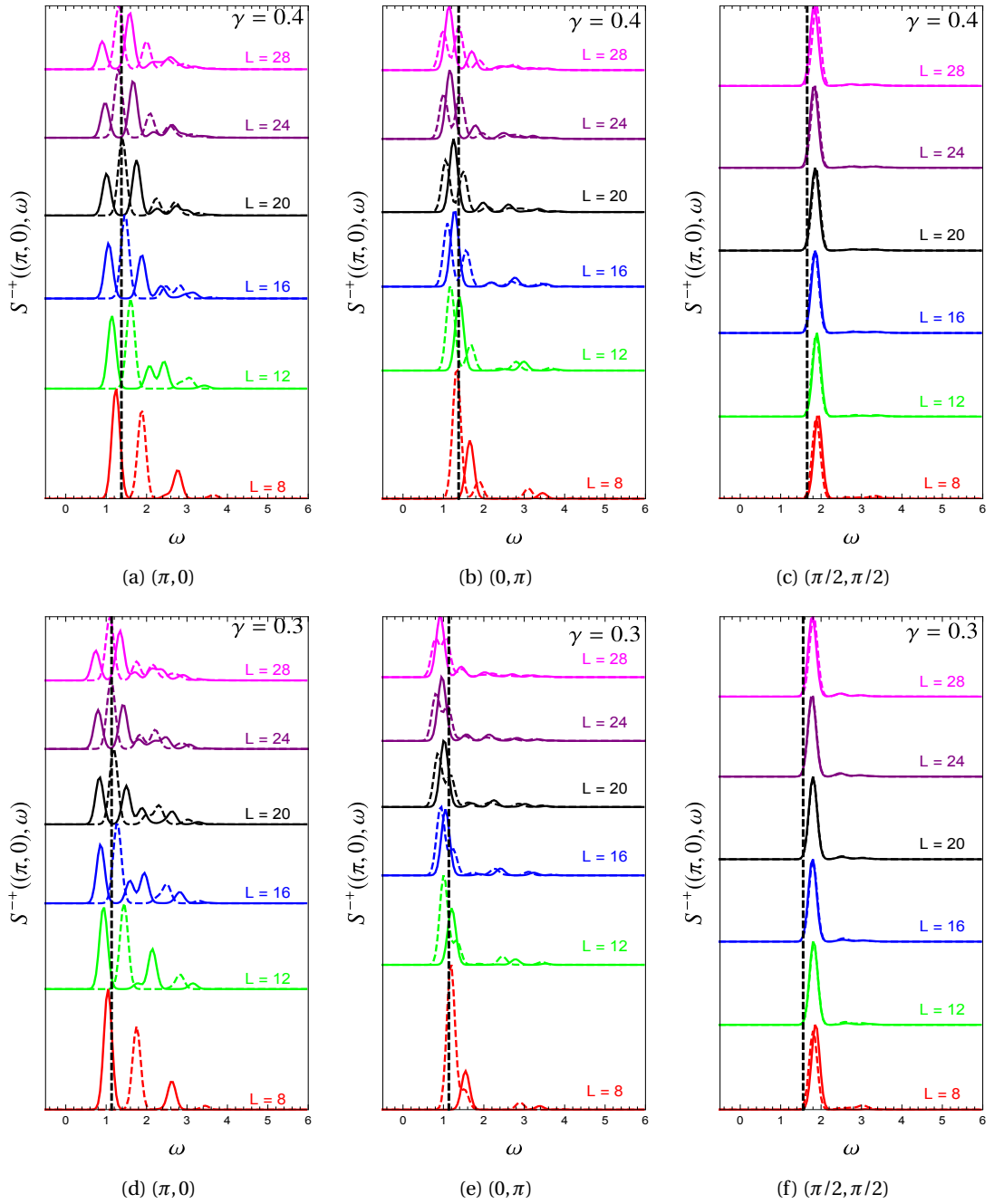


Figure C.8 – Evolution of TDSF for $\gamma = 0.4$ (top) and $\gamma = 0.3$ (bottom), at q-points $(\pi, 0)$ (left), $(0, \pi)$ (center) and $(\pi/2, \pi/2)$ (right) as we increase system size. The solid line represents ABC and dashed line represents the PBC. The dashed vertical line indicates the energy of the self-consistent spin wave result from chapter 3.

Appendix C. Additional figures

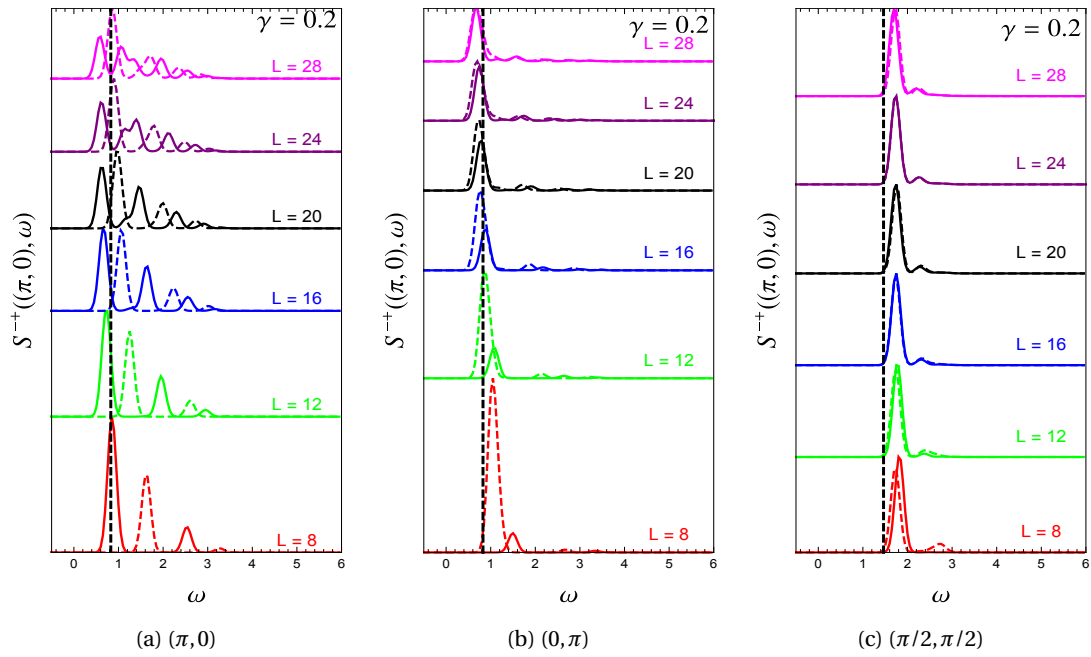


Figure C.9 – Evolution of TDSF for $\gamma = 0.2$ (top), at q-points $(\pi, 0)$ (a), $(0, \pi)$ (b) and $(\pi/2, \pi/2)$ (c) as we increase system size. The solid line represents ABC and dashed line represents the PBC. The dashed vertical line indicates the energy of the self-consistent spin wave result from chapter 3.

RMS of spinon separation

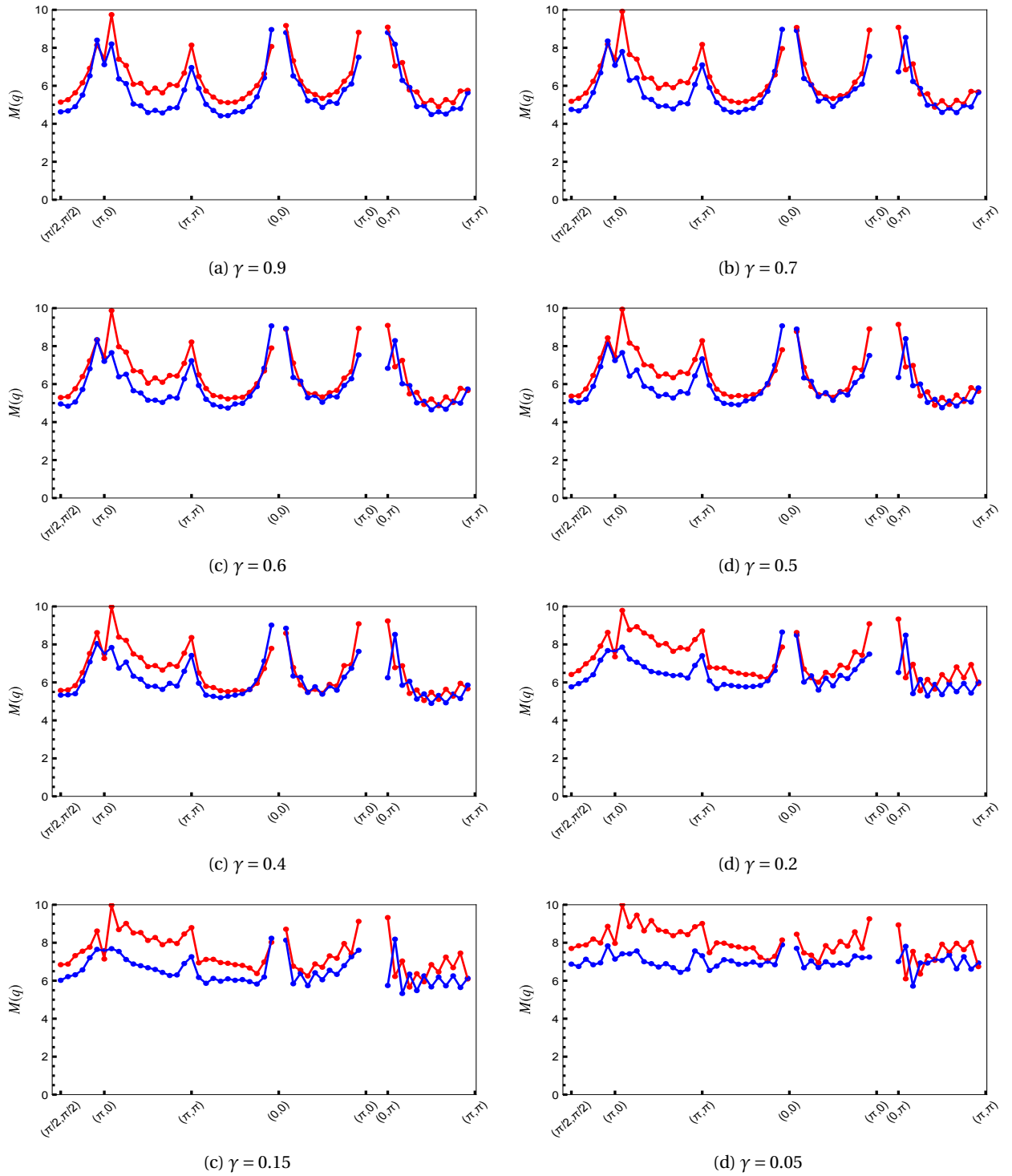


Figure C.10 – Root mean square separation as defined in Eq(5.46) at various γ values. Anti-periodic boundary condition is represented by blue dots and Periodic boundary is represented by red dots.

CDF of spinon separation at L=24 (ABC)

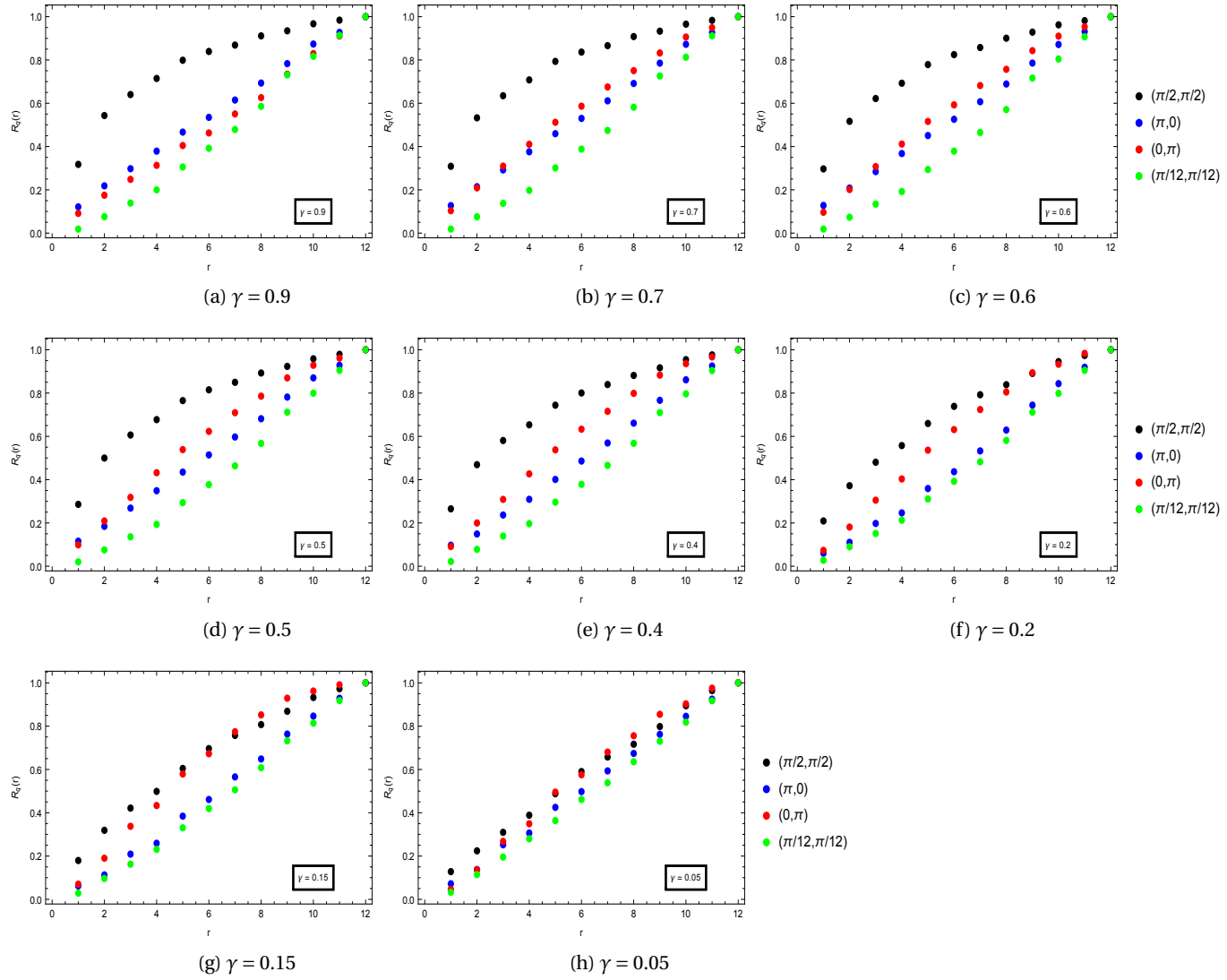


Figure C.11 – CDF of spinon separation at q points $(\pi/2, \pi/2)$ (black), $(\pi, 0)$ (blue), $(0, \pi)$ (red), $(\pi/12, \pi/12)$ (green) for different.

CDF of spinon separation at L=24 (PBC)

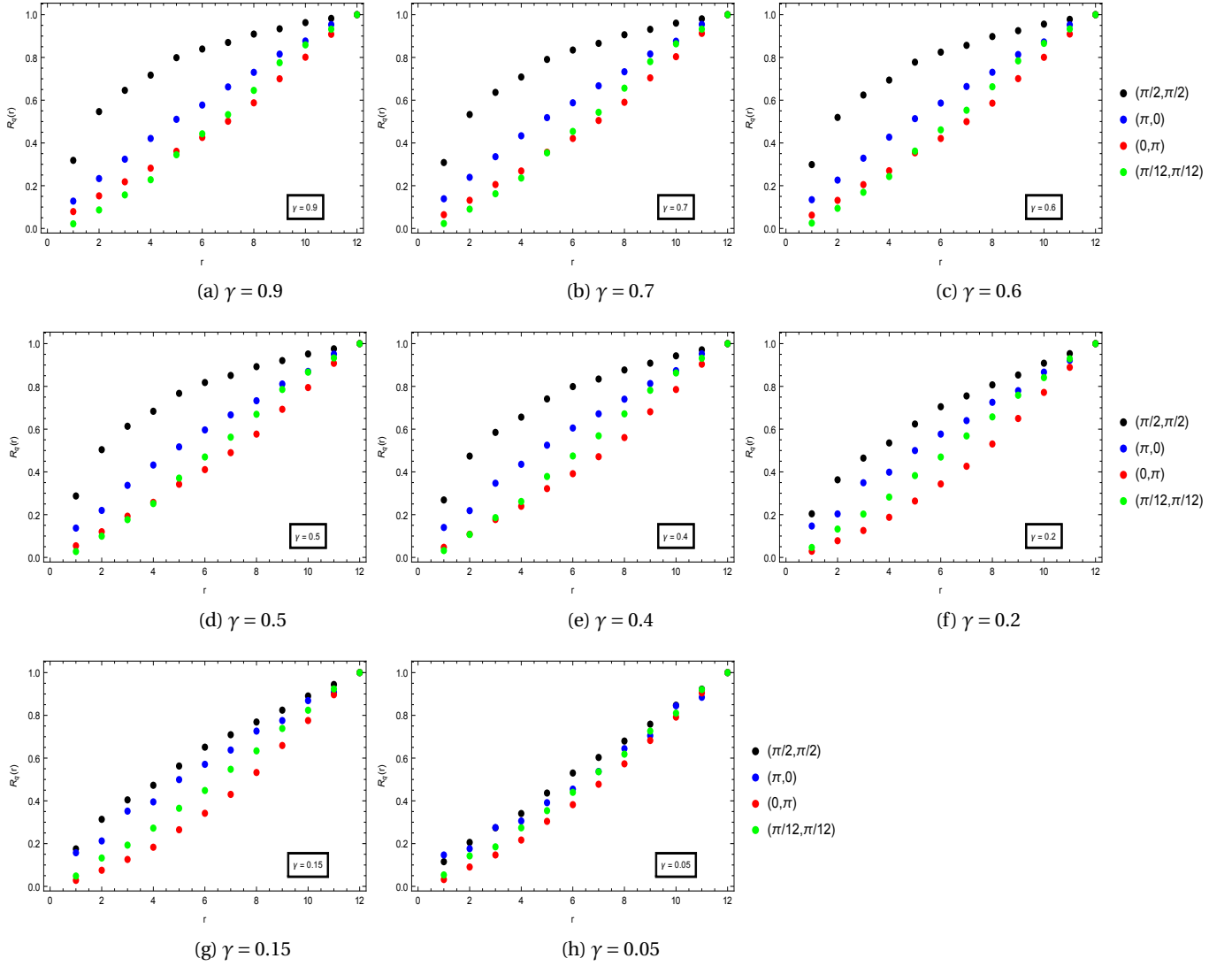


Figure C.12 – CDF of spinon separation at q points $(\pi/2, \pi/2)$ (black), $(\pi, 0)$ (blue), $(0, \pi)$ (red), $(\pi/12, \pi/12)$ (green) for different γ .

CDF of spinon separation at different system sizes with ABC at $q = (\pi, 0)$

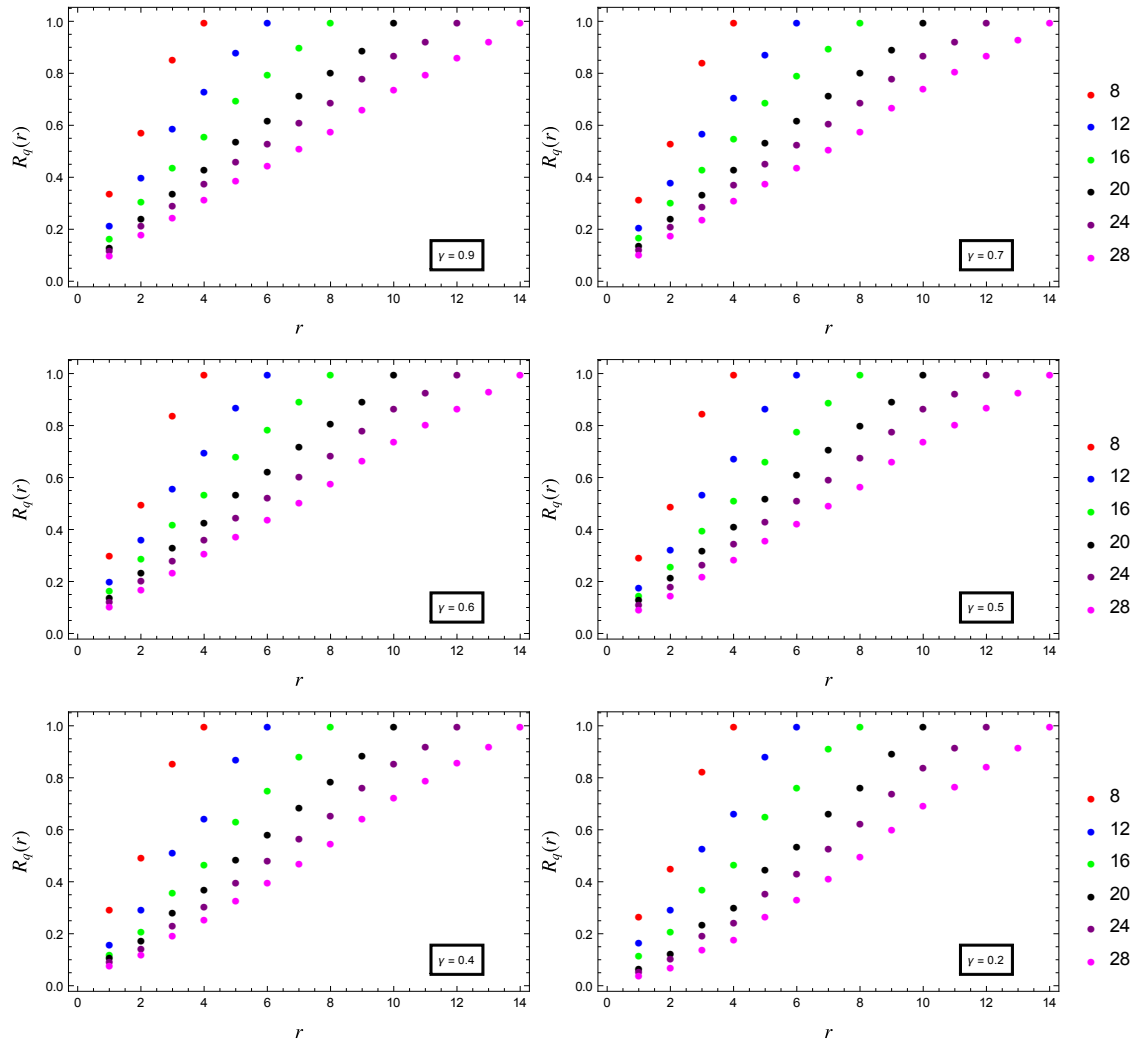


Figure C.13 – CDF of spinon separation at $(\pi, 0)$ for various system sizes $L = 8, 12, 16, 20, 24, 28$ represented by red, blue, green, black, brown and magenta respectively. The system has ABC.

CDF of spinon separation at different system sizes with ABC at $q = (0, \pi)$

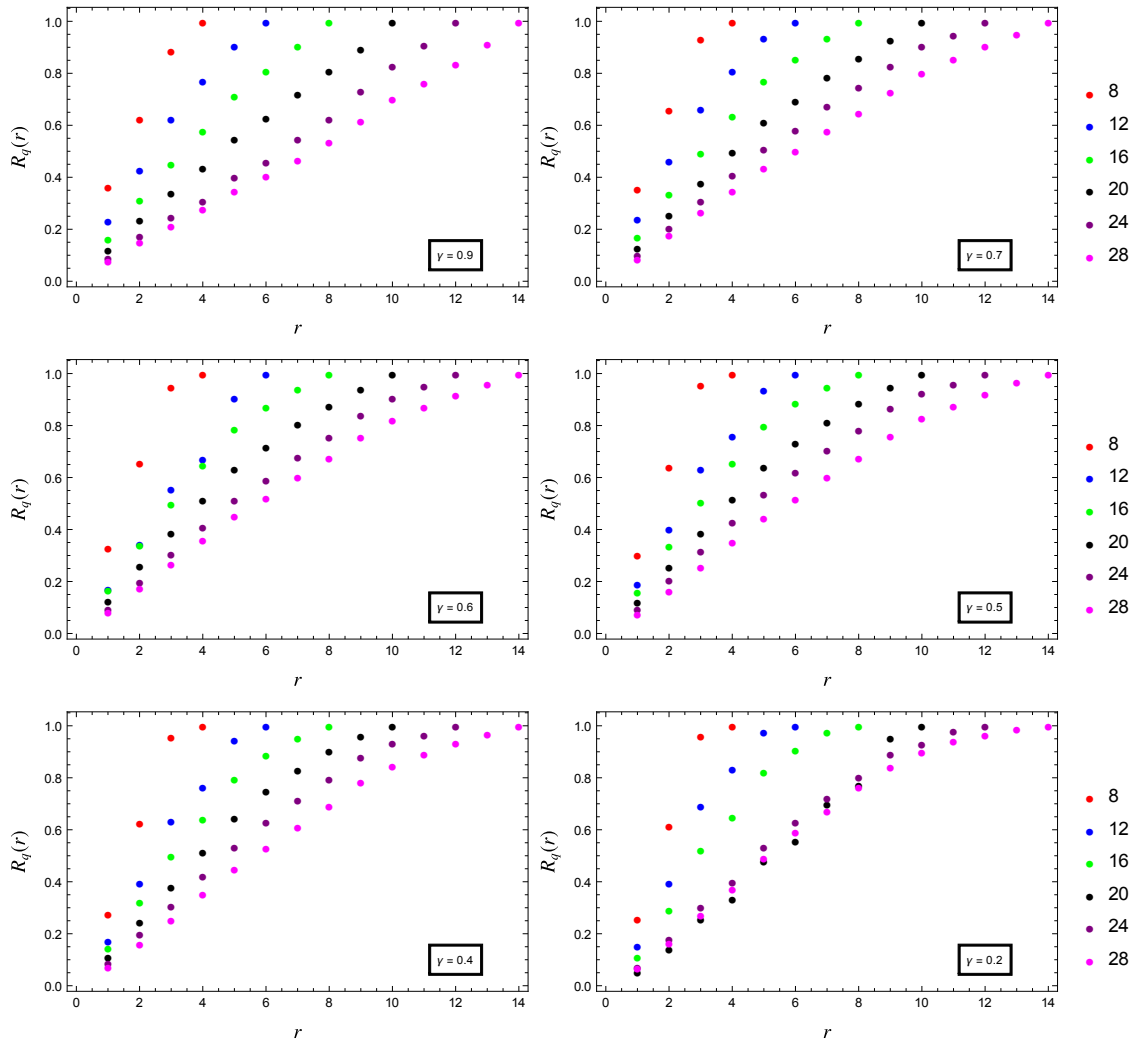


Figure C.14 – CDF of spinon separation at $(0, \pi)$ for various system sizes $L = 8, 12, 16, 20, 24, 28$ represented by red, blue, green, black, brown and magenta respectively. The system has ABC.

CDF of spinon separation at different system sizes with ABC at $q = (\pi/2, \pi/2)$

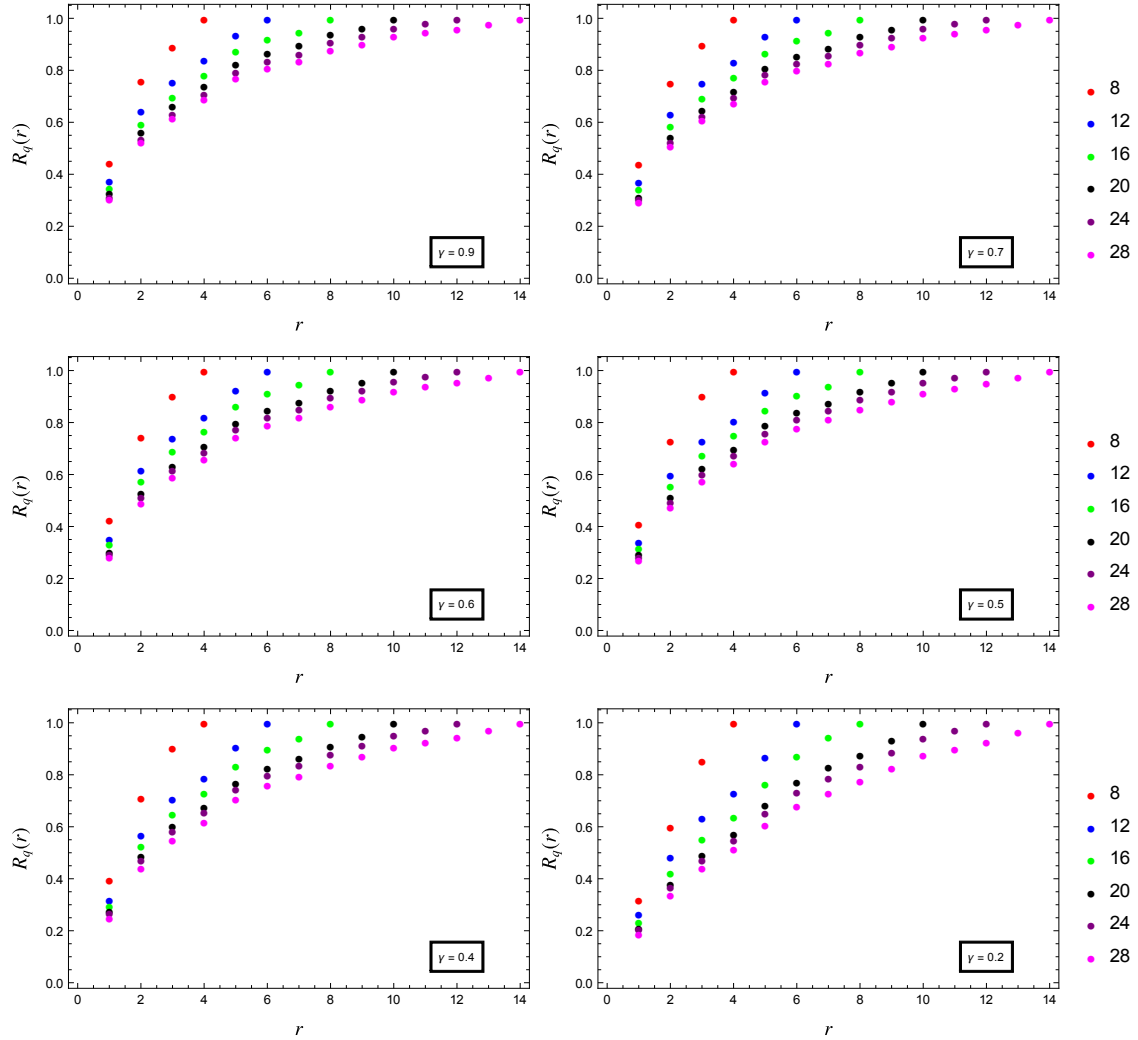


Figure C.15 – CDF of spinon separation at $(\pi/2, \pi/2)$ for various system sizes $L = 8, 12, 16, 20, 24, 28$ represented by red, blue, green, black, brown and magenta respectively. The system has ABC.

CDF of spinon separation at different system sizes with PBC at $q = (\pi, 0)$

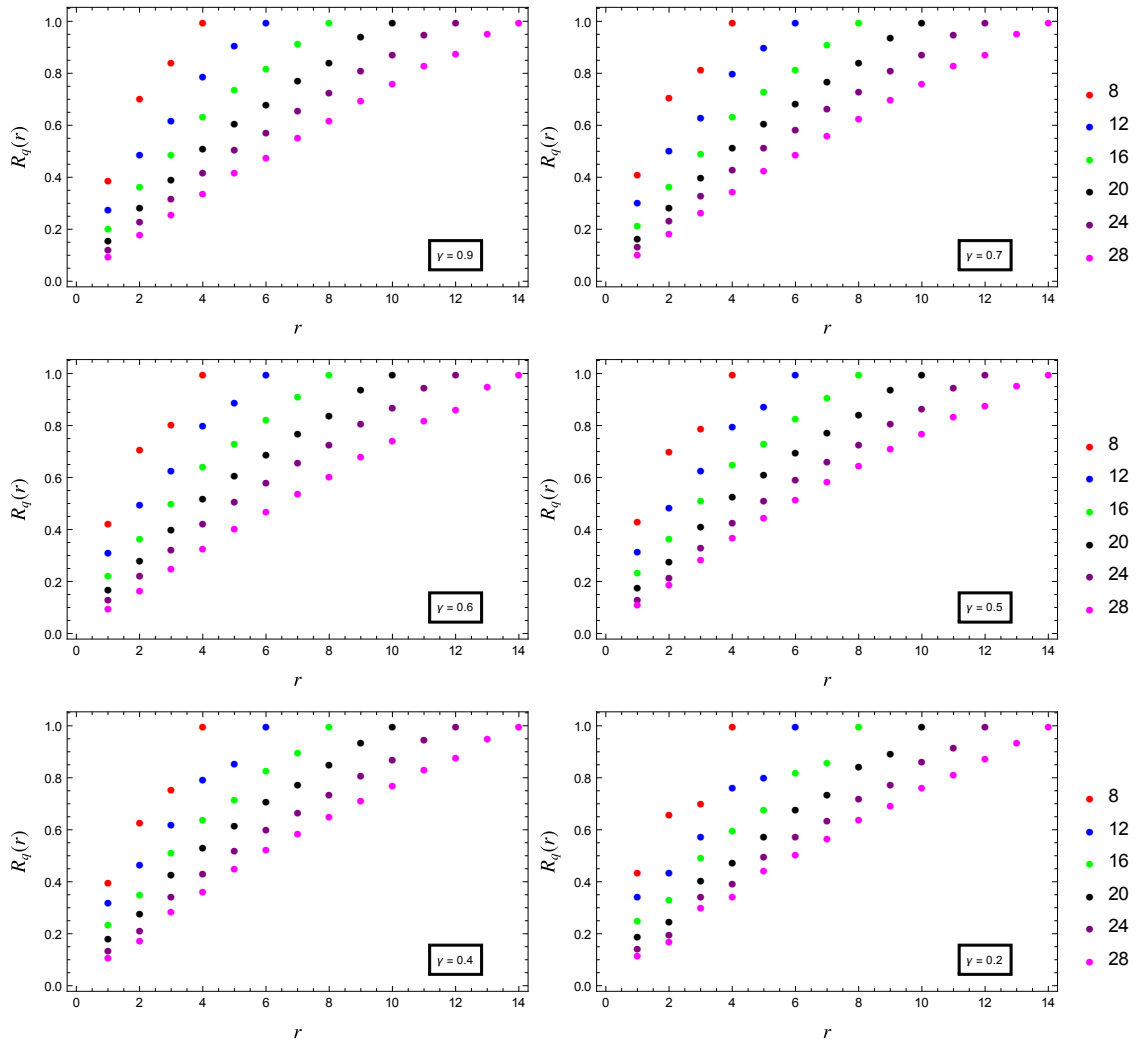


Figure C.16 – CDF of spinon separation at $(\pi, 0)$ for various system sizes $L = 8, 12, 16, 20, 24, 28$ represented by red, blue, green, black, brown and magenta respectively. The system has PBC.

CDF of spinon separation at different system sizes with PBC at $q = (0, \pi)$

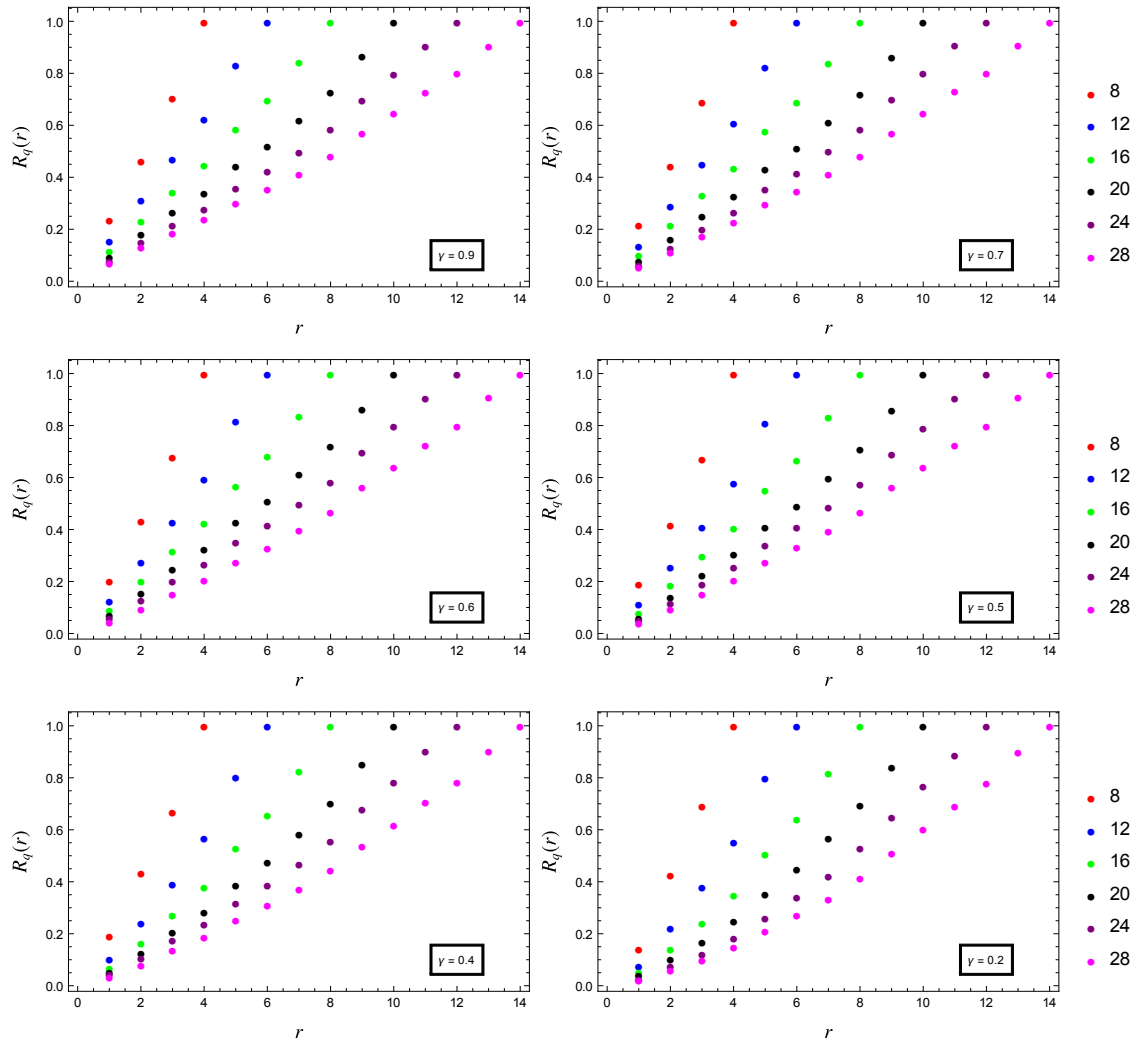


Figure C.17 – CDF of spinon separation at $(0, \pi)$ for various system sizes $L = 8, 12, 16, 20, 24, 28$ represented by red, blue, green, black, brown and magenta respectively. The system has PBC.

CDF of spinon separation at different system sizes with PBC at $q = (\pi/2, \pi/2)$

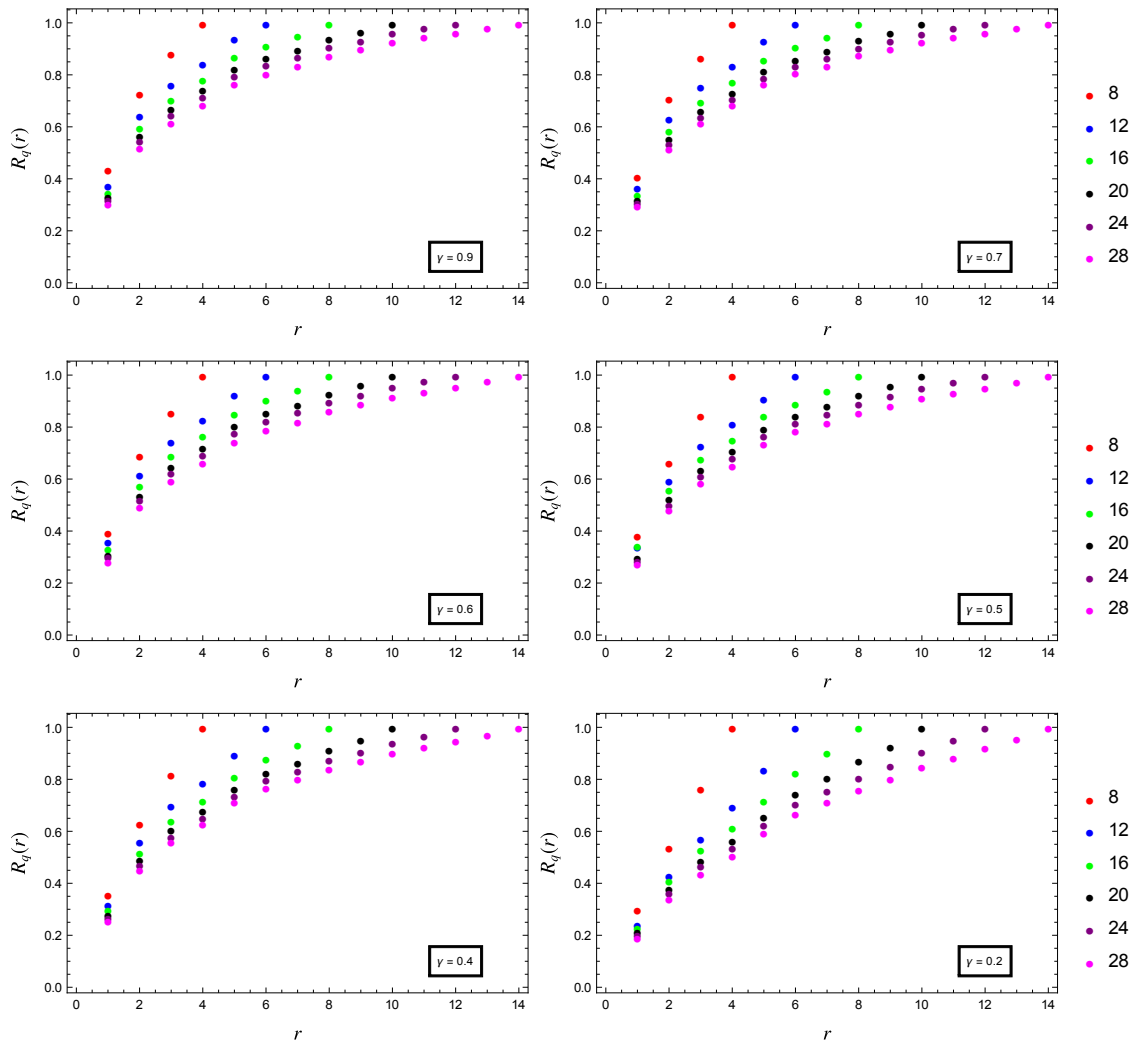


Figure C.18 – CDF of spinon separation at $(\pi/2, \pi/2)$ for various system sizes $L = 8, 12, 16, 20, 24, 28$ represented by red, blue, green, black, brown and magenta respectively. The system has PBC.

Finite size effects on RMS spinon separation for ABC

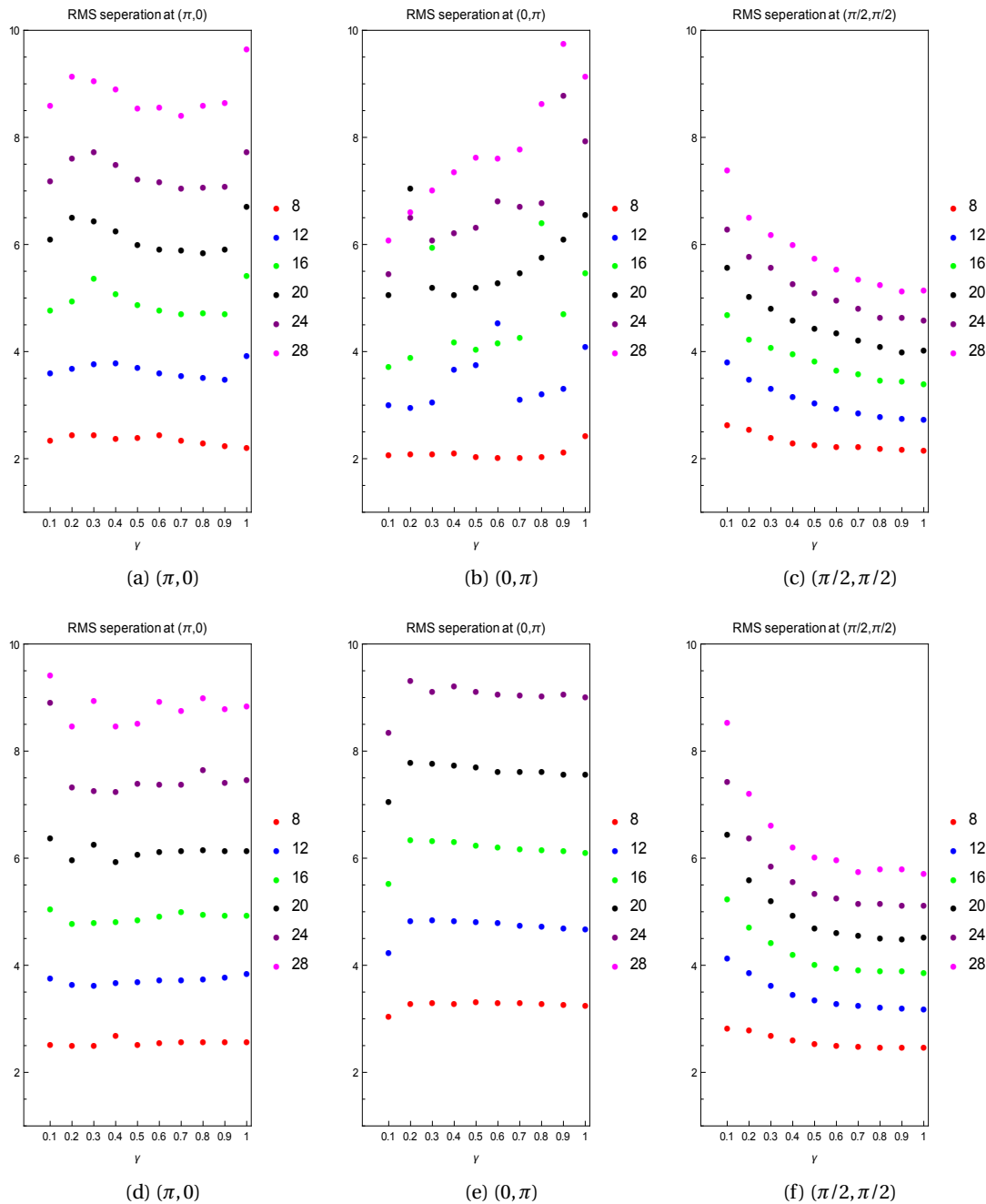


Figure C.19 – Evolution of RMS spinon separation with system size for ABC(top) and PBC(bottom) at q points $(\pi, 0)$ (left), $(0, \pi)$ (center) and $(\pi/2, \pi/2)$ (right).

Bibliography

- Ian Affleck. Exact correlation amplitude for the heisenberg antiferromagnetic chain. *Journal of Physics A: Mathematical and General*, 31(20):4573, 1998. URL <http://stacks.iop.org/0305-4470/31/i=20/a=002>.
- Ian Affleck and Bertrand I Halperin. On a renormalization group approach to dimensional crossover. *Journal of Physics A: Mathematical and General*, 29(11):2627–2631, jun 1996. doi: 10.1088/0305-4470/29/11/003. URL <https://doi.org/10.1088%2F0305-4470%2F29%2F11%2F003>.
- Ian Affleck, Z. Zou, T. Hsu, and P. W. Anderson. $Su(2)$ gauge symmetry of the large- u limit of the hubbard model. *Phys. Rev. B*, 38:745–747, Jul 1988. doi: 10.1103/PhysRevB.38.745. URL <https://link.aps.org/doi/10.1103/PhysRevB.38.745>.
- P. W. Anderson. An approximate quantum theory of the antiferromagnetic ground state. *Phys. Rev.*, 86:694–701, Jun 1952. doi: 10.1103/PhysRev.86.694. URL <https://link.aps.org/doi/10.1103/PhysRev.86.694>.
- P. W. Anderson, G. Baskaran, Z. Zou, and T. Hsu. Resonating–valence-bond theory of phase transitions and superconductivity in $la_2 cuo_4$ -based compounds. *Phys. Rev. Lett.*, 58:2790–2793, Jun 1987. doi: 10.1103/PhysRevLett.58.2790. URL <https://link.aps.org/doi/10.1103/PhysRevLett.58.2790>.
- P.W. Anderson. Resonating valence bonds: A new kind of insulator? *Materials Research Bulletin*, 8(2):153 – 160, 1973. ISSN 0025-5408. doi: [https://doi.org/10.1016/0025-5408\(73\)90167-0](https://doi.org/10.1016/0025-5408(73)90167-0). URL <http://www.sciencedirect.com/science/article/pii/0025540873901670>.
- Leon Balents. Spin liquids in frustrated magnets. *Nature*, 464:199 EP –, Mar 2010. URL <https://doi.org/10.1038/nature08917>.
- J. Bardeen, L. N. Cooper, and J. R. Schrieffer. Theory of superconductivity. *Phys. Rev.*, 108: 1175–1204, Dec 1957. doi: 10.1103/PhysRev.108.1175. URL <https://link.aps.org/doi/10.1103/PhysRev.108.1175>.
- G. Baskaran, Z. Zou, and P.W. Anderson. The resonating valence bond state and high- t_c superconductivity — a mean field theory. *Solid State Communications*, 63(11):973 – 976,

Bibliography

1987. ISSN 0038-1098. doi: [https://doi.org/10.1016/0038-1098\(87\)90642-9](https://doi.org/10.1016/0038-1098(87)90642-9). URL <http://www.sciencedirect.com/science/article/pii/0038109887906429>.
- H. Bethe. Zur theorie der metalle. *Zeitschrift für Physik*, 71(3):205–226, Mar 1931. ISSN 0044-3328. doi: [10.1007/BF01341708](https://doi.org/10.1007/BF01341708). URL <https://doi.org/10.1007/BF01341708>.
- F. Bloch. Zur theorie des ferromagnetismus. *Zeitschrift für Physik*, 61(3):206–219, Mar 1930. ISSN 0044-3328. doi: [10.1007/BF01339661](https://doi.org/10.1007/BF01339661). URL <https://doi.org/10.1007/BF01339661>.
- F. Bloch. Bremsvermögen von atomen mit mehreren elektronen. *Zeitschrift für Physik*, 81(5): 363–376, May 1933. ISSN 0044-3328. doi: [10.1007/BF01344553](https://doi.org/10.1007/BF01344553). URL <https://doi.org/10.1007/BF01344553>.
- M. Brookes. The matrix reference manual. [online]<http://www.ee.imperial.ac.uk/hp/staff/dmb/matrix/intro.html>, 2011.
- D. C. Cabra, A. Honecker, and P. Pujol. Magnetization plateaux in n -leg spin ladders. *Phys. Rev. B*, 58:6241–6257, Sep 1998. doi: [10.1103/PhysRevB.58.6241](https://link.aps.org/doi/10.1103/PhysRevB.58.6241). URL <https://link.aps.org/doi/10.1103/PhysRevB.58.6241>.
- Matteo Calandra Buonaura and Sandro Sorella. Numerical study of the two-dimensional heisenberg model using a green function monte carlo technique with a fixed number of walkers. *Phys. Rev. B*, 57:11446–11456, May 1998. doi: [10.1103/PhysRevB.57.11446](https://link.aps.org/doi/10.1103/PhysRevB.57.11446). URL <https://link.aps.org/doi/10.1103/PhysRevB.57.11446>.
- Jean-Sébastien Caux and Rob Hagemans. The four-spinon dynamical structure factor of the heisenberg chain. *Journal of Statistical Mechanics: Theory and Experiment*, 2006(12): P12013–P12013, dec 2006. doi: [10.1088/1742-5468/2006/12/p12013](https://doi.org/10.1088/1742-5468/2006/12/p12013). URL <https://doi.org/10.1088/1742-5468/2006/12/p12013>.
- Jean-Sébastien Caux, Rob Hagemans, and Jean Michel Maillet. Computation of dynamical correlation functions of heisenberg chains: the gapless anisotropic regime. *Journal of Statistical Mechanics: Theory and Experiment*, 2005(09):P09003–P09003, sep 2005. doi: [10.1088/1742-5468/2005/09/p09003](https://doi.org/10.1088/1742-5468/2005/09/p09003). URL <https://doi.org/10.1088/1742-5468/2005/09/p09003>.
- P. Chandra, P. Coleman, and A. I. Larkin. Ising transition in frustrated heisenberg models. *Phys. Rev. Lett.*, 64:88–91, Jan 1990. doi: [10.1103/PhysRevLett.64.88](https://link.aps.org/doi/10.1103/PhysRevLett.64.88). URL <https://link.aps.org/doi/10.1103/PhysRevLett.64.88>.
- N. B. Christensen, H. M. Rønnow, D. F. McMorrow, A. Harrison, T. G. Perring, M. Enderle, R. Coldea, L. P. Regnault, and G. Aeppli. Quantum dynamics and entanglement of spins on a square lattice. *Proceedings of the National Academy of Sciences*, 104(39):15264–15269, 2007. ISSN 0027-8424. doi: [10.1073/pnas.0703293104](https://www.pnas.org/content/104/39/15264). URL <https://www.pnas.org/content/104/39/15264>.

- R. Coldea, D. A. Tennant, A. M. Tsvetik, and Z. Tylczynski. Experimental realization of a 2d fractional quantum spin liquid. *Phys. Rev. Lett.*, 86:1335–1338, Feb 2001(a). doi: 10.1103/PhysRevLett.86.1335. URL <https://link.aps.org/doi/10.1103/PhysRevLett.86.1335>.
- R. Coldea, S. M. Hayden, G. Aeppli, T. G. Perring, C. D. Frost, T. E. Mason, S.-W. Cheong, and Z. Fisk. Spin waves and electronic interactions in La_2CuO_4 . *Phys. Rev. Lett.*, 86:5377–5380, Jun 2001b. doi: 10.1103/PhysRevLett.86.5377. URL <https://link.aps.org/doi/10.1103/PhysRevLett.86.5377>.
- Sidney Coleman. Quantum sine-gordon equation as the massive thirring model. *Phys. Rev. D*, 11:2088–2097, Apr 1975. doi: 10.1103/PhysRevD.11.2088. URL <https://link.aps.org/doi/10.1103/PhysRevD.11.2088>.
- B. Dalla Piazza, M. Mourigal, N. B. Christensen, G. J. Nilsen, P. Tregenna-Piggott, T. G. Perring, M. Enderle, D. F. McMorrow, D. A. Ivanov, and H. M. Rønnow. Fractional excitations in the square-lattice quantum antiferromagnet. *Nature Physics*, 11:62 EP –, Dec 2014a. URL <http://dx.doi.org/10.1038/nphys3172>. Article.
- Bastien Dalla Piazza. Theories of experimentally observed excitation spectra of square lattice antiferromagnets. 2014b. doi: 10.5075/epfl-thesis-6090. URL <http://infoscience.epfl.ch/record/197821>.
- M. A. de Vries, J. R. Stewart, P. P. Deen, J. O. Piatek, G. J. Nilsen, H. M. Rønnow, and A. Harrison. Scale-free antiferromagnetic fluctuations in the $s = 1/2$ kagome antiferromagnet herbertsmithite. *Phys. Rev. Lett.*, 103:237201, Dec 2009. doi: 10.1103/PhysRevLett.103.237201. URL <https://link.aps.org/doi/10.1103/PhysRevLett.103.237201>.
- G. Delfino and G. Mussardo. Nonintegrable aspects of the multifrequency Sine-Gordon model. *Nucl. Phys.*, B516:675–703, 1998. doi: 10.1016/S0550-3213(98)00063-7.
- G. Delfino, G. Mussardo, and P. Simonetti. Non-integrable quantum field theories as perturbations of certain integrable models. *Nuclear Physics B*, 473(3):469 – 508, 1996. ISSN 0550-3213. doi: [https://doi.org/10.1016/0550-3213\(96\)00265-9](https://doi.org/10.1016/0550-3213(96)00265-9). URL <http://www.sciencedirect.com/science/article/pii/0550321396002659>.
- Keith J. Devlin. *The millennium problems : the seven greatest unsolved mathematical puzzles of our time*. New York : Basic Books, [2002] ©2002, 2002. URL <https://search.library.wisc.edu/catalog/999935001502121>. Includes bibliographical references (pages [229]-230) and index.
- L. D. Faddeev, E. K. Sklyanin, and L. A. Takhtajan. The Quantum Inverse Problem Method. 1. *Theor. Math. Phys.*, 40:688–706, 1980. [Teor. Mat. Fiz.40,194(1979)].
- L.D. Faddeev and L.A. Takhtajan. What is the spin of a spin wave? *Physics Letters A*, 85(6): 375 – 377, 1981. ISSN 0375-9601. doi: [https://doi.org/10.1016/0375-9601\(81\)90335-2](https://doi.org/10.1016/0375-9601(81)90335-2). URL <http://www.sciencedirect.com/science/article/pii/0375960181903352>.

Bibliography

- Ludvig Faddeev. Integrable models in 1+1 dimensional quantum field theory. Technical report, France, 1982. URL http://inis.iaea.org/search/search.aspx?orig_q=RN:14762434. CEA-CONF-6565.
- Francesco Ferrari and Federico Becca. Spectral signatures of fractionalization in the frustrated heisenberg model on the square lattice. *Phys. Rev. B*, 98:100405, Sep 2018. doi: 10.1103/PhysRevB.98.100405. URL <https://link.aps.org/doi/10.1103/PhysRevB.98.100405>.
- P. Fonseca and A. Zamolodchikov. Ising field theory in a magnetic field: Analytic properties of the free energy. *Journal of Statistical Physics*, 110(3):527–590, Mar 2003. ISSN 1572-9613. doi: 10.1023/A:1022147532606. URL <https://doi.org/10.1023/A:1022147532606>.
- W. M. C. Foulkes, L. Mitas, R. J. Needs, and G. Rajagopal. Quantum monte carlo simulations of solids. *Rev. Mod. Phys.*, 73:33–83, Jan 2001. doi: 10.1103/RevModPhys.73.33. URL <https://link.aps.org/doi/10.1103/RevModPhys.73.33>.
- Eduardo Fradkin. *Field Theories of Condensed Matter Physics*. Cambridge University Press, 2 edition, 2013. doi: 10.1017/CBO9781139015509.
- Michael Freedman, Alexei Kitaev, Michael Larsen, and Zhenghan Wang. Topological quantum computation. *Bull. Amer. Math. Soc. (N.S.)*, 40(1):31–38, 2003. ISSN 0273-0979. doi: 10.1090/S0273-0979-02-00964-3. URL <https://doi.org/10.1090/S0273-0979-02-00964-3>. Mathematical challenges of the 21st century (Los Angeles, CA, 2000).
- E. A. Ghioldi, M. G. Gonzalez, L. O. Manuel, and A. E. Trumper. RVB signatures in the spin dynamics of the square-lattice heisenberg antiferromagnet. *EPL (Europhysics Letters)*, 113(5):57001, mar 2016. doi: 10.1209/0295-5075/113/57001. URL <https://doi.org/10.1209/0295-5075/113/57001>.
- T. Giamarchi and Oxford University Press. *Quantum Physics in One Dimension*. International Series of Monogr. Clarendon Press, 2004. ISBN 9780198525004. URL <https://books.google.ch/books?id=1MwTDAAAQBAJ>.
- Claudius Gros. Physics of projected wavefunctions. *Annals of Physics*, 189(1):53 – 88, 1989. ISSN 0003-4916. doi: [https://doi.org/10.1016/0003-4916\(89\)90077-8](https://doi.org/10.1016/0003-4916(89)90077-8). URL <http://www.sciencedirect.com/science/article/pii/0003491689900778>.
- F. D. M. Haldane. Nonlinear field theory of large-spin heisenberg antiferromagnets: Semiclassically quantized solitons of the one-dimensional easy-axis néel state. *Phys. Rev. Lett.*, 50:1153–1156, Apr 1983. doi: 10.1103/PhysRevLett.50.1153. URL <https://link.aps.org/doi/10.1103/PhysRevLett.50.1153>.
- F. D. M. Haldane. Exact jastrow-gutzwiller resonating-valence-bond ground state of the spin- $\frac{1}{2}$ antiferromagnetic heisenberg chain with $1/r^2$ exchange. *Phys. Rev. Lett.*, 60:635–638, Feb 1988. doi: 10.1103/PhysRevLett.60.635. URL <https://link.aps.org/doi/10.1103/PhysRevLett.60.635>.

- Karen A. Hallberg, Peter Horsch, and Gerardo Martínez. Numerical renormalization-group study of the correlation functions of the antiferromagnetic spin-1/2 heisenberg chain. *Phys. Rev. B*, 52:R719–R722, Jul 1995. doi: 10.1103/PhysRevB.52.R719. URL <https://link.aps.org/doi/10.1103/PhysRevB.52.R719>.
- W. K. Hastings. Monte carlo sampling methods using markov chains and their applications. 57 (1):97–109, 1970. ISSN 00063444. doi: 10.2307/2334940. URL <http://www.jstor.org/stable/2334940>.
- N. S. Headings, S. M. Hayden, R. Coldea, and T. G. Perring. Anomalous high-energy spin excitations in the high- T_c superconductor-parent antiferromagnet La_2CuO_4 . *Phys. Rev. Lett.*, 105:247001, Dec 2010. doi: 10.1103/PhysRevLett.105.247001. URL <https://link.aps.org/doi/10.1103/PhysRevLett.105.247001>.
- T. Holstein and H. Primakoff. Field dependence of the intrinsic domain magnetization of a ferromagnet. *Phys. Rev.*, 58:1098–1113, Dec 1940. doi: 10.1103/PhysRev.58.1098. URL <https://link.aps.org/doi/10.1103/PhysRev.58.1098>.
- Robert Jastrow. Many-body problem with strong forces. *Phys. Rev.*, 98:1479–1484, Jun 1955. doi: 10.1103/PhysRev.98.1479. URL <https://link.aps.org/doi/10.1103/PhysRev.98.1479>.
- M. Jeong, F. Bert, P. Mendels, F. Duc, J. C. Trombe, M. A. de Vries, and A. Harrison. Field-induced freezing of a quantum spin liquid on the kagome lattice. *Phys. Rev. Lett.*, 107:237201, Nov 2011. doi: 10.1103/PhysRevLett.107.237201. URL <https://link.aps.org/doi/10.1103/PhysRevLett.107.237201>.
- P. Jordan and E. Wigner. Über das paulische äquivalenzverbot. *Zeitschrift für Physik*, 47(9): 631–651, Sep 1928. ISSN 0044-3328. doi: 10.1007/BF01331938. URL <https://doi.org/10.1007/BF01331938>.
- Michael Karabach, Gerhard Müller, Harvey Gould, and Jan Tobochnik. Introduction to the bethe ansatz i. *Computers in Physics*, 11(1):36–43, 1997. doi: 10.1063/1.4822511. URL <https://aip.scitation.org/doi/abs/10.1063/1.4822511>.
- Michael Karbach, Gerhard Müller, A. Hamid Bougourzi, Andreas Fledderjohann, and Karl-Heinz Mütter. Two-spinon dynamic structure factor of the one-dimensional $s=$ heisenberg antiferromagnet. *Phys. Rev. B*, 55:12510–12517, May 1997. doi: 10.1103/PhysRevB.55.12510. URL <https://link.aps.org/doi/10.1103/PhysRevB.55.12510>.
- C. Kim, A. Y. Matsuura, Z.-X. Shen, N. Motoyama, H. Eisaki, S. Uchida, T. Tohyama, and S. Maekawa. Observation of spin-charge separation in one-dimensional SrCuO_2 . *Phys. Rev. Lett.*, 77:4054–4057, Nov 1996. doi: 10.1103/PhysRevLett.77.4054. URL <https://link.aps.org/doi/10.1103/PhysRevLett.77.4054>.
- Eugene H. Kim and J. Sólyom. Opening of the haldane gap in anisotropic two- and four-leg spin ladders. *Phys. Rev. B*, 60:15230–15244, Dec 1999. doi: 10.1103/PhysRevB.60.15230. URL <https://link.aps.org/doi/10.1103/PhysRevB.60.15230>.

Bibliography

- Alexei Kitaev. Anyons in an exactly solved model and beyond. *Annals of Physics*, 321(1):2 – 111, 2006. ISSN 0003-4916. doi: <https://doi.org/10.1016/j.aop.2005.10.005>. URL <http://www.sciencedirect.com/science/article/pii/S0003491605002381>. January Special Issue.
- Steven A. Kivelson, Daniel S. Rokhsar, and James P. Sethna. Topology of the resonating valence-bond state: Solitons and high- T_c superconductivity. *Phys. Rev. B*, 35:8865–8868, Jun 1987. doi: 10.1103/PhysRevB.35.8865. URL <https://link.aps.org/doi/10.1103/PhysRevB.35.8865>.
- Ryogo Kubo. The spin-wave theory of antiferromagnetics. *Phys. Rev.*, 87:568–580, Aug 1952. doi: 10.1103/PhysRev.87.568. URL <https://link.aps.org/doi/10.1103/PhysRev.87.568>.
- Bella Lake, D. Alan Tennant, Chris D. Frost, and Stephen E. Nagler. Quantum criticality and universal scaling of a quantum antiferromagnet. *Nature Materials*, 4(4):329–334, 2005. ISSN 1476-4660. doi: 10.1038/nmat1327. URL <https://doi.org/10.1038/nmat1327>.
- Bella Lake, Alexei M. Tsvelik, Susanne Notbohm, D. Alan Tennant, Toby G. Perring, Manfred Reehuis, Chinnathambi Sekar, Gernot Krabbes, and Bernd Büchner. Confinement of fractional quantum number particles in a condensed-matter system. *Nature Physics*, 6:50 EP –, Nov 2009. URL <http://dx.doi.org/10.1038/nphys1462>. Article.
- LD Landau. Oscillations in a fermi liquid. *SOVIET PHYSICS JETP-USSR*, 5(1):101–108, 1957a.
- LD Landau. Kinetic equation approach. *Sov. Phys. JETP*, 3:920, 1957b.
- LD Landau. Landau theory of fermi liquids reformulated. *Sov. Phys. JETP*, 8:70, 1959.
- Tao Li and Fan Yang. Variational study of the neutron resonance mode in the cuprate superconductors. *Phys. Rev. B*, 81:214509, Jun 2010. doi: 10.1103/PhysRevB.81.214509. URL <https://link.aps.org/doi/10.1103/PhysRevB.81.214509>.
- S. Liang, B. Douçot, and P. W. Anderson. Some new variational resonating-valence-bond-type wave functions for the spin- $\frac{1}{2}$ antiferromagnetic heisenberg model on a square lattice. *Phys. Rev. Lett.*, 61:365–368, Jul 1988. doi: 10.1103/PhysRevLett.61.365. URL <https://link.aps.org/doi/10.1103/PhysRevLett.61.365>.
- Elliott Lieb, Theodore Schultz, and Daniel Mattis. Two soluble models of an antiferromagnetic chain. *Annals of Physics*, 16(3):407 – 466, 1961. ISSN 0003-4916. doi: [https://doi.org/10.1016/0003-4916\(61\)90115-4](https://doi.org/10.1016/0003-4916(61)90115-4). URL <http://www.sciencedirect.com/science/article/pii/S0003491661901154>.
- Elliott H. Lieb and F. Y. Wu. Absence of mott transition in an exact solution of the short-range, one-band model in one dimension. *Phys. Rev. Lett.*, 20:1445–1448, Jun 1968. doi: 10.1103/PhysRevLett.20.1445. URL <https://link.aps.org/doi/10.1103/PhysRevLett.20.1445>.
- John H. Lowenstein. INTRODUCTION TO THE BETHE ANSATZ APPROACH IN (1+1)-DIMENSIONAL MODELS. In *Les Houches Summer School in Theoretical Physics: Recent Advances in Field Theory and Statistical Mechanics Les Houches, France, August 2-September 10, 1982*, 1982.

- A. Luther and I. Peschel. Calculation of critical exponents in two-dimensions from quantum field theory in one-dimension. *Phys. Rev.*, B12:3908–3917, 1975. doi: 10.1103/PhysRevB.12.3908.
- S. Mandelstam. Soliton operators for the quantized sine-gordon equation. *Phys. Rev. D*, 11: 3026–3030, May 1975. doi: 10.1103/PhysRevD.11.3026. URL <https://link.aps.org/doi/10.1103/PhysRevD.11.3026>.
- J. Brad Marston and Ian Affleck. Large- n limit of the hubbard-heisenberg model. *Phys. Rev. B*, 39:11538–11558, Jun 1989. doi: 10.1103/PhysRevB.39.11538. URL <https://link.aps.org/doi/10.1103/PhysRevB.39.11538>.
- D Mattis and Elliott H. Lieb. Exact solution of a many-fermion system and its associated boson field. *Journal of Mathematical Physics*, 6, 02 1965. doi: 10.1063/1.1704281.
- Nicholas Metropolis, Arianna W. Rosenbluth, Marshall N. Rosenbluth, Augusta H. Teller, and Edward Teller. Equation of state calculations by fast computing machines. *The Journal of Chemical Physics*, 21(6):1087–1092, 1953. doi: 10.1063/1.1699114. URL <https://doi.org/10.1063/1.1699114>.
- T. Miyazaki, D. Yoshioka, and M. Ogata. Anisotropic two-dimensional heisenberg model studied by the schwinger-boson gutzwiller-projection method. *Phys. Rev. B*, 51:2966–2971, Feb 1995. doi: 10.1103/PhysRevB.51.2966. URL <https://link.aps.org/doi/10.1103/PhysRevB.51.2966>.
- Martin Mourigal. Order and dynamics of model quantum antiferromagnets. 2011. doi: 10.5075/epfl-thesis-5081. URL <http://infoscience.epfl.ch/record/165768>.
- Martin Mourigal, Mechthild Enderle, Axel Klöpperpieper, Jean-Sébastien Caux, Anne Stunault, and Henrik M. Rønnow. Fractional spinon excitations in the quantum heisenberg antiferromagnetic chain. *Nature Physics*, 9:435 EP –, Jun 2013. URL <http://dx.doi.org/10.1038/nphys2652>. Article.
- Gerhard Müller, Harry Thomas, Hans Beck, and Jill C. Bonner. Quantum spin dynamics of the antiferromagnetic linear chain in zero and nonzero magnetic field. *Phys. Rev. B*, 24: 1429–1467, Aug 1981. doi: 10.1103/PhysRevB.24.1429. URL <https://link.aps.org/doi/10.1103/PhysRevB.24.1429>.
- H. F. Pen, J. van den Brink, D. I. Khomskii, and G. A. Sawatzky. Orbital ordering in a two-dimensional triangular lattice. *Phys. Rev. Lett.*, 78:1323–1326, Feb 1997. doi: 10.1103/PhysRevLett.78.1323. URL <https://link.aps.org/doi/10.1103/PhysRevLett.78.1323>.
- A.M. Polyakov and P.B. Wiegmann. Goldstone fields in two dimensions with multivalued actions. *Physics Letters B*, 141(3):223 – 228, 1984. ISSN 0370-2693. doi: [https://doi.org/10.1016/0370-2693\(84\)90206-5](https://doi.org/10.1016/0370-2693(84)90206-5). URL <http://www.sciencedirect.com/science/article/pii/0370269384902065>.

Bibliography

- M. Powalski, G. S. Uhrig, and K. P. Schmidt. Roton minimum as a fingerprint of magnon-higgs scattering in ordered quantum antiferromagnets. *Phys. Rev. Lett.*, 115:207202, Nov 2015. doi: 10.1103/PhysRevLett.115.207202. URL <https://link.aps.org/doi/10.1103/PhysRevLett.115.207202>.
- M. Powalski, K. P. Schmidt, and G. S. Uhrig. Mutually attracting spin waves in the square-lattice quantum antiferromagnet. *SciPost Phys.*, 4:001, 2018. doi: 10.21468/SciPostPhys.4.1.001. URL <https://scipost.org/10.21468/SciPostPhys.4.1.001>.
- H. M. Rønnow, D. F. McMorrow, R. Coldea, A. Harrison, I. D. Youngson, T. G. Perring, G. Aeppli, O. Syljuåsen, K. Lefmann, and C. Rischel. Spin dynamics of the 2d spin $\frac{1}{2}$ quantum antiferromagnet copper deuteroformate tetradeuterate (cftd). *Phys. Rev. Lett.*, 87:037202, Jun 2001. doi: 10.1103/PhysRevLett.87.037202. URL <https://link.aps.org/doi/10.1103/PhysRevLett.87.037202>.
- Andrei E. Ruckenstein, Peter J. Hirschfeld, and J. Appel. Mean-field theory of high- t_c superconductivity: The superexchange mechanism. *Physical review. B, Condensed matter*, 36:857–860, 08 1987. doi: 10.1103/PhysRevB.36.857.
- Karl J. Runge. Finite-size study of the ground-state energy, susceptibility, and spin-wave velocity for the heisenberg antiferromagnet. *Phys. Rev. B*, 45:12292–12296, Jun 1992. doi: 10.1103/PhysRevB.45.12292. URL <https://link.aps.org/doi/10.1103/PhysRevB.45.12292>.
- J. Schlappa, K. Wohlfeld, K. J. Zhou, M. Mourigal, M. W. Haverkort, V. N. Strocov, L. Hozoi, C. Monney, S. Nishimoto, S. Singh, A. Revcolevschi, J.-S. Caux, L. Patthey, H. M. Rønnow, J. van den Brink, and T. Schmitt. Spin-orbital separation in the quasi-one-dimensional mott insulator Sr_2CuO_3 . *Nature*, 485:82 EP –, Apr 2012. URL <https://doi.org/10.1038/nature10974>.
- H. J. Schulz. Phase diagrams and correlation exponents for quantum spin chains of arbitrary spin quantum number. *Phys. Rev. B*, 34:6372–6385, Nov 1986. doi: 10.1103/PhysRevB.34.6372. URL <https://link.aps.org/doi/10.1103/PhysRevB.34.6372>.
- D. Sénéchal. *An Introduction to Bosonization*, pages 139–186. Springer New York, New York, NY, 2004. ISBN 978-0-387-21717-8. doi: 10.1007/0-387-21717-7_4. URL https://doi.org/10.1007/0-387-21717-7_4.
- Hui Shao, Yan Qi Qin, Sylvain Capponi, Stefano Chesi, Zi Yang Meng, and Anders W. Sandvik. Nearly deconfined spinon excitations in the square-lattice spin-1/2 heisenberg antiferromagnet. *Phys. Rev. X*, 7:041072, Dec 2017. doi: 10.1103/PhysRevX.7.041072. URL <https://link.aps.org/doi/10.1103/PhysRevX.7.041072>.
- B. Sriram Shastry. Exact solution of an $s=1/2$ heisenberg antiferromagnetic chain with long-ranged interactions. *Phys. Rev. Lett.*, 60:639–642, Feb 1988. doi: 10.1103/PhysRevLett.60.639. URL <https://link.aps.org/doi/10.1103/PhysRevLett.60.639>.

- E. K. Sklyanin. Quantum version of the method of inverse scattering problem. *Journal of Soviet Mathematics*, 19(5):1546–1596, Jul 1982. ISSN 1573-8795. doi: 10.1007/BF01091462. URL <https://doi.org/10.1007/BF01091462>.
- M. Skoulatos, J. P. Goff, C. Geibel, E. E. Kaul, R. Nath, N. Shannon, B. Schmidt, A. P. Murani, P. P. Deen, M. Enderle, and A. R. Wildes. Spin correlations and exchange in square-lattice frustrated ferromagnets. *EPL (Europhysics Letters)*, 88:57005, 12 2009. doi: 10.1209/0295-5075/88/57005.
- S. P. Strong and A. J. Millis. Competition between singlet formation and magnetic ordering in one-dimensional spin systems. *Phys. Rev. Lett.*, 69:2419–2422, Oct 1992. doi: 10.1103/PhysRevLett.69.2419. URL <https://link.aps.org/doi/10.1103/PhysRevLett.69.2419>.
- L. A. Takhtajan and L. D. Faddeev. The Quantum method of the inverse problem and the Heisenberg XYZ model. *Russ. Math. Surveys*, 34(5):11–68, 1979. [Usp. Mat. Nauk34,no.5,13(1979)].
- D. Alan Tennant, Roger A. Cowley, Stephen E. Nagler, and Alexei M. Tsvelik. Measurement of the spin-excitation continuum in one-dimensional KCuF_3 using neutron scattering. *Phys. Rev. B*, 52:13368–13380, Nov 1995. doi: 10.1103/PhysRevB.52.13368. URL <https://link.aps.org/doi/10.1103/PhysRevB.52.13368>.
- J Timonen and A Luther. Continuum-limit correlation functions for the spin-one anisotropic heisenberg chain. *Journal of Physics C: Solid State Physics*, 18(7):1439–1454, mar 1985. doi: 10.1088/0022-3719/18/7/011. URL <https://doi.org/10.1088/0022-3719/18/7/011>.
- S. Tomonaga. Remarks on Bloch’s Method of Sound Waves applied to Many-Fermion Problems. *Prog. Theor. Phys.*, 5:544–569, 1950. doi: 10.1143/PTP.5.544.
- Nandini Trivedi and D. M. Ceperley. Green-function monte carlo study of quantum antiferromagnets. *Phys. Rev. B*, 40:2737–2740, Aug 1989. doi: 10.1103/PhysRevB.40.2737. URL <https://link.aps.org/doi/10.1103/PhysRevB.40.2737>.
- J. van den Brink, W. Stekelenburg, D. I. Khomskii, G. A. Sawatzky, and K. I. Kugel. Elementary excitations in the coupled spin-orbital model. *Phys. Rev. B*, 58:10276–10282, Oct 1998. doi: 10.1103/PhysRevB.58.10276. URL <https://link.aps.org/doi/10.1103/PhysRevB.58.10276>.
- Edward Witten. Nonabelian bosonization in two dimensions. *Comm. Math. Phys.*, 92(4): 455–472, 1984. URL <https://projecteuclid.org/443/euclid.cmp/1103940923>.

Noore Elahi Shaik

Route Cantonale, 39B,
St-sulpice, Lausanne-1025.

D.O.B: 06/07/1992

Phone: +41787236769

email: eshaik3@gmail.com

Nationality: Indian



KEY COMPETENCES

- Sharp analytical skills ; Affinity for complex problems
- Proficient in Languages C,C++ and python ; Skilled with Matlab and Mathematica ;Parallel programing and object oriented Programing
- Languages: Telugu (mother tongue); Hindi (native); English (professional proficiency); French (CEFR B1)

EDUCATION

École Polytechnique Fédérale De Lausanne

Ph.D., Physics

2015-current

M.Sc., Physics

2013-2015

Indian Institute of Technology Guwahati

B. Tech., Engineering Physics

2009-2013

OTHER COMPETENCES

- Teaching experience of 5 years in various physics courses
- Basic knowledge of Financial analysis through CFA Level I, Dec 2018.
- Event management: Volunteer at Photonics 2010, ICANN-2011 conferences
- Team Work: Member of EPFL associations YUVA (2014-2015), CUBALIENTE(2016-2018)

PERSONAL INTERESTS

Learning and performing Afro-Latin dances; Fitness enthusiast; Student of martial art capoeira.

